Development of a Discrete Fluid-Structure Interaction Method for Cardiovascular Applications

A thesis submitted to the University of Manchester
for the degree of Doctor of Philosophy
in the Faculty of Science and Engineering

2019

By
Benjamin Joseph Owen
School of Mechanical, Aerospace and Civil Engineering

Contents

Word Count: $\sim$ 78,000

List of Tables

List of Figures

Nomenclature

Recurring abbreviations and symbols are summarised here. Note that due to the cross-disciplinary nature of this work, some symbols have multiple definitions. In this case, the intended definition will be made explicitly clear in the text.

Abbreviations

AAA	Abdominal aortic aneurysm
BGK	Bhatnagar-Gross-Krook
BGSS	Block Gauss-Seidel scheme
CAD	Coronary artery disease
CHD	Congenital heart disease
CPU	Central processing unit
CSS	Conventional staggered scheme
CT	Computed tomography
DEM	Discrete element method
FEM	Finite element method
FFR	Fractional flow reserve

FSG	Fluid-solid-growth
FSI	Fluid-structure interaction
FVM	Finite volume method
GPU	Graphics processing unit
HPC	High-performance computing
IBM	Immersed boundary method
ICA	Intracranial aneurysm
IVUS	Intravenous ultrasound
LBM	Lattice Boltzmann method
MRI	Magnetic resonance imaging
MRT	Multi-relaxation time
OSI	Oscillitory shear index
RBC	Red blood cell
SN	Spring network
SPH	Smoothed particle hydrodynamics
US	Ultrasound
VAD	Ventricular assist device
WBC	White blood cell

WSS	Wall shear stress
WSSG	Wall shear stress gradient

Dimensionless Quantities

Ma	Mach number
R	Fluid-structure time step ratio
Re	Reynolds number
St	Strouhal number

Greek Symbols

α	Angular acceleration
β	Critical time step constant
$\mathbf{\Pi}$	Stress tensor
$\boldsymbol{\xi}$	Molecular velocity
ϵ	Scaling factor for Lagrangian force
Γ	Lagrangian domain
ν	Kinematic viscosity, Poisson's ratio
Ω	Collision operator, Eulerian domain
ω	Angular velocity
ρ_f, ρ_s	Fluid and structure density

τ	Relaxation parameter
θ	Orientation
$\tilde{\delta}$	Discrete Dirac delta function

Roman Symbols

$\boldsymbol{F}_{ij}$	Force of particle j acting on particle i
$\boldsymbol{M}_{ij}$	Moment of particle j acting on particle i
$\boldsymbol{n}$	Particle orientation vector
$\boldsymbol{r}_{ij}$	Vector between particle i and j
$\dot{U}$	Rate of change in internal energy
A	Cross sectional area
a	Equilibrium bond length, particle translational acceleration
$B_{1,2,3}$	Model axial, shear and bending stiffness parameters
c_s	Lattice speed of sound
$c_{A,D,B}$	Material axial, shear and bending stiffness coefficients
E	Specific energy, Young's modulus
H	Channel height
L	Domain length
p	Pressure

r_{ij}	Distance between particle i and j
U	Internal energy
v	Particle translational velocity
x	Particle position

List of Publications & Awards

The outcomes of this work led to a series of research outputs, in the form of journal publications. Significant contributions to the following list of papers have been made during this PhD program:

1. B. Owen, C. Lowe, N. Ashton, P. Mandal, S. Rogers, W. Wein, C. Mccollum and A. Revell. Computational hemodynamics of abdominal aortic aneurysms: Three-dimensional ultrasound versus computed tomography. *P. I. Mech. Eng. H*, 230(3), 2016

2. B. Owen, N. Bojdo, A. Jivkov, B. Keavney and A. Revell. Structural modelling of the cardiovascular system. *Biomech. Model. Mechan.*, 17(5), 2018

3. B. Owen, A. Nasar, A. Harwood, S. Hewitt, N. Bojdo, B. Keavney, B. Rogers and A. Revell. Vector-based discrete element method for solid elastic materials. *In Review*

4. B. Owen, J. O'Connor, A. Harwood, N. Bojdo, B. Keavney, and A. Revell. A discrete fluid-structure interaction approach for highly deformable elastic bodies. *In Preparation*

5. K. McGurk, B. Owen, W. Watson, O. Ryder, B. Keavney and A. Revell, Heritability and family-based GWAS analyses of turbulent blood flow and roughness of the thoracic ascending aorta: Novel measures of cardiovascular health *In Preparation*

During this PhD programme the following academic awards have been received:

1. **Richard Archer Memorial Prize**

   Demonstrating excellence in the field of Bioengineering.

2. **British Heart Foundation Travel Award**

   Postgraduate travel award to present research with a cardiovascular theme at the BioMedEng18 conference.

3. **Margaret Elizabeth Lee Fellowship**

   Postgraduate travel award to present research at the International Conference on Biomedical Technology 2017.

4. **EPSRC Doctoral Prize Fellowship**

   1 year post-doctoral development fellowship.

Abstract

Development of a Discrete Fluid-Structure Interaction Method for Cardiovascular Applications

Benjamin Joseph Owen

A thesis submitted to the University of Manchester for the degree of Doctor of Philosophy, 2019

The interaction between blood and cardiovascular tissue is known to play a significant role in the development cardiovascular diseases and associated conditions. With the ever increasing availability and performance of computational resources, in conjunction with improved understanding of the disease mechanisms, the integration of numerical analysis into *in silico* tools has become more prevalent. Once viewed as emerging technology, these tools are now being routinely utilised in clinical practice.

However, the majority of these tools consider the fluid or structure in isolation. This is due to the added complexity of coupling the methods and the computational cost incurred through modelling fluid-structure interaction using traditional continuum methods. As a result, discretisations of the structure used in fluid-structure interaction (FSI) methods tend to be simpler representations and offer limited potential to model complex non-linear material properties and discrete effects such as rupture.

The purpose of this work is to develop an efficient fluid-structure interaction method capable of modelling complex phenomena. The inherent parallel performance of discrete numerical methods is explored, with a long-term view to developing the method for use in clinical tools; where speed, robustness and adaptability are paramount. In the present work, the fluid is represented via the lattice Boltzmann method and the structure via the vector-based discrete ele-

ment method, known as the V-model. These solvers are strongly coupled using a version of the immersed boundary method based on direct forcing in a block Gauss-Seidel scheme, where the time step size of the fluid and structure are to be kept independent.

Validation results for the V-model show good agreement with analytical and numerical solutions for static and dynamic cantilever beam cases with constant and time-varying external loads. This demonstrates the V-model's ability to accurately capture the mechanical response of a material before extending the method to model more complex physics. GPU implementation of the V-model demonstrated speed-ups of x50 relative to an optimised serial CPU implementation. The FSI method demonstrated good agreement with numerical benchmark data while stochastic modelling of the structure material properties demonstrated the V-model's potential to model variation in cardiovascular tissue that occurs naturally and due to disease.

The major original contributions of this work include the implementation and elucidation of a recently developed structure model; which is used here for the first time with a lattice Boltzmann scheme. The work also provides first steps towards the use of stochastic modelling using the V-model, the first GPU implementation of the V-model, and development of the first strongly coupled fluid-structure interaction method to include the V-model.

Declaration

No portion of the work referred to in the thesis has been submitted in support of an application for another degree or qualification of this or any other university or other institute of learning.

Copyright

Acknowledgements

I would first like to thank Alistair for his guidance and support throughout this PhD that has gone beyond what can be expected of a supervisor, especially during the emergency meetings when "everything's gone wrong". It is a source of great relief and frustration that you were able to solve so many problems that I had been struggling with for days in literally seconds. I hope to one day also find the Dragon Scroll and gain this power.

I would also like to express my gratitude to Bernard, Adrian and Nick who have been able to impart their vast expertise on such a novice in their respective fields, allowing said novice to conduct this interdisciplinary work.

To Joe, Sam and Josh. Since I'm handing in third, Joe and Josh have used most of the good anecdotes from our time as PhD students. Fortunately "French Accent Mondays" has not yet been mentioned. Good luck with your acknowledgements Sam, should have handed in last year like you always said you would! I also have to thank all the boys at Old Bedians RUFC for providing welcome distraction both on the pitch and in the bar afterwards.

To Kathryn, thank you for your love and support, even as I got grumpier as submission day approached. Your pep talks kept me going and I have no doubt this whole process would have been so much harder without you.

And finally, thank you to my family who have all played a part in helping me get to where I am today. To my parents, Andrew and Vanessa, thank you for inspiring me. You have both been perfect role models and I hope that I have made you proud. Thank you to my brother Josh, and sister Sophie, for reminding me that there are more important things in life than PhDs and journal articles.

Chapter 1

Introduction

1.1 Background & Motivation

In recent years there has been increased interest in the inclusion of numerical analysis within clinical pipelines for the diagnosis and treatment of cardiovascular diseases such as coronary artery disease [10], congenital heart diseases [5, 11] and aneurysms [12]. When coupled with medical imaging, the use of numerical methods has the potential to offer greater insight into patient-specific conditions than traditional clinical practice alone. This enables more informed risk assessment, providing clinicians with greater information upon which to base their treatment decisions. Figure 1.1 shows an example pipeline integrating medical imaging with patient-specific computational modelling. The first examples of the use of computational fluid dynamics (CFD) in mainstream clinical medicine are already here, such as the virtual Fractional Flow Reserve analysis for coronary artery disease [10].

Numerical methods have also been successfully deployed to model cardiovascular structures such as aneurysms where rupture risk assessments can be conducted [12]. Again, patient-specific geometries can be included within the analysis using medical imaging. Many of these methods employ idealised tissue material models [13] to predict the mechanical response of the tissue to given loading conditions, with the tissue modelled as a continuum. However, recent work on the development of virtual histology techniques offers a promising route to including patient-specific material properties in numerical models in the future [14].

Fluid-structure interaction modelling involves the coupling of numerical methods for fluids and structures. Strong, or full two-way coupling may not be always necessary in cases where the structure deformation is small or the difference in time scales between the fluid and structure is large. However, for many cardiovascular diseases fluid-structure interaction (FSI) plays a key role in the pathogenesis or effects resulting from the disease due the high deformation levels and the cyclic nature of the system. It would therefore seem important that this interaction be modelled in any attempt to develop a digital analogue of the human body. However, the computational expense of modelling this interaction is not trivial and has traditionally limited its implementation to simpler representations of the fluid and structure [15] than in a standalone fluid or structure solver [16]. To date, the use of FSI has been limited by prohibitively long computational times, particularly in a clinical framework, where clinicians demand that results are required within a few hours. While this is most clearly evidenced in the heart itself, there have been a number of studies which propose that strong fluid-structure interaction is not essential to the reproduction of clinically observable haemodynamics in the major vessels of the cardiovascular system [17]. However, in many cases this assertion is difficult to fully accept on the basis of current medical imaging technology, where resolution in space and time remains relatively low. It is also generally the case that this conclusion is made on the basis of quite basic material and structure models; where linear behaviour and homogeneous properties are often assumed. It is quite likely that the prominence of fluid-structure coupling in some processes will rise in the coming years, as more detailed material properties are discerned and the availability of advanced FSI algorithms is more widespread. In addition, many cardiovascular diseases are strongly linked to local changes in the cardiovascular structure, including the development of defects such as rupture, or remodelling of tissue such as aneurysm growth. In these cases, an approach which is able to model the associated change in geometry of the structure seems essential.

Discrete methods, unlike traditional continuum methods, are well suited to modelling local changes within structures since particle connections can be easily created and broken according to the conditions experienced during a simulation with little addition treatment required. Examples of bond breaking and bond creating on-the-fly using the vector-based discrete element method are shown in Figure 1.2, demonstrating the capability of discrete methods. Furthermore, discrete methods can easily handle complex geometries. However, in general, discrete methods require far greater resolution than traditionally utilised methods

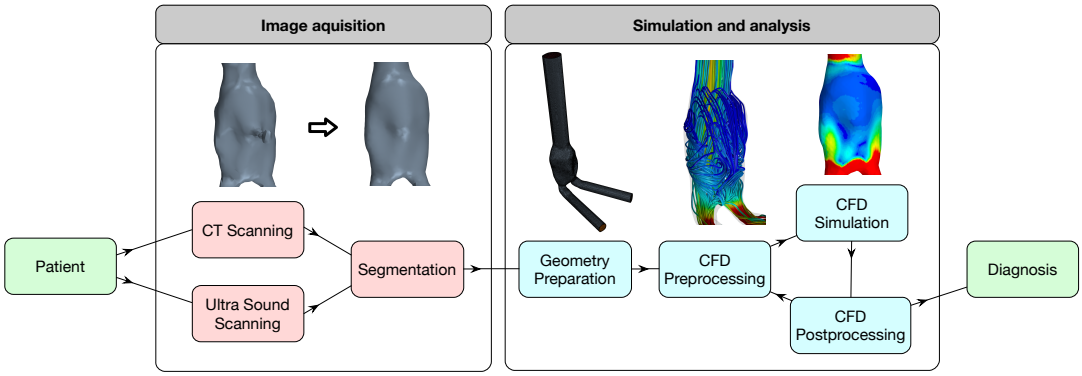

Figure 1.1: Example pipeline of numerical analysis in cardiovascular applications. Adapted from Owen et al. [1].

such as the finite element method, to be able to represent the characteristics of a structure or fluid accurately. As a result, discrete methods require significant and sometimes prohibitive additional computational resources. The use of high-performance computing clusters and parallelisation techniques has been exploited to reduce computational times of discrete methods, however traditional methods can also exploit these benefits to reduce their own computational times. As a consequence, discrete methods have traditionally been restricted to use at smaller length scales in cardiovascular applications as shown in Figure 1.3.

The use of graphics processing unit (GPU) architecture in scientific computing has opened an interesting avenue of research for numerical analysis of cardiovascular diseases. GPUs are an example of throughput-orientated architecture [18]. This type of architecture prioritises maximum throughput by parallelising large amounts of data across a greater number of processors. The clock speed of a GPU processor is far slower than that of a CPU processor, however due to a significantly larger number of processors, the overall throughput of data can be orders of magnitude greater. Discrete methods are well suited to GPU architecture since their governing equations, in general, require explicit and local operations. The computational speed-up of numerical solution of discrete element methods has already been demonstrated to be up to two orders of magnitude faster than previous best CPU implementations [19, 20]. Furthermore simulations can be conducted using portable and affordable hardware rather than relying on connection to large high performance computing clusters, perhaps improving the availability of such analysis [21].

A key motivation for the use of discrete methods involves the material properties

of cardiovascular structures. The mechanical response of the tissue is difficult to accurately predict since mechanical testing of the tissue *in vivo* is not possible. Continuum based models have been developed through *in vitro* mechanical testing on a number of samples of a given tissue, incorporating the hyperelastic and viscoelastic characteristics observed [13, 16]. However, precise properties will be patient-specific and will change over time; for instance the tissue is well known to change in smokers, and in particular where tissue has died. Furthermore, the variation of mechanical response between samples is relatively large, with recent studies suggesting that details of the microstructure should be included in future developments [22]. An alternative way to overcome these challenges is to directly model variation of material properties using discrete methods, as suggested by Brocklehurst et al. [23]. The effect of the natural or diseased variation in material properties can then be explored using stochastic techniques.

In view of this, a strong motivation for this work is to develop an efficient method

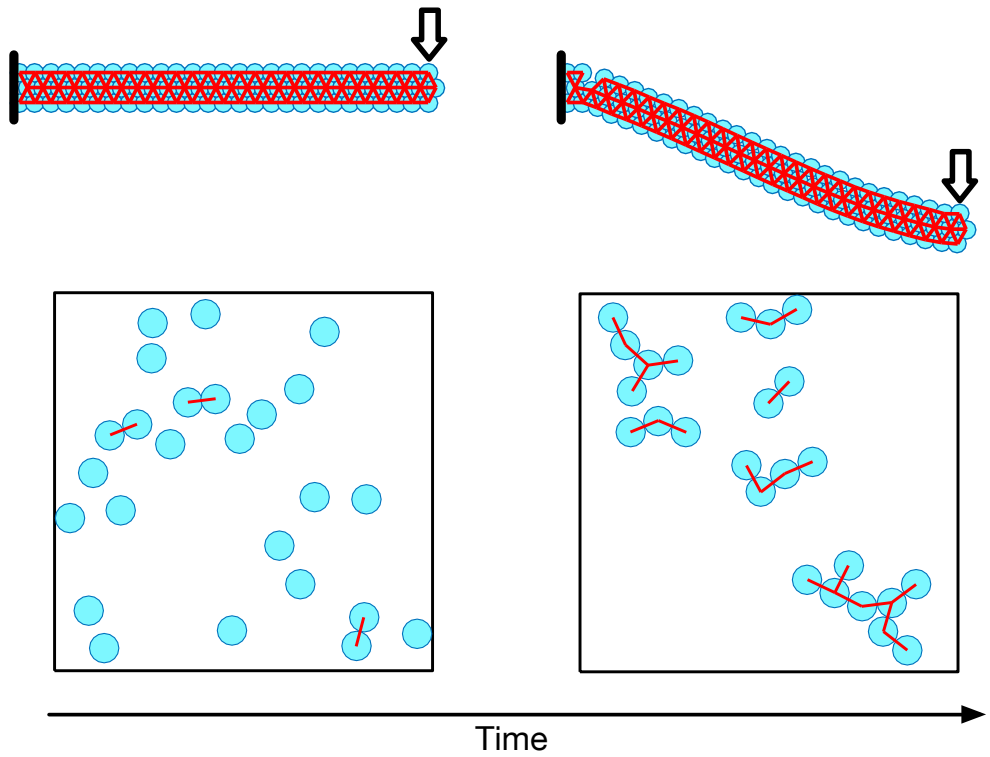

Figure 1.2: Structure remodelling examples using the vector-based discrete element method. Bonds are broken in a cantilever beam once a specified failure criterion is met (top). Bonds are created when particles contact, with the new flexible structure forming (bottom).

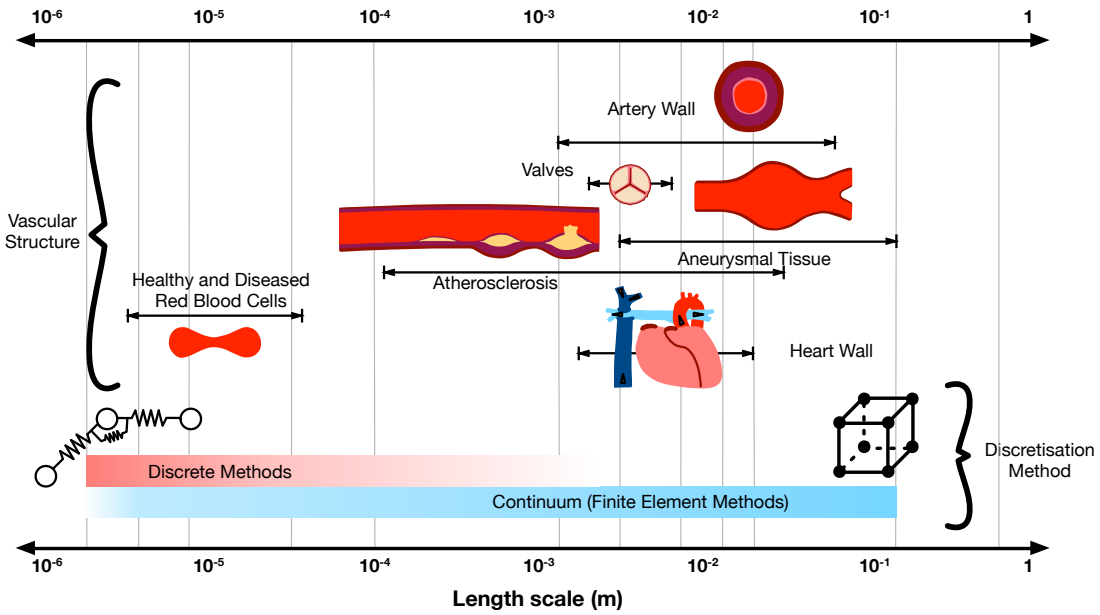

Figure 1.3: Overview of cardiovascular applications modelled using numerical analysis. The length scale of each application and the type of numerical method implemented at each scale is considered. Adapted from Owen et al. [2].

capable of facilitating improved representations of cardiovascular structures, inclusion of patient-specific geometries and the modelling of the complex mechanical dynamics that occur in the cardiovascular system. These include phenomena such as the formation, growth and rupture of aneurysms and atherosclerotic plaques. In order to maintain reasonable computational times, GPU implementation of the methods will be evaluated.

1.2 Project Objectives

The overall goal of this thesis is to develop a fluid-structure interaction method capable of efficient simulation of complex geometries and structural phenomena with a view to long-term inclusion in diagnostic pipelines for cardiovascular diseases. In order to achieve this goal, a number of objectives must be met, as will be discussed in this section.

The first objective is to assess existing numerical methods utilised in modelling cardiovascular applications and to identify opportunities to improve current modelling techniques. A number of studies have been conducted using a variety of

general purpose, commercial numerical solvers, considering both the fluid and structure in isolation. The majority of these studies have employed continuum-based methods, in particular the finite volume and finite element methods. An application-based study is performed, to gain first hand experience of such solvers, with the added benefit of collaboration with a team of clinicians so as to gain insight into their needs and requirements for such a tool.

The second objective is to couple fluid and structure solvers that have the ability to address shortcomings of numerical analysis traditionally employed for cardiovascular applications. The use of a partitioned coupling approach will allow different fluid and structure solvers to be selected based upon their ability to fulfil the identified modelling requirements. While using a partitioned approach allows flexibility in the solvers integrated into the FSI method, additional treatment is required to ensure the conservation of energy at the boundary. This is particularly important in cardiovascular applications since the densities of the fluid and structure are well within an order magnitude and the effect of the structure on the fluid is large. Without the additional treatment of a strong coupling scheme, which can result in additional computational cost, simulations will become inaccurate and unstable.

The third objective is based upon improving the capability and practicality of the method specifically for use in a clinical framework. As highlighted previously, discrete numerical methods can become computationally expensive when deployed at scale. It is therefore necessary to employ parallelisation procedures to reduce the computational time of the simulation. It is already well known that the LBM exhibits strong scaling performance, particularly when implemented on GPU architecture. The suitability of the FSI method will be explored through the implementation of the solvers on the GPU architecture and assessment of the relative speed-up in comparison to CPU architecture. The use of stochastic modelling of the structure material properties will also be explored, with a view to develop statistical material models for cardiovascular tissues.

1.3 Research Outputs

This work led to a series of research outputs, in the form of journal publications. Significant contributions to the following list of papers have been made during

this PhD program:

1. **B. Owen, C. Lowe, N. Ashton, P. Mandal, S. Rogers, W. Wein, C. McCollum and A. Revell. Computational hemodynamics of abdominal aortic aneurysms: Three-dimensional ultrasound versus computed tomography. *P. I. Mech. Eng. H*, 230(3), 2016** [1]

   This work assesses the feasibility of using 3D ultrasound generated patient-specific geometries in numerical analysis of abdominal aortic aneurysm using a commercial solver based on the finite volume method. This study served as a pathway into the cardiovascular modelling field, and is a potential application for the fluid-structure interaction method.

   The following contributions were made to the paper by each author: B. Owen conducted the simulations and lead drafting of the paper. C. Lowe segmented the geometries and provided clinical insight during analysis as well as drafting of the paper. N. Ashton assisted with simulation set up and analysis. P. Mandal provided guidance in simulation analysis. S. Rogers performed the scans while W. Wein created the segmentation software. C. McCollum provided clinical insight and was responsible for devising the project along with A. Revell, who provided extensive guidance in simulation set up, analysis and drafting of the paper.

2. **B. Owen, N. Bojdo, A. Jivkov, B. Keavney and A. Revell. Structural modelling of the cardiovascular system. *Biomech. Model. Mechan.*, 17(5), 2018** [2]

   This review was a product of the initial literature review conducted in the early stages of the present work. The review discusses the current state-of-the-art in structural modelling of the cardiovascular system, providing details on the numerical methods and material models employed across a range of temporal and spatial scales. Scientific advancements gained through the use of numerical modelling in a variety of applications are also discussed in detail, while a timeline of some of the most significant advancements is included, highlighting the general trends in field.

   The following contributions were made to the paper by each author: B. Owen conducted the initial literature review and lead drafting of the pa-

per. N. Bojdo provided guidance on the paper structure and content. A. Jivkov provided technical guidance in reformulating material models and governing equations as well as drafting of the paper. B. Keavney gave clinical insight into each application discussed within the paper and identified areas which are currently under-researched. A. Revell was heavily involved in the drafting of the paper including content and structure.

3. **B. Owen, A. Nasar, A. Harwood, S. Hewitt, N. Bojdo, B. Keavney, B. Rogers and A. Revell. Vector-based discrete element method for solid elastic materials. *In Review***

   This work serves as an introduction to the vector-based discrete element method for elastic bodies, providing details of the methodology and algorithmic implementation. Quasi-static and dynamic validation cases are presented in comparison to analytical data and numerical benchmarks, while details of the V-model implementation on GPU architecture with assessment of associated computational speed-up are provided.

   The following contributions were made to the paper by each author: B. Owen performed simulations, implemented the code on both CPU and GPU and lead drafting of the paper. A Nasar provided simulation guidance as well as paper content. A. Harwood assisted with GPU implementation while N. Bojdo guided paper content. B. Keavney helped draft the paper. A. Revell was heavily involved in all aspects of the paper, particularly guiding paper content.

4. **B. Owen, J. O'Connor, A. Harwood, N. Bojdo, B. Keavney, and A. Revell. A discrete fluid-structure interaction approach for highly deformable elastic bodies. *In Preparation***

   This work introduces a novel, strongly coupled fluid-structure interaction method consisting of the lattice Boltzmann method as the fluid solver, vector-based discrete element method as the structural solver, coupled using the immersed boundary method in an iterative block Gauss-Seidel scheme. Details of the underlying methodology of each method are provided while the coupling procedure is also discussed. Validation cases for the fluid and structure solvers in isolation are provided before comparison with the numerical benchmarking case proposed by Turek and Hron [7] for fluid-

structure interaction with large deformation.

The following contributions were made to the paper by each author: B. Owen adapted the fluid-structure interaction scheme developed by J. O'Connor, to include the V-model and was the lead for paper drafting. J. O'Connor performed the fluid solver validation while A. Harwood assisted with code implementation. N. Bojdo and B. Keavney provided guidance with paper content and structure. A. Revell assisted in the development of the method and paper drafting.

5. **K. McGurk, B. Owen, W. Watson, O. Ryder, B. Keavney and A. Revell, Heritability and family-based GWAS analyses of turbulent blood flow and roughness of the thoracic ascending aorta: Novel measures of cardiovascular health *In Preparation***

   This work investigates the link between two well-known risk factors in cardiovascular disease; genetic mutations and turbulent blood flow. The heritability of turbulent flow in the ascending aorta is calculated from fluidic metrics obtained by Cardiac Magnetic Resonance (CMR) imaging in a cohort of 341 patients from 108 British Caucasian families ascertained for hypertension, with DNA data available. Positive correlations were found between the heritability and a number of fluid metrics including Re_{max} and wall friction estimates. Genome-wide association studies (GWAS) were undertaken to identify the DNA mutations influencing the turbulence metrics and genes were identified that are involved in barrier function and vascular smooth muscle development, including actin structural protein. These findings suggest turbulence analysis should be undertaken in future studies of Alzheimers disease, smoking, cardiac death, and diabetes due to the links with DNA changes of these diseases.

   The following contributions were made to the paper by each author: K. McGurk performed the GWAS analysis and lead paper drafting. B. Owen calculated fluid metrics and assisted with paper drafting. W. Watson and O. Ryder analysed scan results to obtain patient-specific measurements. B. Keavney collected the cohort and provided guidance in genetic analysis and paper content. A. Revell assisted with fluid metric calculation, analysis and paper content.

1.4 Thesis Structure

The research presented in this thesis has lead to a number of journal publications as detailed in the previous section. As a result this thesis is in journal format as permitted by the University of Manchester. The main body of the thesis will detail the methods used throughout this work and the contributions of each journal publication to the field. The journal publications are appended to the thesis. In order to maintain the focus of the thesis, Paper 5 is not included since it is not directly related to the development of numerical analysis tools for cardiovascular applications. A description of each chapter is given below:

Chapter 1 introduces the background, motivation and aims of the research presented.

Chapter 2 provides a review of numerical methods used to model various of applications in the cardiovascular system.

Chapter 3 describes the fluid solver integrated into the fluid-structure interaction method.

Chapter 4 describes the structural solver integrated into the fluid-structure interaction method.

Chapter 5 describes the coupling method integrated into the fluid-structure interaction method and the implicit coupling scheme used to transfer quantities between the fluid and structural solvers.

Chapter 6 discusses the modelling developments made to the structural solver and fluid-structure interaction method while validation of each component, and the fully coupled fluid-structure interaction method are presented.

Chapter 7 provides a concise discussion of the contributions to the field of the research presented.

Chapter 8 concludes by summarising the main findings and provides suggestions for future research. Also included are details of the current development stage of the fluid-structure interaction method towards use in cardiovascular applications, including current issues and limitations.

Appendices contain Papers 1-4, with brief summaries of each provided in Section 1.3

Chapter 2

In Silico Modelling of the Cardiovascular System

This chapter reviews the current state-of-the-art-of *in silico* modelling for the cardiovascular system. A published review article, "Structural modelling of the cardiovascular system" [2], focusing on relevant structural modelling, appears in Appendix B as one of the papers resulting from this thesis; where the full range of material models utilised for cardiovascular modelling are surveyed across a number of temporal and spatial scales. The paper focusses on structural modelling alone, and is not repeated here. In the following chapter a review is provided to focus on the use of CFD methods applied to cardiovascular modelling, for both rigid wall analysis and fluid-structure interaction methods.

2.1 Overview of In Silico Modelling

The vast body of research in the field of *in silico* modelling of the cardiovascular system can be broadly classified into four main areas as shown in Figure 2.1. This work has already had significant impact, covering many aspects of the cardiovascular system, from medical devices to modelling of vessels and the red blood cells that flow though them. Figure 2.2 provides a visual summary of some of the areas to receive a lot attention from the numerical modelling community. While these areas can be classified as standalone areas, in practice, scientific advancements in each of these areas has lead to significant advancement in others and therefore are intrinsically linked and numerical models may develop across more

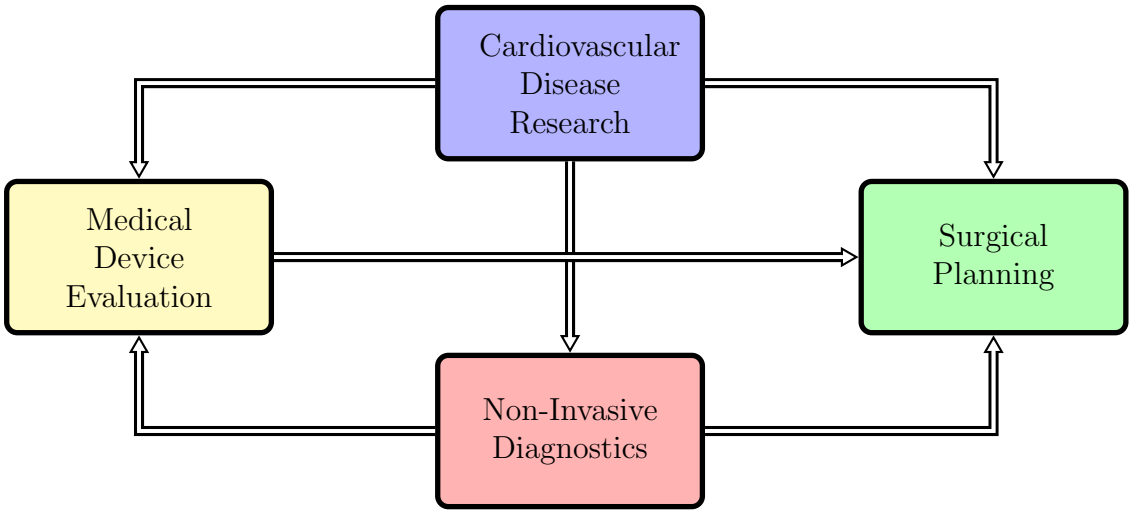

Figure 2.1: Main areas of research and applications of *in silico* modelling of the cardiovascular system

than a single area. The use of fluid-structure interaction methods was initially intended predominantly for high fidelity modelling of small-scale bio-fluid studies, with the aim of understanding the mechanisms behind a disease [24]. However, the increased understanding and user expertise developed via these studies, in conjunction with the increase in computational power available to engineers, has enabled FSI methods to be increasingly applied to patient-specific assessment procedures [25].

Cardiovascular disease research generally requires the highest modelling fidelity, and focuses on the pathogenesis of a disease in order to aid in the development of effective treatments and/or preventative measures. In addition, numerical modelling has also been used extensively in the design and development of medical devices such as left ventricular assist devices (LVADs) [26], prosthetic valves [27] and stents [28]. In recent times, the use of numerical modelling in conjunction with patient-specific geometries, obtained using imaging modalities such as Magnetic Resonance Imaging (MRI), Computed Tomography (CT) and Ultrasound (US), has provided surgeons with additional information prior to surgery. As a result, surgeons are better able to plan surgeries; predicting complications that may arise and adapting their plans accordingly. The ability to include patient-specific geometries within numerical analysis has also increased the feasibility of using numerical analysis as part of non-invasive diagnostic techniques. Arguably the most advanced of these techniques is HeartFlow [10] which is able to determine the level of narrowing within the coronary arteries and subsequent branching vessels and the affect on blood supply to the heart via virtual Fractional Flow

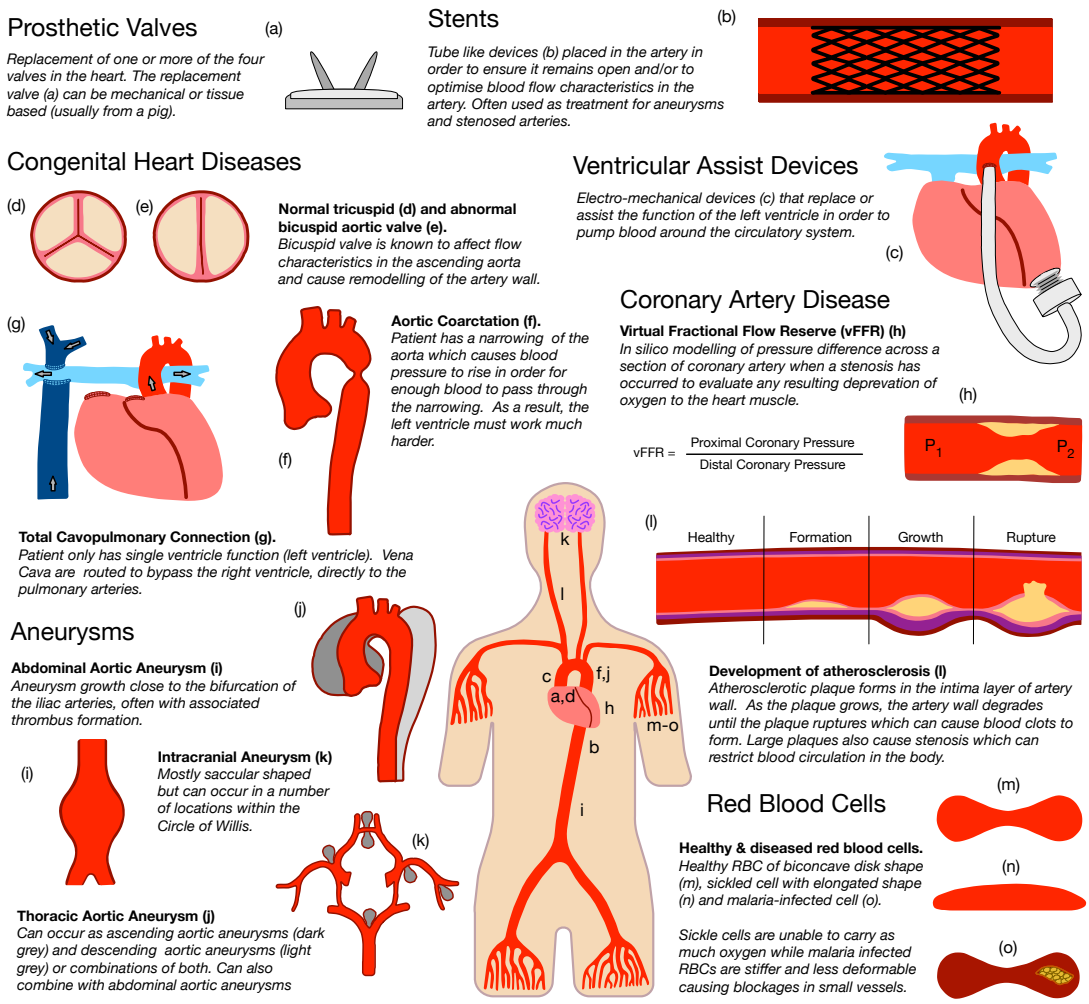

Figure 2.2: Overview of some of the major cardiovascular applications of numerical analysis and in silico modelling. Adapted and extended from Owen et al. [2] to include additional computational fluid dynamic applications.

Reserve (vFFR) analysis.

The development of the fluid-structure interaction method within this work is focused towards long-term inclusion within clinical diagnosis toolchains and therefore the applications discussed in Section 2.3 will focus on literature in the Non-Invasive Diagnostics and Surgical Planning applications. However, where appropriate, significant studies from other applications of cardiovascular research will also be discussed.

2.2 Modelling Approach

2.2.1 Discretisation of Blood

Blood consists of a number of particulates, including red blood cells (RBCs), white blood cells (WBCs) and platelets, suspended in plasma. For a healthy adult, a normal RBC count (cells per mm^3 of blood) is around 4-5 million. The spatial scale of the cardiovascular application therefore has a significant effect on the modelling approach taken and the discretisation methods employed to represent blood. An overview of the type of numerical methods employed at each spatial scale is shown in Figure 2.3, also demonstrating the hierarchy of explicitly modelled characteristics of RBCs which are then used to develop models to be utilised at larger spatial scales.

At small spatial scales such as flow through capillaries, the deformation of RBCs

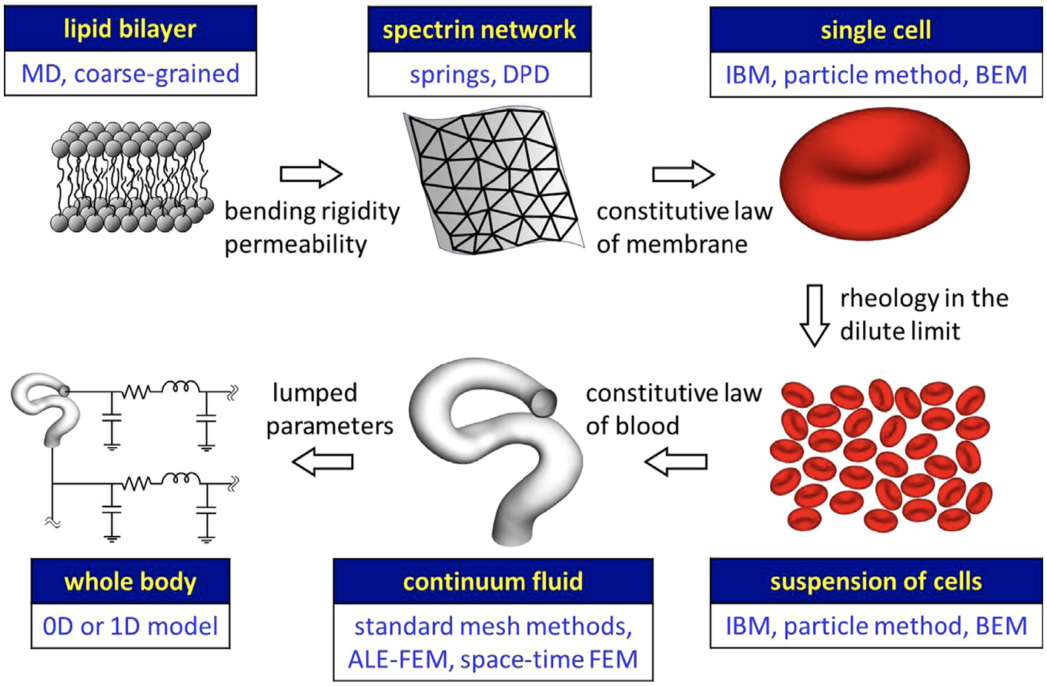

Figure 2.3: Numerical methods traditionally implemented at different spatial scales of the cardiovascular system with each discrete representation of red blood cells and blood. Arrows indicate the passing of a physical quantity directly modelled at a smaller scale, to a larger scale via a coarse-grained model or constitutive relationship. Reprinted from Imai et al. [3] Copyright (2015), with permission from Elsevier.

has a significant effect on the flow characteristics producing the shear thinning effect that gives blood its non-Newtonian properties. As a result, in order to accurately represent blood at this scale, the deformation of RBCs must be considered either indirectly using a non-Newtonian viscosity model or directly using a structural solver to model deformation due to the flow with plasma modelled by a fluid solver. It is worth noting that plasma itself is generally modelled as a Newtonian fluid [29], although recent experimental tests have indicated a viscoelastic nature [30]. In order to model the effects of diseased RBCs such as malaria and sickle cell disease, the deformation of the RBC must be directly considered via the implementation of fluid-structure interaction methods [31–33]

At large spatial scales, e.g. $O(10^{-3}m)$, blood can be considered as a continuum. This approximation is appropriate since the shear thinning effect of red blood cells can be represented via a non-Newtonian fluid model of which a number have been developed [34] or as is often implemented, a larger approximation as a Newtonian fluid [17]. As a result, fluid-structure interaction between the red blood cells (and other particulates) and the plasma is not considered explicitly and the blood is represented via a fluid solver only. It is worth noting that the computational cost of representing discrete, deformable RBCs at large spatial scales is prohibitively large, even using coarse-grained RBC approximations [35].

At even larger spatial scales, e.g. flow through the entire microcirculatory system, 0D and 1D models can be implemented [36,37]. The flow of blood is represented via a series of resistances, capacitances and inductances in 0D models and via a reduced constitutive relationship between pressure in the vessel and area in conjunction with simplified velocity profiles in 1D models. As a result, these models can provide a computationally inexpensive alternative to 3D fluid-structure interaction models if localised conditions are not of interest.

While these models are able to model extensive networks of vessels, simplified versions can also provide boundary conditions for CFD models. The most common of these is the 3-element Windkessel model which provides a boundary condition representing artery compliance and resistance to blood flow. Although coupling the FSI method developed within this work to 0D and 1D models could provide interesting avenues for future research, they are beyond the current scope of the project and therefore excluded from this review. Furthermore, the constitutive relationships governing the deformation of RBCs are discussed within the review article appended to this thesis and therefore are not included here to avoid repe-

tition. The numerical methods used to model the blood (or components of blood) as a fluid as well as numerical methods incorporated into fluid-structure methods to model blood, as discussed in the next section.

2.2.2 Numerical Models

The vast majority of numerical analysis of cardiovascular applications employ continuum-based numerical methods such as the finite volume method (FVM) or the finite element method (FEM) to model blood, either at a large spatial scale where the entirety of blood and its components are modelled as a continuum or at smaller scales where the particulates are directly modelled and the fluid solver represents plasma. In many cases, commercial solvers such as ANSYS CFX [38] and Fluent [39], Star CCM+ [1, 40], and LS-DYNA [41], or general open-source solvers such as OpenFOAM [42] have been utilised for a variety of cardiovascular applications. However, with the increasing interest in numerical analysis of cardiovascular flows, a number of solvers have been developed specifically for cardiovascular flows at large spatial scales.

One such solver is the open-source FEM solver, SimVascular [4] which features a complete pipeline for patient-specific cardiovascular investigations, including patient-specific imaging segmentation and geometry preparation procedures as shown in Figure 2.4. It is also capable of modelling fluid-structure interaction for large vessels [43]. Another solver developed specifically for cardiovascular flow modelling is HemeLB [44] which also includes a complete pipeline for cardiovascular investigations but utilises the lattice Boltzmann method, a mesoscopic method that is incorporated within the FSI method developed within this work and will be discussed in Chapter 3. This solver takes advantage of the high parallelisation performance of the LBM in order to model vessels such as the intracranial arteries via rigid-wall analysis [45].

When fluid-structure interaction methods are implemented at larger spatial scales, mesh fitted methods are generally utilised either in a monolithic approach, using FEM for both the fluid and structure [46, 47], or a partitioned approach where the fluid is solved via FVM and the structure via FEM [48]. While these methods have yielded significant insight into cardiovascular diseases, the structural model employed is generally of reduced complexity than in stand alone structural solvers. One such example is for artery walls where FSI methods have used

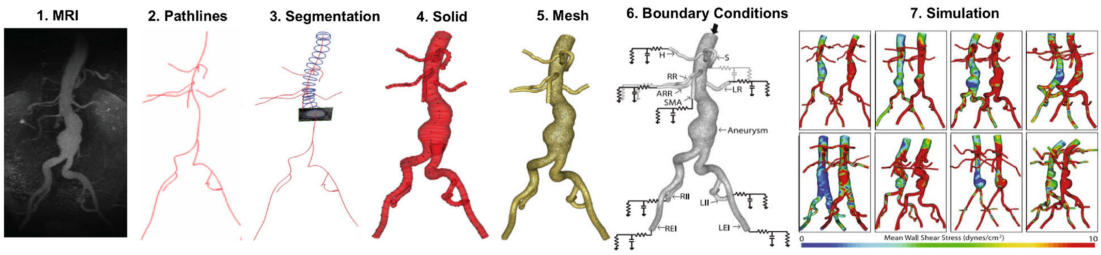

Figure 2.4: Example pipeline for numerical analysis of patient-specific images. Reprinted from Updegrove et al. [4] Copyright (2016), with permission from the Biomedical Engineering Society.

linearly elastic representations [43], despite experimental studies demonstrating viscoelastic properties [49] and the influence of the microstructure [22] which have been used to develop state-of-the-art material models [50]. This is due to the high computational expense of the FSI method and in particular, the mesh fitted schemes employed.

At smaller spatial scales, where fluid-structure interaction is required to effectively account for the deformation of RBCs, a larger variety of numerical methods have been implemented. This is mainly due to the coupling schemes employed at this scale since the moving-mesh methods employed at larger scales are not applicable to cases where RBCs begin to aggregate. As a result, coupling methods such as the immersed boundary method (IBM) must be employed, which allows overlapping and independent meshes for the fluid and structure under consideration. A significant advantage of the IBM is its ability to couple a variety of fluid and structure solvers, allowing solver selection based upon the applicability to a case. For simulations of RBCs a number of combinations have been used e.g. LBM-FEM [32, 51], FVM and combined FEM-DEM [52], and LBM-SN (spring network) [53].

A number of mesh-free methods have also been employed to represent the small spatial scale flows, including smoothed particle hydrodynamics (SPH) [54], the moving particle semi-implicit method (MPS) [55] and dissipative particle dynamics (DPD) [56]. These methods directly impart forces onto a structure such as an RBC in order to model fluid-structure interaction [3]. This approach, along with the immersed boundary approach, results in diffusive boundaries which can lead to loss of accuracy.

2.2.3 Rigid and Flexible Wall Analysis

A key decision when deciding on a modelling approach for numerical analysis of a cardiovascular applications is whether deformation should be considered. For small spatial scales, as previously discussed, the decision is clear since the deformation of each RBC has a large impact of the flow characteristics. However, at larger spatial scales the deformation of arteries, while not insignificant, requires careful assessment based on the application since the additional computational cost of implementing an FSI method may not provide sufficient value. This has been highlighted in the case of intracranial vessels [17] and in coronary arteries [57]. Furthermore, the use of rigid-walled analysis can provide initial and/or qualitative results that can supplement more complex flexible-walled analysis, especially if relationships between the two can be identified. One such example is the over-prediction of the magnitude of Wall Shear Stress (WSS) by rigid-walled analysis of intracranial aneurysms but the qualitative similarity of the WSS distribution field between rigid and flexible-walled predictions [58].

Overall however, with the ever increasing performance and availability of computational resources, in conjunction with the increasing maturity of the field, the general trend is moving towards greater inclusion of FSI in numerical analysis of cardiovascular applications. The extent to which will be discussed in the next section for a number of major applications.

2.3 Cardiovascular Applications

As stated in the introduction to this chapter, the focus of the chapter is to supplement the review article published regarding the structural modelling of the cardiovascular system that is appended to this thesis. As such, the focus here will be restricted to fluid solvers in isolation and as part of FSI models.

2.3.1 Congenital Heart Diseases

The use of CFD in congenital heart diseases (CHDs) has a long history, and in particular in the investigation of the Fontan procedure where the right side of the

heart is bypassed and the superior and inferior vena cava are connected directly to the pulmonary artery. Pioneering studies by de Leval and Dubini et al. [59,60] demonstrated the superior performance of an offset connection due to reduced energy loss through the avoidance of colliding flows. This demonstration of the capability of CFD and numerical modelling has lead to further investigations in the Fontan procedure and other congenital heart diseases, as will be detailed in this section.

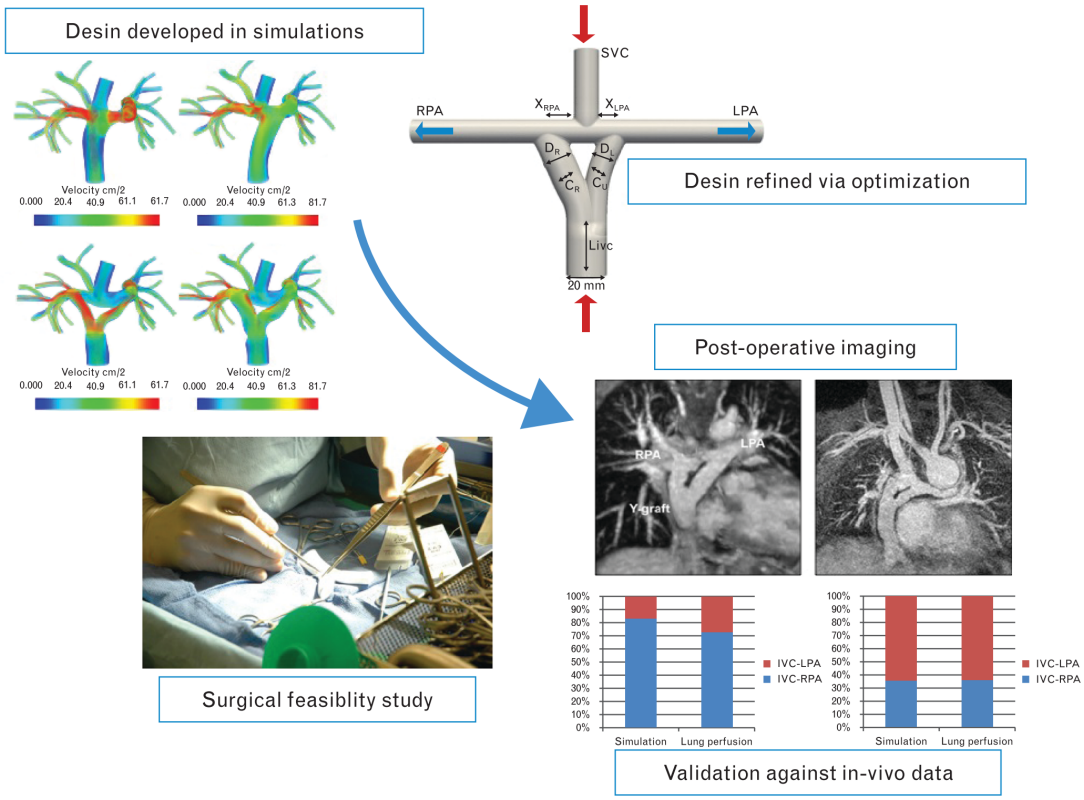

Figure 2.5: Development process of the Fontan Y-graft, from CFD simulations to surgical implementation and post-surgery analysis. Reprinted from Marsden and Feinstein [5] Copyright (2015), with permission from Wolters Kluwer Health.

Further numerical studies of the Fontan procedure led to the first simulation-derived concept for congenital heart diseases, the Fontan Y-graft [61,62], to be used in surgery [63] as depicted in Figure 2.5. In addition, the use of mechanical circulatory support such as the viscous impeller pump [64], as well as the effect of left and right sides of the heart support has been investigated [65], both using CFD.

Tetralogy of Fallot can present a number of complex geometry changes that lead to suboptimal cardiac function. These include mitral valve regurgitation, septal

defects and pulmonary stenosis, all of which can occur simultaneously. As a result, it is not surprising that there have been fewer numerical studies of the disease in comparison to the Fontan procedure, although a recent uptake has begun to develop. A number of studies have focused on the repair of these defects [66] and mitral valve regurgitation [67], including the use CFD analysis of a predicted post-surgery patient-specific geometry [68]. Others have investigated the type and locations of cardiac shunts placed as an intermediary treatment step to ensure sufficient flow through the pulmonary system before further repairs can be completed [69, 70].

Coarctation of the aorta has also been modelled extensively using CFD, perhaps due to the relatively simple geometry in comparison to other CHDs and the availability of patient-specific geometry and flow measurements via MRI. Furthermore, the nature of the disease with the narrowing of the aortic arch, and resulting increase in blood turbulence, means a number of mature numerical method developments such as turbulence models can be translated to this application [71]. Moreover, FSI has also been used to investigate coarctation repair procedures, showing the *Gothic* repair to produce more elevated WSS levels than the *Romanesque* repair, and therefore recommending increased post-surgery surveillance for complications for patients with a *Gothic* repair [72].

2.3.2 Coronary Artery Disease

Coronary artery disease (CAD), where blockages of the coronary arteries result in myocardial infarction, is the most prevalent cardiovascular disease. The formation of atherosclerotic plaques in the arteries, resulting in stenosis, is the major factor its development. The application of numerical analysis to CAD is not trivial due to the highly curved nature of the coronary arteries in conjunction with the translation and deformation of the vessel associated with the cardiac cycle. However, CFD has been successfully applied to CAD in one of two research directions. The first is the investigation of the development of the provoking atherosclerotic plaque, while the other focusses on the physiological significance of the stenosis rather than modelling the plaque itself [73].

Investigation of atherosclerotic plaque development in the coronary artery has focussed on the haemodynamic metrics that are known to prime the vessel wall for plaque formation [74] since the exact formation mechanism is unknown. The

effects of these metrics, such as WSS and its derivatives including Wall Shear Stress Gradient (WSSG), have been assessed using CFD in conjunction with patient-specific geometries derived from imaging modalities such as Computed Tomography (CT) and Intravascular Ultrasound (IVUS). Such studies have identified significant relationships including a link between high WSS levels and high levels of strain within plaque structures, suggesting high WSS can destabilise a plaque and increase the risk of rupture [75].

Studies investigating the physiological significance of the stenosis have been able to provide computational results for metrics which assess the functional significance of the stenosis such as Fractional Flow Reserve (FFR) in good agreement with invasive clinical procedures such as coronary angiography [10]. This has lead to arguably the largest use of CFD and numerical analysis in clinical practice, in the form of virtual FFR provided by HeartFlow which has received F.D.A. approval in the USA and is currently utilised by a number of healthcare providers including the National Health Service in the UK.

2.3.3 Ventricular Assist Devices

Ventricular Assist Devices (VADs) can supplement or replace the pumping function of a ventricle. Fluid-structure interaction has been implemented to model the deformation of the thin membrane that acts as a blood/air barrier for a pneumatically driven pulsatile VAD [76]. However, in the vast majority of studies VADs can be assumed rigid for continuous flow pumps, and therefore CFD only analysis is required to evaluate the performance of the device [26]. As a result, the FSI method developed within this work is perhaps not suitable to this application. However, like many cardiovascular applications, advancements in modelling methods implemented for VADs can be applied to other applications more suitable to the FSI method and therefore should be explored.

One such example, shown in Figure 2.6, is the investigation of pre-existing turbulence models applied to blood flow inside a VAD [6], given that experimental data for blood flow characteristics inside a VAD can be obtained more easily than *in vivo* measurements of a ventricle. In addition, both demonstrate transitionally turbulent blood flow properties, and therefore recommendations derived from VAD models could be applied to *in vivo* ventricular applications such as flow through the ascending aorta with or without explicit modelling of the aortic

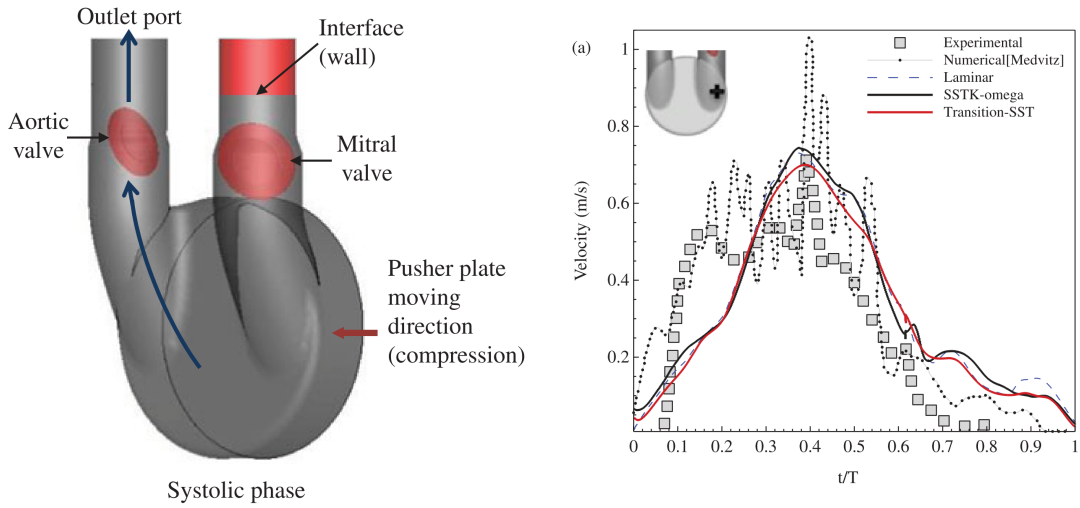

Figure 2.6: Assessment of pre-existing turbulence models in CFD analysis in comparison to the laminar flow assumption and to experimental data. Reprinted from Al-Azawy et al. [6] Copyright (2015), with permission from Taylor and Francis.

valve where turbulence models have also been applied [77].

2.3.4 Aneurysms

Aneurysms are the dilation or bulging of a vessel due to weakening of the wall. Symptoms are generally rare, however rupture of aneurysms can lead to fatalities due to the extent of internal bleeding that occurs. Aneurysms can form at a number of locations in the cardiovascular system, however those that are most extensively studied are intracranial aneurysms (ICA) and abdominal aortic aneurysms (AAA). A significant number of studies have investigated the structural characteristics of aneurysmal tissue, as discussed in Appendix B. Here, the focus will be restricted to the modelling of blood flow through aneurysms and progression to fluid-structure interaction methods.

Steinman et al. [78] investigated the flow characteristics through an intracranial aneurysm geometry derived from medical imaging for the first time in 2003. Since then, research in this field as grown significantly, and can be split into two different focuses. The first is identifying haemodynamic risk factors associated with the formation, progression and rupture of aneurysms, while the second is determining the performance of medical devices employed to treat the disease. These

medical devices include flow diverters, stents and coils. The focus here is limited to identifying haemodynamic risk factors since this is a potential long-term application of the FSI method developed in this body of work. However, the review by Chung and Cebral [79] provides extensive discussion of scientific advancements in regards to CFD and aneurysm medical devices.

Many risk factors associated with flow characteristics have been proposed, including wall shear stress (WSS) [80, 81], oscillatory shear index (OSI) [82, 83], pressure [80, 84] and flow structure complexity [85, 86]. However, a single metric has not been demonstrated as a robust indicator of the likelihood of rupture. Cebral and Meng [87] have linked the high number of reported risk factors with the complexity of the disease and the unknown mechanisms of formation, growth and rupture of aneurysms. Despite this, the preliminary results of International Aneurysm CFD Challenge 2015 [88] demonstrated that experienced CFD Engineers were able to be predict aneurysm rupture with greater accuracy than experienced clinicians where blind assessments were conducted on a series of aneurysms where the outcome was known.

A number of studies have attempted to clarify the performance sensitivity of CFD analysis to variations boundary conditions [89] and geometry variation [90], demonstrating significant differences in risk factors such as WSS and OSI and the need to obtain long segments of the parent artery. Studies such as these have indicated the clear need for validation cases and CFD implementation guidelines to ensure consistent results are output from any numerical analysis.

Numerical analysis of patient-specific aneurysms has also been extended to consider wall motion, either through enforced motion of the wall [91] or through coupling of fluid and structure solvers [92]. However, the benefits of the added model complexity are not clear given that patient-specific wall properties such as wall thickness, are not easily extracted from medical imaging while systematic differences in risk factors have also been shown in the case of the overprediction of WSS [91].

A further extension of numerical analysis is the development of Fluid-Solid-Growth frameworks (FSG) [93, 94]. These frameworks use an FSI method to predict short-term cyclic loads applied to the aneurysm and then remodel the aneurysm geometry via user-defined criteria based on the short-term characteristics predicted. The short-term FSI method is then applied to the new aneurysm

geometry to predict the new conditions experienced by the aneurysm. While validation of these frameworks is difficult, they have the potential to greatly improve understanding of aneurysm progression and rupture.

2.4 Conclusions

As a result of this review, in conjunction with the review article appended to this thesis, key observations can be made with regards to *in silico* modelling of the cardiovascular system:

1. In general, modelling of both the fluid and structure is required for applications where the cardiovascular structure is highly deformable.

2. Numerical models, and in particular structural models, incorporated into fluid-structure interaction methods, have reduced complexity than models that are used when only the fluid or structure is considered in isolation.

3. The use of discrete structural methods has been well explored at small spatial scales, coupled with both continuum and discrete fluid methods.

4. At large spatial scales, the use of discrete structural methods has not been extensively explored, mainly due to computational constraints.

5. New developments in soft tissue material models have begun to include details of the microstructure into continuum models.

6. High computational speed is required in order to translate numerical analysis into clinical medicine.

Based on these observations, there is a clear need for the development of a fluid-structure interaction method that is capable of modelling high levels of deformation, in minimal computational time utilising high performance computing (HPC) or otherwise. It is also clear that the accurate representation of the material properties of cardiovascular tissue has the potential to vastly improve the feasibility of including numerical analysis in clinical practice. Discrete methods for fluid dynamics, in the form of the lattice Boltzmann method, have already

demonstrated their applicability to cardiovascular flows as well as excellent scaling performance. Discrete structural methods have been utilised at small spatial scales however, their use at larger scales is yet to be fully realised, despite recent studies demonstrating their capability.

Chapter 3

Lattice Boltzmann Method

The fluid solver in the novel fluid-structure interaction method developed in this work is based on the lattice Boltzmann method; an increasingly popular alternative to traditional Navier-Stokes based solvers such as the Finite Volume Method (FVM). Within this chapter, the underlying theory, discretisation methods and implementation approaches are detailed while the method selection rational is discussed.

3.1 Overview of the Lattice Boltzmann Method

In fluid dynamic modelling, traditionally there have been two fundamental approaches, macroscale and microscale. The selection of either approach has been highly dependent on the spatial and temporal scale of the fluid in question as shown in Figure 3.1. Microscopic methods are more suited to small scales as they directly model individual particles or molecules via Newton's equations of motion which results in prohibitively large computational costs using current computer hardware for large scale problems. In contrast, macroscopic methods treat the fluid as a continuum, assuming the ratio between the molecular mean free path (the average distance travelled by a moving particle) and the characteristic length scale, known as the Knudsen number, is much smaller than one.

Macroscopic methods employ the Navier-Stokes and continuity equations, usually solved numerically through an iterative system of matrices, to determine the characteristics of the flow. Macroscopic methods are more computationally effi-

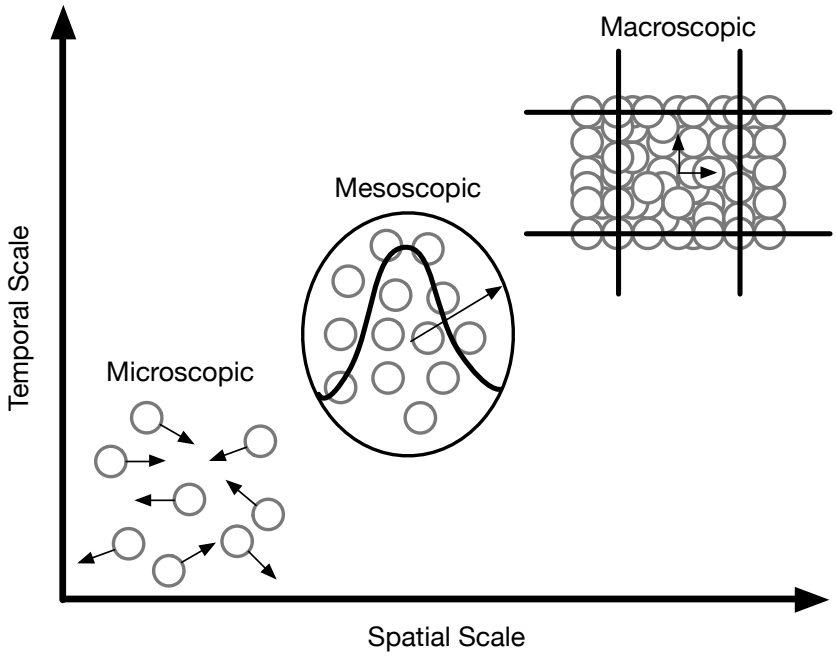

Figure 3.1: Discretisation methods: representation of a fluid using microscopic, mesoscopic and macroscopic methods

cient at large scales, in part due the reduced resolution required in comparison to microscopic methods, however implementation of complex fluid phenomena such as multiphase flows is non-trivial. Furthermore, the iterative and non-local nature of the method means that while research is being done to utilise GPU acceleration to reduce computational times, the method itself is not naturally suited to such hardware.

Mesoscale methods, the classification of method to which the LBM belongs, attempt to bridge the divide between the two traditional classifications, combining the advantages of each. Underpinned by kinetic theory, the macroscopic properties of a fluid are described through the microscopic motion of it's molecules via a distribution function. As a result, individual molecules do not have to be considered directly, significantly reducing the computational requirement to model a fluid in a given space. Furthermore, the local nature of the method and the discretised volume in the form of a uniform lattice (discussed further within this chapter) greatly eases parallelisation resulting in vastly reduced computational times with little additional treatment in comparison to Navier-Stokes based methods. In addition, the LBM's use of explicit time integration schemes means they are well suited to GPU acceleration since the fluid properties calculated in the current time step are only dependent on values from previous time steps. As a

result, the update of a given variable can be completed independent of variables being updated on other parallel processors. While explicit Navier-Stokes based methods exist, the majority are implicit.

3.2 Discretisation

3.2.1 Boltzmann Equation

As previously stated, the LBM is based upon kinetic theory which in turn utilises the Boltzmann equation:

$$\frac{\partial f}{\partial t} + \boldsymbol{\xi} \cdot \nabla f = \Omega(f) \tag{3.1}$$

where f is the distribution function, $\boldsymbol{\xi}$ is the molecular velocity and $\Omega(f)$ is the collision operator. The distribution function, also commonly denoted as $f(\boldsymbol{x}, \boldsymbol{\xi}, t)$, represents the probability of particles or molecules at position $\boldsymbol{x}$ with molecular velocity $\boldsymbol{\xi}$ at time t. Equation 3.1 governs the evolution of the distribution function in contrast to the Navier-Stokes equations which evaluate macroscopic quantities directly. As a result, when using the LBM an additional step is required to obtain the macroscopic quantities of fluid density $\rho(\boldsymbol{x}, t)$, velocity $\boldsymbol{u}(\boldsymbol{x}, t)$ and specific energy $E(\boldsymbol{x}, t)$:

$$\rho(\boldsymbol{x}, t) = \int f(\boldsymbol{x}, \boldsymbol{\xi}, t) \, \mathrm{d}\boldsymbol{\xi} \tag{3.2}$$

$$\rho \boldsymbol{u}(\boldsymbol{x}, t) = \int \boldsymbol{\xi} f(\boldsymbol{x}, \boldsymbol{\xi}, t) \, \mathrm{d}\boldsymbol{\xi} \tag{3.3}$$

$$\rho E(\boldsymbol{x}, t) = \frac{1}{2} \int |\boldsymbol{\xi}|^2 f(\boldsymbol{x}, \boldsymbol{\xi}, t) \, \mathrm{d}\boldsymbol{\xi} \tag{3.4}$$

Equation 3.1 has 7 independent variables, each of which are continuous. As a result, this equation must be discretised in time, spatial and velocity space, in or-

der to reduce the computational requirements of the method. The velocity space can be discretised by restricting the motion of the particles along discrete velocity links. This discretisation results in the semi-discrete form of the Boltzmann equation:

$$\frac{\partial f_i}{\partial t} + \boldsymbol{c}_i \cdot \nabla f_i = \Omega(f_i) \tag{3.5}$$

where $\boldsymbol{c}_i$ is the velocity model discussed in the next section. This discretisation can be performed through a small Mach number approximation [95] or Hermite series expansion [96]. The Hermite expansion permits approximations of the Boltzmann equation up to any arbitrary order, even those not captured by the Navier-Stokes equations [97].

3.2.2 Velocity Model

When selecting a suitable velocity model (sometimes referred to as a velocity set) a compromise occurs between reducing the memory and computational requirements of the solver by limiting the number of discrete velocities, while ensuring that sufficient accuracy is retained in order to represent the problem effectively. The velocity model implemented in this work, the most popular model for two-dimensional fluid flows, is known as D2Q9 (two dimensions and nine velocities) and is depicted in Figure 3.2. This velocity model is symmetrical and has sufficient discrete velocities to ensure isotropy, essential in recovering the Navier-Stokes equations via expansion [98]. The velocities included within the model along with their weighting w_i, which can be calculated using the Gauss-Hermite quadrature rule [99], and lattice speed of sound c_s are defined by:

$$\boldsymbol{c} = \begin{bmatrix} 0 & 1 & -1 & 0 & 0 & 1 & -1 & 1 & -1 \\ 0 & 0 & 0 & 1 & -1 & 1 & -1 & -1 & 1 \end{bmatrix} \frac{\Delta x}{\Delta t} \tag{3.6}$$

$$w_i = \begin{cases} 4/9 & i = 0 \\ 1/9 & i = 1, 2, 3, 4 \\ 1/36 & i = 5, 6, 7, 8 \end{cases}$$

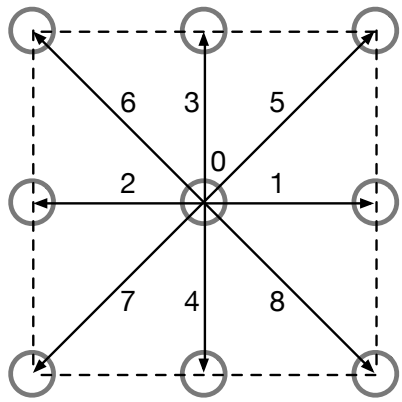

Figure 3.2: Discrete velocity model: D2Q9

$$c_s = \frac{\Delta x}{\Delta t}\frac{1}{\sqrt{3}} \tag{3.7}$$

where Δt and Δx are the time step size and lattice spacing. These can be of any unit such as SI units, however for ease lattice units are generally used giving $\Delta t = \Delta x = 1$.

3.2.3 Space and Time Discretisation

The semi-discrete form of the Boltzmann equation can be further discretised through space and time via the Method of Characteristics [99] to provide the lattice Boltzmann equation, the governing equation for the LBM implementation in this work:

$$f_i(\boldsymbol{x} + \boldsymbol{c}_i\Delta t, t + \Delta t) - f_i(\boldsymbol{x}, t) = \int_0^{\Delta t} \Omega(\boldsymbol{x} + \boldsymbol{c}_i\xi, t + \xi)\, d\xi \tag{3.8}$$

where ξ parametrises a trajectory in space. The left-hand side of Equation 3.8 governs the propagation of the distribution function through space while the right-hand side governs the collisions (local) which can be replaced via a first order approximation using a single point to give:

$$f_i(\boldsymbol{x} + \boldsymbol{c}_i\Delta t, t + \Delta t) - f_i(\boldsymbol{x}, t) = \Delta t\Omega_i(\boldsymbol{x}, t) \tag{3.9}$$

Higher order approximations have been developed [99] however the first order example above is the most commonly implemented since in fact it produces the same form as the second order approximation [99]. As a result, the LBM can be considered second order accurate. The collision operator itself will be defined in Section 3.2.5.

3.2.4 Equilibrium Distribution Function

The equilibrium of fluids is central to kinetic theory and therefore is also integral to the LBM. The Maxwell-Boltzmann distribution (Equation 3.10) states that for a gas with no external forces applied to it will tend to evenly distribute molecular velocities around a mean macroscopic velocity over time. This is due to collisions between the molecules. This state is known as the equilibrium distribution, f^{eq}.

$$f^{eq}(\rho, T, \boldsymbol{\xi}, \boldsymbol{u}) = \frac{\rho}{(2\pi RT)^{d/2}} e^{-|\boldsymbol{\xi}-\boldsymbol{u}|^2/(2RT)} \tag{3.10}$$

Equation 3.10 can be discretised in velocity space, again using Hermite series expansion [99], so that it is dependant only on the local macroscopic values and velocity model factors $\boldsymbol{c_i}$, weighting factor w_i and lattice speed of sound c_s:

$$f^{eq}(\boldsymbol{x}, t) = w_i \rho (1 + \frac{\boldsymbol{c}_i \cdot \boldsymbol{u}}{c_s^2} + \frac{(\boldsymbol{c}_i \cdot \boldsymbol{u})^2}{2c_s^4} - \frac{\boldsymbol{u} \cdot \boldsymbol{u}}{2c_s^2}) \tag{3.11}$$

The macroscopic fluid density (Equation 3.2) and velocity (Equation 3.3) can also be discretised:

$$\rho(\boldsymbol{x}, t) = \sum_i f_i(\boldsymbol{x}, t) \tag{3.12}$$

$$\rho \boldsymbol{u}(\boldsymbol{x}, t) = \sum_i \boldsymbol{c}_i f_i(\boldsymbol{x}, t) \tag{3.13}$$

Furthermore the pressure can be defined according to the equation of state for

the isothermal LBM implementation as described here:

$$p = c_s^2 \rho \tag{3.14}$$

As a result, the Poisson equation does not need to be solved to evaluate the pressure field.

3.2.5 Collision Operator

The Boltzmann collision operator is highly non-linear and difficult to solve. As a result, alternative collision operators have been developed, the most popular of which is the Bhatnagar-Gross-Krook (BGK) approximation:

$$\Omega_i(\boldsymbol{x}, t) = \frac{1}{\tau}[f_i^{eq}(\boldsymbol{x}, t) - f_i(\boldsymbol{x}, t)] \tag{3.15}$$

where τ is the relaxation time. The BGK approximation reduces the complexity of the collision operator by assuming a single relaxation time. This is valid for any fluid since Equation 3.15 will relax towards local equilibrium, while f^{eq} contains the non-linearity required to recover macroscopic quantities of the fluid. More advanced collision operators have been developed with two or multiple relaxation times that are able to increase the stability of a simulation, particularly at high Reynolds number [99]. However, for the work here a single relaxation time is sufficient. The relaxation time is calculated with respect to the fluid viscosity ν via:

$$\tau = \frac{\nu}{c_s^2} + \frac{\Delta t}{2} \tag{3.16}$$

Rearranging Equation 3.16 for fluid viscosity as in Equation 3.17 highlights relaxation time limits, namely that the relaxation time must be greater than 0.5 in order for the fluid viscosity to be positive as is physical. Numerical stability issues can also occur for values close to this boundary while the accuracy of the

simulation can decrease for values greater than 1 [100].

$$\nu = (\tau - \frac{\Delta t}{2})c_s^2 \tag{3.17}$$

By substituting the BGK collision operator into Equation 3.8, the final form of the implemented governing equation can be obtained:

$$f_i(\boldsymbol{x} + \boldsymbol{c}_i\Delta t, t + \Delta t) - f_i(\boldsymbol{x}, t) = \frac{\Delta t}{\tau}[f_i^{eq}(\boldsymbol{x}, t) - f_i(\boldsymbol{x}, t)] \tag{3.18}$$

This equation highlights the advantages of the LBM, demonstrating its explicit and linear nature in terms of the distribution function. As stated previously, non-linearity is instead contained within the local equilibrium function. This allows the macroscopic properties of a flow to be calculated from a relatively simple transport equation.

3.2.6 Forcing Scheme

A number of forcing schemes have been developed in order to include external forces e.g. gravity, in fluid flows modelled via the LBM and are compared in [101]. These schemes are also able to provide the no-slip condition requirement on the surface of the structure at the fluid interface, allowing accurate representation of fluid-structure interaction. The forcing scheme implemented within this work was developed by Guo et al. [101] and provides an additional term to the discretised LBM equation (Equation 3.1) as follows:

$$f_i(\boldsymbol{x} + \boldsymbol{c}_i\Delta t, t + \Delta t) - f_i(\boldsymbol{x}, t) = \frac{\Delta t}{\tau}[f_i^{eq}(\boldsymbol{x}, t) - f_i(\boldsymbol{x}, t)] + \Delta t F_i(\boldsymbol{x}, t) \tag{3.19}$$

where $F_i(\boldsymbol{x}, t)$ is the discretised force density $\boldsymbol{f}(\boldsymbol{x}, t)$ and can be evaluated via:

$$F_i(\boldsymbol{x}, t) = w_i(1 - \frac{1}{2\tau})(\frac{\boldsymbol{c}_i - \boldsymbol{u}}{c_s^2} + \frac{\boldsymbol{c}_i \cdot \boldsymbol{u}}{c_s^4}\boldsymbol{c}_i) \cdot \boldsymbol{f}(\boldsymbol{x}, t) \tag{3.20}$$

An additional term is also required to calculate the macroscopic quantities correctly:

$$\rho(\boldsymbol{x}, t) = \sum_i f_i(\boldsymbol{x}, t) \tag{3.21}$$

$$\rho \boldsymbol{u}(\boldsymbol{x}, t) = \sum_i \boldsymbol{c}_i f_i(\boldsymbol{x}, t) + \frac{\Delta t}{2} \boldsymbol{f}(\boldsymbol{x}, t) \tag{3.22}$$

3.3 Initial and Boundary Conditions

Selecting and correctly imposing initial and boundary conditions has always been a challenging proposition for computational fluid dynamicists. However, when using the LBM this becomes even more difficult since traditional approaches developed for Navier-Stokes based methods have been developed in terms of the macroscopic quantities of the flow. Since the transport equation for the LBM instead describes the change in the probability distribution function, initial and boundary conditions must be developed in terms of the distribution function. This is not trivial since the translation from macroscale to mesoscale is undetermined given there are more degrees of freedom in the mesoscopic system (distribution function components) than in the macroscopic system (macroscopic moments) and therefore boundary closure conditions are required.

3.3.1 Immersed Boundary

The boundary conditions described in the remainder of this chapter are all utilised for stationary boundaries in this work. In order to model not just moving boundaries but also non-rigid boundaries, i.e. fluid-structure interaction, the immersed boundary is implemented. This will be discussed in detail after the structural solver has been introduced in Chapter 5 since it also acts as the coupling method between the fluid and structural solvers.

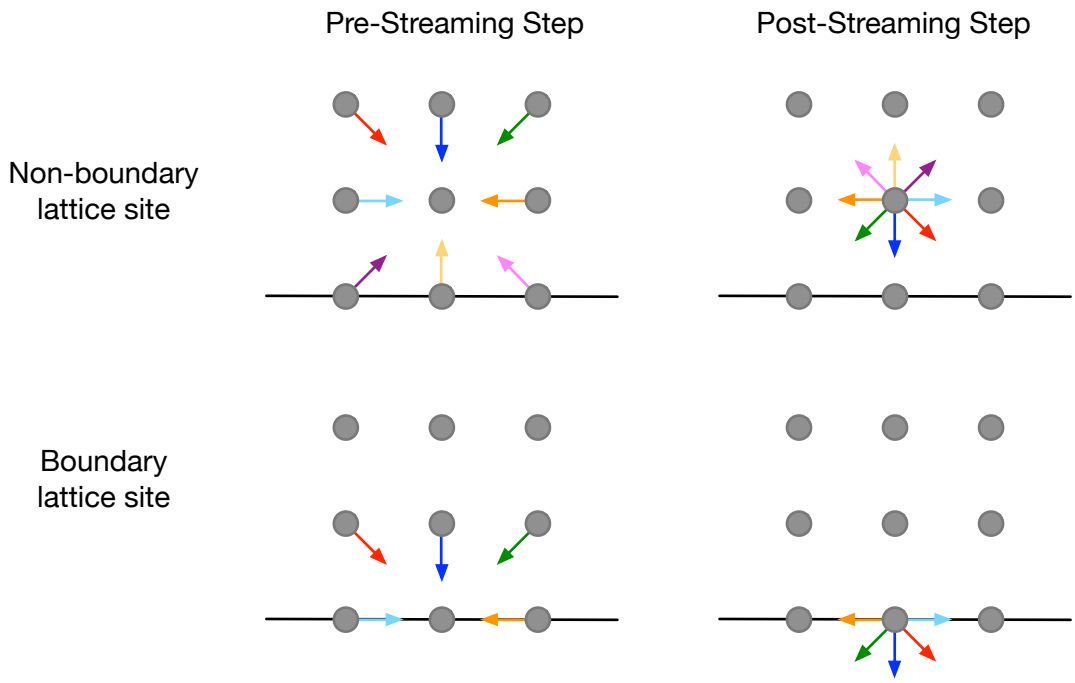

Figure 3.3: Distribution function components pre and post-stream for a non-boundary lattice site and a boundary lattice site without the appropriate boundary condition. Note that the boundary lattice site has an incomplete distribution function set since no lattice sites exist beyond the boundary (black) to provide the missing distribution function components required to satisfy conservation laws.

3.3.2 Periodic Boundary Conditions

Boundary conditions are required in order to fill the distribution function components for all velocity directions at a given boundary, specifically the velocity directions not filled during the streaming step as shown in Figure 3.3. These components will be referred to as unknown components from here onwards.

Periodic boundary conditions are commonly known as the simplest to implement and can be be used in a variety of cases where a repeating flow pattern occurs. In this work, this is true of venous valves when the idealised geometry is considered. The condition is implemented by passing any outgoing distribution function components at the periodic boundary to it's corresponding boundary as shown visually in Figure 3.4 and algebraically as:

$$f_{\hat{\imath}}(x, y, t) = f_i(x + L - \boldsymbol{c}_i \Delta t, y, t) \qquad x = 0 \tag{3.23}$$

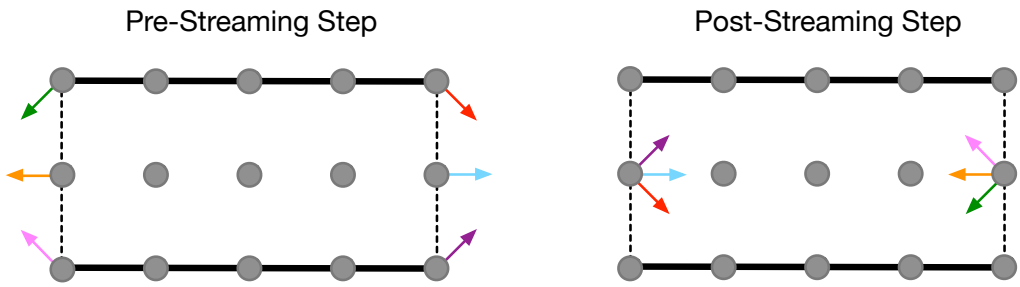

Figure 3.4: Visual representation of periodic boundary conditions for a simplified channel flow of lattice resolution 5x3 where the periodic boundary is represented by a dashed line.

$$f_{\bar{i}}(x, y, t) = f_i(x - L - \boldsymbol{c}_i \Delta t, y, t) \qquad x = L \tag{3.24}$$

where $f_{\bar{i}}(x, y, t)$ are the unknown components of the distribution function at the boundary and L is the length of the domain. Since the distribution function components leaving the domain are re-entering at the opposite side, mass and momentum are always conserved.

3.3.3 Bounceback Boundary Conditions

The no-slip velocity boundary condition is the most implemented fluid-solid interface condition. The bounceback boundary condition ensures the no-slip condition is imposed at the surface of an object in contact with the fluid by reflecting the outgoing distribution function components back to where they came from in the opposite direction. Two main implementations of this boundary condition have been developed, full-way bounceback and half-way bounceback, both of which locate the boundary midway between two lattice points. The difference between the two is the point in time at which the distribution function components are bounced back as shown in Figure 3.5.

In the fullway bounceback scheme, the distribution function components are considered to stream fully to the lattice point beyond the boundary before the direction of the component is reflected in the collision step. The reflected component is then streamed back to its original lattice point in the next time step. As a result, while this boundary condition is suitable for steady conditions, the time delay

reduces the time accuracy of transient flows (first-order accurate). In addition, the scheme requires solid lattice nodes to be included in the domain in order to store outgoing distribution function components until they are bounced back at the next time step.

The halfway bounceback scheme completes the boundary condition within a single time step, improving time accuracy (second-order accurate) and therefore is preferential for time dependent flows. In addition, it does not require solid nodes.

While bounceback has a number of advantages, including ease of implementation, stability of simulation and mass conservation, it does have significant disadvantages. Firstly, modelling of curved surfaces is not possible without additional treatment [102] which subsequently degrades the ease of implementation. Instead, curved surfaces are represented by a "staircase" of resolution equal to that of the lattice. Secondly, the location of the no-slip boundary provided via the bounceback scheme is viscosity dependent when the BGK collision operator is also used. This can result in different flow dynamics for a given Reynolds number when the viscosities are different which is not physical. This can be overcome by using alternative collision models such as MRT [103].

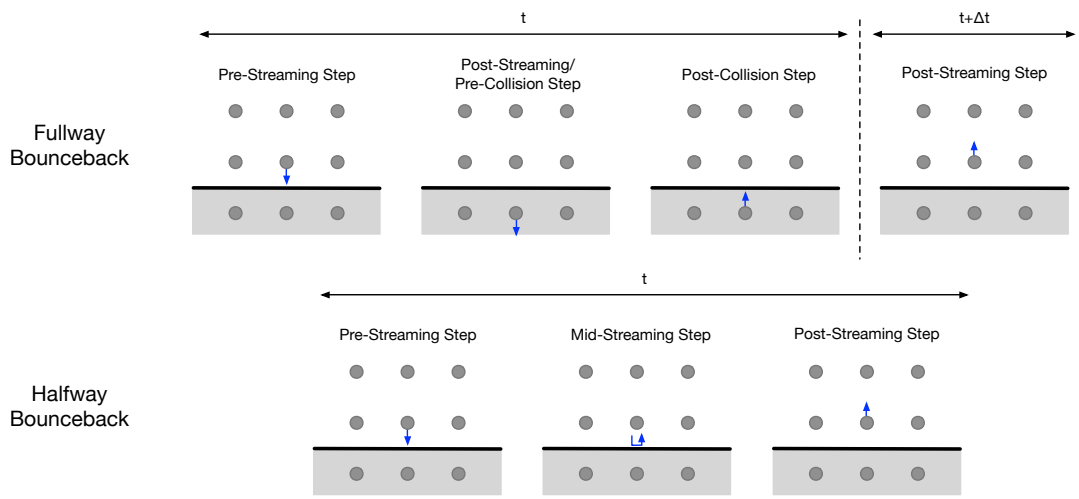

Figure 3.5: Visual representation of fullway and halfway bounceback boundary conditions: f_4 becomes f_3 according to the velocity model in Figure 3.2.

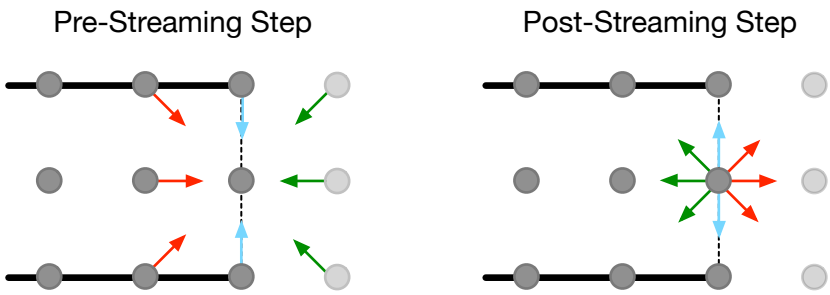

Figure 3.6: Visual representation of regularised boundary conditions where light grey lattice points are beyond the domain and included for visual purposes only. The distribution function components that contribute to each of the density components defined in Eqn 3.25 are shown, where ρ_0 are blue, ρ_+ are green and ρ_- are red. Note the values of each component are recalculated using the regularised boundary condition.

3.3.4 Regularised Boundary Conditions

The regularised boundary condition, developed by Latt et al. [104] is able to impose no-slip conditions as well as velocity and pressure boundaries. Unlike the periodic and bounceback boundary conditions, the regularised boundary condition calculates and replaces the full set of distribution function components at a boundary node. This is achieved by reconstructing each component using the stress tensor which in turn is calculated through the known macroscopic quantities.

In order to understand which macroscopic quantities are known, it is important to consider the macroscopic density in component form:

$$\rho = \rho_0 + \rho_+ + \rho_- \tag{3.25}$$

where ρ_0 is the density component referring to the distribution function components that are planar to the boundary, ρ_+ is the density component referring to the distribution function components that are streaming outside the boundary and ρ_- is the density component referring to the distribution function components that are streaming inside the boundary. These are known as the zero,

outer-normal and inner-normal densities and are calculated via:

$$\rho_0 = \sum_{i|\boldsymbol{c}_{ik}=0} f_i \tag{3.26}$$

$$\rho_+ = \sum_{i|\boldsymbol{c}_{ik}=\boldsymbol{n}} f_i \tag{3.27}$$

$$\rho_- = \sum_{i|\boldsymbol{c}_{ik}=-\boldsymbol{n}} f_i \tag{3.28}$$

where $\boldsymbol{n}$ is the normal vector on the boundary in question pointing into the domain and k is the dimension of the discretised velocity model $\boldsymbol{c}_i$ along which the normal is directed. Substituting these density components into Eqn. 3.13 gives the macroscopic velocity in terms of the density components:

$$\rho \boldsymbol{u}_k = \rho_+ - \rho_- \tag{3.29}$$

From Figure 3.6 it can be seen that the outer-normal densities are unknown and can be eliminated by substituting Eqn. 3.25 into Eqn. 3.29 and rearranging for the desired macroscopic quantity at the boundary, e.g. for a velocity boundary in Eqn. 3.30 and a pressure boundary in Eqn. 3.31:

$$\rho = \frac{1}{1 - \boldsymbol{u}_k}(2\rho_- + \rho_0) \tag{3.30}$$

$$\boldsymbol{u}_k = 1 - \frac{2\rho_- + \rho_0}{\rho} \tag{3.31}$$

Given all the unknown macroscopic quantities have been calculated, the distribution function components can be evaluated using the stress tensor. This is done by first calculating intermediate values of the unknown distribution func-

tion components via the non-equilibrium bounceback assumption [105]:

$$f_i^{neq} = f_j^{neq} \tag{3.32}$$

where $f_i^{neq} = f_i - f_i^{eq}$ and j is the opposite direction to i in the velocity model depicted in Figure 3.2. The first-order terms of the intermediate distribution function values can be obtained via power series expansion:

$$f_i = f_i^{(0)} + \epsilon f_i^{(1)} + O(\epsilon^2) \tag{3.33}$$

where ϵ is the Knudsen number and $f_i^{(0)} = f_i^{eq}$. The first-order terms are then used to calculate the first-order components of the stress tensor:

$$\mathbf{\Pi}^{(1)} = \sum_i \boldsymbol{c}_i \otimes \boldsymbol{c}_i f_i^{(1)} \tag{3.34}$$

The components of the distribution function can all then be reconstructed using the first-order stress tensor through contraction with the tensor $\boldsymbol{Q}_i$:

$$f_i = f_i^{eq} + \frac{w_i}{2c_s^4} \boldsymbol{Q}_i : \mathbf{\Pi}^{(1)} \tag{3.35}$$

where:

$$\boldsymbol{Q}_i = \boldsymbol{c}_i \otimes \boldsymbol{c}_i - c_s^2 \boldsymbol{I} \tag{3.36}$$

and $\boldsymbol{I}$ is an identity matrix.

3.3.5 Initial Conditions

In the present work, uniform density and zero-velocity are set in order to ensure the macroscopic and mesoscopic conditions are consistent at initialisation.

3.3.6 Immersed Boundary

The previously described boundary conditions are all utilised for stationary boundaries in this work. In order to model not just moving boundaries but also non-rigid boundaries, i.e. fluid-structure interaction, the immersed boundary is implemented. This will be discussed in detail after the structural solver has been introduced in Chapter 5 since it also acts as the coupling method between the fluid and structural solvers.

3.4 Summary

This chapter has introduced the fluid solver implemented within the fluid-structure interaction method, the LBM. The underlying governing equations have been discussed with details of their discretisation from kinetic theory, while discretisation of the velocity space and collisions specific to this implementation have also been detailed. Initial and boundary conditions that are commonly implemented in the work conducted have been included. The next chapter introduces the structural solver in the FSI method.

Chapter 4

Vector-based Discrete Element Method

This chapter introduces the structural solver integrated into the fluid-structure interaction method. The vector-based discrete element method, known as the V-model, is a variant of the discrete element method proposed by Kuzkin and Asonov [106]. The method implemented here develops the work of Nasar et al. [107] where the V-model has been adapted for elastic materials rather than granular materials as the original model was intended. A journal article introducing the method, "Vector-based discrete element method for solid elastic bodies" is included in Appendix C, describing the discretised equations, their implementation on both CPU and GPU architecture and validation results using static and dynamic cases. Within this chapter, the foundations of the method will be described including the formulation and discretisation of the governing equations.

4.1 Overview of DEMs for Elastic Bodies

The discrete element method, also known as the distinct element method, was originally proposed by Cundall et al. [108] for rock mechanics and associated applications. For a given material and body, a structure is discretised into a collection of particles that interact with one another as they contact. The deformation of the contacts are directly considered and evolve continuously. A key capability of the method is its ability to model internal forces within a body while also considering collisions with other bodies with little additional treatment re-

quired in the solver. Furthermore, the real material properties such as particle morphology e.g. shape and size, joints, orientation and state can be exactly represented [109]. As a result, the method has been used extensively in sedimentary flows such as soil [110] and sand [111], and in flows where particles are suspended in a fluid [112].

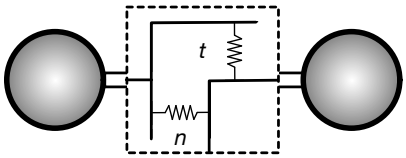

Figure 4.1: Normal (n) and tangential (t) spring connections between two particles.

For DEM representations of continuous materials, the particles are connected using fixed connections. The most simple form of these connections are linear springs. These can be arranged to model normal and tangential forces as shown in Figure 4.1. This has given rise to the use of DEMs in elastic body applications [113,114] including anisotropic materials [115]. By modelling such materials using DEMs, the additional capabilities of the method such as the ability to break or create connections during a simulation can be utilised. As a result, complex physical effects such as cracking or rupture can be more readily modelled than equivalent continuum methods such as FEM [9].

However, due to the relatively high number of particles required to discretise a body with high fidelity in comparison with FEM, the required computational resource can increase dramatically for large spatial or temporal domains. Fortunately, the method is local in nature for elastic body applications and therefore well suited to parallelisation, particularly via GPU hardware. However, a DEM simulation of a continuous body would not be expected to be faster than an FEM simulation of the same body. Instead, GPU acceleration allows DEM simulations to be performed in time frames within an order of magnitude of the FEM simulation while also modelling complex physical effects.

The V-model discretises a structure into a collection of particles connected by elastic bonds. In this implementation, the bonds are rigidly attached to the particles therefore preventing remodelling of the structure during a simulation. In the next section, the formulation of the governing equations will be detailed.

4.2 V-model Formulation

4.2.1 Bond Forces and Moments

In order to derive the governing equations for the V-model, consider two particles i and j connected via flexible bonds which is rigidly attached to each of the particle centres. From Newton's Third Law it is known that the forces $\boldsymbol{F}$ and moments $\boldsymbol{M}$ exerted on each particle, by the other particle must be equal and opposite:

$$\boldsymbol{F}_{ij} = -\boldsymbol{F}_{ji} \tag{4.1}$$

$$\boldsymbol{M}_{ij} + \boldsymbol{M}_{ji} - \boldsymbol{r}_{ij} \times \boldsymbol{F}_{ij} = \boldsymbol{0} \tag{4.2}$$

where $\boldsymbol{r}_{ij} = \boldsymbol{r}_j - \boldsymbol{r}_i$ is the relative position vector between particles i and j. An energy balance for the rate of change of internal energy $\dot{U}$ in the system can be written as:

$$\dot{U} = \boldsymbol{F}_{ij} \cdot \dot{\boldsymbol{r}}_{ij} - \boldsymbol{M}_{ij} \cdot \boldsymbol{\omega}_i - \boldsymbol{M}_{ji} \cdot \boldsymbol{\omega}_j \tag{4.3}$$

where $\boldsymbol{\omega}_i$ and $\boldsymbol{\omega}_j$ are the angular velocities for particles i and j respectively. By defining a set of co-rotating vectors $\boldsymbol{n}_i^{k_1}$ and $\boldsymbol{n}_j^{k_2}$ (where k_1 is the coordinate system for particle i and k_2 is the coordinate system for particle j) that are attached rigidly to the surface of each particle as shown in Figure 4.2.

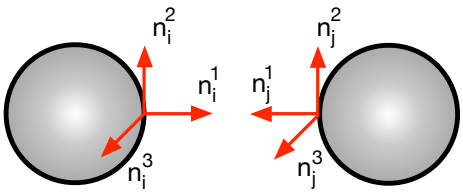

Figure 4.2: Orientation vector sets $\boldsymbol{n}_i^{k_1}$ and $\boldsymbol{n}_j^{k_2}$ rigidly attached to the surface of each particle.

Assuming that particle interactions are not dependent on the relative velocities

between particles, the internal energy can be defined as a function of the relative particle positions $\boldsymbol{r}_{ij}$ and orientations $\boldsymbol{n}_i^{k_1}$ and $\boldsymbol{n}_j^{k_2}$:

$$U = U(\boldsymbol{r}_{ij}, \boldsymbol{n}_i^{k_1}, \boldsymbol{n}_j^{k_2}) \tag{4.4}$$

By differentiating Equation 4.4 with respect to time and using the chain rule, the rate of change in internal energy can be defined in terms of vectors $\boldsymbol{r}_{ij}$, $\boldsymbol{n}_i^{k_1}$ and $\boldsymbol{n}_j^{k_2}$:

$$\dot{U}(\boldsymbol{r}_{ij}, \boldsymbol{n}_i^{k_1}, \boldsymbol{n}_j^{k_2}) = \frac{\partial U}{\partial \boldsymbol{r}_{ij}} \cdot \dot{\boldsymbol{r}}_{ij} + \sum_{k_1} \frac{\partial U}{\partial \boldsymbol{n}_i^{k_1}} \cdot \dot{\boldsymbol{n}}_i^{k_1} + \sum_{k_2} \frac{\partial U}{\partial \boldsymbol{n}_j^{k_2}} \cdot \dot{\boldsymbol{n}}_j^{k_2} \tag{4.5}$$

By using a series of transformation matrices and chain rule manipulations as originally proposed by Price et al. [116] for fluids, and adapted for solids by Kuzkin and Asonov [117], the second and third terms on the RHS of Equation 4.5 can be expressed as:

$$\sum_{k_1} \frac{\partial U}{\partial \boldsymbol{n}_i^{k_1}} \cdot \dot{\boldsymbol{n}}_i^{k_1} = -\left(\sum_{k_1} \frac{\partial U}{\partial \boldsymbol{n}_i^{k_1}} \times \boldsymbol{n}_i^{k_1} \right) \cdot \boldsymbol{\omega}_i \tag{4.6}$$

$$\sum_{k_2} \frac{\partial U}{\partial \boldsymbol{n}_j^{k_2}} \cdot \dot{\boldsymbol{n}}_j^{k_2} = -\left(\sum_{k_2} \frac{\partial U}{\partial \boldsymbol{n}_j^{k_2}} \times \boldsymbol{n}_j^{k_2} \right) \cdot \boldsymbol{\omega}_j \tag{4.7}$$

Substituting Equation 4.6 and 4.7 into Equation 4.5 gives:

$$\dot{U}(\boldsymbol{r}_{ij}, \boldsymbol{n}_i^{k_1}, \boldsymbol{n}_j^{k_2}) = \frac{\partial U}{\partial \boldsymbol{r}_{ij}} \cdot \dot{\boldsymbol{r}}_{ij} - \left(\sum_{k_1} \frac{\partial U}{\partial \boldsymbol{n}_i^{k_1}} \times \boldsymbol{n}_i^{k_1} \right) \cdot \boldsymbol{\omega}_i - \left(\sum_{k_2} \frac{\partial U}{\partial \boldsymbol{n}_j^{k_2}} \times \boldsymbol{n}_j^{k_2} \right) \cdot \boldsymbol{\omega}_j \tag{4.8}$$

Comparing Equation 4.3 and 4.8 allows the forces and moments applied by one particle on another to be calculated in terms of the internal energy, distance

vectors between the particles, and the orientation vectors of each particle:

$$\boldsymbol{F}_{ij} = -\boldsymbol{F}_{ji} = \frac{\partial U}{\partial \boldsymbol{r}_{ij}} \tag{4.9}$$

$$\boldsymbol{M}_{ij} = \sum_{k^1} \frac{\partial U}{\partial \boldsymbol{n}_i^{k_1}} \times \boldsymbol{n}_i^{k_1} \tag{4.10}$$

$$\boldsymbol{M}_{ji} = \sum_{k^2} \frac{\partial U}{\partial \boldsymbol{n}_j^{k_2}} \times \boldsymbol{n}_j^{k_2} \tag{4.11}$$

A set of vector dot products that are invariant with respect to rigid body rotation can be defined:

$$r_{ij} \qquad \boldsymbol{e}_{ij} \cdot \boldsymbol{n}_i^{k_1} \qquad \boldsymbol{e}_{ji} \cdot \boldsymbol{n}_j^{k_2} \qquad \boldsymbol{n}_i^{k_1} \cdot \boldsymbol{n}_j^{k_2} \tag{4.12}$$

where $r_{ij} = |\boldsymbol{r}_{ij}|$ and $\boldsymbol{e}_{ij} = \boldsymbol{r}_{ij}/r_{ij}$, namely the distance and unit vector between and particles i and j respectively. The internal energy of the system can be expressed as functions of these invariants:

$$U = U(r_{ij}, \boldsymbol{e}_{ij} \cdot \boldsymbol{n}_i^{k_1}, \boldsymbol{e}_{ji} \cdot \boldsymbol{n}_j^{k_2}, \boldsymbol{n}_i^{k_1} \cdot \boldsymbol{n}_j^{k_2}) \tag{4.13}$$

These arguments can be separated based upon the mode of deformation they govern, allowing relationships between the material properties and model stiffness parameters to be derived. This procedure is discussed in Section 4.3. Two different approaches have been taken to separating the arguments, with the key difference between them being their treatment of torsional and bending deformations. In the first approach [106] the torsional and bending deformation are described by independent terms whereas in the second approach [118] they are dependent. The approach of [118] implemented within this work defines the internal

energy of a given bond as:

$$U = \frac{B_1}{2}(r_{ij} - a)^2 + \frac{B_2}{2}(\boldsymbol{n}_j^1 - \boldsymbol{n}_i^1) \cdot \boldsymbol{e}_{ij} + B_3(\boldsymbol{n}_i^1 \cdot \boldsymbol{n}_j^1) - \frac{B_4}{2}(\boldsymbol{n}_i^2 \cdot \boldsymbol{n}_j^2 + \boldsymbol{n}_i^3 \cdot \boldsymbol{n}_j^3) \quad (4.14)$$

where a is the free equilibrium length of the bond and B_1, B_2, B_3 and B_4 are model stiffness coefficients for axial, shear, bending and torsional bond deformation, derivable from constitutive relationships and macroscopic material properties. These will be discussed in Section 4.3. Substituting Equation 4.14 into Equation 4.9, 4.10 and 4.11 allows the forces and moments in each bond to be defined as:

$$\boldsymbol{F}_{ij} = B_1(r_{ij} - a) + \frac{B_2}{2r_{ij}}(\boldsymbol{n}_j^1 - \boldsymbol{n}_i^1) \cdot (\boldsymbol{E} - \boldsymbol{e}_{ij}\boldsymbol{e}_{ij}) \quad (4.15)$$

$$\boldsymbol{M}_{ij} = R_i \boldsymbol{n}_i^1 \times \boldsymbol{F}_{ij} + \frac{B_2}{2}\boldsymbol{e}_{ij} \times \boldsymbol{n}_i^1 + B_3 \boldsymbol{n}_j^1 \times \boldsymbol{n}_i^1 - \frac{B_4}{2}(\boldsymbol{n}_j^2 \times \boldsymbol{n}_i^2 + \boldsymbol{n}_j^3 \times \boldsymbol{n}_i^3) \quad (4.16)$$

$$\boldsymbol{M}_{ji} = R_j \boldsymbol{n}_j^1 \times \boldsymbol{F}_{ji} + \frac{B_2}{2}\boldsymbol{e}_{ij} \times \boldsymbol{n}_j^1 - B_3 \boldsymbol{n}_j^1 \times \boldsymbol{n}_i^1 + \frac{B_4}{2}(\boldsymbol{n}_j^2 \times \boldsymbol{n}_i^2 + \boldsymbol{n}_j^3 \times \boldsymbol{n}_i^3) \quad (4.17)$$

where $\boldsymbol{E}$ is an identity matrix and R_i and R_j are the radii of particle i and j. Since the V-model is restricted to 2D in this implementation, no torsional deformation is modelled and $\boldsymbol{n}_{i,j}^2$ and $\boldsymbol{n}_{i,j}^3$ are not required. In addition, for a continuous material, the bonds are attached at the centres of each connecting particle and therefore R_i and R_j are zero. As a result, Equation 4.16 and 4.17 can be reduced to:

$$\boldsymbol{M}_{ij} = \frac{B_2}{2}\boldsymbol{e}_{ij} \times \boldsymbol{n}_i^1 + B_3 \boldsymbol{n}_j^1 \times \boldsymbol{n}_i^1 \quad (4.18)$$

$$\boldsymbol{M}_{ji} = \frac{B_2}{2}\boldsymbol{e}_{ij} \times \boldsymbol{n}_j^1 - B_3 \boldsymbol{n}_j^1 \times \boldsymbol{n}_i^1 \quad (4.19)$$

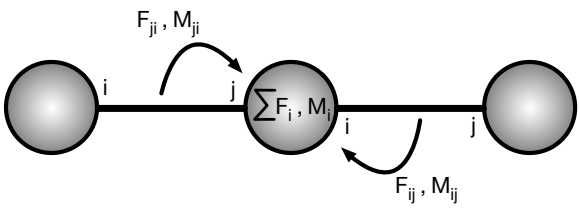

Figure 4.3: Forces and moments calculated in each bond are passed to their respective connecting particle.

Equation 4.15, 4.18 and 4.19 are the governing equations used to calculate forces and moments in the solver implemented in this work. The Section 4.3 will detail how the model stiffness coefficients are calibrated for a given material.

4.2.2 Updating Particle Positions and Orientations

Once the forces and moments have been calculated in all the bonds within a system and passed to each connecting particle, the resultant forces and moments of each particle can be calculated:

$$\boldsymbol{F}_i = \sum_p \boldsymbol{F}_{ij} + \sum_q \boldsymbol{F}_{ji} \tag{4.20}$$

$$\boldsymbol{M}_i = \sum_p \boldsymbol{M}_{ij} + \sum_q \boldsymbol{M}_{ji} \tag{4.21}$$

where p and q refer to the number of bonds connected to the particle which considers that particle to be particle i or particle j respectively. In the configuration shown in Figure 4.3, p and q are both equal to one. The resultant forces and moments are used to update the position and orientation of the particles using a numerical integration scheme via Newton's 2nd Law. This is applied to both translational and rotational motion to find their translational $\boldsymbol{a}_i$ and angular $\boldsymbol{\alpha}_i$ accelerations for each particle:

$$\boldsymbol{a}_i = \frac{\boldsymbol{F}_i}{m_i} \tag{4.22}$$

$$\boldsymbol{\alpha}_i = \frac{\boldsymbol{M_i}}{I_i} \tag{4.23}$$

where m_i and I_i are the mass and moment of inertia of particle i.

4.3 Constitutive Relationships

For a given external load, a constitutive relationship is required to govern the extent of the resulting deformation through the calculation of material stiffness coefficients, taking into account macroscopic material properties such as Young's modulus E and Poisson's ratio ν. Mesh independent relationships must be used in order to relate the model stiffness coefficients B_{1-4} to the material stiffness coefficients for axial C_A, shear C_D, bending C_B and torsion C_T. This is done by considering pure deformation modes, i.e. where only one of axial compression/tension, shear, bending or torsion exist.

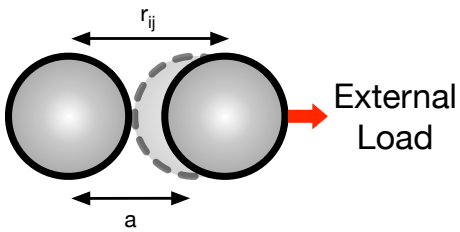

Figure 4.4: Pure axial deformation of a two particle system due to an external load.

Consider two particles connected by a single bond, where one particle has an external load imparted on it in the same direction as the direction vector connecting the particles as shown in Figure 4.4. The resulting deformation is pure axial compression or extension. In this case, Equation 4.15, 4.18 and 4.19 governing the forces and moments present in bond, are reduced to:

$$\boldsymbol{F}_{ij} = B_1(r_{ij} - a) \tag{4.24}$$

$$\boldsymbol{M}_{ij} = \boldsymbol{M}_{ji} = 0 \tag{4.25}$$

By comparing Equation 4.24 with the Hooke's law for a single degree of freedom elastic body:

$$C_A = \frac{\boldsymbol{F}}{\Delta x} \tag{4.26}$$

where Δx is the displacement and is equal to $r_{ij} - a$, it can seen that $B_1 = C_A$. By using the same procedure for the remaining pure deformation modes, relationships between the remaining model and material stiffness coefficients can also be found:

$$C_D = \frac{B_2}{a^2} \qquad C_B = \frac{B_2}{4} + B_3 + \frac{B_4}{2} \qquad C_T = B_4 \tag{4.27}$$

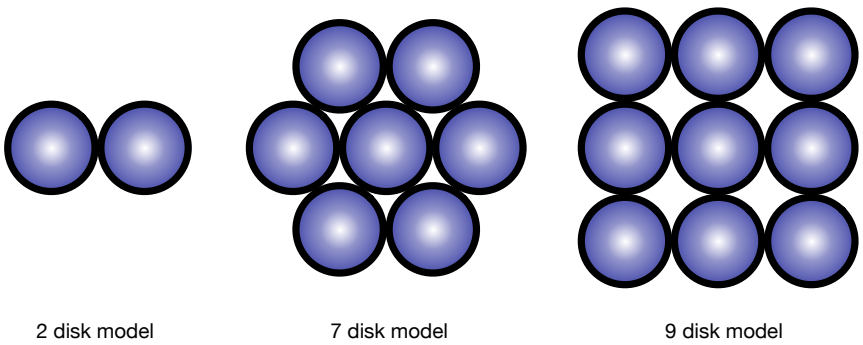

Figure 4.5: Structured particle arrangements commonly used to represent elastic bodies via discrete element methods.

The now defined material stiffness coefficients can also be defined in terms of macroscopic material properties such as Young's modulus E and Poisson's ratio ν via various constitutive models. Many of these models are developed for a given particle arrangement, 2-disk, 7-disk or 9-disk arrangements as shown in Figure 4.5. The most extensively implemented model to represent elastic bodies using DEMs was proposed by Griffiths and Mustoe [119] for the 7-disk arrangement, sometimes referred to as the triangular arrangement [107]. In this model, C_A and C_D are derived by comparing the stiffness matrix of a 2D beam finite element with that of two bonded discrete elements (particles) and then extending this procedure to three bonded particles in a triangular arrangement. Derivations of this procedure can be found in [9]. The model defines the axial and shear stiffness

coefficients as:

$$C_A = \frac{E}{\sqrt{3}(1-\nu)} \tag{4.28}$$

$$C_D = \frac{E(1-3\nu)}{\sqrt{3}(1-\nu^2)} \tag{4.29}$$

However, this formulation was derived for a discrete element method that does not directly consider bending unlike the V-model. As a result, a further constitutive relationship is required for the bending stiffness coefficient. The work by Nasar [107] produced well-validated results for static and dynamic beam bending using the following relationship:

$$C_B = \frac{EI_b}{a} \tag{4.30}$$

where I_b is the moment of inertia of the bond which has a rectangular cross section. Since the V-model is restricted to 2D in this implementation, torsional deformation is not considered and therefore a relationship between material properties and C_T is not required. However, a number of relationships exist with details found in [106].

4.4 Time Integration Scheme

Given that the resultant forces and moments on each particle can be calculated via the governing equations and associated constitutive relationships previously discussed, an appropriate numerical time integration scheme must be employed to update the positions and orientations of each particle, via their linear and angular accelerations and velocities, at the end of each discrete time step. For discrete element methods, a number of schemes are commonly implemented. These can be classified as single time step methods such as the first order accurate leapfrog scheme to the second order accurate central difference discretisation scheme (the most commonly implemented scheme) [120, 121] and multi-step methods such as predictor-corrector schemes [122]. A comprehensive review of time integration

methods for discrete element methods, assessing accuracy and computational expense was conducted by Kruggel-Emden et al. [121].

In this work the scheme known as Beeman's algorithm [123], is implemented having been shown to produce the optimal results in comparison to the Leapfrog algorithm and predictor-corrector methods for the V-model [107]. Using this scheme the translational $\boldsymbol{u}$ and angular $\boldsymbol{\omega}$ velocities are calculated via:

$$\boldsymbol{u}_i^{t+\Delta t} = \boldsymbol{u}_i^t + \frac{1}{6}(2\boldsymbol{a}_i^{t+\Delta t} + 5\boldsymbol{a}_i^t + \boldsymbol{a}_i^{t-\Delta t})\Delta t \tag{4.31}$$

$$\boldsymbol{\omega}_i^{t+\Delta t} = \boldsymbol{\omega}_i^t + \frac{1}{6}(2\boldsymbol{\alpha}_i^{t+\Delta t} + 5\boldsymbol{\alpha}_i^t + \boldsymbol{\alpha}_i^{t-\Delta t})\Delta t \tag{4.32}$$

where t is the current time and Δt is the time step size. The translational and angular velocities are subsequently used to find updated particle positions $\boldsymbol{x}$ and orientations $\boldsymbol{\theta}$:

$$\boldsymbol{x}_i^{t+\Delta t} = \boldsymbol{x}_i^t + \boldsymbol{u}_i^{t+\Delta t}\Delta t + \frac{1}{6}(4\boldsymbol{a}_i^t - \boldsymbol{a}_i^{t-\Delta t})\Delta t^2 \tag{4.33}$$

$$\boldsymbol{\theta}_i^{t+\Delta t} = \boldsymbol{\theta}_i^t + \boldsymbol{\omega}_i^{t+\Delta t}\Delta t + \frac{1}{6}(4\boldsymbol{\alpha}_i^t - \boldsymbol{\alpha}_i^{t-\Delta t})\Delta t^2 \tag{4.34}$$

4.5 Determining the Critical Time Step Size

The critical time step of a DEM is the time step size judged to be the limit of stability within a simulation. These instabilities tend to accumulate over time, for example over a number of oscillations of an excited beam, and therefore their presence is not always obvious, yet may affect transient characteristics of a structure, such as deformation, significantly. Currently, a universal criterion does not exist. However a number of works have proposed models to estimate its size, based on upon empirical data and Gerschgorins theorem, that contain variables that are case dependent [120, 124, 125]. Many of these criteria relate the critical time step size to the smallest period of oscillation resulting from the highest

natural frequency:

$$\Delta t_{crit} = \frac{2}{\omega_{max}} \tag{4.35}$$

and are functions of minimum particle mass, particle connection stiffness coefficients and the number of connections per particle, known as the "coordination number". However, these criteria include a safety factor less than 1 in order to ensure stability of the simulation and are recommended as estimates rather than definitive criteria. Defining a robust critical time step size for DEMs is still an active area of research within the community [125].

The critical time step formulation implemented here can be defined as:

$$\Delta t_{crit} = \beta \sqrt{\frac{m_i}{k}} \tag{4.36}$$

where m_i is the mass of a particle i and k is equal to the largest material stiffness coefficient, usually C_A. For the purposes of this work a conservative safety factor, $\beta = 0.05$ has been used to ensure stability of the method and robustness of validation results. This factor is smaller than those defined by literature, however for longer timescale problems, such as the validation case in Section 6.4, numerical instabilities were observed to build up over time cause the simulation to *crash* using those defined by literature. This conservative safety factor is also in agreement with a general estimation for the time step size of FEM simulations; 1/20th of the period of oscillation that should be captured [126].

4.6 Summary

This chapter describes the method used to model the deformation of structures, namely the vector-based discrete element method, that is integrated into the fluid-structure interaction method. The formulation of the governing equations from the internal energy of a system is detailed along with an outline of its numerical implementation. Discussion of particle arrangement and time step considerations are also included. The next chapter introduces the method used to couple the

fluid and structure solvers, the immersed boundary method, along with details of the full fluid-structure interaction method implementation in algorithm form.

Chapter 5

Immersed Boundary Method

This chapter describes the method, known as the immersed boundary method (IBM), used to couple the fluid and structural solvers so the fluid-structure interaction can be modelled. Details of the formulation, including the interpolation and spreading procedures, are provided. Furthermore, its integration into a coupling scheme, both weakly and strongly coupled, are discussed. Algorithms of a complete, coupled time step for each coupling scheme are provided, where the time step size of the structure solver is smaller than that of the fluid. A novel force mapping approach between the IBM and the V-model that allows independence of the fluid and structure resolution is presented. The chapter begins with the rationale behind the choice of coupling approach.

5.1 Coupling Approach Rationale

Fluid-structure interaction methods can be classified into two main groups through the coupling approach employed; monolithic or partitioned. A key difference between these approaches is how they ensure the kinematic and dynamic interface conditions are satisfied at the boundary between the fluid and structure. A monolithic approach will automatically ensure these conditions are satisfied due to solving the governing equations of the fluid and the structure synchronously. In contrast, partitioned approaches must directly ensure these conditions are met since the governing equations are solved sequentially [127]. Many simpler partitioned approaches do not strictly satisfy these conditions which is known as weak coupling and will be discussed later in this section.

The kinematic condition is the no-slip condition, stating that the fluid velocity $\boldsymbol{u}$ at the boundary must be equal to that of the boundary itself and can be defined as:

$$\boldsymbol{u}(\boldsymbol{X}) = \frac{d\boldsymbol{X}}{dt} \tag{5.1}$$

where $\boldsymbol{X}$ is the position at the boundary where the fluid velocity is measured. The dynamic interface condition states that the traction $\boldsymbol{T}$ of the fluid and structure on either side of the interface must be equal:

$$\boldsymbol{T}_s(t) + \boldsymbol{T}_f(t) = 0 \tag{5.2}$$

where the traction of the structure and fluid can be defined in terms of the fluid and structure stress at the interface $\boldsymbol{\sigma}_{f,s}$ and the interface normal vectors $\boldsymbol{n}_{f,s}$:

$$\boldsymbol{T}_s = \boldsymbol{\sigma}_s \cdot \boldsymbol{n}_s \qquad \boldsymbol{T}_f = \boldsymbol{\sigma}_f \cdot \boldsymbol{n}_f \tag{5.3}$$

Satisfying Equations 5.1 and 5.2 infers that momentum and energy have been conserved across the interface [128].

Further differences exist between monolithic and partitioned approaches which result in them being more advantageous in certain applications. Monolithic methods are more stable and provide greater accuracy than partitioned approaches [127] however they can be difficult to implement for large deformations where the interface is difficult to discretise. Furthermore, since the same numerical method must be used for both the fluid and the structure, this can lead to serious constraints if the same method is not suitable for both. Different numerical methods that are suitable for the fluid and the structure can be coupled together using partitioned approaches [129, 130]. However, since they are solved in a staggered arrangement, accuracy and stability issues can become apparent without careful treatment, especially if the interface conditions are not met. More complex coupling schemes can improve accuracy and stability but are inherently more computationally expensive and more difficult to implement [131]. Taking these advantages and disadvantages into account, a partitioned approach was

deemed the most optimal for this work, given that the focus is to provide a tool that can be translated into clinical practice.

One of the key criteria for selection of the fluid and structure solvers, the LBM and V-model, is computational speed. This can be achieved through GPU acceleration or otherwise. Grid generation in CFD is computationally expensive, especially for moving boundaries between the fluid and structure where remeshing must occur at regular intervals to account for the moving boundary. As a result it must be restricted to minimal occurrences in order for the FSI method to maintain the speed of computation of fluid and structure solvers.

Non-conforming methods, such as the IBM, are able to remove the need to remesh the fluid, even with a moving boundary, by decoupling the fluid governing equations from the boundary representation through independent overlapping meshes for the structure and fluid. In spite of this, the necessary boundary conditions on the surface of the structure are imposed as will be discussed in this chapter. This is particularly important for complex and highly deformable geometries which, when using body-conforming coupling methods such as Arbitrary Lagrangian-Eulerian approach (ALE) [132], can produce poor quality cells at the interface between the fluid and structure due to the structural deformation and/or require the domain to be remeshed at regular intervals. Using a non body-conforming method results in no additional treatment or computational load regardless of the magnitude of deformation or geometry complexity, assuming the spatial and temporal resolutions are equal. Figure 5.1 illustrates the differences between the body conforming and non-conforming approaches for an arbitrary geometry.

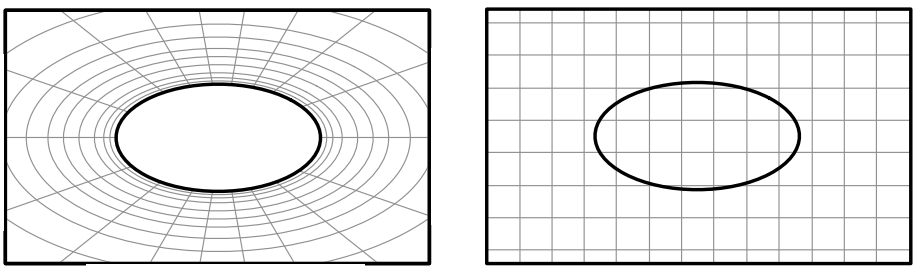

Figure 5.1: Fluid domain discretisation for conforming (left) and non-conforming (right) boundary conditions.

5.2 Immersed Boundary Method

The IBM was originally proposed by Peskin to model blood flow through the aortic valve by imposing the motion of the valve leaflets [133]. However, the IBM is able to replicate the effect of the boundary whether it be stationary or moving, rigid or flexible, by adding a source term to the fluid governing equations that imposes the kinematic constraint. As a result, the fluid grid (Eulerian) and structure boundary (Lagrangian) are free to move over one another, with the only interaction between the two via the IBM forces applied to impose the boundary condition. Since this is the only interaction between the solvers, forces need to be accurately transferred between grids via adjacent grid points using interpolation and extrapolation procedures which are discussed in the next section.

Since the original immersed boundary method was proposed, a number of developments have been made. A comprehensive review of these methods was conducted by Mittal and Iaccarino [134] for the interested reader. The next section describes the immersed boundary method variant that is implemented in this work, an implicit direct forcing method proposed by Pinelli et al. [135] and extended by Li and Favier [131].

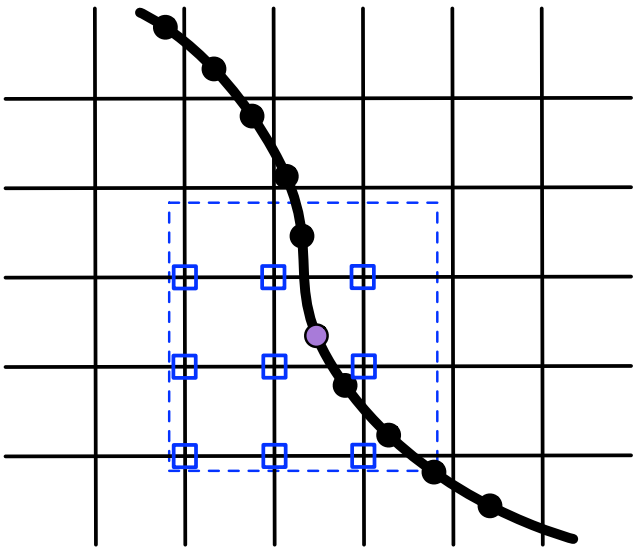

Figure 5.2: Support stencil (blue) around a given Lagrangian immersed boundary marker (purple) which in turn is placed on the boundary (black). Fluid points within the support stencil for the marker being considered, are included within the interpolation and spreading procedures.

5.2.1 Interpolation and Spreading

Given that the IBM allows forces at the boundary to be passed from one mesh (Eulerian) to another mesh (Lagrangian), in both directions, the information must be interpolated and spread since the locations of mesh points of each mesh in the vicinity of the boundary will not coincide as shown in Figure 5.2. The interpolation procedure, passes a force $\boldsymbol{f}$ in the Eulerian reference frame, denoted by lower-case notation, to the Lagrangian reference frame $\boldsymbol{F}$, denoted by upper-case notation, and in continuous form is defined as:

$$\boldsymbol{F}(\boldsymbol{X}) = \int_{\Omega} \boldsymbol{f}(\boldsymbol{x})\delta(\boldsymbol{x} - \boldsymbol{X})d\boldsymbol{x} \tag{5.4}$$

where $\boldsymbol{x}$ is the position in the Eulerian reference frame Ω, $\boldsymbol{X}$ is the position in the Lagrangian reference frame Γ and δ is the Dirac Delta function which is discussed later. As can seen in Figure 5.2, the Eulerian components that contribute to the interpolation procedure are located at discrete points rather than a continuous contribution. As a result, Equation 5.4 is discretised as:

$$\boldsymbol{F}(\boldsymbol{X}) = \sum_{\Omega} \boldsymbol{f}(\boldsymbol{x})\hat{\delta}(\boldsymbol{x} - \boldsymbol{X})\Delta x \Delta y \Delta z \tag{5.5}$$

where x, y, z are Eulerian coordinates and $\hat{\delta}$ is the discrete form of the Dirac Delta function.

The spreading procedure does the opposite, passing a force $\boldsymbol{F}$ in the Lagrangian reference frame to the Eulerian reference frame $\boldsymbol{f}$, in continuous form:

$$\boldsymbol{f}(\boldsymbol{x}) = \int_{\Gamma} \boldsymbol{F}(\boldsymbol{X})\delta(\boldsymbol{x} - \boldsymbol{X})d\boldsymbol{X} \tag{5.6}$$

which like the interpolation procedure, is discretised in two dimensions as:

$$\boldsymbol{f}(\boldsymbol{x}) = \sum_{\Gamma} \boldsymbol{F}(\boldsymbol{X})\hat{\delta}(\boldsymbol{x} - \boldsymbol{X})\epsilon \Delta q \Delta r \Delta s \tag{5.7}$$

where q, r, s are Lagrangian coordinates and ϵ is a scaling factor developed for the specific implicit immersed boundary method used in this work, which will be discussed in Section 5.2.3.

The discretised interpolation procedure (Equation 5.5) and the discretised spreading procedure (Equation 5.7) will be referred to for the remainder of this chapter using the shorthand notation:

$$\boldsymbol{F}(\boldsymbol{X}) = I[\boldsymbol{f}(\boldsymbol{x})] \qquad \boldsymbol{f}(\boldsymbol{x}) = S[\boldsymbol{F}(\boldsymbol{X})]$$

5.2.2 The Dirac Delta Function

The Dirac delta function is a weighting function used to define the support stencil and the contributions of a quantity at a given location within the stencil. Given that it is used to transfer quantities between the Eulerian and Lagrangian reference frames, it must be defined in the same way for both the interpolation and spreading procedures in order to ensure quantities such as linear and angular momentum are conserved [136]. The Dirac delta function used within this work was originally proposed by Roma et al. [137] and has been used extensively by the immersed boundary community [138–140]. It has been chosen due to its relatively small stencil which reduces the computational resource required, i.e. fewer lattice points are included within the interpolation and spreading procedures. It also adequately suppresses the lattice within these procedures, providing a continuous variation in a given quantity. The four point stencil proposed by Peskin et al. [136] has the advantages listed above for the 3-point stencil while also producing a smoother field, however requires larger computational resource due to the additional lattice sites within the stencil. Figure 5.3 demonstrates the variation of the function across the 3-point stencil region in one and two-dimensions while it can be expressed algebraically in discrete form as:

$$\hat{\delta}(r) = \begin{cases} \frac{1}{3}(1 + \sqrt{-3r^2 + 1} & |r| \leq 0.5 \\ \frac{1}{6}(5 - 3|r| - \sqrt{-3(1 - |r|)^2 + 1} & 0.5 \geq |r| \leq 1.5 \\ 0 & \text{otherwise} \end{cases} \tag{5.8}$$

where r is the distance in lattice units between the lattice point inside the stencil and the immersed boundary marker under consideration.

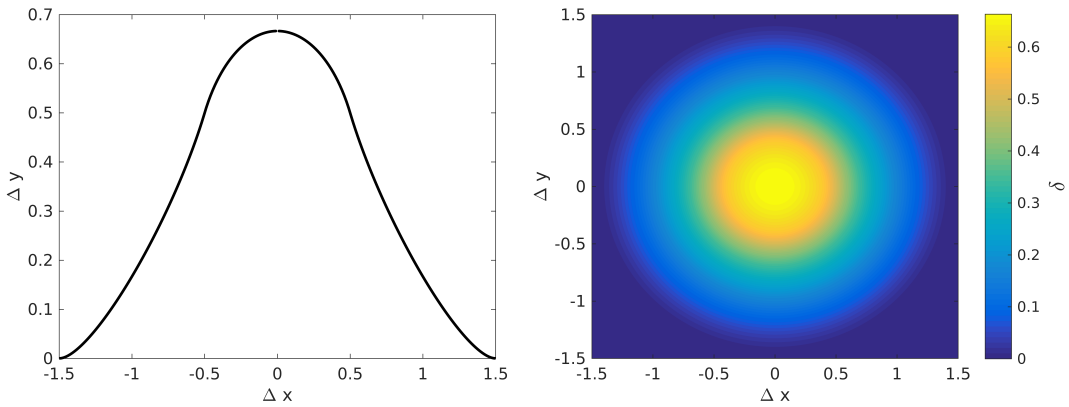

Figure 5.3: Discrete Dirac delta function for 3 point stencil implemented in this work in (left) one dimension and (right) two dimensions.

5.2.3 Scaling Factor

The addition of a scaling factor within the method was proposed by Pinelli et al. [135] to solve the issue where a lattice point can be included within multiple stencils since they can overlap. As a result, the no-slip condition cannot be strictly enforced since during the spreading procedure the lattice points receive contributions from different immersed boundary markers. Using the proposed scaling factor ensures that the force spread back to the Eulerian frame is equal to that of the interpolation. This can be shown by considering again the discrete form of the interpolation procedure (Eqn 5.5):

$$\boldsymbol{F}(\boldsymbol{X}) = \sum_{\Omega} \boldsymbol{f}(\boldsymbol{x})\hat{\delta}(\boldsymbol{x} - \boldsymbol{X})\Delta x \Delta y$$

Substituting $\boldsymbol{f}(\boldsymbol{x})$ for the discrete form of the spreading procedure (Eqn 5.7) yields:

$$\boldsymbol{F}(\boldsymbol{X}) = \sum_{\Omega} \hat{\delta}(\boldsymbol{x} - \boldsymbol{X})\Delta x \Delta y \sum_{\Gamma} \boldsymbol{F}(\boldsymbol{X})\hat{\delta}(\boldsymbol{x} - \boldsymbol{X})\epsilon \Delta q \Delta r \tag{5.9}$$

By defining $A_{n,m}$ as product of the lattice point weightings within a stencil using the discrete form of the Dirac delta function multiplied by the size of the stencil:

$$A_{k,l} = \Delta s \sum_{\Omega} \hat{\delta}(\boldsymbol{x} - \boldsymbol{X}_k)\hat{\delta}(\boldsymbol{x} - \boldsymbol{X}_l) \tag{5.10}$$

Substituting 5.10 into 5.9 and rearranging yields:

$$\boldsymbol{F}(\boldsymbol{X}_k) = \sum_{l=1}^{N} A_{k,l}\epsilon_m \boldsymbol{F}(\boldsymbol{X}_l) \tag{5.11}$$

which can be expressed in matrix form as:

$$\boldsymbol{A\epsilon} = \boldsymbol{1} \tag{5.12}$$

5.3 Coupling with the LBM

The coupling procedure implemented between the LBM and the IBM in this work was proposed by Li et al. [131] which itself was an advancement on the procedure developed by Favier et al. [138]. The advancement of the method comes in the form of abolishing the requirement to calculate the fluid field twice within a single time step by including the forces calculated by the IBM as an immediate correction to the fluid velocity field. As a result, the computational efficiency of the coupling procedure is significantly improved. For a rigid body, the procedure over a single time step can be summarised at a high level as:

1. calculate fluid density and predicted fluid velocity (and subsequent momentum) fields via LBM governing equations

2. interpolate the predicted momentum and density field onto the immersed boundary markers

3. calculate the corrective force in the Lagrangian frame

4. spread the corrective force back to the Eulerian grid

5. correct the predicted velocity field with the force density

In order to calculate the fluid density, the LBM governing equations can be used without any additional treatment as stated in Section 3.2. However, to calculate the predicted velocity field and dependent momentum field, the macroscopic velocity (Eqn 3.22) must be decomposed into a predicted velocity field and a force-correction term:

$$\rho \boldsymbol{u}(\boldsymbol{x}, t) = \rho \boldsymbol{u}^*(\boldsymbol{x}, t) + \frac{\Delta t}{2} \boldsymbol{f}(\boldsymbol{x}, t) \tag{5.13}$$

where $\boldsymbol{u}^*$ is the predicted velocity. The fluid velocity at the boundary and the structure velocity at the boundary $\boldsymbol{U}_s$ must be equal, therefore using the previously defined interpolation procedure yields:

$$\boldsymbol{U}_s = I[\boldsymbol{u}] \tag{5.14}$$

Transforming Eqn 5.13 into the Lagrangian frame using the interpolation procedure and substituting $\boldsymbol{u}(\boldsymbol{x})$ via Eqn 5.14 gives:

$$I[\rho(\boldsymbol{x}, t)]\boldsymbol{U}_s(\boldsymbol{X}, t) = I[\rho \boldsymbol{u}^*(\boldsymbol{x}, t)] + \frac{\Delta t}{2} \boldsymbol{F}(\boldsymbol{X}, t) \tag{5.15}$$

Rearranging for the corrective force in the Lagrangian frame $\boldsymbol{F}(\boldsymbol{X}, t)$:

$$\boldsymbol{F}(\boldsymbol{X}, t) = 2 \frac{I[\rho(\boldsymbol{x}, t)]\boldsymbol{U}_s(\boldsymbol{X}, t) - I[\rho \boldsymbol{u}^*(\boldsymbol{x}, t)]}{\Delta t} \tag{5.16}$$

Given that the boundary velocity is known, the corrective force can be transformed to the Eulerian reference frame and spread onto the lattice:

$$\boldsymbol{f}(\boldsymbol{x}, t) = S[\boldsymbol{F}(\boldsymbol{X}, t)] \tag{5.17}$$

The velocity field can then be updated through the addition of the corrective force using Eqn 5.13. Additional steps in the algorithm are required for a moving boundary as discussed in the next section.

5.4 Coupling with the V-model

In the previous work where the V-model has been included within an FSI method, via IBM to a SPH fluid solver by Nasar et al. [130], the immersed boundary markers must be located on the V-model particle centres in a 1:1 ratio. Since the FSI method developed within this work models fluid via the LBM, the restriction of the ratio between immersed boundary markers and V-model particles can cause significant problems because the LBM resolution must therefore be equal to that of the V-model. If the markers are too far apart a leaky boundary can occur while additional and unnecessary computational cost occurs if the markers are too close [135]. As a result, if an increase in resolution of the LBM solver is required, the V-model resolution must also be increased, often unnecessarily. As a consequence, the computational efficiency of the method is reduced since the critical time step of the V-model is generally at least an order of magnitude smaller than that of the LBM. The issue of differing time steps is partially overcome using a smaller time step for the V-model and will be discussed in Section 5.5.1. However, the ratio of fluid and structure time steps is restricted for fast-moving and highly deformable bodies since the immersed boundary force is calculated at the fluid time step and creating a lag and reducing accuracy. As a result, a method to relax the 1:1 ratio between V-model particles and immersed boundary markers has been developed as presented in Section 5.4.1.

5.4.1 Force Mapping

The immersed boundary method applies a force density to the structure surface. This can be modelled as a uniform distributed load, and therefore discretised as a point load acting at the same point as the immersed boundary marker location of magnitude equal to the force density multiplied by the distance it acts over. This point force is then split into components based on the relative position of the immersed boundary marker between the nearest two V-model particles at the

boundary (in contact with the fluid) as shown in Figure 5.4.

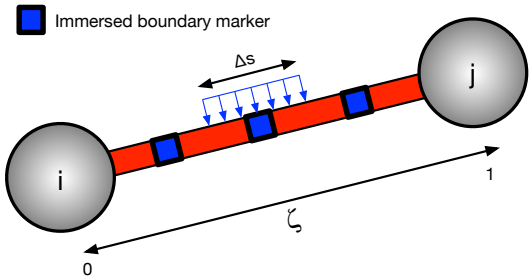

Figure 5.4: Immersed boundary markers (blue) placed along a bond (red) connecting two particles at the fluid-structure interface. Note that the particle diameters have been significantly reduced and the aspect ratio of the bonds increased in order to improve clarity of the immersed boundary marker placement.

Here, a linear interpolation procedure to evaluate the split of components that should be passed to each particle, is implemented. The variation of contribution over the bond is shown in Figure 5.5 and is defined as follows:

$$F_{IBM,i} = 1 - \zeta \qquad F_{IBM,j} = \zeta \tag{5.18}$$

where ζ is the relative distance between the particles in the range 0 to 1. Validation of this procedure is included in Section 6.5 where excellent agreement is presented for a case where a uniform distributed load is discretised directly to the V-model particle centres and through the linear interpolation procedure.

5.4.2 Velocity and Position Update

The procedure to update the velocity $\boldsymbol{u}_s$ and position $\boldsymbol{x}_s$ of the immersed boundary markers at the boundary of the deforming structure also makes use of the relative position of the marker between the two nearest V-model particles on the boundary and can be evaluated via:

$$\boldsymbol{u}_s(\zeta) = \boldsymbol{u}_i + \zeta(\boldsymbol{u}_j - \boldsymbol{u}_i) \tag{5.19}$$

$$\boldsymbol{x}_s(\zeta) = \boldsymbol{x}_i + \zeta(\boldsymbol{x}_j - \boldsymbol{x}_i) \tag{5.20}$$

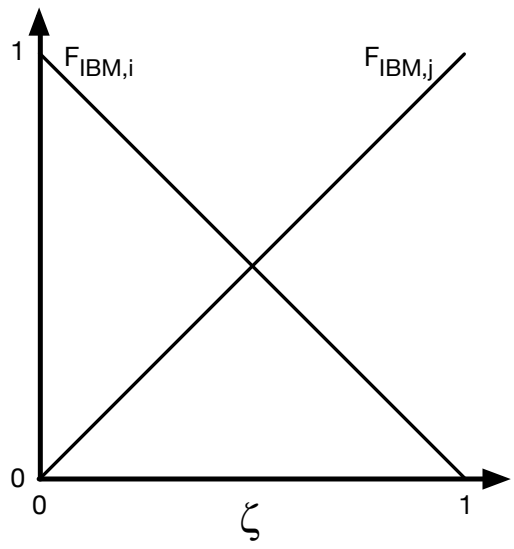

Figure 5.5: Linear shape function used to interpolate immersed boundary forces onto nearest boundary V-model particles.

5.5 Fluid-Structure Coupling

The fluid-structure interaction coupling framework used within this body of work was originally implemented by O'Connor [141] for a fluid-structure interaction method consisting of a lattice Boltzmann fluid solver, finite element structural solver, coupled together using the immersed boundary method presented in this section. Here, the finite element structural solver has been replaced by the V-model, highlighting a significant advantage of the partitioned approach to coupling, namely the modularity and the ability to substitute solvers based on their suitability to an application. The scheme makes use of both weak and strong coupling procedures as will be described in this section, while the time-stepping setup required modification as will be now described.

5.5.1 Fluid and Structure Time Step Ratio

In Section 4.5, the critical time step for the V-model, using an explicit time integration scheme, was defined. This time step is in general significantly smaller than that of the LBM solver for a sensible lattice resolution and stable lattice viscosity. As a result, in order to reduce the time step size of the LBM, the lattice

resolution must be increased, over-resolving the domain, in order to maintain stability within the method. The increase in resolution results in an excessive computational resource requirement or computational time, compounded by the fact that the resource requirement scales with the square of the increase in spatial resolution. In order to overcome this, the ratio of fluid time steps to structure time steps can be de-constrained, allowing multiple structure time steps to be modelled for each fluid time step as shown in Figure 5.6. The ratio of fluid and structure time steps R is given by:

$$R = \frac{\Delta t_f}{\Delta t_s} \tag{5.21}$$

where Δt_f is the fluid time step size and Δt_s is the structure time step size. In this implementation R is restricted to integer values to ensure interaction between the solvers occurs when each solver is at the same point in time.

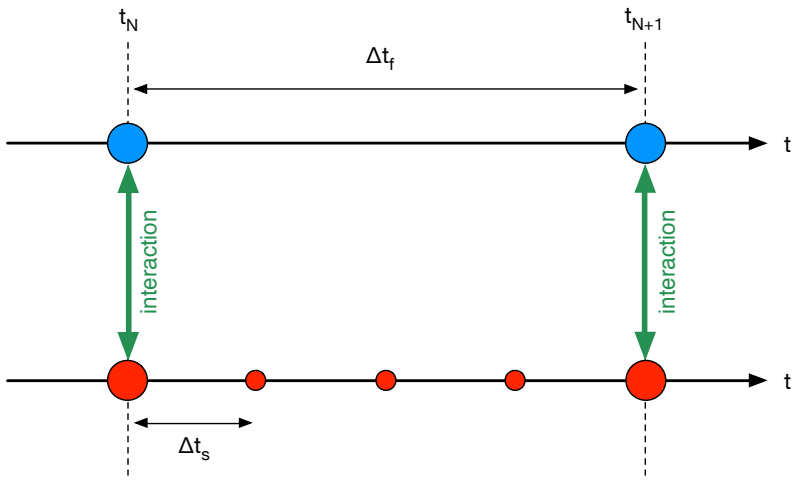

Figure 5.6: Schematic of the fluid-structure coupling highlighting the interaction between the solvers and the smaller time steps executed by the structural solver.

5.5.2 Weak Coupling

As previously discussed, partitioned fluid-structure interaction approaches are required to directly ensure that the kinematic and dynamic interface conditions are satisfied. However, reasonable approximations can be obtained for problems where the kinematic condition is not strictly satisfied, usually when the densities of the fluid and the structure are at least an order of magnitude apart, i.e. for

heavy structures in comparison to the fluid. This is known as weak coupling. The strong coupling scheme discussed in the next section, is an advancement of the weak scheme so it is included here for completeness.

Conventional Staggered Scheme

The most widely implemented weak coupling scheme is the Conventional Staggered Scheme (CSS). Its popularity lies mainly in its ease of implementation and efficiency. The fluid and structure governing equations are solved in series within a single time step with no iteration, resulting in a lag between the fluid force applied to the structure as shown in Figure 5.7. This lag causes the interface conditions to not be strictly met. As a result, artificial energy is created at the interface which not only can significantly distort interaction characteristics but also create stability problems in the method.

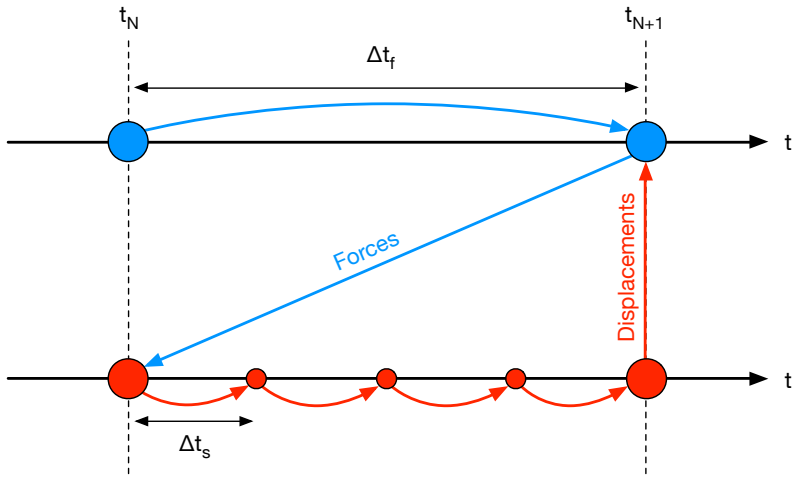

Figure 5.7: Schematic of the weakly coupled Conventional Staggered Scheme.

For cardiovascular applications, the density ratios between the fluid and structure are generally well within an order of magnitude, causing the added-mass effect instability and therefore weak coupling is not suitable. However, for other applications including one of the fluid-structure interaction validation cases, included in Section 6.4, it can be implemented without significant accuracy or stability concerns.

Algorithm

The weakly coupled algorithm for fluid-structure interaction implemented in this work can be summarised as:

1. Execute the LBM solver to obtain predicted fluid velocity field
2. Interpolate forces from the fluid to the boundary
3. Calculate correction force required for no slip condition
4. Spread force back to fluid and correct predicted velocity field
5. Execute the V-model solver, updating particle positions based on IBM force
6. Advance to the next time step

5.5.3 Strong Coupling

For partitioned fluid-structure interaction coupling schemes, when the interface conditions are satisfied directly by the coupling scheme, the fluid and structure solvers are said to be strongly coupled. A number of schemes have been developed to ensure the interface conditions are met [142, 143]. Here the block Gauss-Seidel approach is implemented.

Block Gauss-Seidel Scheme

The block Gauss-Seidel scheme (BGSS) is an implicit method that solves the fluid and structure governing equations sequentially. The forces and displacements calculated by the solvers are passed back to the start of the time step to the other solver through iteration as shown in Figure 5.8. A number of iterations can be conducted, only moving onto the next time step once the interface conditions have been met using the following stopping criteria:

$$\boldsymbol{r}_k = \boldsymbol{U}_{f,k} - \boldsymbol{U}_{s,k} \approx \boldsymbol{0} \tag{5.22}$$

where $\boldsymbol{r}_k$ is the residual of a given iteration, $\boldsymbol{U}_{f,k}$ and $\boldsymbol{U}_{s,k}$ are the velocities at the boundary (located at the immersed boundary markers) calculated via the fluid and structural solvers respectively.

As a result of the iterative procedure, the BGSS has improved accuracy and stability characteristics in comparison to the CSS, especially for problems where added-mass features prominently. A potential drawback of the method is the number of iterations required for convergence to be achieved can increase the computational expense significantly. However, additional treatments can be employed to reduce the required number of iterations as will be discussed.

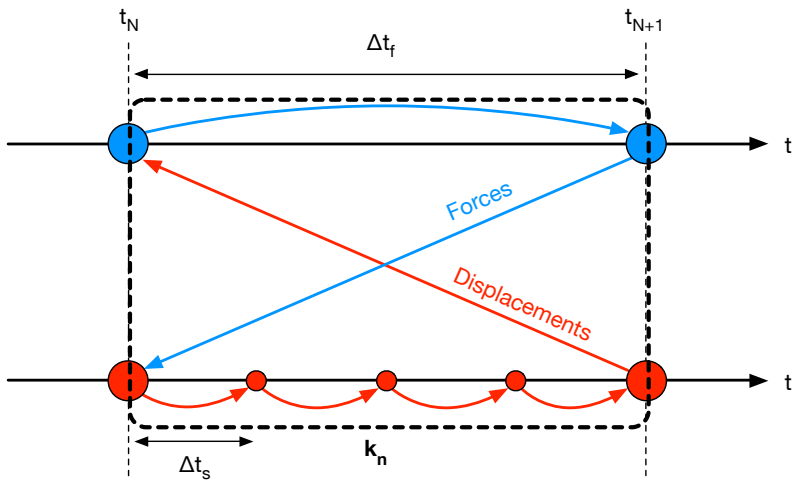

Figure 5.8: Schematic of the strongly coupled block Gauss-Seidel Scheme. Iterative procedure is indicated through the black dashed box.

Aitken's Method

Convergence acceleration of the implicit procedure can be achieved by relaxing the displacement of the boundary $\boldsymbol{U}_s^t$ through the use of the displacement of the previous time step $\boldsymbol{U}_s^{t-1}$:

$$\boldsymbol{U}_s^t = \omega \boldsymbol{U}_s^* + (1-\omega)\boldsymbol{U}_s^{t-1} \tag{5.23}$$

where $\boldsymbol{U}_s^*$ is the unrelaxed boundary displacement calculated by the V-model solver and ω is the relaxation parameter of value between zero and unity. The choice of relaxation parameter value can have a large effect on the stability and

rate of convergence of the iterative scheme with small values usually resulting in high stability but slow rate of convergence while large values increase the rate of convergence but incur stability issues. The optimal parameter is case and time dependent within a specific case due to its reliance on the level of interaction between the fluid and structure.

Algorithm

The strongly coupled algorithm for fluid-structure interaction implemented in this work can be summarised as:

1. Execute the LBM solver to obtain predicted fluid velocity field
2. Interpolate forces from the fluid to the boundary
3. Calculate correction force required for no slip condition
4. Spread force back to fluid and correct predicted velocity field
5. Execute the V-model solver, updating particle positions based on IBM force
6. Calculate the interface velocity residual
7. if converged, advance to Step 9
8. else relax the boundary displacement and return to Step 2
9. Advance to the next time step

5.6 Summary

This chapter details the method used to couple the fluid and structural solver, namely the immersed boundary method. The rationale behind its choice and details of the underlying formulation are included. The procedures used to couple the method to the fluid and structure solvers are discussed, where the novel structure coupling has been developed during the this work to allow independent

fluid and structure resolutions. Finally, basic algorithms of its implementation in weakly and strongly coupled form are included. The next chapter will provide details of the fluid-structure interaction method developments and the validation of its components.

Chapter 6

Method Development and Validation

The previous three chapters have provided details of the fluid and structure solvers implemented within the fluid-structure interaction (FSI) method along with the coupling approach. This chapter will highlight the development of each model, first individually and then integrated within the FSI method, including their implementation on different computing architectures. A series of test cases are presented that incrementally validate each aspect of the model.

6.1 V-model Development and Validation

The V-model was originally proposed by Kuzkin and Asonov [106] for granular materials and extended by [107] for elastic bodies. A journal paper serving as an introduction to the V-model, detailing implementation and validation of the method is included in the Appendix C. In the paper, validation cases are presented for problems under constant and time dependent loading. Furthermore, an example case for stochastic modelling of material properties is included. So as to avoid unnecessary repetition, the cases included in the paper are not included within this section. Focus is instead restricted to additional cases and more detailed analysis than would be appropriate for inclusion in the paper itself.

The V-model implementation within this work builds upon that of Nasar [107], who translated and applied the approach to work with smoothed particle hydro-

dynamics. The present work extends the novelty of this method by considering for the first time implementation and optimisation on GPU and the capability to model material variation within a structure. In addition, a bespoke discretisation algorithm has been developed for non-orthogonal arbitrary geometries, based upon a seed-filling approach which is referred to as the V-model particle generator.

6.1.1 Validation: Cantilever Beam under Gravity

The well known computational benchmark for fluid-structure interaction methods proposed by Turek and Hron [7] also includes validation case proposals for the structural solver in isolation and is presented here. This case consists of a homogeneous beam with material properties stated in Table 6.1, under a reduced gravitational load of 2 m/s^2 as shown in Figure 6.1.

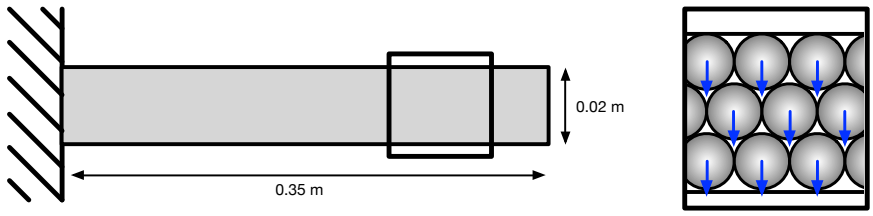

Figure 6.1: Schematic of a homogeneous cantilever beam under gravitational load. Blue arrows indicate gravitational load acting on each V-model particle.

Table 6.1: Material properties of cantilever beam in dynamic validation case.

Material Property	Value (Units)
Young's modulus	1.4 (MPa)
Poisson's ratio	0.4
Density	1000 (kg/m^3)

The constitutive model used primarily in the validation cases presented in Appendix C, proposed by Griffiths and Mustoe [119], is limited to Poisson's ratio of less than 1/3. This is due to the formulation of the shear stiffness coefficient (Eqn 4.29) providing a non-physical negative coefficient for larger Poisson's ratio values. In order to represent the material properties of the beam accurately,

specifically the Poisson's ratio of the beam, the constitutive model employed by the V-model must be modified. As a result, the constitutive model proposed by Gaeini et al. [144] was also explored. For this model, the axial and bending stiffness coefficients remain the same as the previously implemented model (Eqn 4.28 and 4.30) but the shear stiffness coefficient is replaced by:

$$C_D = \frac{E}{4(1+\nu)} \tag{6.1}$$

Results are presented using this constitutive model. The tip deflection time histories for the V-model at different resolutions are compared with results obtained using a validated in-house, non-linear FEM solver [141] in Figure 6.2. As the resolution of the V-model increases, convergence towards the FEM solution can be seen. Furthermore, close agreement with validation data can be seen regarding the predicted frequency of the beam while the maximum tip deflection is in excellent agreement with validated data as described by Table 6.2.

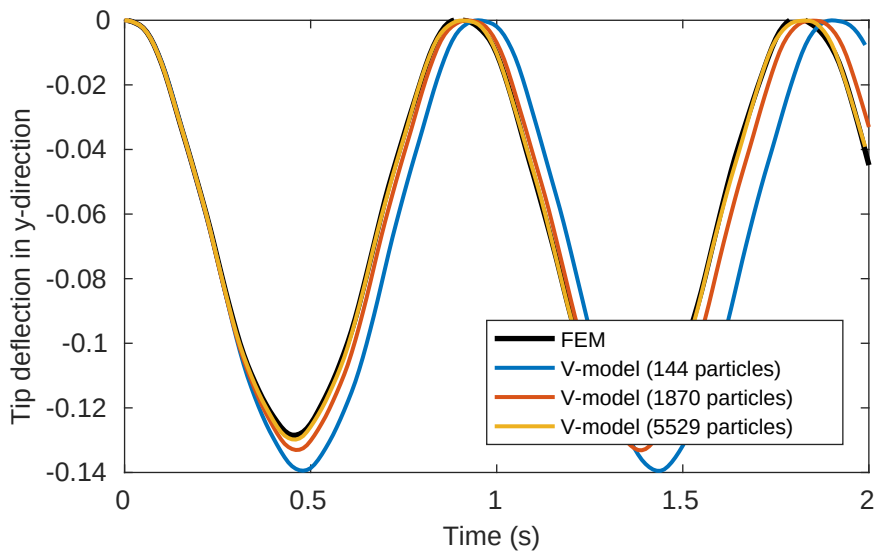

Figure 6.2: Tip defection time history of the V-model at increasing resolution compared to a non-linear FEM solution for the structure only validation case proposed by Turek and Hron [7]

Table 6.2: Tip deflection results in the y-direction

Solver (Resolution)	Equilibrium Position	Amplitude	Frequency
Turek & Hron [7]	0.0636	0.0652	1.100
O'Connor [141]	0.0642	0.0643	1.099
V-model (144 particles)	0.0698	0.0697	1.053
V-model (1870 particles)	0.0665	0.0665	1.087
V-model (5529 particles)	0.0650	0.0649	1.094

6.1.2 Development: V-model on GPU Architecture

As previously explained, a key motivation for the use of the V-model as the structural solver implemented in the fluid-structure interaction method is its local and linear underlying governing equations. These are solved via simple operations which are well suited to GPU architecture. The V-model was first implemented on CPU architecture in order to gain experience with the method before developing a GPU-based solver. The CPU solver was able to serve as an effective debugging tool. In addition, once optimised it was able to serve as a benchmark to evaluate the speed up gained using GPU architecture. Details of the GPU solver implementation will be discussed in this section along with the relative GPU acceleration.

Implementation and Data Structure

The V-model GPU solver was implemented using NVIDIA CUDA API. When using GPU architecture, two copies of each dataset must exist, one in the host memory (CPU) and one on the device (GPU) since any data input and output from the GPU must be via the CPU. This is because the CPU and the GPU have separate address spaces for memory. Processes running on each can only access their own address space therefore data must be copied from one address space to the other in order for respective processes to access it. The data stored in device memory was structured in 1-D arrays for each of the bond and particle properties e.g. particle position in the x-direction, where the index of array refers to the bond or particle ID. Structuring the data in this way has a number of

benefits such as dispensing with the need to flatten higher-dimensional indices. Memory requirements are also reduced by reducing the need for memory padding, maximising cache memory usage and increasing instruction-level parallelism. The algorithm assumes a thread per particle (or bond) structure where a thread is responsible for all the operations on a single particle (or bond) within a kernel launch. The kernel launch itself has an associated overhead and therefore have been combined where possible to improve performance.

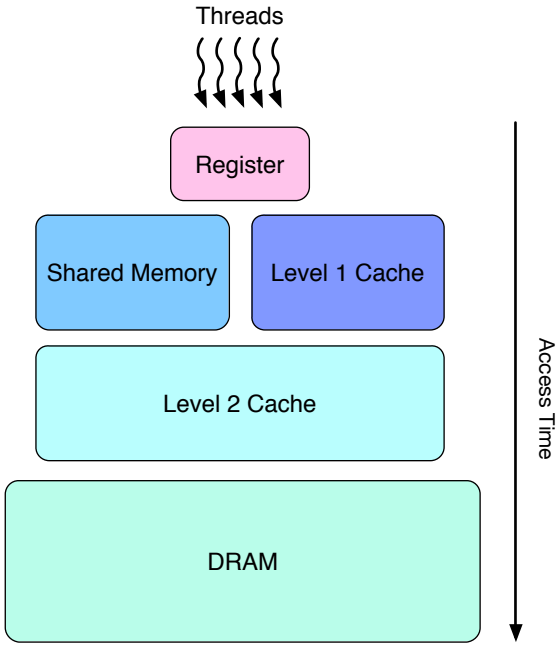

Figure 6.3: GPU memory organisation with distance from the threads indicating memory access speed and area of block indicating storage capacity.

An important performance feature to consider when using GPU architecture is that, in general, reading data from memory takes much longer than performing operations on the data. Unlike data copied from the host, variables declared at runtime store data in registers where possible. Data stored in registers have high access speeds, however registers have limited storage capacity and therefore once full, data will be stored in higher levels of cache before being stored in DRAM (dynamic random-access memory) once all levels of cache are full. The hierarchy is shown in Figure 6.3. Given that the threads are arranged in warps that are able to share cache memory, it is crucial to optimise cache coherence, whereby the data required for a thread, has been stored in cache by a previous thread in the same warp. Furthermore, given the performance benefits of accessing registers, any variables created locally should be stored in register memory. However, if

a number of threads are creating local variables with the same value, the variable can be stored in shared memory in order to maximise data storage in the registers.

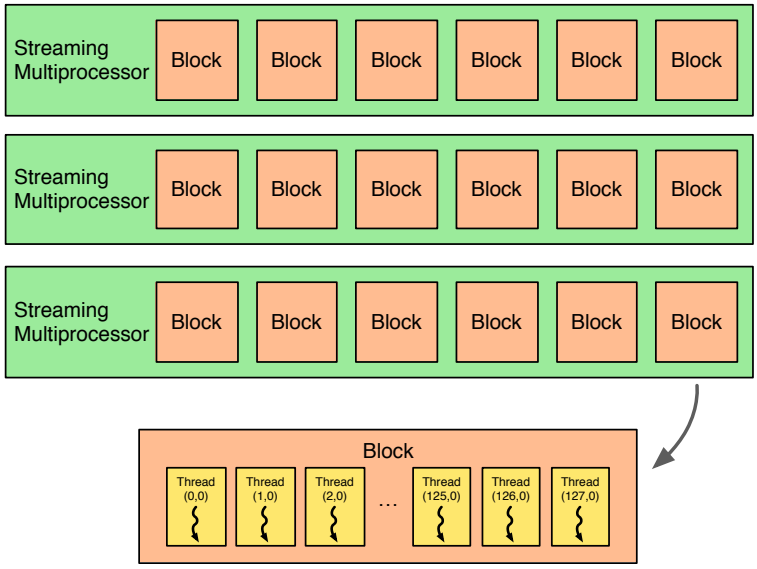

Figure 6.4: Schematic of GPU architecture where the grid layout and block dimensions are governed by the kernel launch parameters.

Code that is run on the device is arranged into kernels. Each kernel is launched in turn, parallelising the code as specified by the user in the kernel launch parameters. These parameters arrange the threads into warps and blocks (which have shared memory) with specified dimensions and pass these to the streaming multiprocessors as shown in Figure 6.4. For maximum efficiency, threads should be spawned in complete warps and therefore the number of V-model particles and bonds should match the block dimensions. On development of the GPU V-model solver, it was found that kernel launch parameters of four warps per block, with 32 threads per warp should be used where possible to hide any latency; where a thread can be used to compute operations for a different particle while it is effectively waiting for instructions for its original particle.

Benchmarking GPU performance

In order to assess the relative speed-up using GPU architecture, the dynamic cantilever beam under gravity case presented in Section 6.1.1, where the results were obtained using the CPU solver, is run using the GPU solver. This was

done first to ensure the results were identical using the different architectures and second to evaluate the relative speed-up using the GPU. The tests were run on two different GPUs, a GTX1060 with 6GB of RAM and a GTX1080Ti with 11GB of RAM while the CPU solver was run on a Intel Core i7-7700HQ 2.8GHz/3.80 GHz with 16GB of RAM. It is worth noting that the CPU solver is run in serial. There have been relatively few prior studies of the GPU acceleration of DEMs [145,146]. Zhang et al. [147] calculated the speed-up relative to a serial CPU solver and will serve as a comparison here.

While the GPU implementation has been implemented according to CUDA programming best practises, algorithm optimisation represents future work in this study and as a result further speed-up may be possible. This issue is discussed in detail in Appendix C including the use of single and double precision calculations with appropriate GPU hardware; the current implementation is double precision.

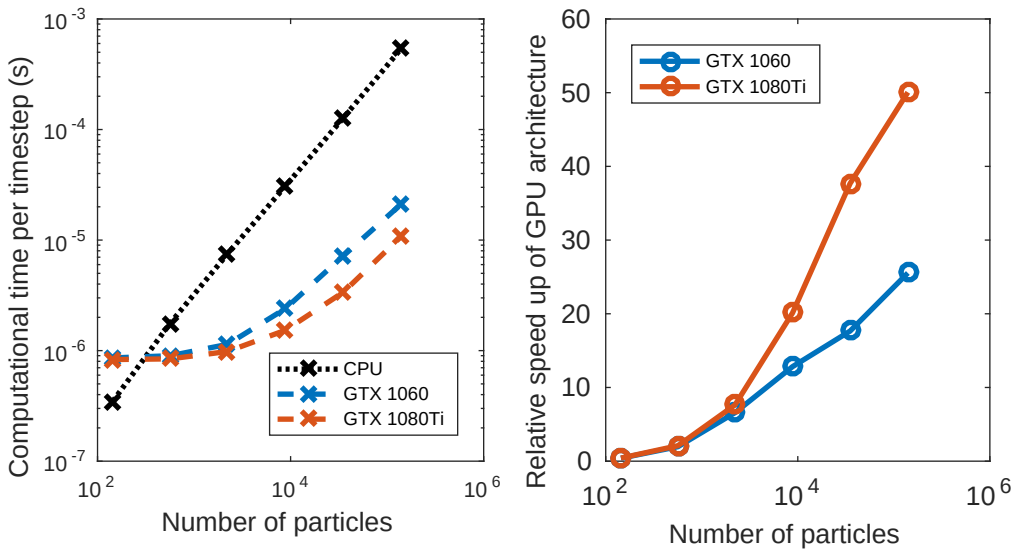

Figure 6.5: (Left) Computational time required per time step for different resolutions using V-model solver implemented on CPU and GPU hardware (GTX1060 and GTX1080Ti). (Right) Relative speed up using the GTX1060 and GTX 1080Ti in comparison to the serial CPU solver.

The maximum relative speed-up was measured to be around 25 using the GTX 1060 GPU and around 52 using the GTX 1080Ti, both when using the highest resolution of the V-model tested ($\approx 1.4\times10^5$ particles) as shown in Figure 6.5. Both speed-ups compare well with previous GPU accelerations of DEMs [147].

The CPU solver exhibits a quadratic increase in computational time with reso-

lution as expected given the sequential nature of the solver and the increase in length of any loops in the solver resulting from the increase in resolution. In contrast, both GPU implementations initially demonstrate minimal increase in computational time per time step as the resolution increases due to the thread per particle structure of the algorithm. When the resolution is low, the number of particles representing a geometry is smaller than the number of particles that can be efficiently parallelised at one time. This is roughly equal to the optimum number of threads per block multiplied by the number of streaming multiprocessors, multiplied by two since the CUDA runtime is able to reassign CUDA cores on the fly to a different block when the CUDA cores in a block are idle. As a result, at least two blocks should be assigned to each streaming processor for optimum performance.

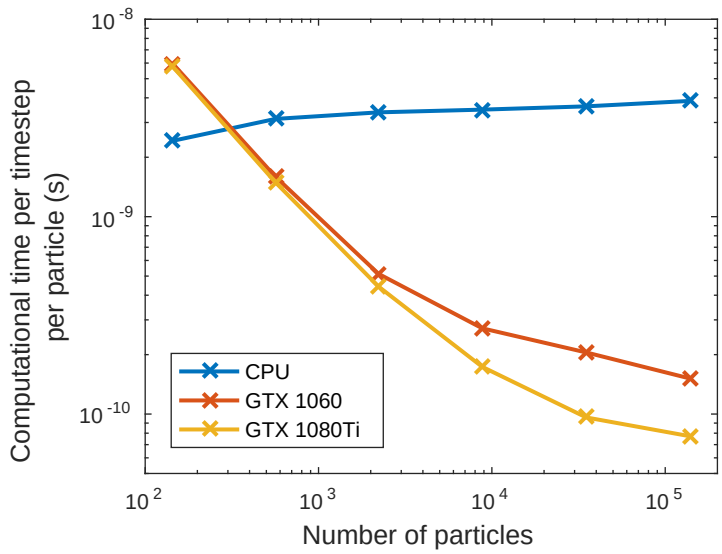

Figure 6.6: Computational time required per time step per particle for different resolutions using V-model solver implemented on CPU and GPU hardware (GTX1060 and GTX1080Ti).

Once the resolution of the V-model is larger than the full-parallelisation resolution, both GPU implementations begin to exhibit quadratic increase in computational time with resolution, again as expected once threads perform operations on multiple particles sequentially per kernel launch. This observation is further highlighted in Figure 6.6, showing the computational time required per time step for a single particle. For the CPU solver, the time per particle remains almost constant as the resolution increases resulting in the second order increase in computational time observed earlier. Both GPU implementations exhibit an initial decrease in time per particle with a decreasing rate, tending towards a constant

time per particle. For the GTX 1080Ti implementation, the decrease in time per particle is at a lower rate, indicating the higher number of particles the hardware is able to handle before saturation (full parallelisation) occurs.

The GPU accelerations measured here provide encouragement for further development of the V-model, especially when extending the V-model in three dimensions, as planned in future work, the computational resource requirement will increase significantly. Further details of the V-model GPU implementation are included within the journal article in Appendix C including algorithm design and pseudo code.

6.2 IB - LBM Validation

The immersed boundary and lattice Boltzmann (IB-LBM) solver are tested for a rigid boundary in order to verify the coupling between the fluid and boundary. The IB-LBM implementation included within the FSI method was originally developed by O'Connor [141] who presented validation of the IB-LBM implementation via flow around a rigid cylinder. This test was rerun to ensure code development had not altered the solution and is included here for completeness. Note that the LBM solver has also been validated by O'Connor [141] and is included within the journal article in Appendix D.

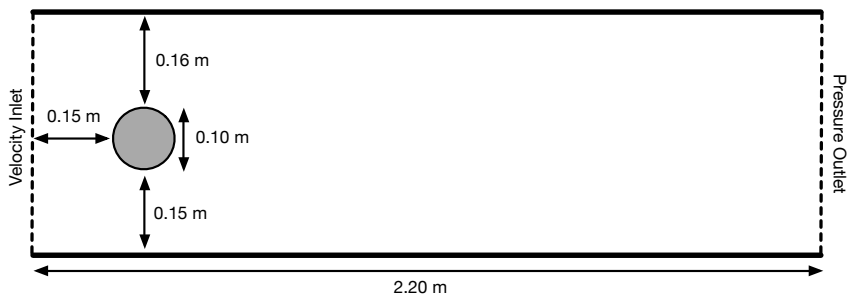

Figure 6.7: Schematic of flow around a rigid cylinder case. Solid black lines denote no-slip boundaries.

The case was originally presented by Schäfer et al [8], and consists of a rigid cylinder subjected to flow with parabolic velocity inlet, fixed pressure outlet, and no-slip walls at the top and bottom of the domain as shown in Figure 6.7 and with properties given in Table 6.3.

Table 6.3: Rigid cylinder validation case properties.

Fluid Property	Value (Units)	Structure Property	Value (Units)
Density	1 (kg/m^3)	Diameter	0.1 (m)
Inlet velocity	1 (m/s)		
Reynolds number	100		

The flow is initially at rest throughout the domain, and the parabolic inlet condition ramped according to:

$$u_x(t) = \begin{cases} u_x^{in}(t)\frac{1-cos(\pi t/2)}{2} & t \leq 2 \\ u_x^{in}(t) & t > 2 \end{cases} \tag{6.2}$$

As the inlet velocity is ramped, an unsteady von Kármán street forms aft of the cylinder resulting in time varying lift and drag coefficients of the cylinder. Validation data for this case incorporates this variation, in the form of maximum lift and drag coefficients and the Strouhal number of the flow.

Figure 6.8 shows the time variation of the drag and lift coefficients in comparison with the upper and lower bounds of the maximum coefficient value from the validated data. It can be seen that the lift coefficient is within the bounds and therefore in good agreement with the validation data. However, the drag coefficient is over-predicted. This over-prediction has been attributed to the use of the immersed boundary method by O'Connor [141] and the blurred boundary created by the support stencil used effectively increasing the diameter of the circle. It is not thought to effect the lift coefficient since the blurred boundary is present at both the top and bottom of the cylinder. This observation was also present in additional studies of this case where the immersed boundary was implemented demonstrating the correct behaviour of the present method relative to prior studies [148, 149].

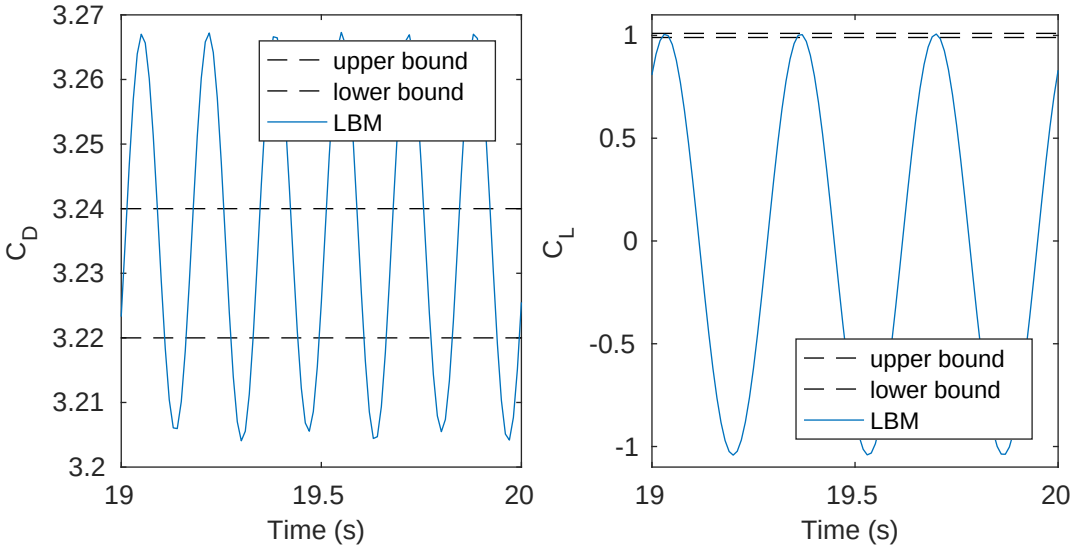

Figure 6.8: Coefficients of drag (left) and lift (right) over time for the flow around a rigid cylinder case with upper and lower bounds for the maximum value of each coefficient from numerical benchmark data [8].

6.3 IB - V-model Development and Validation

In order to validate the interpolation procedure developed in Section 5.4 to allow multiple immersed boundary markers to act on a V-model particle, i.e. allow higher resolution of the fluid than the structure, a test case was designed whereby a cantilever beam is subject to a distributed load on it's top surface. The distributed load is then discretised and applied directly to the V-model particles to provide validation results.

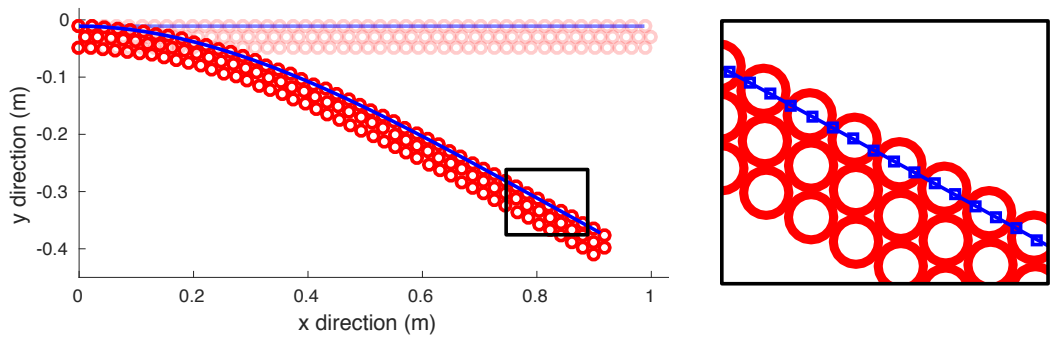

Figure 6.9: Cantilever beam deflection under distributed load. (Left) Load is discretised through dummy immersed boundary markers located along the blue line on the top surface of the beam. (Right) Zoom highlights exact marker locations along the boundaries, independent of particle centre locations.

Figure 6.9 shows the beam deflection with the distributed load applied through the dummy immersed boundary markers located on the top surface of the beam in comparison to the load applied directly to the V-model particles. It can be seen in Figure 6.10 that as the dummy immersed boundary marker resolution is increased, the resulting tip deflection tends towards the direct loading case. However, it does not match this result exactly due to the discretisation of the load on the last particle at the tip of the beam. This particle receives loads through the dummy immersed boundary markers from one side and therefore has half the load as the other particles. While this causes a difference between the direct loading and immersed boundary loading results, it can be described as discretisation decision as opposed to an error, while the magnitude of the difference decreases with increasing resolution.

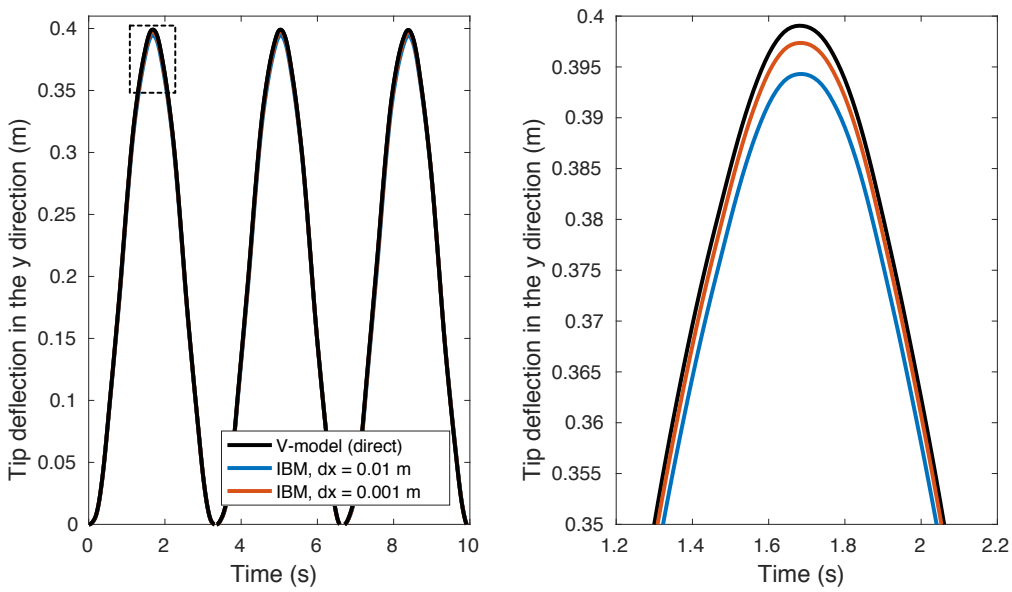

Figure 6.10: Tip deflection time histories for a cantilever beam under a uniform distributed load where load is discretised directly onto the V-model particles and via dummy immersed boundary particles at different resolutions using a linear interpolation method. (Left) Entire time history. (Right) Zoomed area corresponding to dashed box on left figure.

6.4 Fluid-structure Interaction Development and Validation

6.4.1 Validation: Flexible Beam in a Tank

This case was originally proposed by Gluck et al. [150] and has been further investigated in additional studies [132,149]. The numerical methods implemented in each study are included in Table 6.4 along with the domain size modelled. The case consists of a flexible plate (beam in two dimensions) within a tank where the fluid is initially at rest. A time-dependent distributed load of 75 N/m is then applied to the beam according to:

$$F(t) = \begin{cases} 75.0 & t \leq 0.5 \\ 0.0 & t > 0.5 \end{cases} \tag{6.3}$$

Once the load has been removed, the beam is allowed to oscillate around its equilibrium position with the viscosity of the fluid damping the amplitude of the oscillation. The effect of viscosity variation is tested using viscosities of 0.2, 1 and 5 Pa.s (referred to as low, medium and high viscosities throughout the analysis) and the time history of the beam tip deflection recorded and compared against that of previous studies.

Table 6.4: Summary of numerical methods and domain set-up, employed by previous works. FVM = finite volume method, FEM = finite element method, LBM = lattice Boltzmann method, ALE = arbitrary Lagrangian Eulerian, IBM = immersed boundary.

Article	Fluid	Structure	Coupling	Domain Size
Gluck et al. [150]	FVM	FEM	ALE	unspecified
Namkoong et al. [132]	FEM	FEM	ALE	6m × 50m
Lee and Lee [149]	LBM	FEM	IBM	5m × 20m

Table 6.5: Flexible beam in a tank validation case properties.

Fluid Property	Value (Units)	Structure Property	Value (Units)
Density	1 (kg/m^3)	Length	1.0 (m)
Viscosity	0.2, 1.0, 5.0 (Pa.s)	Width	0.06 (m)
		Density	2550 (kg/m^3)
		Young's Modulus	2.5 (MPa)
		Poisson's ratio	0.33

Figure 6.11 is a schematic of the case while Table 6.5 contains the fluid and structure material properties. Note that the originally proposed case was in three dimensions with a depth of 0.4m and a distributed load of 30 N/m^2. In order to convert the case to two dimensions, a distributed load of 75 N/m is instead applied. In addition, it is worth noting that this validation case could be carried out with nondimensional parameters. However, the case definition proposed by Gluck et at. [150] is followed here.

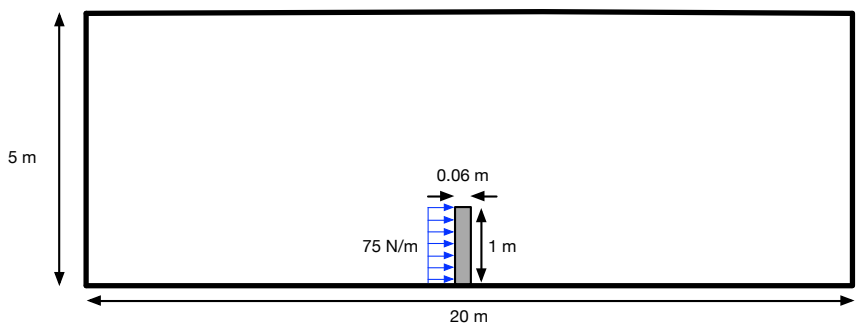

Figure 6.11: Schematic of the cantilever beam in a tank case.

From the tip deflection time histories shown in Figure 6.12, excellent agreement with results from previous researchers can be seen for the low and medium fluid viscosity cases. However, for the high viscosity case over damping of the structure can be seen. Table 6.6 contains the damping ratio for each of the viscosities in comparison to those calculated from previous studies, calculated via the logarithmic decrement method. This method is accurate for damping ratios in the under-damped region such as those presented in this case. It can be seen that the discrete FSI method developed here is within the range of damping ratios for both the low and medium viscosity cases, however a much larger damping ratio is predicted for the high viscosity case resulting in the over-damping and reduced

Table 6.6: Damping ratio for the discrete FSI method (LBM-IBM-V-Model) for each fluid viscosity in comparison with validation data.

Viscosity	Model	Damping ratio
0.2	Gluck	0.01241
	Namkoong	0.00734
	Lee and Lee	0.01004
	LBM-IBM-V-Model	0.00931
1	Gluck	0.02530
	Namkoong	0.02531
	Lee and Lee	0.02850
	LBM-IBM-V-Model	0.02806
5	Gluck	0.10444
	Namkoong	0.07066
	Lee and Lee	0.09563
	LBM-IBM-V-Model	0.12770

tip deflection observed in Figure 6.12. It is worth noting the range in results from previous researchers has been attributed to the different methods employed by each and the domain dimensions of the tank used [107]. It is also worth noting that in the high viscosity case, the viscosity is significantly larger than the viscosity of blood and therefore the method performs well in the viscosity range of concern.

6.4.2 Validation: Laminar Flow around a Rigid Cylinder and Attached Flexible Flag

The benchmark validation case for highly deformable structures in laminar flow conditions was proposed by Turek and Hron [7] and has been used extensively by the fluid-structure interaction community [127, 151, 152]. This case consists of a flag which is excited due to the vortex shedding from a proceeding cylinder. The results are included within a journal article, "A discrete fluid-structure interaction approach for highly deformable elastic bodies" in Appendix D and therefore are not repeated here.

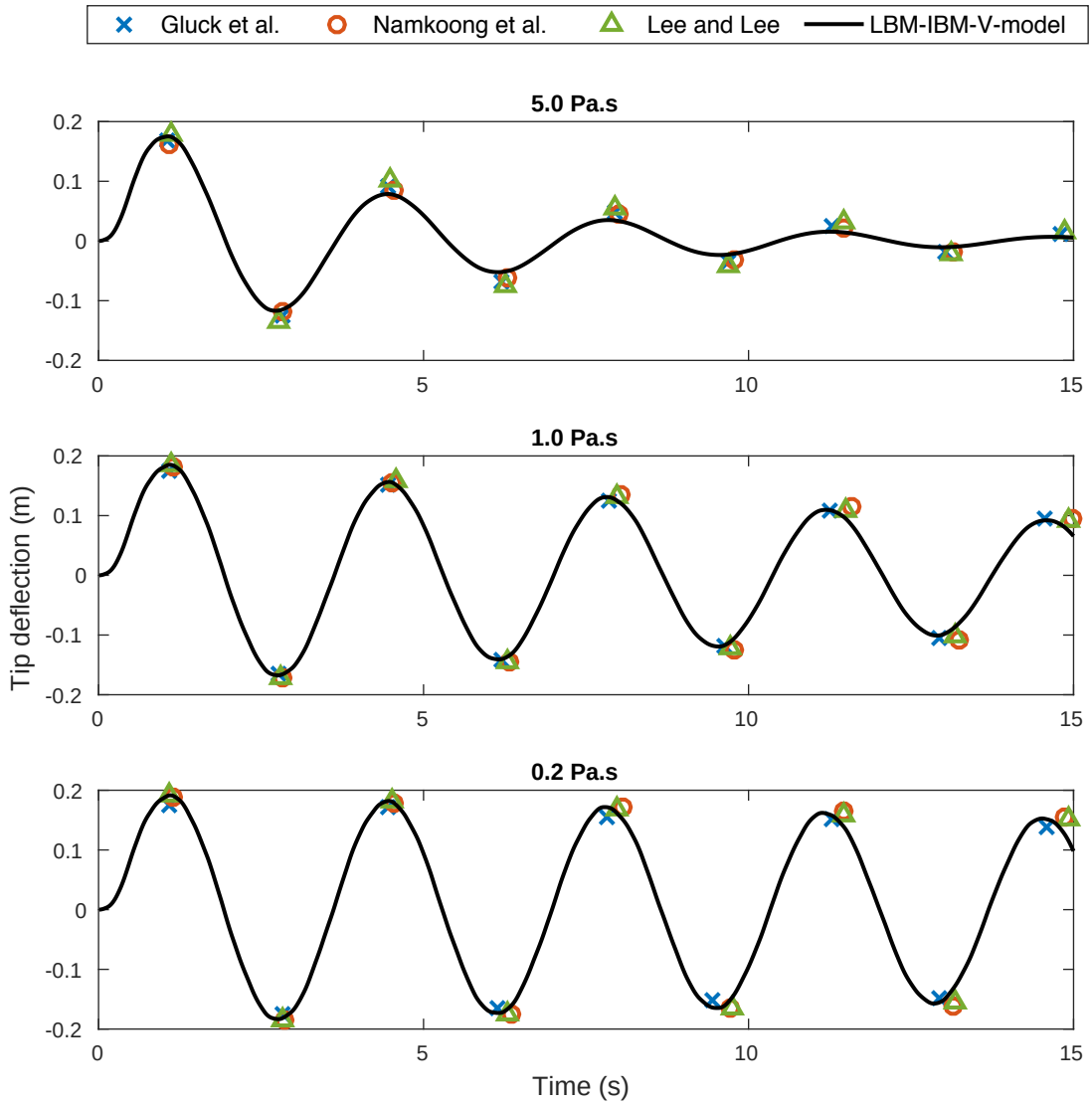

Figure 6.12: Tip deflection time histories for a flexible beam with initial distributed load oscillating in a tank of stationary fluid where the viscosity of the fluid damps the amplitude of oscillation.

6.5 Time Step Ratio Validation

As previously described in Section 5.5.1 there is a significant difference between the operational time steps of the LBM and V-model solvers i.e. the fluid will be spatially over-resolved in order to reduce its time step size to match that of the structural solver. Using smaller sub time steps for the V-model allows for more efficient computation but can lead to error accumulation when employing the weakly coupled scheme described in Section 5.5.2 since the immersed boundary

force applied to the structure is not updated until the next fluid time step. This error accumulation is greater when the magnitude of the time gradient of the immersed boundary forces is large. This error does not occur when using the strongly coupled scheme due to the iterative nature of the scheme, however it may lead to slower convergence.

Using the validation case presented in Section 6.4, simulations are configured using different ratios between time steps R ranging from 1 to 20. The spatial resolution remains constant for all configurations, enabling direct comparison of the relative accuracy and computational times between the configurations. However, the resolution of the discretised structure is reduced due to the increased computational cost of using the same time step size for the fluid and structure. This increase is prohibitively large using the resolution used in the validation study.

Table 6.7: Maximum tip deflection, damping ratio and frequency error (%) for each time step ratio.

Time step ratio	Maximum tip deflection	Damping ratio	Frequency
2	0.0113	0.241	<0.01
5	0.0451	0.930	<0.01
10	0.118	2.132	<0.01
20	0.231	4.499	<0.01

The maximum tip deflections, frequency and damping ratios of each case are included in Table 6.7 and while the tip deflection time history is shown in Figure 6.13. It can be seen that using different ratios has minimal effect on the frequency of beam oscillation. This is to be expected since the frequency of oscillation is dominated by beam stiffness rather than the flow characteristics and while the damping ratio has some effect on the frequency, the relatively small variation in damping ratio results in <0.01% difference in the predicted frequency. The amplitude of oscillation is initially in good agreement for each of the configurations, however the cumulative effect of the damping ratio error results in significant differences in amplitude after 5 oscillations when using large time step ratios as shown in Figure 6.13. Given the cyclic nature of cardiovascular flows, and the general rule of thumb to allow 3 cycles to occur for transient simulations before flow field measurements should be taken, these results indicate care should taken

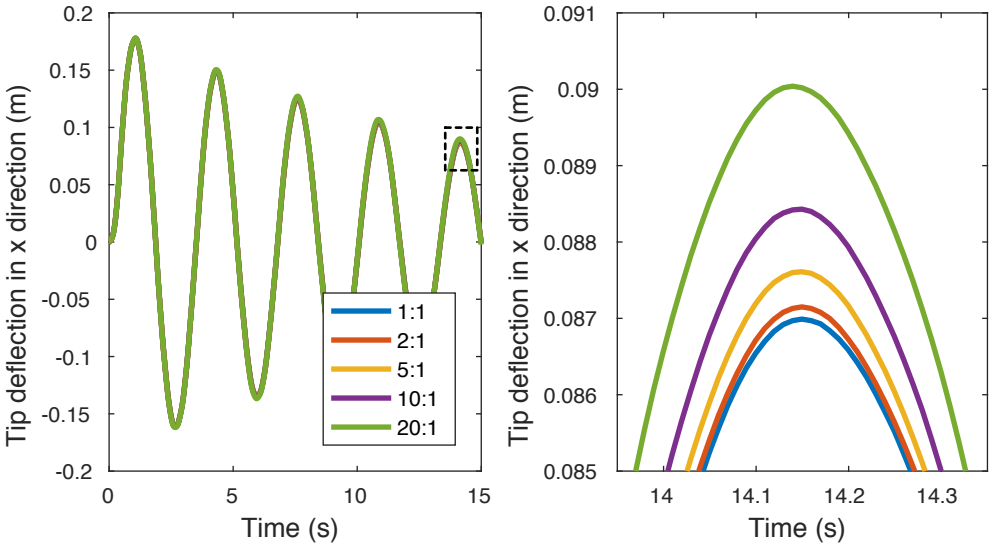

Figure 6.13: Tip deflection time histories for the 1 Pa.s viscosity case presented in Section 6.4 using different fluid to structure time step ratios. (Left) Entire time history. (Right) Zoomed area corresponding to dashed box on left figure.

when utilising large time step ratios.

The objective of introducing time step ratios between fluid and structure solvers is to reduce the computational time required to model a given problem. For each of the time step ratio configurations, the total computational time and the computational time per time step is presented in Figure 6.14. It can be seen that as the time step ratio is increased, the total computational time reduces as a result of the reduced number of fluid time steps that are modelled. Correspondingly, the computational time per time step increases due to the increased number of loops of the V-model solver that occur per fluid time step.

6.6 Software Development

As part of this body of work, a number of pieces of software have been developed or adapted in order to implement the fluid-structure interaction method presented. These are summarised in Table 6.8 with indication of the current development status including whether the code as been validated.

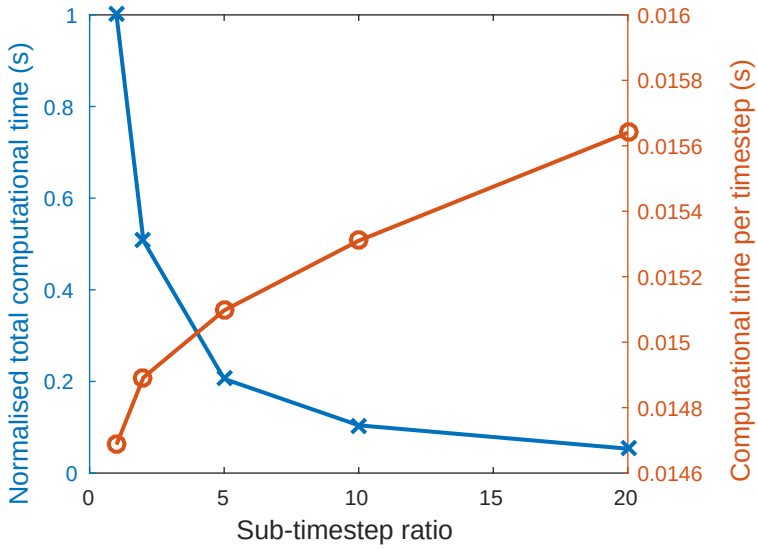

Figure 6.14: Normalised computational time to simulate the full time domain and computational time per time step for each of the fluid to structure time step ratios.

Table 6.8: Summary of software developed during this PhD

Code	Development Process	Validation Status
V-model (CPU)	Bespoke	Validated
V-model (GPU)	Bespoke	Validated
FSI (CPU)	Development of O'Connor [141]	Validated
FSI (CPU + GPU)	Development of O'Connor [141]	Ongoing

Bespoke V-model solvers were written for both CPU and GPU architectures in C++ and CUDA C respectively. Version control was also utilised during the development process via Git. Both codes are currently unlicensed, however future work will consist of publishing the codes in relevant journals such as Software X along with open-source licences.

The fluid-structure interaction method involved adapting a pre-existing C++ code developed by O'Connor [141], replacing the nonlinear FEM solver with the V-model. This code exploits the object orientated nature of C++ allowing the modularity of the structural solver; the FEM and V-model solvers can be interchanged as appropriate. The adapted FSI code is unlicensed (as is the original FSI code) but again future work will look to publish this code with an open-source

license.

6.7 Summary

This chapter serves as a concise summary of the model developments undertaken during this work in order to facilitate the research output in the form of journal articles appended to this thesis. Furthermore, validation for each of the developments has been included, along with validation of the solvers in isolation and as a fully coupled fluid-structure interaction method. The next chapter, in keeping with a journal format thesis, summarises the significance and contributions to the field of each the research outputs generated from this work, the journal articles appended to this thesis.

Chapter 7

Contributions to the Field

Detailed results are presented in the form of four journal papers that are appended to this thesis. The present chapter outlines the major contributions of each with their relevance to the three main objectives of the PhD; repeated here for clarity:

1. **Establish current best practice**
   Assess current literature and undertake initial evaluation of traditionally employed numerical methods via a brief application-based study; to gain greater understanding of the field and to identify opportunities to improve upon current best practice.

2. **Development of LBM-DEM FSI method**
   Integrate the best candidate discrete element solver into a partitioned FSI scheme. The selected methods will have the ability to meet challenges identified in the first objective.

3. **Preparing the FSI method for cardiovascular applications**
   The developed FSI method must be able to provide clinicians with analysis within short timeframes. In order to do this, many core parallelisation of the method is implemented. Furthermore, the capability of the structural solver to include stochastic material models is investigated.

7.1 Establish Current Best Practice

In order to effectively assess numerical methods that are often utilised for cardiovascular applications, a short application based study involving computational fluid dynamics analysis of abdominal aortic aneurysms (AAA) was conducted. This study lead to a publication in the form of **Paper 1**, and involved collaboration with clinicians. This work compared CFD studies of geometries extracted from both 3D ultrasound (3DUS), and high-resolution CT imaging, in particular to assess the potential of 3DUS - a much cheaper and less invasive approach. Important patient-specific haemodynamic metrics linked to the risk of aneurysm rupture were computed and compared. The flow was modelled using the FVM based commercial solver, STAR CCM+, a tool commonly used for cardiovascular applications.

Comparison of the 3DUS and CT derived geometries demonstrated a good degree of qualitative similarity between the two. In particular, both imaging modalities were able to capture the presence of an intraluminal thrombus and the associated reduction in lumen volume at the front of the aneurysm. This high-level analysis provided confidence to proceed with numerical analysis of the geometries.

The geometry preparation procedure was evaluated through the comparison of geometry quality, measured by face aspect ratio and volume shrinkage, resulting from commonly implemented smoothing algorithms; basic Laplacian, HC Laplacian (extended Laplacian) and the Taubin low-pass filter. As a result of this investigation, it was clear that the basic Laplacian algorithm provided geometries of lesser quality than that of the extended Laplacian and Taubin low-pass filter. It was therefore excluded from the remaining analysis. The Taubin low-pass filter produced the highest quality geometries, however since the improvement against the HC Laplacian was minor, CFD analysis was performed using both geometries in order to explore the sensitivity of smoothing algorithm with associated geometry quality to such analysis. Wall shear stress (WSS), a metric strongly associated with the formation, growth and rupture of AAAs, was selected as the sensitivity parameter. It was demonstrated that the observed difference due to the smoothing algorithms was minimal, with both able to capture the main characteristics of the WSS distribution, even in areas of flow recirculation.

While the WSS distributions predicted by CT and 3DUS had quantitative differ-

ences, both geometries identified the same area of minimum WSS, an indicator of location likely to rupture. Discussion with clinicians corroborated the predicted site of rupture - the area at the neck of the artery - as a likely location. This result demonstrates the feasibility of using 3DUS generated geometries in future numerical analysis to the community and led to the initiation of an additional PhD project at the University of Manchester to investigate the feasibility of modelling fluid-structure interaction via 3DUS generated geometries.

The evaluation of CFD methodologies applied to cardiovascular applications was intended to be supplemented by a traditional literature review in the early stages of the PhD program. During this survey however, it became apparent that a number of high-quality, CFD-focussed cardiovascular modelling review papers were already available in the literature, while an equivalent application-specific review across scales and applications for structural modelling had yet to be conducted. The purpose of **Paper 2** is to fill this gap and act as an accessible introduction to newcomers to the cardiovascular modelling field.

A major contribution from this paper is the summary of general modelling considerations that are undertaken when approaching this field. For newcomers, this is not always intuitive and in many published studies, this level of detail is often assumed. By explicitly providing an overview of these considerations, it increases the accessibility of other studies to a wider audience. In addition, a comparison of discrete and continuum modelling approaches is provided with details of underlying assumptions and governing equations as well as advantages and disadvantages of each. Again, this side-by-side comparison is often assumed knowledge by journal publications in the field and therefore through this comparison, accessibility to literature is increased.

Details of material models commonly implemented in a range of cardiovascular applications are also included within this paper. These methods range from general purpose models such as the neo-Hookean, to re-purposed models such as the Mooney-Rivlin, to tissue specific models such as that proposed by Holzapfel et al. [13] for coronary arteries. A key contribution here is the reformulation of each model to ensure consistency between each. This demonstrates the relationships between them and clarifies the additional terms introduced by models representing more complex physical characteristics such as viscoelasticity.

After discussing the methodologies implemented in cardiovascular applications,

the paper explores the scientific advancements produced through their utilisation in a number of major applications including the heart, vessels, aneurysms, atherosclerotic plaques and red blood cells (RBCs). While a number of application specific review papers already exist, e.g. entirely focussed on modelling of intracranial aneurysms, this work was intended to be more holistic. By reviewing the field as a whole, general trends in developments independent of application were identified, suggesting that developments in one application could be translated to others relatively quickly. The paper concludes with a timeline of some of the major advancements in the different applications which can provide the reader with starting points to conduct their own literature reviews.

7.2 Development of an LBM-DEM FSI method

Given the opportunity identified in the first objective to implement discrete methods in cardiovascular applications, it was first necessary to assess the capability and performance of these methods. The lattice Boltzmann method, used as the fluid solver, is relatively mature in the field demonstrating both accuracy and the capability to integrate complex physics [32, 153]. However, the vector-based discrete element method (V-model) is much less mature having been recently proposed by Kuzkin and Asonov [106] for granular materials. Furthermore, its application to elastic bodies is even more recent [107] and therefore formally establishing its ability to represent the dynamics of elastic bodies accurately and the potential to incorporate complex physics is essential. This forms a key contribution in the form of **Paper 3**. The V-model is validated for quasi-static and dynamic validation cases under a variety of external loads. The performance of the method is compared against analytical solutions and numerical results obtained via a commercial non-linear FEM solver (ABAQUS 2017). In particular, the validation of a time-varying load represents the first dynamic validation of the V-model for such a case.

In addition, the order of convergence of the V-model was robustly measured to be first order, using the constant load dynamic case and ensuring constant beam aspect ratio. This is the first published assessment for the V-model and one of the first for any discrete element method representation of an elastic body. Analysis such as this is common place for more mature methods, and therefore by conducting these investigations it provides other researchers with more confidence

in the method should they decide to implement it themselves.

A further key contribution from **Paper 3** is the extensive discussion of numerical implementation details. A pseudo-code algorithm is included outlining the initial set-up of vectors and matrices containing particle properties such as position, velocity and acceleration. The importance of the matrix containing the bond connectivity is emphasised; where the particle ID of the two particles connected by the bond is stored. This matrix forms the main loop for the algorithm of the basic implementation presented in the paper and as such is fundamental to the solver. As a result of the in-depth discussion of the numerical implementation, the reader should be able to easily reproduce the solver for their own investigations.

Paper 4 presents the coupled FSI solver using the LBM fluid solver and the V-model structural solver coupled via the IBM. Formulation details of each method are provided, including details and rationale behind the inclusion of developments from other studies such as the three-point stencil used to couple the LBM and IBM. In this paper, each of the solvers is validated in isolation to demonstrate the robustness of the fully-coupled FSI solver validation results. In particular, the V-model validation case was proposed by Turek and Hron [7] as an intermediary step towards the FSI validation case. Here, the flexible flag of the FSI case is subjected to a reduced gravitational force with the tip deflection validated against the numerical benchmark. This case is significant for a two reasons. Firstly, excellent agreement is observed with the numerical benchmark results with less than 1% error between the tip deflection predicted using the V-model and the validation data. Secondly, this represents the first published validation case using the V-model to model an elastic material with a Poisson ratio greater that 1/3 using a constitutive model. Previous studies have directly enforced a shear coefficient [130] rather than via a constitutive model due to the restriction imposed by the previously implemented constitutive model [119].

Validation of the FSI method was conducted by incorporating the validated flexible flag, with the new constitutive model capable of modelling higher Poisson ratios, into the FSI validation case. Good agreement was demonstrated for the tip deflection against the numerical benchmark data (<5%). This is in spite of the variation in coupling approach between benchmark data and the present work. The numerical benchmark results were produced using a monolithic solver, where the fluid and structure governing equations are solved simultaneously. This type of approach is well known to produce highly accurate results in comparison to the

partitioned approach implemented within the presented FSI method where the governing equations are solved sequentially [127]. As a result of this validation, the coupling of the solvers can be considered correct, and further developments can be made to the method by the community.

7.3 Development of the FSI method towards cardiovascular applications

One of the key motivations behind the use of the V-model is its capability to model complex phenomena. This is explored in **Paper 3** where stochastic modelling of the structure material properties is implemented. As an example case, two values of bond Young's modulus are distributed throughout the discretised structure where the ratio between the two Young's moduli (E_1,E_2) is 5:1. 100 random distributions were simulated with different relative contributions of each Young's modulus, ranging from 90%/10% through to 10%/90%, in order to demonstrate the sensitivity of mechanical response to the distribution. The tip deflection of the associated homogeneous beams (where all bond stiffnesses are set to either E_1 or E_2) were used to indicate boundaries in which the tip response of the different distributions should lie between. The results of this case demonstrated a large range in response due to the distribution but in a consistent manner for each combination of stiffnesses and within the bounds of the homogeneous beams. This highlights the V-model's ability to capture this variation, especially given that little additional treatment of the solver was necessary and no additional computational resource was required. Using a similar stochastic variation with cardiovascular material models has the potential to improve our understanding of the effect of the natural variation in mechanical properties of cardiovascular tissue as well as its changes through disease.

A drawback generally quoted in the use of discrete element methods such as the V-model is the computational cost. On discussion with clinicians, it has emerged that computational times for numerical analysis within a clinical setting should not exceed more than a few hours. As a result, the implementation of the FSI method must be further developed in order to reduce the computational time. The LBM and the V-model are well suited to parallelisation through the use of GPUs. Extensive work has been published with regard to GPU acceleration of

LBM solvers [20, 21, 154] however this is not the case for the V-model. **Paper 3** details the first implementation of a GPU-based V-model solver, discussing its implementation in relation to that of a CPU-based solver. Acceleration testing of the solvers demonstrated the GPU-based solver to be around 20 times faster than that of the serial CPU-based solver despite using modest GPU hardware, a GeForce GTX1060 6Gb card (∼£200 at the time of writing). As stated in the paper, further acceleration is expected using so called general-purpose GPUs (GPGPU) which have been designed with scientific computing in mind.

The GPU-based V-model solver also allowed the resolution of V-model particles to be drastically increased in the validation cases presented in the paper. To the best of the author's knowledge, the number of particles that were simulated were at least an order of magnitude larger than in previously published results. As a result of this increased resolution, the V-model is able to more accurately capture the dynamics of the problem. Furthermore, additional data points for the convergence rate assessment could be obtained given that in order to maintain the aspect ratio of the structure using the implemented particle arrangement, the number of particles across the width of the beam must be doubled for each increase in resolution.

With regards to developing the FSI method specifically, details of an iterative, strongly coupled scheme are included within **Paper 4**. This is the first strongly coupled FSI method to include the V-model and has a significant impact on the ability of the FSI method to model cardiovascular conditions. Since the density of cardiovascular structures and blood are very similar, approximately 2:1, there is a strong added-mass effect which reduces accuracy and stability of the model. Without the iterative coupling scheme presented in **Paper 4** ensuring the interface conditions are satisfied at the boundaries, the FSI method is unable to be applied to cardiovascular applications. In addition, the paper demonstrates the ability to implement different time step sizes for the fluid and structure solvers, while maintaining accuracy in the solution. This coupling scheme could therefore be applied to any fluid or structure solver where the difference between the critical timesteps are large. This often occurs when using discrete methods are coupled.

7.4 Summary

In line with the University of Manchester regulations for a Journal Format Thesis, this chapter summarises the main contributions of the journal papers output from the research presented in this body of work. The contributions are grouped in relation to the objectives of the project, demonstrating both the significance of the research output and the fulfilment of the project aims.

Chapter 8

Summary and Future Work

8.1 Summary

The PhD project presented in this thesis has focussed on the development and implementation of a novel fluid-structure interaction method incorporating discrete numerical methods capable of modelling complex physics with the long-term aim of applying the method to cardiovascular problems. This thesis is in journal format, as is permitted by the University of Manchester, with the research outputs in the form of journal papers appended to the thesis.

The main body of the thesis begins by introducing the motivation behind this work, namely improving the clinical treatment of cardiovascular diseases in Chapter 1. This can be done by providing clinicians with additional information upon which to based their decisions through numerical analysis and in particular through modelling the interaction between blood and cardiovascular structures. Examples of numerical analysis in clinical settings already exist and have proven effective, for example the virtual Fractional Flow Reserve analysis (vFFR) which is able to replace angiograms in a number of instances [10].

The opportunity to utilise discrete numerical methods was identified through a survey of literature in the field in Chapter 2 and Appendix B, supplemented by a brief application-based study of abdominal aortic aneurysms using commercial numerical solvers in Appendix A. Discrete numerical methods are more readily able to model complex physics that occur in many diseases such as rupture and aggregation, than continuum methods that have been traditionally used in nu-

merical analysis of large scale cardiovascular applications. However, the computational cost of discrete methods is significantly higher that continuum methods due to the increased resolution required to accurately represent a problem and therefore their use has been restricted severely at large scales. The use of high performance computing (HPC) to massively parallelise simulations has tempered this limitation, however access to such facilities is not always possible and can be expensive financially. Graphics Processing Units (GPUs) can offer significant reductions in computational time, again through large scale parallelisation, with smaller hardware requirements. The discrete numerical methods, the lattice Boltzmann method (LBM) and vector-based discrete element method (V-model), integrated into the FSI method are well suited to GPU architecture due to the local nature of the methods. As a result, their use at large scales $O(10^{-2}\text{m})$ for cardiovascular applications is feasible.

Discussion of the underlying methodologies for the LBM, V-model and the coupling method, the immersed boundary method (IBM), are included in Chapters 3, 4 and 5. In addition, details of the strong coupling scheme, the block Gauss-Seidel scheme (BGSS) are included. The FSI method is strongly coupled due to the conditions experience in the majority of cardiovascular applications; the density of blood and the cardiovascular structure under investigation are well within an order of magnitude and therefore a large added-mass effect exists, reducing the accuracy and stability of weakly coupled schemes.

A detailed summary of model developments that facilitated the research included in the journal papers is included as a standalone chapter in Chapter 6. Significant modelling developments include the development of the first GPU V-model solver, a coupling scheme capable of integrating different time steps between the LBM and V-model and a linear interpolation procedure between the IBM and V-model allowing independent resolutions of the fluid and structure to be modelled.

The main body of the thesis concludes with a detailed discussion of the contributions to the field made by the journal publications appended to the thesis. The major contributions include the development of a novel, strongly coupled fluid-structure interaction method incorporating the V-model and the first GPU implementation of the V-model.

8.2 Future Work: Development for Cardiovascular Applications

The FSI method presented in this thesis will be further developed during an EPSRC Doctoral Prize Fellowship immediately following this work. This section summarises the current development status of the validated FSI method towards cardiovascular applications with details of on-going work that will be completed during the fellowship. Furthermore current issues and limitations will be discussed in conjunction with potential method developments to resolve them.

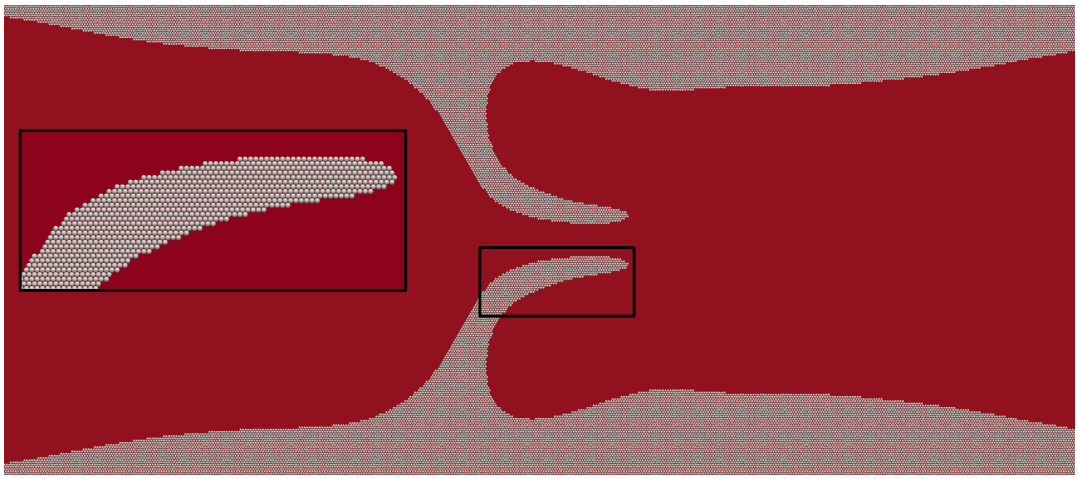

Figure 8.1: Realistic venous valve case setup using the FSI method. Valve and vessel walls discretised using the V-model particle generator with 10,000 particles.

8.2.1 Overview of Current Development Progress

Since the FSI model has been validated for structures undergoing high levels of deformation in Chapter 6 and Appendix D, it can be applied to realistic valve geometries such as that shown in Figure 8.1. The geometry has been discretised with ∼30,000 particles using the V-model particle generator which will be discussed in Section 8.2.2. While this level of discretisation should be sufficient to capture the dynamics of the structure, further development of the FSI method is required in order to effectively model this type of geometry and its interaction with a fluid. In particular, these developments are required in order to reduce the computational time of any simulation and to increase the stability of the method.

An overview of the numerical method development currently on-going to achieve these aims is shown in Figure 8.2. Each of these developments will be discussed individually in this chapter.

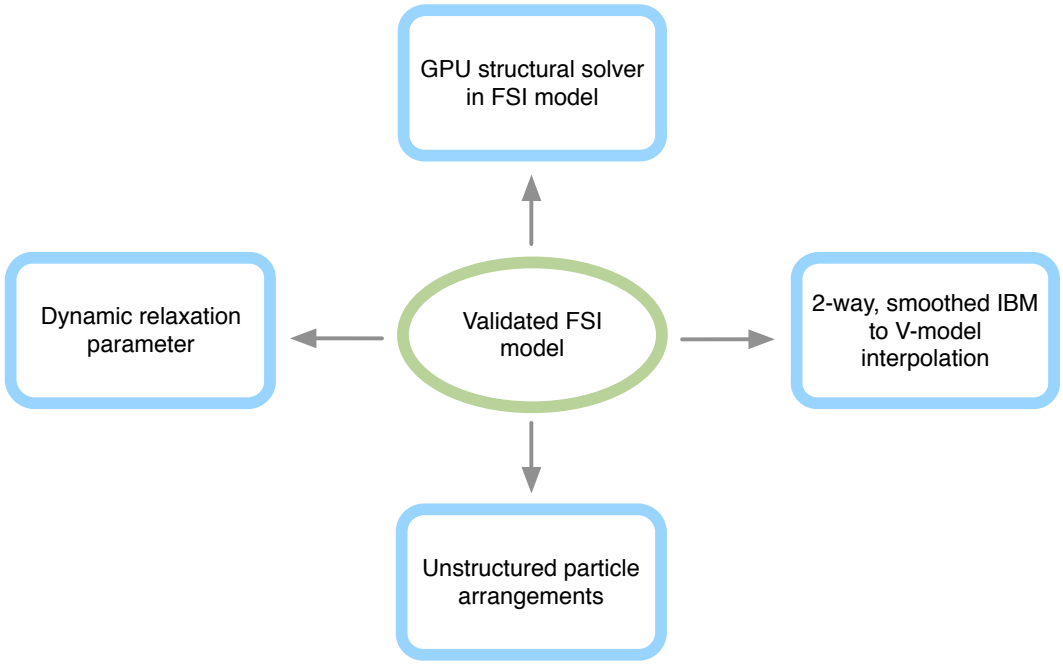

Figure 8.2: Numerical modelling developments in progress in order to improve the stability and computational speed of the FSI method.

8.2.2 V-model Particle Generator

In the validation cases presented in this work, the structure has been rectangular in shape in the form of beams and flags. For the structured particle arrangements of the V-model, either in the 7-disk (triangular) or 9-disk (rectangular) configurations, discretising these geometries via robust algorithms is straightforward. However, since the long-term aim of this work is to apply the FSI method to patient-specific cardiovascular geometries, the development of a V-model particle generator capable of discretising any geometry, irrespective of complexity, is critical.

The method developed here for geometry discretisation is able to fill a given area defined by a boundary in Cartesian coordinates with V-model particles using a seed-fill algorithm. This process is shown in Figure 8.3 for an idealised

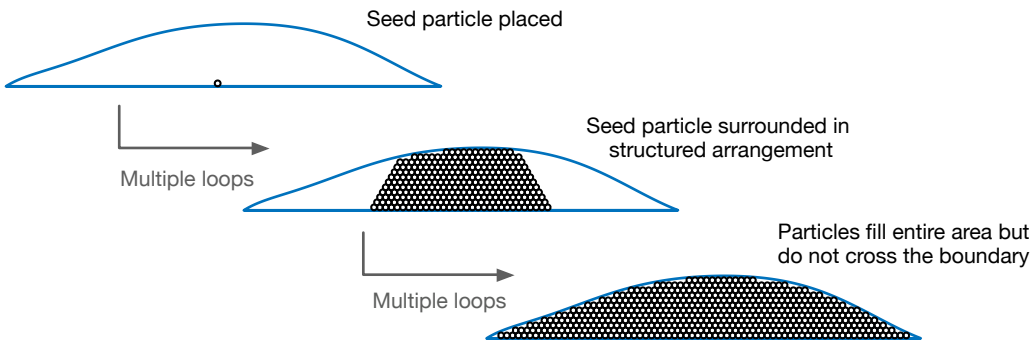

Figure 8.3: Progression of the seed filling algorithm used to generate structure arrangements of V-model particles within a boundary. Initial seed particle (top) is then surrounded by further particles (middle) until the boundary is reached and the area is filled (bottom).

atherosclerotic plaque geometry at low resolution for visualisation purposes. Once the particles have been created, the bonds between them are identified using a nearest neighbour search. For FSI applications, the immersed boundary markers are placed along the boundary bonds, therefore requiring identification of both the boundary particles and corresponding bonds. This procedure is completed through identifying particles with incomplete particle connections, i.e. particles with less than six attached bonds in the triangular structured arrangement, and eliminating particles that are located at the edge of the computational domain for both the fluid and the structure e.g. located at an inlet or outlet. The final step is to identify particles upon which boundary conditions will act such as clamped particles via identifying particles located in user defined clamped areas. The algorithm can be summarised as follows:

1. Define geometry area with boundary Cartesian coordinates

2. Fill geometry area with V-model particles in structured arrangement using seed-fill algorithm

3. Create bonds between particles

4. Identify boundary particles and bonds

5. Identify particles on which boundary conditions act

6. Export data to file to be read by V-model or FSI solver

The algorithm developed here is restricted to two dimensions although extension into three dimensions should be straightforward along with alternative structured arrangements [155]. On extension of the V-model for unstructured particle arrangements, more sophisticated packing algorithms are required. The current procedure has been used to create the realistic venous valve case geometry in Section 8.2.1 and is applicable to 2-D patient-specific geometries.

8.2.3 Coupling Scheme Relaxation Parameter

A constant relaxation parameter is currently implemented in the iterative coupling scheme as described in Section 5.5.3. The relaxation parameter is set to a constant value in the range of 0 to 1. In general, values closer to zero increase the stability of the scheme but require more iterations. As a result, an optimum value should be implemented in order to ensure stability but not increase the computational resource requirement unnecessarily. However, this value is often case and time dependent. In addition, the coupling between the solvers is currently less stable than would be expected and therefore lower relaxation parameter values are required to maintain stability particularly when the structure deformation is large. The computational time is therefore larger than would be expected also. By using a dynamic relaxation parameter scheme such as Aitken's Delta Squared method [141], the relaxation parameter can be optimised throughout the simulation and reduce the number of iterations required. The relaxation parameter is updated via:

$$\omega_k = -\omega^{k-1} \frac{(r_{k-1})^T (r_k - r_{k-1})}{|r_k - r_{k-1}|^2} \tag{8.1}$$

where ω is the relaxation parameter, r is the residual relating to the difference between the velocity of the fluid and structure at the boundary and k is the iteration number. Aitken's Delta Squared method is one of the most popular approaches for accelerating implicit coupling schemes due to ease of implementation and convergence efficiency. Previous studies have shown decreases in overall computational time using this method [156].

8.2.4 Integration of GPU V-model Solver into FSI Method

Work is currently in progress to integrate the GPU-based V-model solver, presented in Section 6.1.2 and Appendix C, into the FSI method. Due to the difference in critical time steps between the LBM and V-model, a smaller structural time step is used in the FSI coupling scheme as shown in Figure 5.8. These additional time steps for the structure increase the computational resource requirement for the method, although the increase is small in the case of the validation case presented in Section 6.4 and Appendix D. However, due to the small density ratio of blood and cardiovascular tissue, the time step ratios required for the venous valve case are an order of magnitude larger than in the validation cases. This has little effect on the accuracy of the method since the strong coupling scheme is iterative. However, it severely restricts the resolution of the V-model particles that can be modelled using the CPU-based solver since the computational resource requirement is drastically larger.

The GPU-based V-model solver has demonstrated computational speed-ups of around 50 times that of the serial CPU-based solver when used in isolation. As a result, its implementation with the current FSI solver will have a significant impact, decreasing the computational time required to model cases such as the realistic valve case depicted in Figure 8.1. Furthermore, the integration of the GPU-based V-model solver will serve as a useful intermediary stage in the long-term development of a fully GPU-based FSI solver.

8.2.5 Interpolation between IBM and V-model

The interpolation procedure between the immersed boundary method and the V-model developed during this PhD has been used to produce good agreement with the numerical benchmarking case proposed by Turek and Hron [7]. This case features large deformation over short time periods and as such is considered a robust test of an FSI method. However, the geometry of the flexible flag is easily discretised using the structured triangular arrangement of V-model particles. Consequentially, the boundary between the fluid and structure created by the immersed boundary markers, which follow the path between the centres of the V-model particles, represents the geometry of the flexible flag accurately. Some

error does exist since the immersed boundary discretised beam is effectively one particle thinner that the V-model discretised beam as shown in Figure 8.4. However, this error decreases with increasing V-model resolution since the particle diameter also decreases and is further reduced by the diffusive boundary created by the IBM.

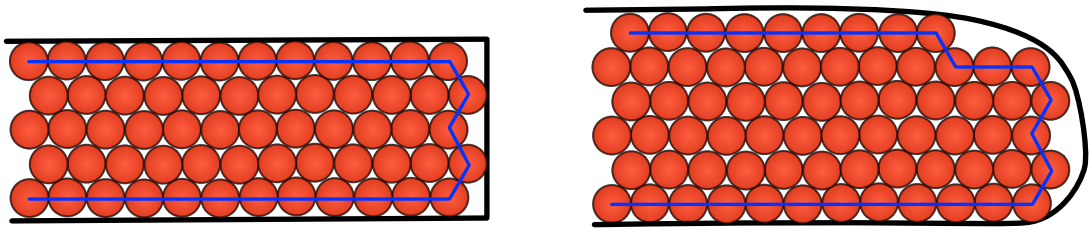

Figure 8.4: V-model particle discretisation of a beam (left) and an arbitrary shape (right) where the black line signifies the geometry boundary and the blue line signifies the path on which the immersed boundary markers lie.

On extension of the FSI method towards cardiovascular applications where patient-specific geometries will be used, it became clear that for bodies with boundaries with high curvature, the structured particle arrangement can struggle to accurately represent the boundary. This is especially true at low resolutions. Since the immersed boundary markers still follow the centres of the V-model particles at the boundary, this discretisation is also a less accurate representation of the geometry, often demonstrating a *jagged* boundary as shown in Figure 8.4. This can cause instabilities at the boundary, causing simulations to fail. Work is currently in progress to develop an interpolation procedure that will allow the immersed boundary markers to be placed along the edge of the V-model particles, with the immersed boundary force interpolated on to the centre of the V-model particles as shown in Figure 8.5.

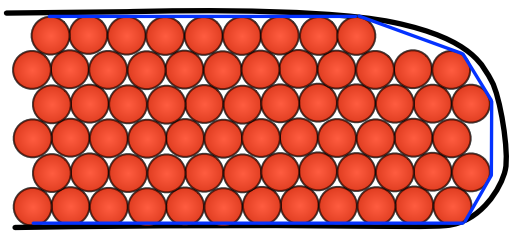

Figure 8.5: Alternative path for the immersed boundary markers, following the outermost edge of the boundary V-model particles as opposed to the centres of the V-model particles as shown in Figure 8.4.

8.2.6 V-model Particle Arrangement

An alternative solution to the issue described in the previous section is to implement an unstructured particle arrangement that is able to accurately resolve the boundary. Previous work by Tavarez et al. [9] has implemented an unstructured particle arrangement for a traditional DEM as shown in Figure 8.6. Using the unstructured particle arrangement, they were able to demonstrate good retention in accuracy in comparison to an FEM solution when modelling the dynamic response of a cantilever beam.

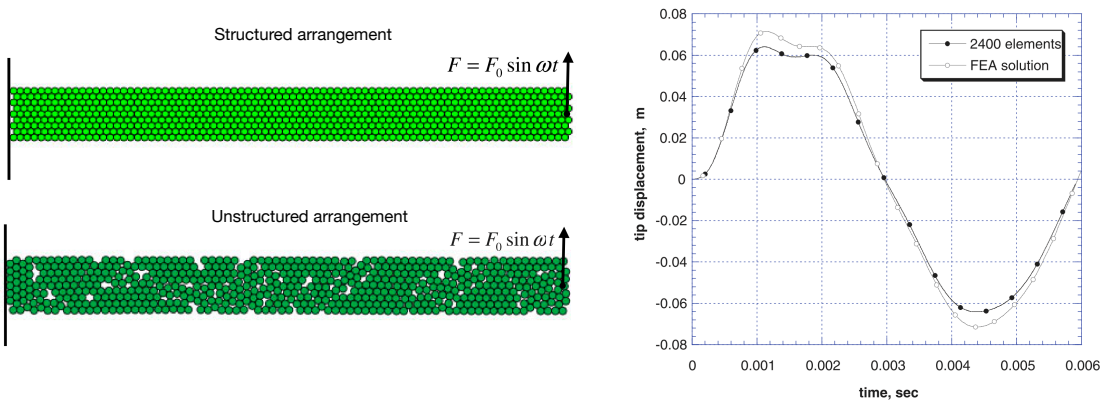

Figure 8.6: Structured (top left) and unstructured (bottom left) particle arrangements for DEM simulation of cantilever beam subject to time-varying load. Unstructured tip deflection time history in comparison to FEM solution. Adapted from [9].

Initial work on this development has demonstrated accuracy of the V-model is retained when loosening the structured arrangement by around 2% of the bond length of the equivalent structured arrangement. However, for larger variation in the arrangement the method becomes unstable. As a result, it may be necessary to remove the condition that particles are the same size in order to effectively model the unstructured arrangement. This will require reformulation of the underlying governing equations as described by Kuzkin and Asonov [106].

8.2.7 Long-term Future Work

In addition to the on-going work, extension of the FSI method into three dimensions will be necessary to capture the geometric variation of cardiovascular

structures. GPU implementation of the full FSI method will reduce computational times and will facilitate the 3D development given its associated increase in computational resource requirement.

References

[1] B. Owen, C. Lowe, N. Ashton, P. Mandal, S. Rogers, W. Wein, C. Mccollum, and A. Revell. Computational hemodynamics of abdominal aortic aneurysms : Three-dimensional ultrasound versus computed tomography. *Journal of Engineering in Medicine*, 230(3):201–210, 2016.

[2] B. Owen, N. Bojdo, A. Jivkov, B. Keavney, and A. Revell. Structural modelling of the cardiovascular system. *Biomechanics and Modeling in Mechanobiology*, 17(5):1–26, 2018.

[3] Y. Imai, T. Omori, Y. Shimogonya, T. Yamaguchi, and T. Ishikawa. Numerical methods for simulating blood flow at macro, micro, and multi scales. *Journal of Biomechanics*, 49(11):2221–2228, 2015.

[4] A. Updegrove, N. M. Wilson, J. Merkow, H. Lan, A. L. Marsden, and S. C. Shadden. SimVascular: An Open Source Pipeline for Cardiovascular Simulation. *Annals of Biomedical Engineering*, 45(3):525–541, 2017.

[5] A. L. Marsden and J. A. Feinstein. Computational modeling and engineering in pediatric and congenital heart disease. *Current Opinion in Pediatrics*, 27(5):587–596, 2015.

[6] M. G. Al-Azawy, A. Turan, and A. Revell. Assessment of turbulence models for pulsatile flow inside a heart pump. *Computer methods in biomechanics and biomedical engineering*, 5842(March):1–15, 2015.

[7] S. Turek and J. Hron. Proposal for Numerical Benchmarking of Fluid-Structure Interaction between an Elastic Object and Laminar Incompressible Flow. *Fluid-Structure Interaction*, pages 371–385, 2007.

[8] M. Schäfer, S. Turek, F. Durst, E. Krause, and R. Rannacher. Benchmark

Computations of Laminar Flow Around a Cylinder. *Flow Simulation with High-Performance Computers II*, pages 547–566, 1996.

[9] F. A. Tavarez and M. E. Plesha. Discrete element method formodelling solid and particulate materials Federico. *International Journal for Numerical Methods in Engineering*, 70:379–404, 2007.

[10] C. A. Taylor, T. A. Fonte, and J. K. Min. Computational fluid dynamics applied to cardiac computed tomography for noninvasive quantification of fractional flow reserve: Scientific basis. *Journal of the American College of Cardiology*, 61(22):2233–2241, 2013.

[11] G. Biglino, C. Capelli, J. Bruse, G. M. Bosi, A. M. Taylor, and S. Schievano. Computational modelling for congenital heart disease: how far are we from clinical translation? *Heart*, 103:98–103, 2017.

[12] T. C. Gasser, A. Nchimi, J. Swedenborg, J. Roy, N. Sakalihasan, D. Böckler, and A. Hyhlik-Dürr. A novel strategy to translate the biomechanical rupture risk of abdominal aortic aneurysms to their equivalent diameter risk: Method and retrospective validation. *European Journal of Vascular and Endovascular Surgery*, 47(3):288–295, 2014.

[13] G. A Holzapfel, G. Sommer, C. T. Gasser, and P. Regitnig. Determination of layer-specifc mechanical properties of human coronary arteries with nonatherosclerotic intimal thickening and related constitutive modeling. *Heart and Circulatory Physiology*, pages 2048–2058, 2005.

[14] J. Pu, G. S. Mintz, E. S. Brilakis, S. Banerjee, A. R. R. Abdel-Karim, B. Maini, S. Biro, J. B. Lee, G. W. Stone, G. Weisz, and A. Maehara. In vivo characterization of coronary plaques: Novel findings from comparing greyscale and virtual histology intravascular ultrasound and near-infrared spectroscopy. *European Heart Journal*, 33(3):372–383, 2012.

[15] C. C. Long, M-C. Hsu, Y. Bazilevs, J. A. Feinstein, and A. L. Marsden. Fluid-structure interaction simulations of the Fontan procedure using variable wall properties. *International Journal for Numerical Methods in Biomedical Engineering*, 28(1):807–827, 2012.

[16] F. B. C. Cansz, H. Dal, and M. Kaliske. An orthotropic viscoelastic material

model for passive myocardium: theory and algorithmic treatment. *Computer Methods in Biomechanics and Biomedical Engineering*, 18(11):1160–1172, 2015.

[17] P. D. Morris, A. Narracott, H. von Tengg-Kobligk, D. A. Silva Soto, S. Hsiao, A. Lungu, P. Evans, N. W. Bressloff, P. V. Lawford, D. R. Hose, and J. P. Gunn. Computational fluid dynamics modelling in cardiovascular medicine. *Heart (British Cardiac Society)*, pages heartjnl–2015–308044–, 2015.

[18] J. E. Stone, D. J. Hardy, I. S. Ufimtsev, and K. Schulten. GPU-accelerated molecular modeling coming of age. *Journal of Molecular Graphics and Modelling*, 29(2):116–125, 2010.

[19] N. Govender, D. N. Wilke, and S. Kok. Blaze-DEMGPU: Modular high performance DEM framework for the GPU architecture. *SoftwareX*, 5:62–66, 2015.

[20] Z. Wang, Y. Zhao, A. P. Sawchuck, M. C. Dalsing, and H. Yu. GPU acceleration of Volumetric Lattice Boltzmann Method for patient-specific computational hemodynamics. *Computers and Fluids*, 115:192–200, 2015.

[21] A. R. G. Harwood and A. J. Revell. Interactive flow simulation using Tegra-powered mobile devices. *Advances in Engineering Software*, 115(August 2017):363–373, 2018.

[22] J. A. Niestrawska, C. Viertler, P. Regitnig, T. U. Cohnert, G. Sommer, and G. A. Holzapfel. Microstructure and mechanics of healthy and aneurysmatic abdominal aortas: experimental analysis and modelling. *Journal of The Royal Society Interface*, 13(124):20160620, 2016.

[23] P. Brocklehurst, I. Adeniran, D. Yang, Y. Sheng, H. Zhang, and J. Ye. A 2D electromechanical model of human atrial tissue using the discrete element method. *BioMed Research International*, 2015:854953, 2015.

[24] D. Tang, C. Yang, J. Zheng, P. K. Woodard, J. E. Saffitz, G. A. Sicard, T. K. Pilgram, and C. Yuan. Quantifying Effects of Plaque Structure and Material Properties on Stress Distributions in Human Atherosclerotic Plaques Using 3D FSI Models. *Journal of Biomechanical Engineering*, 127(7):1185, 2005.

[25] L. Wang, Z. Wu, C. Yang, J. Zheng, R. Bach, D. Muccigrosso, K. Billiar, A. Maehara, G. S. Mintz, and D. Tang. IVUS-Based FSI Models for Human Coronary Plaque Progression Study: Components, Correlation and Predictive Analysis. *Annals of Biomedical Engineering*, 43(1):107–121, 2014.

[26] K. H. Fraser, M. E. Taskin, B. P. Griffith, and Z. J. Wu. The use of computational fluid dynamics in the development of ventricular assist devices. *Medical Engineering and Physics*, 33(3):263–280, 2011.

[27] F. Hellmeier, S. Nordmeyer, P. Yevtushenko, J. Bruening, F. Berger, T. Kuehne, L. Goubergrits, and M. Kelm. Hemodynamic Evaluation of a Biological and Mechanical Aortic Valve Prosthesis Using Patient-Specific MRI-Based CFD. *Artificial Organs*, 42(1):49–57, 2018.

[28] F. Auricchio, M. Conti, M. De Beule, G. De Santis, and B. Verhegghe. Carotid artery stenting simulation: From patient-specific images to finite element analysis. *Medical Engineering and Physics*, 33(3):281–289, 2011.

[29] M. Ju, S. S. Ye, B. Namgung, S. Cho, H. T. Low, H. L. Leo, and S. Kim. A review of numerical methods for red blood cell flow simulation. *Computer Methods in Biomechanics and Biomedical Engineering*, 18(2):130–140, 2015.

[30] S. Varchanis, Y. Dimakopoulos, C. Wagner, and J. Tsamopoulos. How viscoelastic is human blood plasma? *Soft Matter*, 14(21):4238–4251, 2018.

[31] H. Lei and G. E. M. Karniadakis. Quantifying the rheological and hemodynamic characteristics of sickle cell anemia. *Biophysical Journal*, 102(2):185–194, 2012.

[32] T. Krüger, M. Gross, D. Raabe, and F. Varnik. Crossover from tumbling to tank-treading-like motion in dense simulated suspensions of red blood cells. *Soft Matter*, 9(37):9008–9015, 2013.

[33] Z. Hashemi, M. Rahnama, and S. Jafari. Lattice Boltzmann Simulation of Healthy and Defective Red Blood Cell Settling in Blood Plasma. *Journal of Biomechanical Engineering*, 138(5):051002, 2016.

[34] J. Boyd, J. M. Buick, and S. Green. Analysis of the Casson and Carreau-

Yasuda non-Newtonian blood models in steady and oscillatory flows using the lattice Boltzmann method. *Physics of Fluids*, 19(9), 2007.

[35] T. W. Pan and T. Wang. Dynamical simulation of red blood cell rheology in microvessels. *International Journal of Numerical Analysis and Modeling*, 6(3):455–473, 2009.

[36] L. Formaggia, F. Nobile, A. Quarteroni, and A. Veneziani. Multiscale modelling of the circulatory system : a preliminary analysis. *Computing and Visualization in Science*, 2(2-3):75–83, 1999.

[37] J. Carson and R. Van Loon. An implicit solver for 1D arterial network models. *International Journal for Numerical Methods in Biomedical Engineering*, 33(7):1–16, 2017.

[38] A. Ruiz-Soler, F. Kabinejadian, M. A. Slevin, P. J. Bartolo, and A. Keshmiri. Optimisation of a novel spiral-inducing bypass graft using computational fluid dynamics. *Scientific Reports*, 7(1):1–14, 2017.

[39] P. Segers, L. Taelman, J. Degroote, J. Bols, and J. Vierendeels. The aortic reservoir-wave as a paradigm for arterial haemodynamics: insights from three-dimensional fluid-structure interaction simulations in a model of aortic coarctation. *Journal of Hypertension*, 33(3):554–63; discussion 563, 2015.

[40] J. E. Hippelheuser, A. Lauric, A. D. Cohen, and A. M. Malek. Realistic non-Newtonian viscosity modelling highlights hemodynamic differences between intracranial aneurysms with and without surface blebs. *Journal of Biomechanics*, 47(15):3695–3703, 2014.

[41] D. R. Einstein, K. S. Kunzelman, P. G. Reinhall, M. A. Nicosia, and R. P. Cochran. Nonlinear Fluid-Coupled Computational Model of the Mitral Valve. *Journal of Heart Valve Disease*, 3(14):376–385, 2005.

[42] B. C. Good, S. Deutsch, and K. B. Manning. Hemodynamics in a Pediatric Ascending Aorta Using a Viscoelastic Pediatric Blood Model. *Annals of Biomedical Engineering*, 44(4):1019–1035, 2016.

[43] A. B. Ramachandra, A. M. Kahn, and A. L. Marsden. Patient-Specific

Simulations Reveal Significant Differences in Mechanical Stimuli in Venous and Arterial Coronary Grafts. *Journal of Cardiovascular Translational Research*, 9(4):279–290, 2016.

[44] M. D. Mazzeo and P. V. Coveney. HemeLB: A high performance parallel lattice-Boltzmann code for large scale fluid flow in complex geometries. *Computer Physics Communications*, 178(12):894–914, 2008.

[45] U. D. Schiller, H. Chandrashekar, D. Groen, R. A. Richardson, P. V. Coveney, F. Robertson, and R. Coy. Validation of Patient-Specific Cerebral Blood Flow Simulation Using Transcranial Doppler Measurements. *Frontiers in Physiology*, 9(June):1–13, 2018.

[46] G. Xiong, C. A. Figueroa, N. Xiao, and C. A. Taylor. Simulation of blood flow in deformable vessels usingsubject-specific geometry and spatially varying wall properties. *International Journal for Numerical Methods in Biomedical Engineering*, 27:1000–1016, 2011.

[47] M. Xenos, N. Labropoulos, S. Rambhia, Y. Alemu, S. Einav, A. Tassiopoulos, N. Sakalihasan, and D. Bluestein. Progression of Abdominal Aortic Aneurysm Towards Rupture: Refining Clinical Risk Assessment Using a Fully Coupled Fluid-Structure Interaction Method. *Annals of Biomedical Engineering*, 43(1):139–153, 2014.

[48] S. Krittian, U. Janoske, H. Oertel, and T. Böhlke. Partitioned FluidSolid Coupling for Cardiovascular Blood Flow. *Annals of Biomedical Engineering*, 38(4):1426–1441, 2010.

[49] Y. Zou and Y. Zhang. The orthotropic viscoelastic behavior of aortic elastin. *Biomechanics and Modeling in Mechanobiology*, 10(5):613–625, 2011.

[50] H. Chen and G. S. Kassab. Microstructure-based constitutive model of coronary artery with active smooth muscle contraction. *Scientific Reports*, 7(1):1–15, 2017.

[51] Z. Wu, Z. Xu, O. Kim, and M. Alber. Three-dimensional multi-scale model of deformable platelets adhesion to vessel wall in blood flow. *Philosophical Transactions of the Royal Society A: Mathematical, Physical and Engineering Sciences*, 372(2021), 2014.

[52] D. Xu, E. Kaliviotis, A. Munjiza, E. Avital, C. Ji, and J. Williams. Large scale simulation of red blood cell aggregation in shear flows. *Journal of Biomechanics*, 46(11):1810–1817, 2013.

[53] I. Cimrák, I. Jan, K. Bachratá, and H. Bachrat. On elasticity of spring network models used in blood flow simulations in ESPResSo. In *III International Conference on Particle-based Methods Fundamentals and Applications*, volume 89, pages 1–12, 2013.

[54] M. Soleimani, S. Sahraee, and P. Wriggers. Red blood cell simulation using a coupled shellfluid analysis purely based on the SPH method. *Biomechanics and Modeling in Mechanobiology*, (2016), 2018.

[55] K. Tsubota, S. Wada, and T. Yamaguchi. Particle method for computer simulation of red blood cell motion in blood flow. *Computer methods and programs in biomedicine*, 83(2):139–146, 2006.

[56] D. A. Fedosov, M. Dao, G. E. M. Karniadakis, and S. Suresh. Computational biorheology of human blood flow in health and disease. *Annals of Biomedical Engineering*, 42(2):368–387, 2014.

[57] S. Sankaran, M. E. Moghadam, A. M. Kahn, E. E. Tseng, J. M. Guccione, and A. L. Marsden. Patient-specific multiscale modeling of blood flow for coronary artery bypass graft surgery. *Annals of Biomedical Engineering*, 40(10):2228–2242, 2012.

[58] R. Torii, M. Oshima, T. Kobayashi, K. Takagi, and T. E. Tezduyar. Fluid-structure interaction modeling of a patient-specific cerebral aneurysm: Influence of structural modeling. *Computational Mechanics*, 43(1):151–159, 2008.

[59] G. Dubini, M. R. de Leval, R. Pietrabissa, F. M. Montevecchi, and R. Fumero. A Numerical Fluid Mechanical Study Of Repaired Congenital Heart Defects. Application To The Total Cavopulmonary Connection. *Journal of biomechanics*, 29(1):111 – 121, 1996.

[60] M. R. De Leval, G. Dubini, F. Migliavacca, H. Jalali, G. Camporini, A. Redington, and R. Pietrabissa. Use of computational fluid dynamics in the design of surgical procedures: Application to the study of competitive flows

in cavopulmonary connections. *Journal of Thoracic and Cardiovascular Surgery*, 111(3):502–513, 1996.

[61] D. D. Soerensen, K. Pekkan, D. de Zélicourt, S. Sharma, K. Kanter, M. Fogel, and A. P. Yoganathan. Introduction of a New Optimized Total Cavopulmonary Connection. *Annals of Thoracic Surgery*, 83(6):2182–2190, 2007.

[62] A. L. Marsden, A. J. Bernstein, V. M. Reddy, S. C. Shadden, R. L. Spilker, F. P. Chan, C. A. Taylor, and J. A. Feinstein. Evaluation of a novel Y-shaped extracardiac Fontan baffle using computational fluid dynamics. *Journal of Thoracic and Cardiovascular Surgery*, 137(2):394–403.e2, 2009.

[63] M. H. Martin, J. A. Feinstein, F. P. Chan, A. L. Marsden, W. Yang, and V. M. Reddy. Technical feasibility and intermediate outcomes of using a handcrafted, area-preserving, bifurcated Y-graft modification of the Fontan procedure. *Journal of Thoracic and Cardiovascular Surgery*, 149(1):239–245.e1, 2015.

[64] Y. Delorme, K. Anupindi, A.E. Kerlo, D. Shetty, M. Rodefeld, J. Chen, and S. Frankel. Large eddy simulation of powered Fontan hemodynamics. *Journal of Biomechanics*, 46(2):408–422, 2013.

[65] G. A. Giridharan, M. Ising, M. A. Sobieski, S. C. Koenig, J. Chen, S. Frankel, and M. D. Rodefeld. Cavopulmonary assist for the failing Fontan circulation: Impact of Ventricular Function on Mechanical Support Strategy. *American Society of Artificial Internal Organs Journal*, 60(May 2012):707–715, 2014.

[66] A. Das, R. K. Banerjee, and W. M. Gottliebson. Right ventricular inefficiency in repaired tetralogy of Fallot: Proof of concept for energy calculations from cardiac MRI data. *Annals of Biomedical Engineering*, 38(12):3674–3687, 2010.

[67] Mi. J. Chern, M. T. Wu, and H. L. Wang. Numerical investigation of regurgitation phenomena in pulmonary arteries of Tetralogy of Fallot patients after repair. *Journal of Biomechanics*, 41(14):3002–3009, 2008.

[68] A. S. Rao and P. G. Menon. Presurgical planning using image-based in silico anatomical and functional characterization of Tetralogy of Fallot with

associated anomalies. *Interactive Cardiovascular and Thoracic Surgery*, 20(2):149–156, 2015.

[69] S. Piskin, G. Unal, A. Arnaz, T. Sarioglu, and K. Pekkan. Tetralogy of Fallot Surgical Repair: Shunt Configurations, Ductus Arteriosus and the Circle of Willis. *Cardiovascular Engineering and Technology*, 8(2):107–119, 2017.

[70] S. Piskin, H. F. Altin, O. Yildiz, I. Bakir, and K. Pekkan. Hemodynamics of patient-specific aorta-pulmonary shunt configurations. *Journal of Biomechanics*, 50:166–171, 2017.

[71] J. Lantz, T. Ebbers, J. Engvall, and M. Karlsson. Numerical and experimental assessment of turbulent kinetic energy in an aortic coarctation. *Journal of Biomechanics*, 46(11):1851–1858, 2013.

[72] M. Szopos, N. Poussineau, Y. Maday, C. Canniffe, D. S. Celermajer, D. Bonnet, and P. Ou. Computational modeling of blood flow in the aorta - Insights into eccentric dilatation of the ascending aorta after surgery for coarctation. *Journal of Thoracic and Cardiovascular Surgery*, 148(4):1572–1582, 2014.

[73] J. Zhang, L. Zhong, B. Su, M. Wan, J. S. Yap, J. P. L. Tham, L. P. Chua, D. N. Ghista, and R. S. Tan. Perspective on CFD studies of coronary artery disease lesions andhemodynamics: A review. *International Journal for Numerical Methods in Biomedical Engineering*, 30(6):659–680, 2015.

[74] P. F. Davies. Mechanical sensing mechanisms: shear stress and endothelial cells. *Journal of Vascular Surgery*, 13(4):729–731, 1991.

[75] F. J. H. Gijsen, P. W. Serruys, P. J. de Feyter, A. F. W. van der Steen, C. J. Slager, Frits Mastik, W. J. van der Giessen, J. J. Wentzel, A. Thury, J. A. Schaar, and J. C. H. Schuurbiers. Strain distribution over plaques in human coronary arteries relates to shear stress. *American Journal of Physiology-Heart and Circulatory Physiology*, 295(4):H1608–H1614, 2008.

[76] C. C. Long, A. L. Marsden, and Y. Bazilevs. Fluid-structure interaction simulation of pulsatile ventricular assist devices. *Computational Mechanics*, 52(5):971–981, 2013.

[77] G. Marom. Numerical Methods for FluidStructure Interaction Models of Aortic Valves. *Archives of Computational Methods in Engineering*, 22(4):595–620, 2015.

[78] D. A. Steinman, J. S. Milner, C. J. Norley, S. P. Lownie, and D. W. Holdsworth. Image-Based Computational Simulation of Flow Dynamics in a Giant Intracranial Aneurysm. *AJNR Am. J. Neuroradiol.*, 24(4):559–566, 2003.

[79] B. Chung and J. R. Cebral. CFD for Evaluation and Treatment Planning of Aneurysms: Review of Proposed Clinical Uses and Their Challenges. *Annals of Biomedical Engineering*, 43(1):122–138, 2014.

[80] H. Baek, M. V. Jayaraman, and G. E. Karniadakis. Wall shear stress and pressure distribution on aneurysms and infundibulae in the posterior communicating artery bifurcation. *Annals of Biomedical Engineering*, 37(12):2469–2487, 2009.

[81] K. Fukazawa, F. Ishida, Y. Umeda, Y. Miura, S. Shimosaka, S. Matsushima, W. Taki, and H. Suzuki. Using computational fluid dynamics analysis to characterize local hemodynamic features of middle cerebral artery aneurysm rupture points. *World Neurosurgery*, 83(1):80–86, 2015.

[82] G. Lu, L. Huang, X. L. Zhang, S. Z. Wang, Y. Hong, Z. Hu, and D. Y. Geng. Influence of hemodynamic factors on rupture of intracranial aneurysms: Patient-specific 3D mirror aneurysms model computational fluid dynamics simulation. *American Journal of Neuroradiology*, 32(7):1255–1261, 2011.

[83] J. Xiang, S. K. Natarajan, M. Tremmel, M. Ding, J Mocco, L. N. Hopkins, A. H. Siddiqui, E. I. Levy, and M. Hui. Hemodynamic-Morphologic Discriminants for Intracranial Aneurysm Rupture. *Stroke*, 42(1):144–152, 2011.

[84] T. Hassan, M. Ezura, E. V Timofeev, T. Tominaga, T. Saito, T. Akira, T. Kazuyoshi, and T. Yoshimoto. Computational Simulation of Therapeutic Parent Artery Occlusion to Treat Giant Vertebrobasilar Aneurysm. *American Journal of Neuroradiology*, 25(1):63–68, 2004.

[85] J. R. Cebral, M. A. Castro, J. E. Burgess, R. S. Pergolizzi, M. J. Sheridan,

and C. M. Putman. Characterization of cerebral aneurysms for assessing risk of rupture by using patient-specific computational hemodynamics models. *American Journal of Neuroradiology*, 26(10):2550–2559, 2005.

[86] D. M. Sforza, C. M. Putman, E. Scrivano, P. Lylyk, and Juan R. Cebral. Blood-flow characteristics in a terminal basilar tip aneurysm prior to its fatal rupture. *American Journal of Neuroradiology*, 31(6):1127–1131, 2010.

[87] J.R. Cebral and H. Meng. Counterpoint: Realizing the Clinical Utility of Computational Fluid Dynamics-Closing the Gap. *American Journal of Neuroradiology*, 33(3):396–398, 2012.

[88] K. Kono and K. Valen-Sendstad. The 2015 Aneurysm CFD Challenge, Preliminary Results: Is CFD ready for clinical use? In *Proceedings of Computational Fluid Dynamics in Medicine and Biology II*, 2015.

[89] V. M. Pereira, O. Brina, A. Marcos Gonzales, A. P. Narata, P. Bijlenga, K. Schaller, K. O. Lovblad, and R. Ouared. Evaluation of the influence of inlet boundary conditions on computational fluid dynamics for intracranial aneurysms: A virtual experiment. *Journal of Biomechanics*, 46(9):1531–1539, 2013.

[90] Z. Zeng, D. F. Kallmes, M. J. Durka, Y. Ding, D. Lewis, R. Kadirvel, and A. M. Robertson. Sensitivity of CFD Based Hemodynamic Results in Rabbit Aneurysm Models to Idealizations in Surrounding Vasculature. *Journal of Biomechanical Engineering*, 132(9):091009, 2010.

[91] L. Dempere-Marco, E. Oubel, M. Castro, C. Putman, A. Frangi, and J. Cebral. CFD Analysis Incorporating the Influence of Wall Motion: Application to Intracranial Aneurysms. In *Medical Image Computing and Computer-Assisted Intervention MICCAI 2006*, pages 438–445. 2006.

[92] A. Valencia, P. Burdiles, M. Ignat, J. Mura, E. Bravo, R. Rivera, and J. Sordo. Fluid Structural Analysis of Human Cerebral Aneurysm Using Their Own Wall Mechanical Properties. *Computational and Mathematical Methods in Medicine*, 2013(293128):1–18, 2013.

[93] P. N. Watton, N. A. Hill, and M. Heil. A mathematical model for the

growth of the abdominal aortic aneurysm. *Biomechanics and Modeling in Mechanobiology*, 3(2):98–113, 2004.

[94] C. Figueroa, S. Baek, C. A. Taylor, and J. D. Humphrey. A computational framework for fluid-solid-growth modeling in cardiovascular simulations. *Computer Methods in Applied Mechanics and Engineering*, 198(45-46):3583–3602, 2009.

[95] X. He and L. S. Luo. A priori derivation of the lattice boltzmann equation. *Physical Review E - Statistical Physics, Plasmas, Fluids, and Related Interdisciplinary Topics*, 55(6):6333–6336, 1997.

[96] X. Shan and X. He. Discretization of the velocity space in the solution of the boltzmann equation. *Physical Review Letters*, 80(1):65–68, 1998.

[97] X. Shan, X. F. Yuan, and H. Chen. Kinetic theory representation of hydrodynamics: A way beyond the Navier-Stokes equation. *Journal of Fluid Mechanics*, 550:413–441, 2006.

[98] T. Krüger, F. Varnik, and D. Raabe. Shear stress in lattice Boltzmann simulations. *Physical Review E - Statistical, Nonlinear, and Soft Matter Physics*, 79(4):1–14, 2009.

[99] T. Krüger, H. Kusumaatmaja, A. Kuzmin, O. Shardt, G. Silva, and E. M. Viggen. *The Lattice Boltzmann Method: Principles and Practice*. Springer Nature, 2017.

[100] D. J. Holdych, D. R. Noble, J. G. Georgiadis, and R. O. Buckius. Truncation error analysis of lattice Boltzmann methods. *Journal of Computational Physics*, 193(2):595–619, 2004.

[101] Z. Guo, C. Zheng, and B. Shi. Discrete lattice effects on the forcing term in the lattice Boltzmann method. *Physical Review E - Statistical Physics, Plasmas, Fluids, and Related Interdisciplinary Topics*, 65(4):6, 2002.

[102] M. Bouzidi, M. Firdaouss, and P. Lallemand. Momentum transfer of a Boltzmann-lattice fluid with boundaries. *Physics of Fluids*, 13(11):3452–3459, 2001.

[103] D. D'Humieres, I. Ginzburg, M. Krafczyk, P. Lallemand, and L. Luo. Multiple-relaxation-time lattice Boltzmann. *Philosophical Transactions of the Royal Society A: Mathematical, Physical and Engineering Sciences*, 360(1792):437–451, 2002.

[104] J. Latt, B. Chopard, O. Malaspinas, M. Deville, and A. Michler. Straight velocity boundaries in the lattice Boltzmann method. *Physical Review E - Statistical, Nonlinear, and Soft Matter Physics*, 77(5):1–16, 2008.

[105] Q. Zou and X. He. On pressure and velocity flow boundary conditions and bounceback for the lattice Boltzmann BGK model. *Physics of Fluids*, 9(6):1591–1598, 1996.

[106] V. A. Kuzkin and I. E. Asonov. Vector-based model of elastic bonds for DEM simulation of solids. *Mechanical Engineering*, 86(5):1–10, 2012.

[107] A. M. A. Nasar. *Eulerian and Lagrangian Smoothed Particle Hydrodynamics as Models for the Interaction of Fluids and Flexible Structures in Biomedical Flows*. PhD thesis, University of Manchester, 2016.

[108] P. A. Cundall. A Computer Model for Simulating Progressive, Large-scale Movement in Blocky Rock System. In *Proceedings of the International Symposium on Rock Mechanics*, pages 129–136, Nancy, 1971.

[109] A. Manne and D. Neelima Satyam. A review on the discrete element modeling of dynamic laboratory tests for liquefaction assessment. *Electronic Journal of Geotechnical Engineering*, 20(1):21–46, 2015.

[110] E. Izadi and A. Bezuijen. Simulating direct shear tests with the Bullet physics library: A validation study. *PLoS ONE*, 13(4):1–28, 2018.

[111] Y. H. Wang, D. Xu, and K. Y. Tsui. Discrete element modeling of contact creep and aging in sand. *Journal of Geotechnical and Geoenvironmental Engineering*, 134(September):1407–1411, 2008.

[112] H. Zhang, Y. Tan, S. Shu, X. Niu, F. X. Trias, D Yang, H. Li, and Y. Sheng. Numerical investigation on the role of discrete element method in combined LBM-IBM-DEM modeling. *Computers & Fluids*, 94:37–48, 2014.

[113] K. Liu and W. Liu. Application of discrete element method for continuum dynamic problems. *Archive of Applied Mechanics*, 76(3-4):229–243, 2006.

[114] M. A. Celigueta, S. Latorre, F. Arrufat, and E. Oñate. Accurate modelling of the elastic behavior of a continuum with the Discrete Element Method. *Computational Mechanics*, 60(6):997–1010, 2017.

[115] A. Truszkowska, Q. Yu, P. A. Greaney, T. M. Evans, and J. J. Kruzic. A discrete element method representation of an anisotropic elastic continuum. *Journal of the Mechanics and Physics of Solids*, 121:363–386, 2018.

[116] S. L. Price, A. J. Stone, and M. Alderton. Explicit formulae for the electrostatic energy, forces and torques between a pair of molecules of arbitrary symmetry. *Molecular Physics*, 52(4):987–1001, 1984.

[117] V. A. Kuzkin and A. M. Krivtsov. Description for mechanical properties of graphene using particles with rotational degrees of freedom. *Doklady Physics*, 56(10):527–530, 2011.

[118] V. A. Kuzkin. Addendum to "Vector-based model of elastic bonds for simulation of granular solids". 1:3–6, 2015.

[119] D. V. Griffiths and G. G. W. Mustoe. Modelling of elastic continua using a grillage of structural elements based on discete element concepts. *International Journal for Numerical Methods in Engineering*, 50(7):1759–1775, 2001.

[120] C. O'Sullivan and J. D. Bray. Selecting a suitable time step for discrete element simulations that use the central difference time integration scheme. *Engineering Computations*, 21(2/3/4):278–303, 2004.

[121] H. Kruggel-Emden, M. Sturm, S. Wirtz, and V. Scherer. Selection of an appropriate time integration scheme for the discrete element method (DEM). *Computers and Chemical Engineering*, 32(10):2263–2279, 2008.

[122] K. Samiei. *Assessment of Implicit And Explicit Algorithms in Numerical Simulation of Granular Matter*. PhD thesis, Université du Luxembourg, 2012.

[123] D. Beeman. Some multistep methods for use in molecular dynamics calculations. *Journal of Computational Physics*, 20(2):130–139, 1976.

[124] J. A. Fleischmann. *Micromechanics-Based Continuum Constitutive Modeling of Isotropic Non-Cohesive Particulate Materials, Informed and Validated by the Discrete Element Method*. PhD thesis, Univeristy of Wisconsin-Madison, 2013.

[125] M. Otsubo, C. O'Sullivan, and T. Shire. Empirical assessment of the critical time increment in explicit particulate discrete element method simulations. *Computers and Geotechnics*, 86:67–79, 2017.

[126] I. M. Smith, D. V. Griffiths, and L. Margetts. *Programming the finite element method*. John Wiley and Sons, 5th edition edition, 2013.

[127] M. Heil, A. L. Hazel, and J. Boyle. Solvers for large-displacement fluid-structure interaction problems: Segregated versus monolithic approaches. *Computational Mechanics*, 43(1):91–101, 2008.

[128] C. Farhat, M. Lesoinne, and P. LeTallec. Load and motion transfer algorithms for fluid/structure interaction problems with non-matching discrete interfaces: Momentum and energy conservation, optimal discretization and application to aeroelasticity. *Computer Methods in Applied Mechanics and Engineering*, 157(1-2):95–114, 1998.

[129] T. Krüger, D. Holmes, and P. V. Coveney. Deformability-based red blood cell separation in deterministic lateral displacement devices-A simulation study. *Biomicrofluidics*, 8(5):0–15, 2014.

[130] A. M. A. Nasar, B. D. Rogers, A. Revell, and P. K. Stansby. Flexible slender body fluid interaction: Vector-based discrete element method with Eulerian smoothed particle hydrodynamics. *Computers and Fluids*, 179:563–578, 2019.

[131] Z. Li and J. Favier. A non-staggered coupling of finite element and lattice Boltzmann methods via an immersed boundary scheme for fluid-structure interaction. *Computers and Fluids*, 143:90–102, 2017.

[132] K. Namkoong, H. G. Choi, and J. Y. Yoo. Computation of dynamic fluid-

structure interaction in two-dimensional laminar flows using combined formulation. *Journal of Fluids and Structures*, 20(1):51–69, 2005.

[133] C. S. Peskin. Flow patterns around heart valves: A numerical method. *Journal of Computational Physics*, 10(2):252–271, 1972.

[134] R. Mittal and G. Iaccarino. Immersed Boundary Methods. *Annual Review of Fluid Mechanics*, 37(1):239–261, 2005.

[135] A. Pinelli, I. Z. Naqavi, U. Piomelli, and J. Favier. Immersed-boundary methods for general finite-difference and finite-volume Navier-Stokes solvers. *Journal of Computational Physics*, 229(24):9073–9091, 2010.

[136] C. S. Peskin. The immersed boundary method. *Acta Numerica*, pages 479–517, 2002.

[137] A. M. Roma, C. S. Peskin, and M. J. Berger. An Adaptive Version of the Immersed Boundary Method. *Journal of Computational Physics*, 153(2):509–534, 1999.

[138] J. Favier, A. Revell, and A. Pinelli. A Lattice Boltzmann - Immersed Boundary method to simulate the fluid interaction with moving and slender flexible objects. *Journal of Computational Physics*, 261:145–161, 2014.

[139] J. O'Connor, A. Revell, P. Mandal, and P. Day. Application of a lattice Boltzmann-immersed boundary method for fluid-filament dynamics and flow sensing. *Journal of Biomechanics*, pages 1–9, 2015.

[140] A. A. Delouei, M. Nazari, M. H. Kayhani, and S. Succi. Immersed Boundary Thermal Lattice Boltzmann Methods for Non-Newtonian Flows Over a Heated Cylinder: A Comparative Study. *Communications in Computational Physics*, 18(02):489–515, 2015.

[141] J. O'Connor. *Fluid-structure interactions of wall-mounted flexible slender structures*. PhD thesis, University of Manchester, 2018.

[142] U. Kuttler, M. Gee, Ch. Forster, A. Comerford, and W.A. Wall. Coupling strategies for biomedical fluidstructure interaction problems. *International*

Journal for Numerical Methods in Biomedical Engineering, 26(3-4):305–321, 2010.

[143] P. Segers, J. Vierendeels, S. K. Dahl, S. Annerel, T. Claessens, P. Verdonck, L. R. Hellevik, J. Degroote, B. Skallerud, and P. Van Ransbeeck. Application of a strong FSI coupling scheme for the numerical simulation of bileaflet mechanical heart valve dynamics: study of wall shear stress on the valve leaflets. *Progress in Computational Fluid Dynamics, An International Journal*, 12(2/3):68, 2014.

[144] M. Gaeini, S. Mihradi, and H. Homma. Discrete Element Model for Continuum Dynamic Problems. *Journal of Solid Mechanics and Materials Engineering*, 2(12):1478–1486, 2008.

[145] J. Xu, H. Qi, X. Fang, L. Lu, W. Ge, X. Wang, M. Xu, F. Chen, X. He, and J. Li. Quasi-real-time simulation of rotating drum using discrete element method with parallel GPU computing. *Particuology*, 9(4):446–450, 2011.

[146] Y. Shigeto and M. Sakai. Parallel computing of discrete element method on multi-core processors. *Particuology*, 9(4):398–405, 2011.

[147] L. Zhang, S. F. Quigley, and A. H.C. Chan. A fast scalable implementation of the two-dimensional triangular Discrete Element Method on a GPU platform. *Advances in Engineering Software*, 60-61:70–80, 2013.

[148] C. C. Liao, Y. W. Chang, C. A. Lin, and J. M. McDonough. Simulating flows with moving rigid boundary using immersed-boundary method. *Computers and Fluids*, 39(1):152–167, 2010.

[149] J. Lee and S. H. Lee. Fluid-structure interaction analysis on a flexible plate normal to a free stream at low Reynolds numbers. *Journal of Fluids and Structures*, 29:18–34, 2012.

[150] M. Gluck, M. Breuer, F. Durst, A. Halfmann, and E. Rank. Computation of fluid-structure interaction on lightweight structures. *Journal of Wind Engineering and Industrial Aerodynamics*, 89(14-15):1351–1368, 2001.

[151] S. Turek, J. Hron, M. Razzaq, H. Wobker, and M. Schäfer. Numerical benchmarking of fluid-structure interaction: A comparison of different dis-

cretization and solution approaches. *Lecture Notes in Computational Science and Engineering*, 73 LNCSE:413–424, 2010.

[152] A. R. G. Harwood, J. O'Connor, J. Sanchez Muñoz, M. Camps Santasmasas, and A. J. Revell. LUMA: A many-core, FluidStructure Interaction solver based on the Lattice-Boltzmann Method. *SoftwareX*, 7:88–94, 2018.

[153] D. V. Papavassiliou, N. H. Pham, O. E. Kadri, and R. S. Voronov. Lattice Boltzmann methods for bioengineering applications. In *Numerical Methods and Advanced Simulation in Biomechanics and Biological Processes*, pages 415–429. Elsevier, 2017.

[154] M. J. Mawson and A. J. Revell. Memory transfer optimization for a lattice Boltzmann solver on Kepler architecture nVidia GPUs. *Computer Physics Communications*, 185(10):2566–2574, 2014.

[155] R. Peikert, D. Würtz, M. Monagan, and C. de Groot. Packing circles in a square: A review and new results. In L D Davisson, A G J MacFarlane, H Kwakernaak, J L Massey, Ya Z Tsypkin, A J Viterbi, and Peter Kall, editors, *System Modelling and Optimization*, pages 45–54, Berlin, Heidelberg, 1992. Springer Berlin Heidelberg.

[156] R. Haelterman, A. Bogaers, and J. Degroote. A Comparison of Different Quasi-Newton Acceleration Methods for Partitioned Multi-Physics Codes. In *Transactions on Engineering Technologies*, pages 135–152. 2018.

Appendices

Appendix A

Paper I - Computational hemodynamics of abdominal aortic aneurysms: Three-dimensional ultrasound versus computed tomography

The following journal paper is published in, *Proceedings of the Institution of Mechanical Engineers, Part H: Journal of Engineering in Medicine.*

The full paper is accessible online at: https://doi.org/10.1177/0954411915626742

Note: The authors accepted manuscript is included rather than the published version, as the larger columns are more suited to the layout and binding requirements of the thesis.

Computational Hemodynamics of Abdominal Aortic Aneurysms: 3D Ultrasound versus Computed Tomography

Benjamin Owen*[a], Christopher Lowe[b], Neil Ashton[a], Partha Mandal[a], Steven Rogers[b], Wolfgang Wein[c], Charles McCollum[b], Alistair Revell[a]

[a]*School of Mechanical, Aerospace and Civil Engineering, University of Manchester, UK*
[b]*Institute of Cardiovascular Sciences, University of Manchester, UK*
[c]*Imfusion GmbH, Munich, Germany*

Abstract

The current criterion for surgical intervention in Abdominal Aortic Aneurysms, based upon a maximal aortic diameter, is considered conservative due to the high mortality rate in case of rupture. The research community is actively investigating the use of computational mechanics tools combined with patient specific imaging to help identify more accurate criteria. Widespread uptake of a successful metric will however be limited by the need for Computed Tomography, which is at present the primary image extraction method on account of the location and complex shape of the aneurysms. The use of 3D UltraSound (3D US) as the scanning method is more attractive on account of increased availability, reduced cost and reduced risk to patients. The suitability of 3D US is assessed for this purpose in the present work; Computational Fluid Dynamics simulations were performed on geometries obtained from the same patient using both Ultrasound and Computed Tomography. The influence of different smoothing algorithms is investigated in the geometry preparation stage and the Taubin Low-Pass Filter was found to best preserve geometry features. Laminar, Newtonian, steady-state simulation analysis identified hemodynamic characteristics to be qualitatively similar in terms of Wall Shear Stress, Velocity and Vorticity. The study demonstrates the potential for 3D US to be integrated into a more accessible patient specific modelling tool able to identify the need for surgical intervention of Abdominal Aortic Aneurysms.

Keywords: Abdominal Aortic Aneurysms, Computational Fluid Dynamics, 3D Ultrasound, Patient Specific

1. Introduction

The pathogenesis of abdominal aortic aneurysms is complex. Inflammatory and proteolytic processes appear to be the dominant mechanisms controlling aneurysm expansion, acting in conjunction with other less well characterized mechanisms, including hemodynamic stress, infection and autoimmunity [1]. The Risk factors for AAA are well established - male sex, advanced age, smoking and a family history in first-degree male relatives [2, 3, 4, 5]. Rupture of an AAA is catastrophic with an overall mortality of 90% [6, 7] and is the cause of over 6000 deaths per year in the UK [8]. The growth rate and rupture risk of AAAs is unpredictable; only smoking (increases growth, doubles rupture risk) and diabetes (slows growth) have been proven as patient-specific factors. The cause of rupture is thought to be due to a number of factors [9], one of which being low Wall Shear Stress (WSS) in specific areas of the aneurysm.

Based on population studies, a maximal aortic diameter of 5.5cm for men and 5.0cm for women, is considered the threshold for elective repair [10] equating to the point at which risk of rupture is thought to outweigh the risk of surgery. This is clearly not an individualised approach and means that the timing of surgery may not be optimal - currently around 10 AAA repairs are performed to prevent

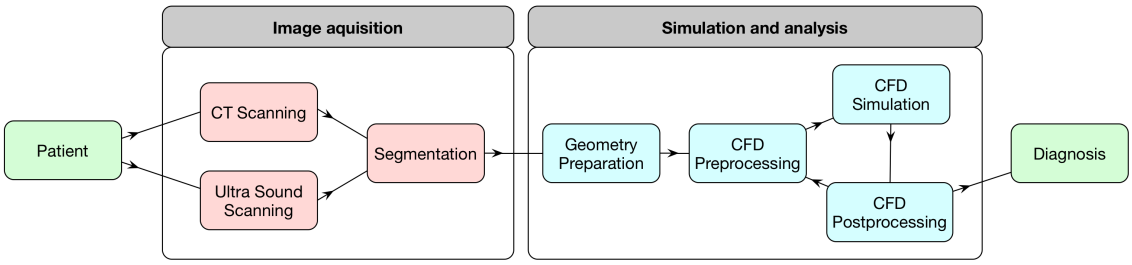

Figure 1: Tool Chain employed for the present study.

one rupture [11]. There is clearly a need for more patient-specific growth and rupture risk prediction to identify AAA patients at high rupture risk [12].

Recent attempts to improve this criterion have involved the use of Computed Tomography (CT) scans to obtain 3D models of patient specific geometry, often in conjunction with the application of Computational Fluid Dynamics (CFD) and Finite Element Analysis (FEA) to predict WSS in the aneurysm [10, 13, 14, 15, 16, 17]. These attempts have demonstrated the potential benefits of patient specific geometry in the prediction of rupture for AAAs, as the characterisation of aneurysmal flow patterns is most sensitive to aneurysm geometry over other variables [18]. However, this technique has not been widely implemented clinically as CT scanning is expensive, delivers a significant radiation dose and requires iodinated intravenous contrast, which is associated with cumulative nephrotoxity [19]. 3D Ultrasound (3D US) is a novel imaging modality that has the potential to overcome these issues and be applied to a wide patient population given that US is already used as the preliminary tool to identify AAAs in patients [20]. Given this, 3D US systems that are readily available at point of care would reduce waiting times. The techniques used for the generation of patient specific geometry (such as those presented in this paper) involve the use of 3D freehand ultrasound with external magnetic tracking, and interactive segmentation software. This system incorporates a graphical user interface (Vascular Suite ImFusion, Munich) which is suitable to be operated by bedside clinicians. This significantly reduces the time-line in the patient specific tool chain.

In the current work, additional smoothing is required to prepare the geometry for CFD simulation. A number of different algorithms have been identified as suitable for smoothing of patient specific geometries [21]. We here focus on a paired CT-US data set, both of which are smoothed using each algorithm in turn (Laplacian, HC Laplacian and Taubin Low-Pass Filter) in order to assess the importance and effects of geometry smoothing on fluid simulations. In this work, the accuracy of the simulation results using 3D US geometries will be compared against those obtained through CT scans in order to validate this technique. While most patient-specific approaches reported in previous studies have focussed on structural analysis of the aneurysm wall using FEA, there is an identified need to incorporate effects of the blood flow in order to improve accuracy of rupture prediction and ultimately a coupled fluid-structure approach is sought [1, 22, 11]. In general, WSS induced by flow simulations will be more sensitive to geometric resolution and inlet/outlet effects than wall stresses obtained by structural analysis alone, whereby loading pressures are generally imposed to be constant. A more stringent test of the potential of 3D US versus CT scan is thus identified in the comparison of CFD predictions from each source, which forms the focus of the present work.

2. Methods

Figure 1 represents the tool chain for each of the two scanning techniques used in the present study. The current study is limited to a single paired dataset in order to demonstrate the potential and the limitations of using 3D US approach, while future and ongoing work will aim to quantify this across a wider range of paired datasets. Patients undergoing CT angiography for planning of AAA repair at

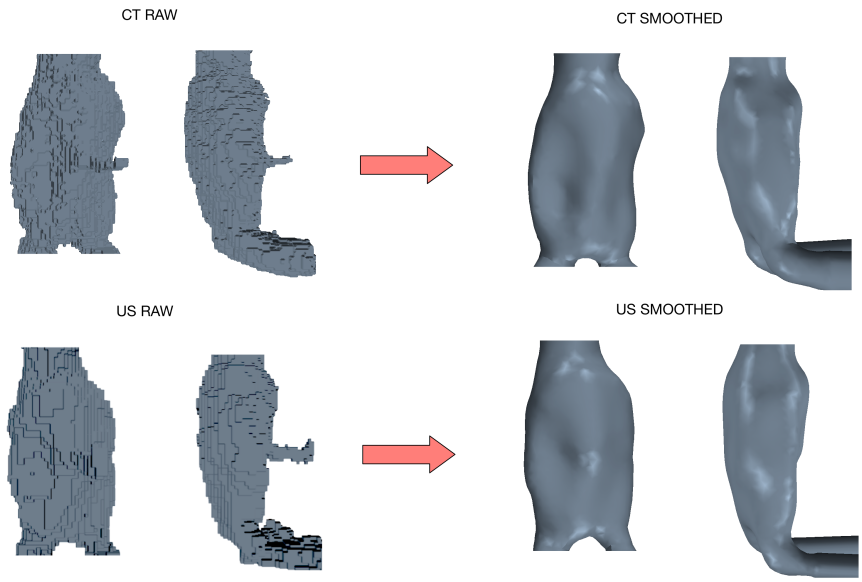

Figure 2: Geometry Preparation from CT and 3D US Data

University Hospital South Manchester were identified via the radiology department and gave informed consent. Ethical approval was granted by the National Research Ethics Committee (13/NW/0468).

In the following we provide details of the independent steps in the process, from imaging through to diagnosis, as represented by Figure 1. Steps are categorised as either image acquisition or simulation & analysis, while diagnosis is regarded as a separate process here. We differentiate between image segmentation and geometry preparation since the former requires physiological knowledge and the latter is associated with facilitation of the simulations.

CT scanning. CT angiography was performed using a 128-slice Siemens SOMATOM Perspective scanner (Siemens Medical, Munich, Germany). Patients were positioned supine and images at 1mm slices were acquired from the aortic arch to the femoral heads. Arterial phase images were acquired using a bolus dose of 100 mL of the iodinated contrast medium Omnipaque 240 (GE Healthcare, UK) administered at a flow rate of 3 mL/s.

3D US scanning. 3D US data was acquired using a Phillips IU22 ultrasound console (Phillips, Amsterdam, Netherlands) using a C5-1 curved array transducer. An electromagnetic tracking system (Ascension, Vermont, USA) comprising of a field generator and two tracking sensors that attach to the ultrasound probe, is used together with a 3D guidance software. The positional information generated by the movement of the sensors in the magnetic field allows the system to orientate the US probe in time and space. This positional data allows the 2D US frames to be assembled into a 3D volume.

Segmentation. CT and 3D US data were exported to prototype analysis software able to perform segmentation on both datasets (ImFusion Suite, ImFusion GmbH, Munich). An interactive segmentation algorithm was used where the operator briefly places seeds inside and outside the lumen in a number of images slices. The 'inside' and 'outside' regions are then propagated and defused in the whole image, defining the lumen from the surrounding aortic wall or thrombus [23]. Other structures of the AAA (e.g. wall, thrombus) can also be segmented in the same way. Errors in the segmentation were corrected by the user and the algorithm re-run to increase accuracy. The ImFusion software then uses a marching cube algorithm to convert the contours generated by the segmentation into a surface mesh

[24] that can be exported as a stereolithography file. Segmentation took less than 10 minutes for CT and less than 20 minutes for 3D US.

Geometry Preparation. Before smoothing each geometry, smaller arteries that branch from the descending aorta were removed, in this case flow from the lumen into a patent lumbar artery, as seen in Figure 2. By removing these smaller branches, the complexity of the simulation could be reduced. This decision was taken since the error associated with excluding these branches was deemed to be smaller than the effect from the simple simulation set up for this preliminary study. However, it should be noted that both imaging techniques were able to identify this artery in the same location.

The resolution of each geometry was then increased further via the application of the Butterfly Subdivision algorithm [25]. Each geometry was imported into MeshMixer [26] to prepare the inlet and outlets of each aneurysm for fluid simulation. Due to the high acoustic impedance of bone, US does not pass well through the rib cage and the image can also be obscured by other features such as bowel gas; resulting in difficulty obtaining large portions of the upstream aorta geometry. Furthermore, the aneurysm outlet arteries (iliac arteries), tend to follow the downward curvature of the pelvis, increasing the distance between the skin and the artery; which makes it challenging to obtain the downstream geometry using US. In an attempt to mitigate these restrictions we restricted our focus on the aneurysm itself, and assumed approximate constant cross-section in both up and downstream directions by extruding planar cuts of the available data as shown in Figure 2.

The aneurysm lumen geometries were then smoothed in MeshLab [27] using Laplacian [28], HC Laplacian [29] and Taubin Low-Pass Filter [30]. The Laplacian algorithm is widely used for a number of applications [31] and is available in most commercial software packages [32]. However, the Laplacian is known is suffer from shrinkage [33]. Previous research has indicated HC Laplacian and Taubin Low-Pass Filter are better optimized for medical applications in general [21] however, it was crucial that this be validated for AAA geometries from 3D US scans.

CFD Preprocessing. The inlet plane was extruded upstream by a distance of around three times the diameter of the abdominal aorta and an analytical profile was applied at the inlet, as defined by Eqn 1, where u_{mean} is the mean velocity corresponding to a mean Reynolds number of 660[34], r is the radial distance from the centre of the vessel and r_{max} is the vessel radius. This procedure enables the inlet section to be shortened in order to minimise the effects of boundary conditions, and thereby represent a more realistic blood flow profile in the region of the aneurysm [35, 36].

$$u_{inlet} = u_{mean}\left(1 - \left(\frac{r}{r_{max}}\right)^2\right) \tag{1}$$

The outlets were also extended in a similar manner in order to prevent backflow from affecting the fluid characteristics inside the aneurysm. It was found that the process to prepare the 3D segmented geometry for simulation could be completed by an experienced user in under 10 minutes.

The computational grid was generated using 10 layers of prism cells with sufficient resolution to adequately resolve the boundary layer and polyhedral cells used in the remaining domain. A grid refinement study was conducted on a single geometry based on meshes generated with 3 cross-sectional resolutions corresponding to total cell counts of 0.5, 1.7 and 5 million polyhedral cells. It was found that mesh convergence was reached by the second mesh containing $1.7M$ cells, for which a view of the cross-section is displayed in Figure 3.

CFD Simulation. All simulations were conducted using the commercial finite-volume code, STAR CCM+. For the purpose of this pilot study, a steady segregated incompressible solver was employed, assuming Newtonian laminar flow. A second-order upwind scheme was used to discretise the convective terms of the momentum equations. Since no patient specific flow velocity data was available, the Reynolds number was assumed to be 660 based upon the average inflow velocity and inlet diameter. The fluid's viscosity was set to 0.004kg/ms to represent a Newtonian blood flow and the density was set to 1050kg/m^3. A Poiseuille Flow was used at the inlet to represent a more realistic blood flow

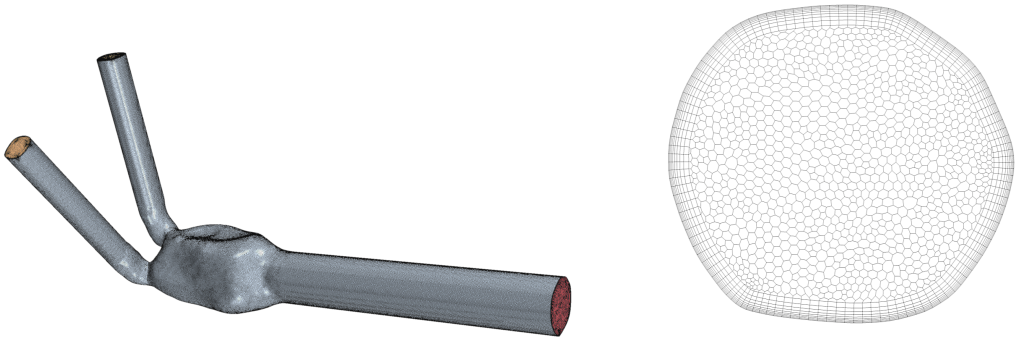

Figure 3: Mesh used in the CFD analysis (top) full domain, (btm) cross sectional detail.

Metric	Laplacian	HC Laplacian	Taubin Low-Pass Filter
No. of faces	38 894	39 728	39 614
No. of vertices	19 449	20 010	19 882
Shrinkage %	98.27	99.11	99.85
Mean Aspect Ratio	0.670	0.768	0.778

Table 1: Mesh Quality Assessment of Smoothing Algorithms

profile [35] while enabling a shortening of the inlet section as described above. The cases were run on 64 cores for 1,700,000 cells (30,000 cells per core). Time per iteration was around 0.5s and the calculation continued until residuals dropped below $1x10^{-6}$; on average this required a total of 5,500 iterations, amounting to a simulation time of 45 minutes.

CFD Postprocessing. The resulting WSS was extracted and compared for both smoothing algorithms to assess the sensitivity of the flow simulation to different smoothing algorithms. The WSS characteristics of the CT and 3D US scans were then compared to determine the potential viability of 3D US scans as a basis for surgical intervention for AAAs. The internal flow field was also assessed via a combination of streamlines and contours of both flow velocity and vorticity.

3. Results

3.1. Assessment of smoothing algorithms

The geometry from the segmentation stage remains unsuitable for CFD analysis, on account of remaining protrusions and tight internal corners. As such additional smoothing was undertaken using several common approaches employed in the literature and for each algorithm applied, we assessed the quality of the resulting surface mesh. The quality metrics, summarised in Table 1 include the number of faces and vertices, rate of shrinkage and the mean aspect ratios of faces. As mentioned previously, the Laplacian smoothing algorithm is known to suffer from shrinkage [29]. This results in the geometry converging to a single point if applied excessively. Even small amounts of shrinkage can cause geometry detail levels to be significantly reduced as well as artificially reducing the patient specific Reynolds number through the reduction of the characteristic distance, in this case the aorta diameter.

The face aspect ratio profile of geometries is of particular importance when creating the mesh for CFD analysis. Low aspect ratios can cause mesh distortion resulting in inaccurate solutions and slow convergence. Figure 4 shows the distribution of face aspect ratio for each algorithm when applied to the geometry output from the segmentation stage. The Laplacian smoothing is shown to result in a

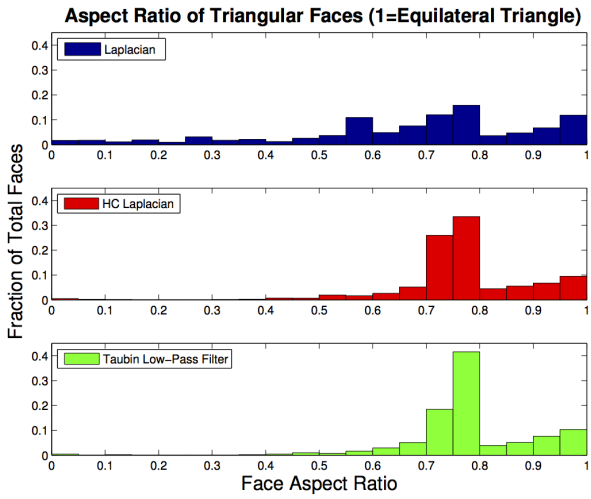

Figure 4: Histogram of Face Aspect Ratio for Laplacian, HC Laplacian and Taubin Low-Pass Filter

greater number of faces which have a lower value value aspect ratio. Indeed a smearing effect is in evidence. In contrast, the HC Laplacian algorithm and Taubin Low-Pass Filter retain a superior level of aspect ratio over the entire mesh; both exhibiting a modal face value of around 0.75.

The HC Laplacian algorithm and Taubin Low-Pass Filter were identified as suitable for CFD analysis based upon the superior quality of the resulting smoothed mesh and in the subsequent section we compare the impact of selecting either one or other of these approaches.

3.2. Analysis of Wall Shear Stress

In terms of providing evidence to assess the risk of aneurysm rupture, WSS levels are often deemed to play a crucial role, as reported in the introductory sections. Figure 5 provides a comparison of WSS distribution for the selected combinations of image sources and smoothing algorithms. It can been that the differences between geometries resulting from the two smoothing algorithms are minimal when compared to the those differences arising from the two methods of scanning. Negative axial WSS is shown in various locations indicating areas of flow recirculation. Encouragingly there are qualitative similarities between the predicted WSS distributions arising from both the CT and 3D US data. Areas of lowest WSS are identified in similar locations for both scanning methods and smoothing algorithms, as demonstrated by the minimum points located in the top right of the aneurysm wall in the front view and located at the top of the side view. In the clinical experience of the authors, the site of AAA rupture is highly variable but has been observed at sites similar to the region of low WSS identified in this simulation. It is therefore feasible to suggest this region may ultimately be the site of rupture and notable that it is unrelated to the site of maximal aortic diameter.

Figure 6 provides the means for a closer inspection of WSS levels. The axial WSS, τ_{wall}, is plotted along the artery walls along a probe in both a vertical plane (dark blue) and a horizontal plane (light blue) for all combinations of imaging technique and smoothing algorithm. It can be seen that the range of results all follow a trend, picking up maxima and minima at similar locations. In the vertical plane (on the left of Figure 6 and corresponding to the dark blue plane), there is an initial rise at a distance of 0.02m from the inlet, followed by a drop and a plateau in the region $0.03 < x < 0.08$. Beyond this point, the variation of WSS is heavily influenced by the exit and bifurcation region; giving rise to a large negative value corresponding to a flow recirculation. While the qualitative trends are similar, values arising from the 3D US derived data are higher by a factor of between 1.5 and 2 than values from the CT data. Differences are expected to be more pronounced at the start and end of the aneurysm, on account of the non-linear influence of small geometric variations in these regions.

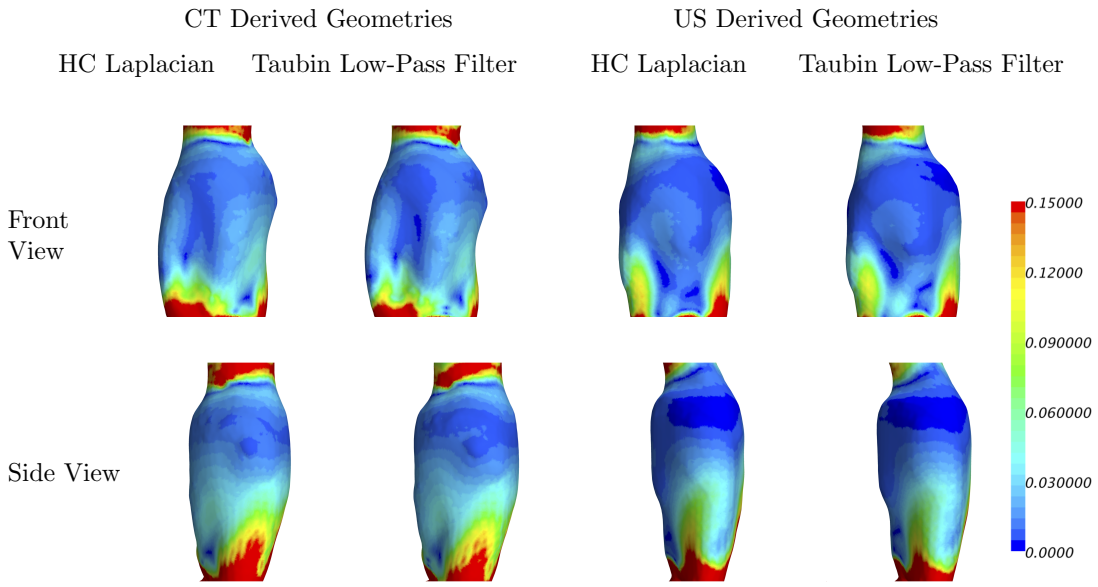

Figure 5: Wall Shear Stress (Pa) for each combination of image source and smoothing algorithm

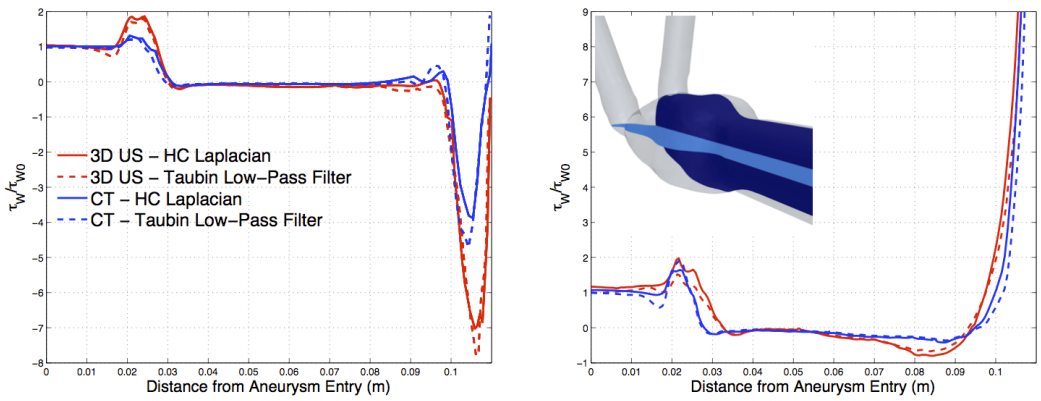

Figure 6: Axial Wall Shear Stress for each scanning technique

Nevertheless, away from these locations the agreement is observed to be within 10%. Oscillations in the magnitude of WSS can be seen around the exit of the aneurysm. This is partly caused by the irregularity of the cross sectional area of the aneurysm geometry in this region and also the increased complexity of the flow due to the bifurcation of the aorta into the iliac arteries and the wall between the branches.

The axial WSS profiles obtained in the horizontal (light blue) plane indicate a somewhat broader variation. Again, the agreement between CT and 3D US derived simulations is reasonably close. Peak values are once again predicted at around 0.02m from the inlet, but there is a difference in the subsequent predicted variation in that 3D US predictions indicate an earlier minima than that from CT simulations. This corresponds to variations in the profile of the aneurysm geometry and the associated distribution of the WSS as seen in Figure 5 (Front Views).

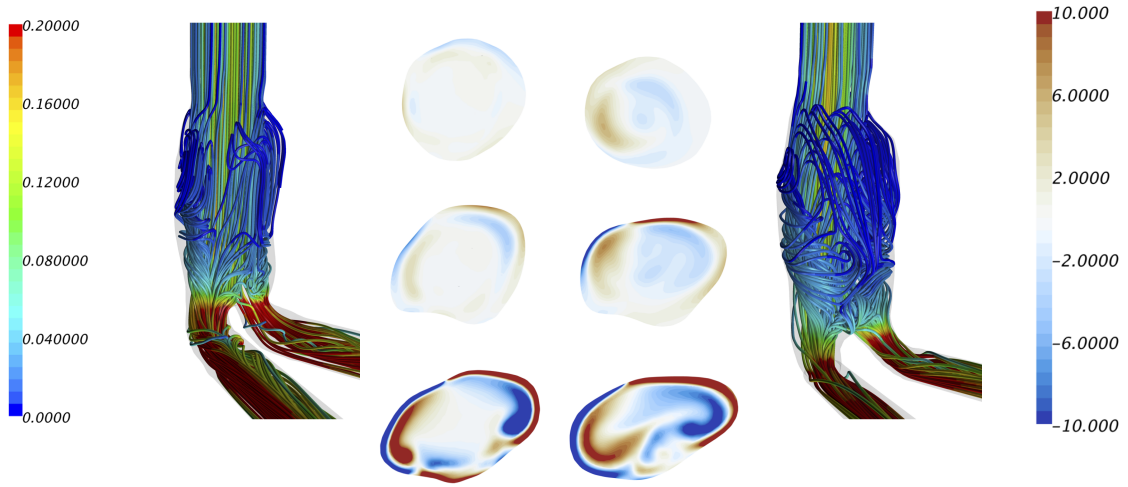

Figure 7: Streamlines and Contours of Velocity (m/s) and Vorticity (1/s) for Taubin Low-Pass Filter smoothed CT (left) and 3D US (right) geometries

3.3. Analysis of predicted flow field

Switching our attention to the internal flow field, we consider here a comparison between CT and US geometries smoothed using the Taubin Low-Pass Filter only, on account of small details reported in the previous section. Figure 7 displays streamlines of velocity and contours of vorticity plotted at various cross-planes. The streamlines demonstrate once again that the overall bulk flow is comparable between simulations derived from both CT and US sources; with the majority of the flow identified as high velocity bulk flow passing through the middle of the aneurysm. There are notable differences which occur in the lower velocity (blue) streamlines, in the vicinity of the aneurysm walls where geometric inconsistencies are more pronounced. Fortunately, the predicted levels of WSS don't appear to be overly sensitive to these differences.

This pattern is also demonstrated in the vorticity contour plots. The flow is observed to become more complex as it reaches the aneurysm outlets, with counter rotating vortices forming inside the aneurysm (shown in vorticity image 1 and 2). These vortices then breakdown as the flow approaches the outlets of the aneurysm resulting in non-uniform flow properties along the aneurysm wall. This results in the variation in the WSS across the wall that were previously identified.

4. Discussion

Steady CFD simulations of AAA patient specific geometries obtained from a single patient through CT and 3D US scans were performed and analysis of the derived hemodynamic conditions conducted. In addition, the effects of commercially available smoothing algorithms were assessed with the aim of identifying an optimum algorithm in the fluid simulation of AAAs.

It was found that the basic Laplacian smoothing algorithm was not suitable for AAA applications, creating meshes with higher rates of shrinkage and lower average aspect ratios than the HC Laplacian and Taubin Low-Pass Filter. The Taubin Low-Pass Filter provided the highest quality meshes causing no shrinkage to the geometry, the least reduction in visual detail and the highest quality average aspect ratio.

The Taubin Low-Pass Filter and HC Laplacian methods were then selected for CFD simulation. From the results it could be seen that there was little variation quantitatively in the hemodynamic

characteristics between the smoothing algorithms. However, given that the HC-Laplacian algorithm causes higher levels of mesh shrinkage, for future simulations incorporating a patient specific inlet velocity profile, the flow Reynolds number will be artificially reduced using the HC-Laplacian algorithm.

The hemodynamic characteristics exhibited a larger dependence on imaging source, as can be expected. However, it is noted that these geometric differences were not so great as to significantly impact the predicted distribution of wall shear stress, which is commonly understood to be one of the most important metrics in computational hemodynamic analysis of Aneurysm rupture. Predictions resulting from the 3D US derived data identified broadly the same locations of minimum WSS as those from CT scans, with predicted values remaining close across the majority of the flow. In addition, the axial WSS profiles obtained through both scanning techniques indicated very similar qualitative flow characteristics in terms of flow recirculation and the presence of bifurcation. The velocity streamlines and cross sectional contours were again qualitatively similar.

The tool chain for patient-specific geometries obtained through 3D US methods is more efficient than its CT counterpart, and more practical; and it's usage would radically broaden accessibility of patient specific computational hemodynamics analysis. Geometries obtained through CT scan require more outsourced steps in the tool chain, therefore increasing the time before a decision for surgical intervention can take place. Additionally, given the cost and risk to the patient, CT cannot be performed on multiple occasions if the aneurysm grows. This leads to a conservative criterion for surgical intervention given the mortality rate of an aneurysm rupture. In contrast, the 3D US technique can be performed as and when necessary given the availability and relatively small cost in comparison to CT scanning. This also allows the 3D US scan to be iterated if the quality of the geometry is not sufficient after the segmentation and smoothing stages.

The research presented in this paper demonstrates the potential for 3D Ultrasound to be used as an alternative to CT scanned patient specific geometries in the decision to surgically intervene for AAAs. The hemodynamic characteristics have been shown to be quantitatively similar for a relatively simple CFD simulation. Additionally, the tool chain for the technique incorporating 3D Ultrasound scanning was found to be more favourable to clinicians, allowing more of the method to be conducted bedside and iterated due to the low cost and high availability relative to CT scanning.

Mesh quality analysis found the Taubin Low-Pass Filter to be the most optimal commercially available smoothing algorithm producing high quality faces and preventing shrinkage of the geometry during smoothing iterations. The HC-Laplacian smoothing algorithm also performed favourably.

It should be emphasised that the research presented here is preliminary in nature, and aims only to demonstrate the potential of the 3D Ultrasound technique as a viable alternative to CT derived geometry. To this end, it has been shown that careful execution of the segmentation, image smoothing and CFD preprocessing stages can enable comparable analysis under the conditions of steady, laminar and Newtonian flow. Ongoing work will endeavour to repeat simulations for a number of additional pairs of CT and 3D US derived geometries to understand limitations and the sensitivity to different body types and aneurysm forms. Furthermore, analysis will incorporate increasing complexity in order to push towards more realistic simulation. Work will continue by assessing the impact on wall shear stress prediction when using a pulsatile velocity inlet condition, with patient-specific profiles obtained through Doppler ultrasound, as well as a non-Newtonian model for blood. We also plan to incorporate Finite Element Analysis of the artery wall, as well as the thrombus if present. The aorta itself undergoes a periodic motion related to the cardiac cycle, combining both translation and deformation. The precise details of this motion are not trivial and are undoubtedly patient-specific, but current assumptions of a rigid wall will most likely have an influence on the predicted rupture location. Future work could try to investigate the impact of these effects by employing recent developments in CFD which utilise mesh deformation and translation techniques such as Arbitrary-Lagrangian-Eulerian and Overset Mesh methods [37, 38]. By increasing the complexity of the simulation, we expect the differences between the imaging techniques to highlighted in greater detail and therefore provide a more meaningful answer to whether 3D Ultrasound can be used as a more accurate and efficient metric to indicate risk of rupture.

Declaration of conflicting interests

The author(s) declared no potential conflicts of interest with respect to the research, authorship and/or publication of this article.

References

[1] M. M. Thompson, Controlling the expansion of abdominal aortic aneurysms, British Journal of Surgery 90 (8) (2003) 897–898.

[2] E. Larsson, F. Granath, J. Swedenborg, R. Hultgren, A population-based case-control study of the familial risk of abdominal aortic aneurysm, Journal of Vascular Surgery 49 (1) (2009) 47–51.

[3] R. Scott, S. Bridgewater, H. Ashton, Randomized clinical trial of screening for abdominal aortic aneurysm in women., The British journal of surgery 89 (3) (2002) 283–5.

[4] K. A. Vardulaki, N. M. Walker, N. E. Day, S. W. Duffy, H. A. Ashton, R. A. P. Scott, Quantifying the risks of hypertension, age, sex and smoking in patients with abdominal aortic aneurysm, British Journal of Surgery 87 (2) (2000) 195–200.

[5] T. B. Wilmink, C. R. Quick, N. E. Day, The association between cigarette smoking and abdominal aortic aneurysms., Journal of vascular surgery 30 (6) (1999) 1099–105.

[6] R. A. Scott, H. A. Ashton, D. N. Kay, Abdominal aortic aneurysm in 4237 screened patients: prevalence, development and management over 6 years., The British journal of surgery 78 (9) (1991) 1122–1125.

[7] F. L. Moll, J. T. Powell, G. Fraedrich, F. Verzini, S. Haulon, M. Waltham, J. A. Van Herwaarden, P. J. E. Holt, J. W. Van Keulen, B. Rantner, F. J. V. Schlösser, F. Setacci, J. B. Ricco, Management of abdominal aortic aneurysms clinical practice guidelines of the European society for vascular surgery, European Journal of Vascular and Endovascular Surgery 41 (SUPPL. 1) (2011) S1–S58.

[8] J. J. Earnshaw, Doubts and dilemmas over abdominal aortic aneurysm, British Journal of Surgery 98 (5) (2011) 607–608.

[9] D. Reed, C. Reed, G. Stemmermann, T. Hayashi, Are Aortic Aneurysms Caused by Atherosclerosis?, Circulation 85 (1) (1992) 205–211.

[10] E. Soudah, E. Y. K. Ng, T. H. Loong, M. Bordone, U. Pua, S. Narayanan, CFD modelling of abdominal aortic aneurysm on hemodynamic loads using a realistic geometry with CT, Computational and Mathematical Methods in Medicine 13 (Article ID 472564) (2013) 9 pages.

[11] B. J. Doyle, P. R. Hoskins, T. M. McGloughlin, Computational rupture prediction of AAAs: what needs to be done next?, Journal of endovascular therapy : an official journal of the International Society of Endovascular Specialists 18 (2) (2011) 226–229.

[12] E. L. Chaikof, D. C. Brewster, R. L. Dalman, M. S. Makaroun, K. A. Illig, G. A. Sicard, C. H. Timaran, G. R. Upchurch, F. J. Veith, SVS practice guidelines for the care of patients with an abdominal aortic aneurysm: Executive summary, Journal of Vascular Surgery 50 (4) (2009) 880–896.

[13] E. A. Finol, C. H. Amon, Flow-induced wall shear stress in abdominal aortic aneurysms: Part I–steady flow hemodynamics., Computer methods in biomechanics and biomedical engineering 5 (4) (2002) 309–318.

[14] J. Biasetti, T. C. Gasser, M. Auer, U. Hedin, F. Labruto, Hemodynamics of the normal aorta compared to fusiform and saccular abdominal aortic aneurysms with emphasis on a potential thrombus formation mechanism, Annals of Biomedical Engineering 38 (2) (2010) 380–390.

[15] A. Teutelink, E. Cancrinus, D. Van De Heuvel, F. Moll, J. P. De Vries, Preliminary intraobserver and interobserver variability in wall stress and rupture risk assessment of abdominal aortic aneurysms using a semiautomatic finite element model, Journal of Vascular Surgery 55 (2) (2012) 326–330.

[16] D. A. Steinman, J. S. Milner, C. J. Norley, S. P. Lownie, D. W. Holdsworth, Image-Based Computational Simulation of Flow Dynamics in a Giant Intracranial Aneurysm, AJNR Am. J. Neuroradiol. 24 (4) (2003) 559–566.

[17] P. Berg, C. Roloff, O. Beuing, S. Voss, S.-I. Sugiyama, N. Aristokleous, A. S. Anayiotos, N. Ashton, A. Revell, N. W. Bressloff, A. G. Brown, B. J. Chung, J. R. Cebral, G. Copelli, W. Fu, A. Qiao, A. J. Geers, S. Hodis, D. Dragomir-Daescu, E. Nordahl, Y. B. Suzen, M. O. Khan, K. Valen-Sendstad, K. Kono, P. G. Menon, P. G. Albal, O. Mierka, R. Münster, H. G. Morales, O. Bonnefous, J. Osman, L. Goubergrits, J. Pallares, S. Cito, A. Passalacqua, S. Piskin, K. Pekkan, S. Ramalho, N. Marques, S. Sanchi, K. R. Schumacher, J. Sturgeon, H. Švihlová, J. Hron, G. Usera, M. Mendina, J. Xiang, H. Meng, D. a. Steinman, G. Janiga, The Computational Fluid Dynamics Rupture Challenge 2013 - Phase II: Variability of Hemodynamic Simulations in Two Intracranial Aneurysms, Journal of Biomechanical Engineering 137 (December) (2015) 1–13.

[18] J. E. Hippelheuser, A. Lauric, A. D. Cohen, A. M. Malek, Realistic non-Newtonian viscosity modelling highlights hemodynamic differences between intracranial aneurysms with and without surface blebs, Journal of Biomechanics 47 (15) (2014) 3695–3703.

[19] J. H. Rundback, D. Nahl, V. Yoo, Contrast-induced nephropathy, Journal of Vascular Surgery 54 (2) (2011) 575–579.

[20] H. A. Ashton, M. J. Buxton, N. E. Day, L. G. Kim, T. M. Marteau, R. A. P. Scott, S. G. Thompson, N. M. Walker, The Multicentre Aneurysm Screening Study (MASS) into the effect of abdominal aortic aneurysm screening on mortality in men: a randomised controlled trial., Lancet 360 (9345) (2002) 1531–1539.

[21] R. Bade, J. Haase, B. Preim, Comparison of Fundamental Mesh Smoothing Algorithms for Medical Surface Models., SimVis 1 (c) (2006) 1–16.

[22] A. K. Venkatasubramaniam, M. J. Fagan, T. Mehta, K. J. Mylankal, B. Ray, G. Kuhan, I. C. Chetter, P. T. McCollum, A comparative study of aortic wall stress using finite element analysis for ruptured and non-ruptured abdominal aortic aneurysms., European journal of vascular and endovascular surgery : the official journal of the European Society for Vascular Surgery 28 (2) (2004) 168–176.

[23] C. Couprie, L. Grady, L. Najman, H. Talbot, Power watershed: A unifying graph-based optimization framework, IEEE Transactions on Pattern Analysis and Machine Intelligence 33 (7) (2011) 1384–1399.

[24] W. E. Lorensen, H. E. Cline, Marching cubes: A high resolution 3D surface construction algorithm, ACM SIGGRAPH Computer Graphics 21 (4) (1987) 163–169.

[25] N. Dyn, D. Levine, J. A. Gregory, A butterfly subdivision scheme for surface interpolation with tension control, ACM Transactions on Graphics 9 (2) (1990) 160–169.

[26] MeshMixer, MeshMixer (2015).
URL `http://www.meshmixer.com/`

[27] MeshLab, MeshLab (2015).
URL `http://meshlab.sourceforge.net/`

[28] D. Field, Laplacian Smoothing and Delaunay Triangulations, Communications of Applied Numerical Methods 4 (6) (1988) 709–712.

[29] J. Vollmer, R. Mencl, H. Müller, Improved Laplacian Smoothing of Noisy Surface Meshes, Computer Graphics Forum 18 (3) (1999) 131–138.

[30] G. Taubin, Curve and surface smoothing without shrinkage, in: Proceedings of IEEE International Conference on Computer Vision, 1995.

[31] S. A. Canann, M. B. Stephenson, T. Blacker, Optismoothing: An optimization-driven approach to mesh smoothing, Finite Elements in Analysis and Design 13 (2-3) (1993) 185–190.

[32] S. Canann, J. Tristano, M. Staten, An approach to combined Laplacian and optimization-based smoothing for triangular, quadrilateral, and quad-dominant meshes, in: 7Th International Meshing Roundtable, 1998, pp. 15–17.

[33] Z. Ji, L. Liu, G. Wang, A global Laplacian smoothing approach with feature preservation, in: Proceedings - Ninth International Conference on Computer Aided Design and Computer Graphics, CAD/CG 2005, Vol. 2005, 2005, pp. 269–274.

[34] C. C. L. Asbury, J. W. J. Ruberti, E. E. I. Bluth, R. R. A. Peattie, Experimental investigation of steady flow in rigid models of abdominal aortic aneurysms, Annals of Biomedical Engineering 23 (1) (1995) 29–39.

[35] A. S. Les, S. C. Shadden, C. A. Figueroa, J. M. Park, M. M. Tedesco, R. J. Herfkens, R. L. Dalman, C. a. Taylor, Quantification of hemodynamics in abdominal aortic aneurysms during rest and exercise using magnetic resonance imaging and computational fluid dynamics, Annals of Biomedical Engineering 38 (4) (2010) 1288–1313.

Appendix B

Paper II - Structural Modelling of the Cardiovascular System

The following journal paper is published in, *Biomechanics and Modeling in Mechanobiology* .

The full paper is accessible online at: https://doi.org/10.1007/s10237-018-1024-9

Note: The authors accepted manuscript is included, rather than the published version, as the larger columns are more suited to the layout and binding requirements of the thesis.

Structural Modelling of the Cardiovascular System

Benjamin Owen*[a], Nicholas Bojdo[a], Andrey Jivkov[a], Bernard Keavney[b], Alistair Revell[a]

[a]*School of Mechanical, Aerospace and Civil Engineering, University of Manchester, UK*
[b]*Institute of Cardiovascular Sciences, University of Manchester, UK*

Abstract

Computational modelling of the cardiovascular system offers much promise, but represents a truly interdisciplinary challenge, requiring knowledge of physiology, mechanics of materials, fluid dynamics and biochemistry. This paper aims to provide a summary of the recent advances in cardiovascular structural modelling, including the numerical methods, main constitutive models and modelling procedures developed to represent cardiovascular structures and pathologies across a broad range of length and time scales; serving as an accessible point of reference to newcomers to the field. The class of so-called hyperelastic materials provide the theoretical foundation for the modelling of how these materials deform under load, and so an overview of these models is provided; comparing classical to application-specific phenomenological models. The physiology is split into components and pathologies of the cardiovascular system and linked back to constitutive modelling developments, identifying current state-of-the-art in modelling procedures from both clinical and engineering sources. Models which have originally been derived for one application and scale are shown to be used for an increasing range and for similar applications. The trend for such approaches is discussed in the context of increasing availability of high performance computing resources, where in some cases computer hardware can impact the choice of modelling approach used.

Keywords: Cardiovascular Structure, Continuum, Modelling, Discrete

1. Introduction

Modelling the cardiovascular system in the human body necessitates a complex interplay of strongly coupled multi-scale and multi-physics mechanisms and effects. In the past four decades, computational models have advanced significantly from what were once quite basic tools and methods, to what today have the potential to become integral components of clinical practise. Accurate and reliable *in silico* modelling has clear advantages over both *in vivo* and *in vitro* experiments; including repeatability of testing, a risk-free non-invasive testing and analysis, and the potential to isolate and understand key physiological mechanisms.

Previous studies have generally focused on a single application, from understanding the deformation characteristics and phase transitions of red blood cells [1] to the rupture of aneurysmal walls [2] and associated intraluminal thrombus [3].

Despite significant progress in the past few decades many challenges remain. One of the most prominent of these is 'fluid-structure interaction', refering to the strong coupling between the unsteady haemodynamics and the structure of the cardiovascular system components, including vessel walls, valves and the blood cells themselves. Fluid-structure interaction (FSI) is a central topic in computational cardiovascular modelling, and in recent years, interest and an increased ability to investigate these effects has enabled it to emerge from being a peripheral topic of modelling and simulation to a core aspect of biomedical simulation across a number of scales from individual cells [4] to the heart [5].

The purpose of this paper is to provide an overview of the different structural models employed in computational modelling of the cardiovascular system, primarily as part of a coupled fluid-solid approach but also as standalone models.

Section 2 discusses considerations that must be taken when deciding the modelling procedures and methods that should be implemented for a given application while Section 3 briefly describes and contrasts the two main families of modelling methods employed: continuum and discrete. An overview of material models is also given in this section, to highlight differences in how models determine the deformation of the structure for a given loading condition. Section 4 discusses application to various cardiovascular structures and pathologies organised in relation to characteristic length scale, in each case providing both a mechanical description of the physiology and a review of the related modelling work, summarising aspects of the structural models employed. The review concludes with a discussion of the direction of travel for this field. Particular attention is given to the choice between high-fidelity models that can aid our understanding of disease progression, and faster but low-order accuracy models that can be incorporated into clinical tools in the foreseeable future.

2. General modelling considerations

Vascular systems encompass a broad range of length scales: from the pumping heart (order 0.1m) and reducing five orders of magnitude further to the diameter of a single red blood cell (order 1×10^{-6}m). Quite naturally then, a range of numerical models and methods have been developed and adapted to the specific physical effects and prevalent dynamics at each scale. The dynamics of a single red blood cell, while pertinent to developing an understanding of certain pathologies, has negligible contribution to the deformation of the walls of large vessels. While the quasi-continuum motion of a million such cells is certainly of consequence and therefore requires careful consideration. The computational modeller will generally limit their focus to a domain representing two or possibly three orders of magnitude, broadly to strike a compromise between reasonable computational resource requirements and sufficient precision to provide insight into the mechanics of the particular question at hand.

This practice of limiting the scope of the simulation has further practical motivation, since many aspects of the cardiovascular system warrant different modelling approaches, based on what one hypothesises to be the prevailing dynamics. In the case of blood, it may either be modelled as a set of flexible structures suspended within a fluid, or at larger scales simply as a continuum fluid with little or no semi-empirical representation of 'non-Newtonian' behaviour. While incompressible fluid mechanics are governed by the Navier-Stokes equations and approximations thereof, the modelling imparted to represent the structural components tends to depend more on the nature and the relevance of their motion. As scales change, so does the most relevant model for the job at hand, although with a wealth of related studies in the literature, the choice is far from simple.

It has become clear that many diseases and disorders are comprised of mechanisms and factors that occur across a number of time and length scales. As such, recent studies have begun to explore the potential to develop methods that are able to perform multiple-scale simulations in both time and length, in order to investigate how changes at smaller length and time scales can lead to variability at larger scales [6, 7]. With the focus of the present review limited to the structural models rather than the frameworks for multiscale simulation, of which structural models are a component, we refer the reader to recent reviews of multiscale modelling in the cardiovascular system [8, 9].

At the structural level, representation methods can be classified into two families: Continuous and Discrete. An overview of each is given in Section 3 along with basic algorithms and extensions to the methods that have been developed. Discrete, or 'particle-based' methods are generally more inherently able to capture defects that might occur to a localised region of a structure, i.e. by offering the potential for modelling the solid as an inhomongeneous or heterogeneous continuum. By virtue of this, discrete methods generally require significantly greater computational resource to model a unit of domain than continuum methods; the latter are almost always employed where the spatial domain of interest is large [10, 11, 12]. Discrete methods come into their own where the aim is to examine effects which involve smaller scales [13, 14, 15]. With improvements in computational power [16, 17] and the increased use of novel hardware such as graphical processing units (GPU) - an architecture which is

naturally well suited to discrete methods [18, 19] - the boundaries between these methodologies are shifting [15].

Improvements in the capability of computational fluid-structure interaction modelling will increase the feasibility of such methods being integrated into diagnostic tools used in clinical practice - for example as a means of assessing rupture risk of abdominal aortic aneurysms [20]. In such cases the key driver for a numerical method is not accuracy alone, but also speed and robustness. Speed, since a fast simulation can enable diagnostic procedures to be completed bedside in a clinical environment. Robustness, since the quality of the patient-specific information at hand will vary tremendously, and the selected numerical methods should be able to cope with this without significant loss of accuracy. It is then of importance to note that in order to achieve speeds of practical use in the clinical environment, there will need to be a compromise with accuracy. Such a trade-off is not only practical but also entirely sensible, in order to supply the 'clinical indicator' needed to summarise the condition, *with the proviso* that the reduction in accuracy is quantified such that it can be considered appropriately.

For larger structures such as the heart or blood vessels, the tissues are comprised of layers with differing material properties, each of which plays a different role in its function. Given that these layers can be numerous and/or thick compared to the dimensions of their constituent cells, materials at this scale are generally modelled as a continuum, taking average properties across each layer. At smaller scales, structures are smaller, more homogeneous and permit use of particle based methods. Recently, hybrid approaches have been developed in modelling cardiovascular problems, in an attempt to merge the strengths of each. However, these hybrid approaches have generally involved coupling a continuum fluid solver and a discrete structural solver or vice versa in a fluid-structure interaction method [21, 22]. A hybrid structural solver [23] for cardiovascular applications has the potential to increase the feasibility of modelling localised defects, such as aneurysm rupture, at larger length scales than using a discrete method alone.

3. Modelling approach: computational implementation

Both continuum and discrete methods solve the same governing equation, Eqn. 1 relating an external force $\mathbf{F}$ to the resultant displacement $\mathbf{X}$ and its derivatives where $\mathbf{M}$, $\mathbf{C}$ and $\mathbf{K}$ are global matrices for mass, damping and stiffness.

$$\mathbf{M}\ddot{\mathbf{X}} + \mathbf{C}\dot{\mathbf{X}} + \mathbf{K}\mathbf{X} = \mathbf{F} \tag{1}$$

The attraction of continuum approaches is that they use the well-established governing equations of continuum mechanics, the solutions of which are performed with well-established numerical schemes. In the context of structural modelling, the majority of continuum approaches use the finite element (FE) method to discretise the structure and involve one of the material models, such as those included in Figure 1 and Table 1, as constitutive equations to describe the specific behaviour and characteristics of the structural component under consideration. The FE method is widely used to model both fluids [32, 33] and solids [34]. A drawback of the continuum approaches is that representing localised phenomena, such as damage or rupture of material, requires the introduction of special, often non-physical, measures. A number of developments to tackle this deficiency have been made over the years, such as the extended FE method (X-FEM) [35] and immersed FE method [36]. Despite promising advances, in this regard the continuum approach remains inferior to discrete methods, which allow for natural evolution of localised processes.

3.1. Implementation of continuum approaches

The first step of continuum methods is to create a discretised representation of the continuous medium; generally by defining a set of component elements in the form of a mesh. The number of elements required is determined by the accuracy and the level of approximation within each cell. The specific type of element and the nature of the approximation therein depend on the details of the structure that they represent. Each element will contain a number of nodes as shown in Figure 1,

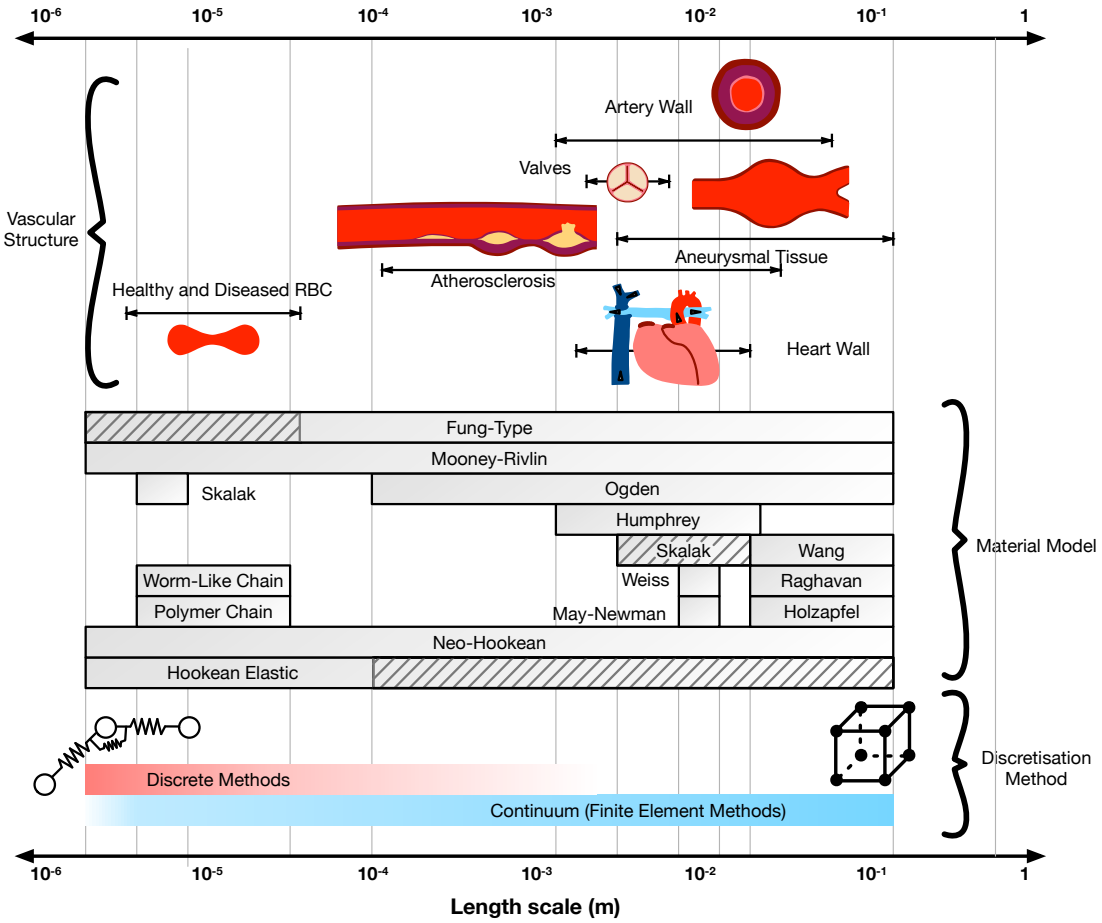

Figure 1: Structural models used in vascular applications with popular material models and discretisation methods, classified with respect to length scale and the applications to which they have been applied. Hashed lines indicate scales where material models have been used but not commonly.

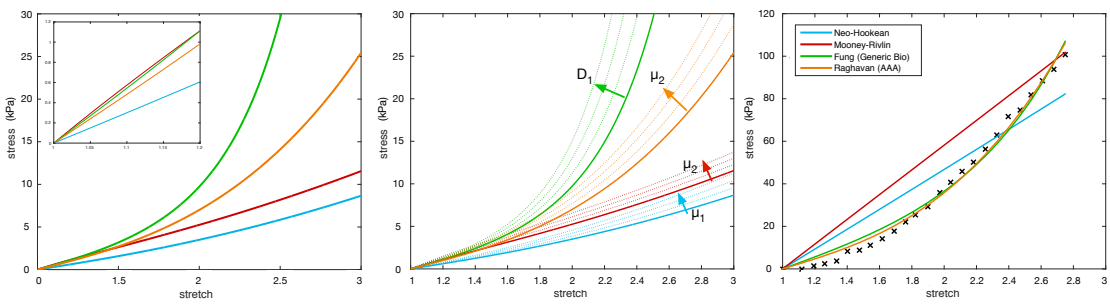

Figure 2: Stress-stretch profiles for some commonly implemented material models for small deformations (inset left) and large deformations (left). Each model can be adjusted through varying constants in the strain energy distribution function given in Table 1 (middle). Each is adapted via a least-squares regression algorithm and compared to the Raghavan stress-stretch profile, whose coefficients have been fitted to experimental results [25] (right).

Table 1: Strain energy distribution functions for a selection of major material models used in cardiovascular structural modelling: a brief description of each is provided with the original target application.

Neo-Hookean (simple hyperelasticity) $\mathbf{W} = \frac{\mu}{2}(I_1 - 3) - \mu \mathbf{ln} J + \frac{\lambda}{2}(\mathbf{ln} J)^2$	Linear elasticity and the neo-Hookean model provide similar deformation profiles at small strains. However, for larger strains the neo-Hookean model provides increasingly better description of deformation and is shown to be suitable where strains are up to 20% [24]. In many cases, cardiovascular tissues are considered as incompressible (J=1) reducing the strain energy function to the first term only. λ, μ are Lame constants of linear elasticity. μ also known as shear modulus.
Mooney-Rivlin (incompressible) $\mathbf{W} = \frac{\mu}{2}(I_1 - 3) + \mu_1(I_2 - 3)$	The incompressible Mooney-Rivlin model contains an additional term dependent on the second invariant of the deformation tensors. Originally developed for rubber like materials, it has been used as a simple representation of many cardiovascular structures across a number of scales, especially in scenarios where the deformation of healthy tissue may not be of primary concern, e.g. the development of various diseases. Second order formulations have also been used for a number of applications. μ_1 is a material constant requiring calibration against stress-strain data.
Abdominal aortic aneurysm model $\mathbf{W} = \frac{\mu}{2}(I_1 - 3) + \mu_2(I_1 - 3)^2$	Raghavan et al. [25] developed one of the first models specific to abdominal aortic aneurysmal tissue. Based upon a higher order Mooney-Rivlin model, the first term is retained from the neo-Hookean model while the second term is also a function of the first invariant since the model assumes tissue is stress-free in principle stretch directions 2 and 3 while material constants μ and μ_2 are estimated through fitting to uniaxial tensile experimental data. $\mu = 17.4N/m^2$; $\mu_2 = 188.1N/m^2$
Fung-type anisotropic coronary artery model $\mathbf{W} = \frac{\mu}{2}(I_1 - 3) + \frac{k_1}{k_2}(\exp(k_2[(1-\rho)(I_1-3)^2 + \rho(I_4 - 1)^2]) - 1)$	Holzapfel et al. [26] extended a previously developed multi-layer arterial wall model [27] for coronary arteries. The model includes an exponential isotropic term as proposed by Fung [28] and an anisotropic term relating to I_4 which contributes according to the angle between fibre reinforcement and circumferential direction in each layer. k_1 is a stress-like parameter; k_2, ρ are dimensionless parameters $I_4 = \lambda_\theta^2 \cos^2\phi + \lambda_z^2 \sin^2\phi$
Fung-type viscoelastic anisotropic myocardium model $\mathbf{W} = \frac{a}{2b}\exp(b(I_1 - 3)) + \sum_{i=f,s} \frac{a_i}{2b_i}(\exp(b_i(I_{4i} - 1)^2) - 1) + \frac{a_{fs}}{2b_{fs}}(\exp(b_{fs} I_{8fs}^2) - 1) + \frac{1}{2}\sum_{i=f,s,n} \mu_i(\epsilon_i - \alpha_i)^2$	Cansiz et al. [29] incorporated the anisotropic hyperelastic model proposed by Holzapfel & Ogden [30] (first 3 terms) which modelled the orthogonal nature of the myocardium in the fibre, sheet and sheet normal directions. The model was extended to reflect the viscoelastic nature of the myocardium with an additional term (final term) relating to the strain-rate dependence of material response. $a, b, a_f, b_f, a_s, b_s, a_{fs}, b_{fs}$ are material constants. f, s, n are fibre, sheet and sheet normal directions. $I_{4i} = \mathbf{i_0} \cdot \bar{\mathbf{C}}\mathbf{i_0}$, $I_{8fs} = \mathbf{f_0} \cdot \bar{\mathbf{C}}\mathbf{s_0}$ where $\mathbf{i_0}$ is a unit vector in given direction. μ_i, ϵ_i, α_i are non-equilibrium shear moduli, logarithmic strains and strain-like internal variables
Red blood cell model $\mathbf{W} = \frac{a}{4}\left(\frac{1}{2}I_1^2 + I_1 - I_2\right) + \frac{b}{8}I_2^2$	Skalak et al. developed a 2D stored energy potential for RBC membranes [31]. The first term provides the typically smaller stress caused by deformation with constant area, while the second term gives the typically large isotropic stress which is dependent on area change. redefined $I_1 = \lambda_1^2 + \lambda_2^2 - 2$ and $I_2 = \lambda_1^2\lambda_2^2 - 1$. Equivalent to making $I_1 = 0$ in absence of in-plane deformation, and $I_2 = 0$ in absence of in-plane area change

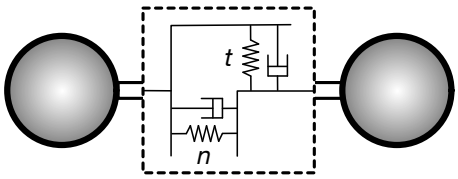

Figure 3: Two discrete particles connected via spring-dashpot system for normal (n) and tangential (t) components of bond deformation. Variations of the method can neglect damping but may use nonlinear springs to better represent the properties of a given material. Similar models can also be used for contact dynamics between distinct bodies that collide.

whose motion due to a given load $\mathbf{F}$ is governed by Eqn. 1 where $\mathbf{X}$ contains the nodal displacements for each degree of freedom. Within the FE settings, the gradient of nodal displacements provides the strain tensor within the element, the constitutive relation provides elemental stress tensor from strain tensor, and the divergence of elemental stresses provides nodal forces $\mathbf{F}$.

3.2. Implementation of discrete approaches

Discrete approaches use a set of points that form 2D or 3D networks representative of a surface or a volume, conceptually similar to modelling in molecular dynamics. These networks are usually of triangular arrangement for biological tissues, as studies have shown it to be the most representative [37]. Each particle is connected within the framework to other particles via springs or bonds as shown in Figures 1 & 3. By changing the constitutive relation between load and deformation, the material properties of the object can be modelled. Additional connections can be added between faces (created by three particles) to replicate bending resistance [15]. In addition, contact forces between unconnected particles that collide can be included, providing the capability to model interaction between separate solid bodies such as valve leaflets [38].

By modelling individual particles, these models can capture small defects within the system to a greater extent than a continuum method. This capability lends itself particularly well to investigation of disease progression in a range of applications such as malaria [39]. However, since even a small object such as a red blood cell consists of a very high number of particles, discrete methods can in general have prohibitively high computational power requirements for all but the smallest of objects. So called *coarse-graining* of these high resolution models has allowed objects to be represented via a smaller number of particles which in turns enables larger objects to be modelled using reasonable computational resources. However, a trade off occurs in the level of coarse-graining required to reduce computational resource requirement and the ability to model the same full resolution behaviour.

3.3. Material Models

The deformation of biomaterials is represented predominantly by models with reversible behaviour to reflect the periodic nature of the cardiac cycle. These include the simplest linear or Hookean elasticity used in early cardiovascular structure models, the simplest nonlinear or neo-Hookean elasticity, and a number of tailored nonlinear elasticity models, such as Mooney-Rivlin, Fung [28] and Skalak [31]. Such models are applied to particular structure, e.g. red blood cell membrane, artery wall, etc., to calculate its deformation under given load conditions.

Notably, the linear elasticity is attractive due to its simplicity of implementation and computational speed, but its application is limited to very small deformations.[1] This is not sufficient for representing deformation of a biological material in most cases, hence the development and use of more suitable constitutive relationships.

[1]It can be demonstrated that the accuracy in calculating the strain using a linear elastic model is equal to that of the accuracy in approximating $\mathbf{ln}(\mathbf{1}+\mathbf{x})$ with $\mathbf{x}$, the larger the strain or $\mathbf{x}$, the larger the error.

The class of nonlinear elasticity models used for deformation of biological tissue is known as hyperelastic materials. For these, the stress-strain relationship is nonlinear but irreversible processes such as plastic deformation are prohibited, restricting the modelling capability to pre-growth and rupture phenomena. Physically, this means that an increase in stress does not produce the same increase in strain, but on removal of stress the material returns to the initial configuration. The stress-strain relationship of hyperelastic materials are derived from a *stored energy potential*, which in the most general case is a function of the deformation gradient.

Many cardiovascular structures demonstrate anisotropic properties due to their structure, i.e. fibre dispersion through the tissue. It is widely accepted that these properties must be included within any material model in order to provide an accurate representation of the structure. However in some studies where the deformation of the structure is not the focus such as medical device evaluation, isotropic models can be implemented as a first step for simplicity.

Through experimentation is has been demonstrated that some cardiovascular structures such as the myocardium are viscoelastic in nature [40]. However, the significance of this property is debated due to the increased complexity of the model and the relative contribution of viscous effects to the overall deformation of the structure. As a results models incorporating strain-rate dependence have only recently been regularly included in studies where the viscoelastic nature of the cardiovascular structure isn't the main focus. It is also acknowledged that additional experimental testing of phenomena such as hysteresis and creep to validate viscoelastic models is needed but poses a significant problem due to the change in characteristics of tissue samples *in vitro* [29].

A number of material models have been developed and integrated into computational modelling procedures of the cardiovascular system. Some have been adapted from models developed for other applications while some have been specifically developed from experimental testing of biological tissues. Figure 1 summarises the range of length scales and applications that the major material models have been used while Table 1 defines a selection of these models in terms of strain energy distribution functions and invariants, giving in turn a brief description and the intended application. Figure 2 compares the stress-stretch relationship for each of the models and demonstrates how they can be adapted based on the parameter values chosen to fit a given dataset [25]. Details of stress-strain energy function derivation can be found in Bonet & Wood [41].

3.3.1. Fluid-Solid-Growth Models

Recently there has been increasing interest in simulating remodelling of cardiovascular structures through the use of fluid-solid-growth models (FSG). In order to overcome the issue of concurrently accounting for effects occuring over disparate time-periods, these models incorporate multiple time scales. A small time scale, of the order of seconds, employs a fluid-structure interaction model to predict remodelling stimuli metrics such as tensile stress and wall shear stress. These values then are fed into growth and remodelling models which operate on much longer time scale, of the order of months [6]. FSG models redefine geometry, initial conditions and material properties that are then used in the short time scale FSI model. Applications where FSGs have been implemented are discussed later in Section 4.3.1, although specific details are beyond the scope of this review. For further details readers are directed to the following reviews [42, 43] and major studies [44, 6, 45, 46].

4. Review of Structural Modelling

This section provides an in-depth review of the application of different structural mechanics models to different components of the cardiovascular system and pathologies. These components occupy a broad range of physical scales and therefore it is not surprising to see a variety of modelling methods applied. Each of the strands examined has in general evolved independently of others, reflecting the tendency of a researcher or group to focus on one of these topics in relative isolation. As such, the simultaneous review of these factors provides the reader with the opportunity to identify common challenges and solutions; offering the potential for knowledge transfer from one area to another.

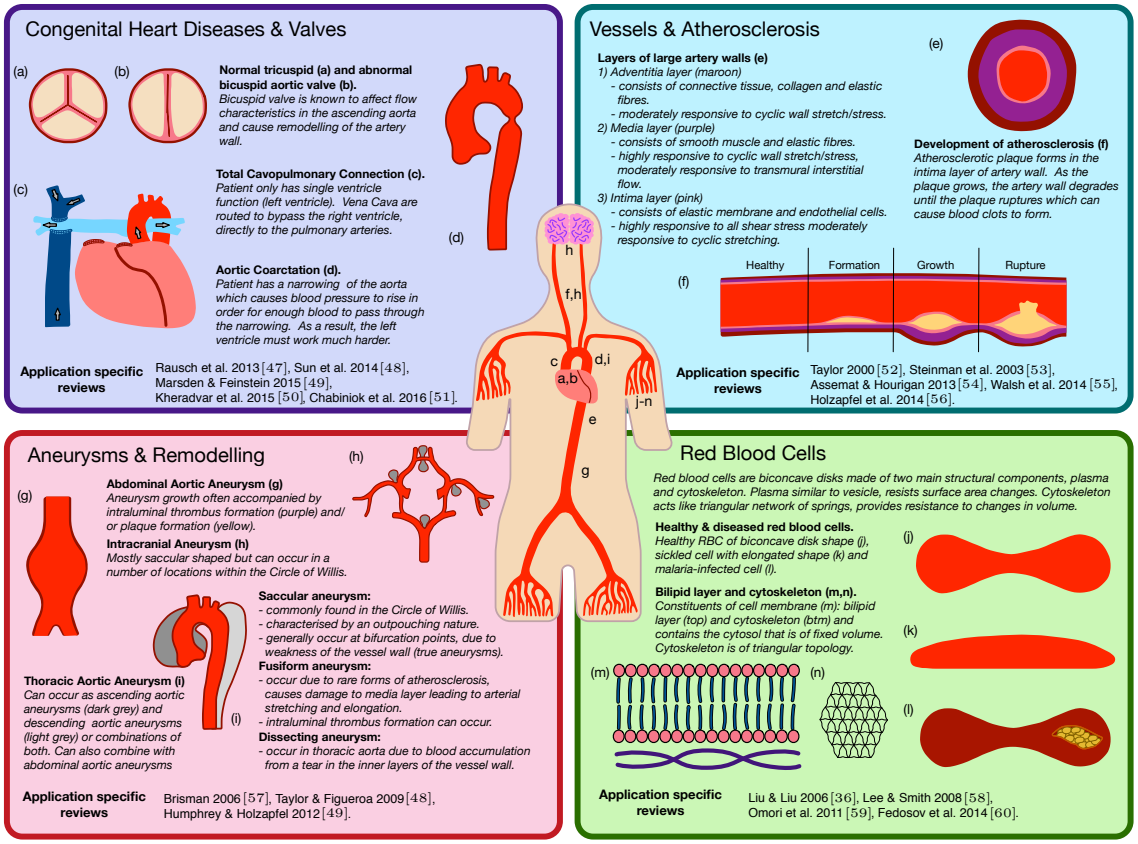

Figure 4: Overview of cardiovascular applications included within this review: applications are classified within each subheading in Section 4 and an basic description of the physiology of the application is given in each case. Previously published reviews that are specific to a given application are highlighted for each classification.

An overview of the four areas considered is given in Figure 4, providing also basic physiology in order to supplement details of modelling method progression. Given the broad scope of this review, it has not been practical to evaluate each area in exhaustive detail. Instead we refer the interested reader to a series of more focused reviews, which are listed in Figure 4. In turn, these papers can provide greater insight into the specific modelling developments in each area.

4.1. Heart

Efficient heart function is dependent on a number of factors, including the performance of the left ventricle walls in ejecting high velocity flow through the aorta. Subtle changes in the flow within the chamber can strongly influence changes in the structure of the chamber walls, for example hypertrophic cardiomyopathy, which can reduce the efficiency of ejection of blood from the left ventricle due to the enlargement of the heart wall.

The heart undergoes a strong cyclic deformation driven by electrophysiological actuation, whereby muscle walls are effectively forced and valves are somewhat passive - in that they are actuated as a result of proximal pressure differential. As a result, much of the recent research focus has been placed on developing electro-mechanical methods (rather than FSI methods) capable of accurately reproducing deformation profiles during the cardiac cycle [61]. This usually consists of a passive myocardium model and an active contraction model. A detailed review of these models was conducted by Trayanova [62]. Here the focus will be the modelling of passive mechanical properties.

4.1.1. Myocardium

The walls of the heart consist of three different layers; endocardium, myocardium and epicardium. Both the endocardium, the inner most layer, and the epicardium, the outer most layer, are thin membranes and therefore generally not modelled directly, although their contribution to residual stress is often included [30]. As a result, the attention of the structural modeller is focused on the myocardium which is made up of sheets of parallel myocytes in which the majority direction of fibres varies from

Later, shear experimental testing of porcine [40] and human [63] myocardium, found the passive mechanical properties of myocardium can be classified as nonlinear, orthotropic and viscoelastic. Holzapfel & Odgen [30] developed a constitutive relationship that replicated the orthotropic nature of the material based of the directions of the fibre, sheet (perpendicular to the fibre) and sheet normal. This model was able to closely replicate the results from shear tests conducted by Dokos et al. [40], whereas transversely isotropic models had been unable to match. However, it neglected viscous effects resulting from blood flow through the myocardium, stating that they could be neglected due to the short time frame of the cardiac cycle.

Later studies extended the Holzapfel & Odgen model to include viscoelastic effects identifying its contribution to applications such pacemaker lead penetration of ventricular walls [64, 65]. In these studies, the authors focused on developing a framework for viscoelastic models to be implemented rather than a specific model. Cansiz et al. [29] coupled the hyperelastic Holzapfel & Ogden model in parallel to a viscous model. The resulting constitutive model showed excellent agreement with the shear tests of Dokos et al. and also when used to model a generic biventricular heart model, this approach demonstrated a marked difference compared to using the hyperelastic model alone; demonstrating the necessity of including viscous effects.

Patient-specific geometries have been modelled using MRI and CT scans [66]. Krishnamurthy et al. [67] used CT scans to create an end-diastole geometry of the left ventricle for a specific patient before using MRI data from a donor heart to include fibre orientation details within the model. This semi-automated method was tested for five patients and was shown to give good agreement in parameters such as ejection fraction and peak cavity pressures.

The vast majority of studies have employed finite element methods to model the heart walls, and have been integrated into various multiphysics models [61, 51]. However, a recent study has modelled human atrial tissue using a discrete element model integrated into an electro-mechanical method citing the limitations of modelling the tissue as a continuous medium and therefore neglecting cell arrangement [68]. By *clumping* particles together to represent a cell as showing in Figure 5, changes in cell arrangement can be investigated. The use of discrete methods at such large spatial scales demonstrates the potential of using these methods in other large scale cardiovascular applications.

4.1.2. Congenital Heart Disease

Fluid-structure interaction is well known to be a critical factor in a number of congenital heart diseases. Congenital heart disease refers to a group of heart defects that occur at birth. These include incorrect function of a single ventricle, tetralogy of Fallot (a hole between the ventricles), aortic coarctation (a narrowing of the aorta), and transposition of the great vessels. All of these defects have been studied numerically from a haemodynamic perspective [69, 70, 71], but fewer studies have been conducted using FSI methods. However, such studies has been proven to have a major role in simulating and preventing the development of subsequent structural defects and recent reviews have begun to explore the implementation of numerical modelling in clinical practise of CHDs [72, 73].

Single ventricle patients are treated using a procedure independently developed by Fontan and Kreutzer, known as a total cavopulmonary connection (TCPC) [74]. It involves routing the superior and inferior vena cava directly to the pulmonary arteries, bypassing the heart therefore requiring only a single ventricle to provide the energy for the entire system. Initial FSI studies of TCPCs used idealised geometries with the hyperelastic Ogden model [75] for arterial wall stiffness [76, 77]. It was found that the use of flexible arterial walls instead of rigid walls results in significant differences between power efficiencies, a key metric in determining the suitability of circuit design and therefore the ability of the adapted cardiovascular system to operate appropriately. Further studies have extended the

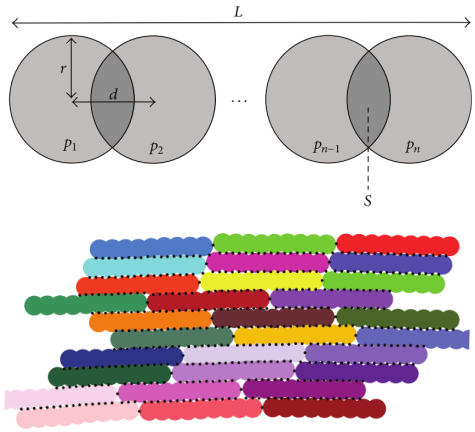

Figure 5: A discrete element method approach to modelling human atrial tissue using *clumping* of particles to create cells. Clumps are treated as rigid during each timestep, therefore the position and velocity of a clump is affected by surrounding clumps. The deformation of a single clump is modified prior to each timestep according to the electrical and mechanical behaviour of a single cell. Simulation results were able to capture local effects caused by varying cell alignment within the tissue [68].

capabilities of CHD modelling, including patient-specific geometries [78], variable wall properties [79] and hyperelastic stiffnesses. In particular, the integration of variable wall thickness by Long et al. [79] via a model based upon measured thickness at the inlet and outlets of the geometry and applying Laplace's equation to determine the thickness of the interior, is of particular interest since the issue of wall thickness exists across a number of cardiovascular applications including that of aneurysms.

Aortic coarctation has been investigated extensively using numerical modelling. However, the majority of these studies have focused solely on the haemodynamics of the problem [80, 69]. Some studies have included the structural response in an aortic coarctation [81] but the application has not been the full focus of the investigation, rather the modelling procedure.

4.1.3. Heart Valves

Heart valve defects are another common congenital heart disease. The most extensively investigated using numerical methods are those in the left side of the heart; the mitral and the aortic valves [82]. The aortic valve can sometimes develop as bicuspid rather than tricuspid as is usual. This can cause abnormal flow patterns to be ejected from the left ventricle, resulting in undesirable flow characteristics downstream and remodelling of the aortic wall to occur [83]

Since the main function of valves is to control the flow of blood, it is inherently a fluid-structure interaction problem. However, many studies looking at artificial valves model the valve leaflets as rigid since they are made from stiff materials and instead focus on the haemodynamic effects [84, 85] or have described the behaviour of the valve and neglected the interaction with blood [86, 87]. In order to simulate the characteristics of heart valves under various conditions, constitutive relations have been developed [88, 89]. May-Newman et al. developed a relation specific to the mitral valve while Billiar et al. presented a relation specific to the aortic valve [90]. Both relations describe large deformations and nonlinear behaviour of the cusps. However, the mitral valve relation describes the material as transversely isotropic and the aortic valve relation describes the material as highly anisotropic, caused by the fibre arrangement with each valve. The techniques used to develop these constitutive relations are different. May-Newman et al. used a method proposed by Humphrey et al. [91, 92] where the relationship is derived from experimental data whereas the method used by Billiar et al. developed the relationship from the characteristics of individual components of the tissue which then combine to give the properties of the material [93, 94].

Through the development of these models, the performance of bioprosthetic and mechanical valves can be improved. In addition, greater understanding of the pathogenesis and effects of various diseases of heart valves can also be obtained.

4.2. Vessels

The primary motivation for simulating large arteries is to study various diseases that develop within their structure, including atherosclerosis and various types of aneurysms (discussed in detail in Section 4.3). In order to model these diseases accurately, a model of a healthy vessel must first be defined. The modelling of large vessels has traditionally been restricted to utilisation of continuum methods. This is due to high computational demand of particle based methods that has been unattainable for efficient simulation using reasonable resources for a large number of particles required at such scales. With the use of parallelisation methods and ever improving computational resources, the use of particle methods has become less limited and may in the future be used to simulate the mechanics of defects in large arteries.

Artery walls are anisotropic in nature. However, isotropic models much as the neo-Hookean and Mooney-Rivlin have been shown to give reasonable representations. Anisotropic models such as those proposed by Holzapfel et al. [27, 26] require details of the arrangement of fibres within the wall which has traditionally been obtained *in-vitro* with varying degrees of difficulty depending on the artery location. However, recent improvements in imaging fidelity (MRI) have allowed fibre orientation to be identified via an automated process [95, 96, 97].

The model developed by Holzapfel et al. consisted of a 3D two layer framework for modelling a healthy aorta [27] to simulate passive time-dependent stress and deformation states under various loading conditions. The process included viscoelastic, nonlinear mechanics, suited to an FE method, and allowed material properties to to be modified for a specific mechanically relevant arterial layer. This model was developed further via a new constitutive relationship describing the passive mechanical response of arterial tissue [98].

A strain energy function developed specifically for aged arteries found that arterial stiffening with age is caused by changes in the collagen arrangement in the artery wall rather than changes in elastic properties of the arterial wall as previously thought [99].

4.2.1. Atherosclerosis

It is widely accepted that arterial stiffening is the first key stage in the development of atherosclerosis [100]. This results from the response of white blood cells (WBC) to inflammation caused within the inner artery wall through the accumulation of lipids under the endothelium layer [54]. The presence of atherosclerotic lesions has previously been linked to the formation of intraluminal thrombus due to the disruption of the fibrous cap allowing blood flow to interact with the thromobogenic plaque core [101] and thought to play a role in the pathogenesis of aneurysms [102]. The formation of intraluminal thrombus and atherosclerotic lesions, known as stenosis, obstructs flow within the lumen and can reduce the oxygen supply to downstream tissue. This can lead to angina and in extreme cases, myocardial infarctions. The rupture of atherosclerotic plaques is also known to cause heart attacks and strokes [103]. Although the mechanism under which rupture occurs is not fully understood, mechanical forces and vessel surface conditions are believed to be significant factors [103].

The material properties of atherosclerotic plaques are difficult to measure *in-vivo*. Consequently, models used to simulate these material properties have been developed using *in-vitro* measurements by removing plaques from the vascular system and treating them as a homogeneous material [54]. In addition to this, many studies use mechanical models developed from *in-vitro* atherosclerotic plaques from one location in the cardiovascular system and apply them to another [104]. This is widely regarded as an oversimplified assumption given that the response of atherosclerotic plaques in differing locations have potentially different characteristics in the given physiological conditions of the location as well as differing responses to interventional procedures such as the placement of stents [105]. Holzapfel et al. [56] has stated the need for an *in-silico* procedure to preoperatively measure the mechanical

properties of atherosclerotic plaques in the carotid artery of patients in order to develop constitutive models specific to the carotid artery and to the patient in particular.

Early computational analysis used 2D geometries, both idealised [104] and patient-specific [106], identifying concentrations of circumferential stress in the plaque as playing an important role in plaque rupture. 3D patient-specific geometries were included via a number of imaging modalities e.g. MRI [107], Ultrasound [108] and Computed Tomography [109] after it was found that stresses within the plaque were 3D in nature [103]. External pressure was identified as a key parameter in the rupture of plaque in an early 3D study [110] while the inclusion of residual stress, providing the circumferential stresses in the artery wall (tensile in the outer layer, compressive in the inner [111]) led to the identification of many additional factors such as external loading, geometrical configuration and intra plaque stresses [112]. Residual stresses are difficult to measure experimentally as they must be recorded in-vivo. One method to model the residual stress proposed by Huang et al. [113] is to use an approximation of the initial stresses.

Atherosclerotic plaques have been readily represented using generic hyperelastic models such as neo-Hookean [114, 115] and Mooney-Rivlin [116, 117]. Through such studies, our understanding of the mechanics of plaque rupture has improved. The thickness of the fibrous cap and the size of the lipid core of the plaque are known to determine the risk of plaque rupture [104] however, mechanical stresses and remodelling the vascular structure are also factors. Blood induced stresses have been shown to be more influential in the formation of atherosclerotic lesions in certain locations within a vascular geometry [118].

A popular criteria for rupture of an atherosclerotic plaque is a threshold tissue stress of $300kPa$ with many studies suggesting structural stress has more influence on the risk of rupture than that induced from blood flow (e.g. wall shear stress). However, experimental studies on human arteries have shown this value to vary significantly [119, 120, 121].

A number of FSI models have attempted to simulate the conditions under which a plaque will rupture taking into account mechanical stresses, intraplaque haemorrhages [122], micro-calcifications in the plaque [123] and variations in fibrous caps [124]. It is expected that these models will improve significantly given the recent advancements in obtaining patient-specific data (e.g. experimentally, imaging).

4.2.2. Coronary Arteries

The myocardium is supplied with oxygen rich blood by the coronary arteries; the left coronary artery (LCA) supplying left atrium and left ventricle, while the right coronary artery (RCA) supplies the right atrium and right ventricle along with the atrioventricular and sinoatrial nodes. These arteries are of interest since they are a location prone to development of atherosclerotic plaques, which can reduce heart function.

Modelling of the coronary arteries is not straightforward since they follow the motion of the myocardium during the cardiac cycle. The contraction of the individual heart chambers during the cycle also affects the curvature of the coronary arteries [125] while artery wall compliance has been found in a number of studies comparing rigid wall CFD to flexible wall FSI, to significantly affect wall shear stress distributions and magnitudes.

The coronary arteries are known to be highly anisotropic and nonlinear in character. Holzapfel et al. [26] proposed a three-layer constitutive model specific to coronary arteries based upon the two-layer framework proposed by the same group [27]. This model includes an anisotropic term that contributes only when fibre orientation relative to the circumferential direction is sufficient. This provides a good representative general model for coronary arteries when patient specific data for fibre orientation within the tissue is unavailable.

However, very few models specific to the coronary arteries have attempted to include anisotropic properties, instead implementing isotropic hyperelastic models. This is perhaps due to the focus of many structural investigations of coronary arteries being the development and treatment of atherosclerotic plaques present in the artery. In particular, the deployment of intraluminal stents and their interaction with the vessel wall has been well studied as reviewed by Martin et al. [126]. Isotropic

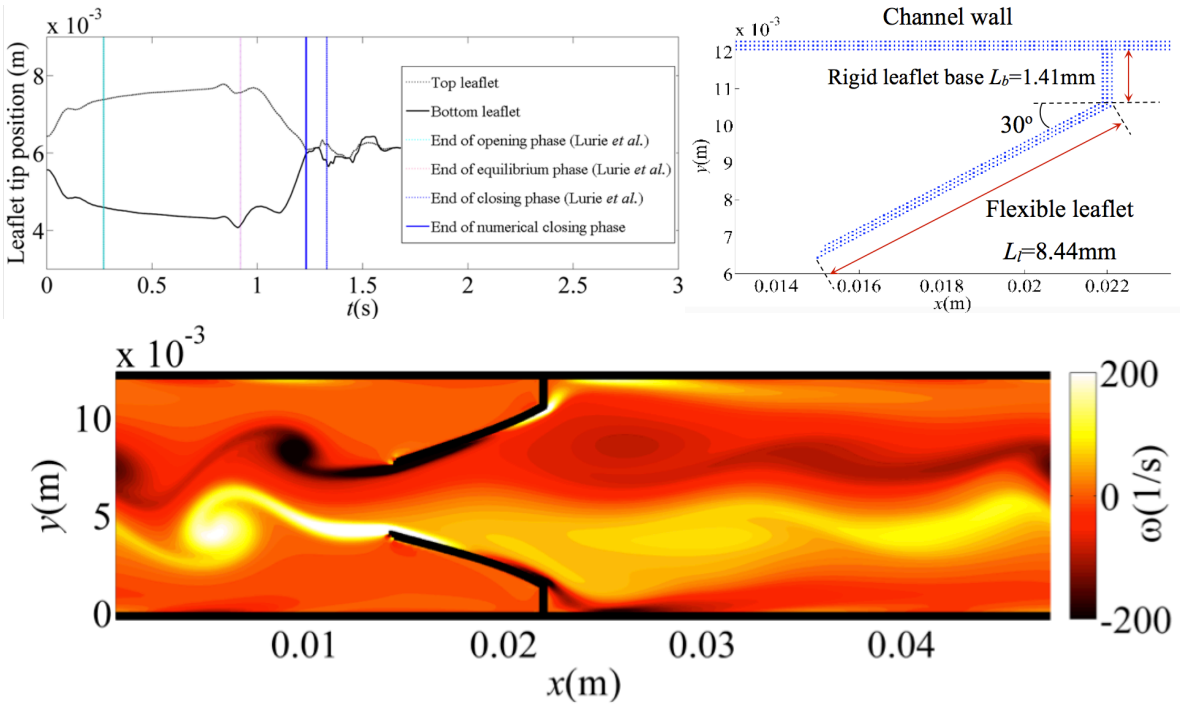

Figure 6: Idealised venous valve study using a vector-based discrete element method as structural solver for flexible leaflets (top right). Deformation profile of the valve compared favourably with experimental observations and was able to match opening, equilibrium and closing phases of the valve cycle (top left). One example of a discrete element method implemented at large cardiovascular length scale [38].

hyperelastic models implemented include variants of reduced polynomial [127, 128] and Mooney-Rivlin models [129].

In studies of stent deployment, the deformation of the stent is also considered, usually via finite element analysis [130, 129]. By modelling the interaction between the stent and vessel, the risk of restenosis of the vessel can be assessed - a significant issue post stent deployment. Patient-specific geometries have been included through the use of intravascular ultrasound [131].

4.2.3. Venous valves

Venous valves are bicuspid in nature and are located to divide veins into smaller segments, allowing blood to be transported back to the heart despite gravitational forces. This is especially important in large veins located in the legs. Here, the two leaflets are attached at the vein wall and have free edges located in the lumen. A sinus region aft of the valve leaflets allows flow that has detached from the valve leaflets to reattach to the vein wall [132]. The structural properties of veins differ from that of arteries, with veins able to experience large deformations, allowing the vein to collapse under external forces supplied by the surrounding muscles and to distend under internal pressures [133]. The sinus region in turn has different structural properties than the rest of the vein wall, allowing larger deformations under pressures experienced during normal function.

The mechanism of valve opening and closing has been studied *in-vivo* using B-flow ultrasound that allows the visualisation of the valve cusps while details of blood flow characteristics can also be captured [134]. Using these imaging techniques, the mechanism for valve opening and closing has been split into four distinct phases [132].

Blood clots can form in areas of recirculation behind the leaflets of venous valves. In deep veins, commonly the legs, this can lead to Deep Vein thrombosis. Given complications of deep vein thrombosis are potentially life threatening very few numerical studies have investigated the disease using structural modelling of the valve. Those that have have mainly focussed on the fluid characteristics with a rigid valve [135] or on the clot formation [136]. Figure 6 shows one such FSI study with flexible idealised valve leaflets using a discrete element structural solver [38]. Results from this study replicated the cyclic deformation profile seen during experimental observations while also producing the stationary flow behind the valve known as the proximal pocket.

Since there are a significant number of studies of heart valve characteristics, one potential avenue for future investigation is to adapt these models to venous valve applications.

4.2.4. Resistance vessels

The components of the cardiovascular system that have been discussed in preceding sections have involved the heart, buffer vessels (aorta and other large arteries) and metabolic vessels (capillaries and red blood cells). These structures have, in general, been extensively studied numerically. However, while they contribute significant amount to the system, there are other less studied structures that will require study in the future, resistance vessels and capacitance vessels.

These are muscular arterioles that regulate blood pressure and temperature through changing the diameter of the lumen. Stenosis can cause improper function of the vessel, causing vascular remodelling which may not always operate efficiently leading to diseases such as hypertension. No computational studies have been found during the literature search conducted in this review. Given the link between these vessels and hypertension, this may be a interesting avenue for future research.

4.3. Aneurysms

Aneurysms are the dilation of an artery wall due to the degradation of elastic fibres and loss of smooth muscle function which also contributes to the expansion of aneurysm diameter [137]. Within the human body, three main types of aneurysm commonly occur, abdominal aortic aneurysms, thoracic aneurysms and intracranial aneurysms. It is widely accepted that all three share the same pathogenesis of degradation of elastic fibres in formation. However, some key factors that have been linked to the cause of AAAs are known not to be a cause of other types of aneurysms. The presence of atherosclerosis is an example; while it has been repeatedly reported as a cause of AAAs [138], it is thought to occur as a consequence of intercranial aneurysms [42]. In spite of this, due to the relative similarity in pathogenesis, advances in the modelling of each type of aneurysm should be considered for their potential general benefit when studying an individual type [137].

4.3.1. Abdominal Aortic Aneursysms & Associated Thrombus

Abdominal Aortic Aneurysms (AAA) occur when the maximum diameter of the abdominal aorta increases by 50% or the diameter is greater than 3.0cm. Computational haemodynamic studies have suggested that the infrarenal aorta experiences reversed flow due to the bifurcation of the aorta into the iliac arteries and has been linked to the dilation of the aorta wall [139]. Around 75% of AAA contain an intraluminal thrombus (ILT) [140] although the contribution of thrombus to aneurysm rupture risk is debated. Some studies suggest it can reduce the thickness of the artery wall in that area [141, 142] while others have claimed the thrombus provides a stress-shield wall [143, 144]. Alternatively, other studies have suggested the presence of ILT can reduce stresses on the aneurysm wall without significantly effecting the location that maximum stress occurs [145]. However, it is widely accepted that the presence of a thrombus increases inflammation which is recognised as a key role in the mechanics of AAA formation [42].

Mechanical properties of AAAs have been measured experimentally in a number of studies in order to improve the accuracy of material models under structural analysis. It was reported that aneurysmal wall tissue is stiffer than that of healthy tissue [146] and biaxial tests were conducted on a large cohort of AAAs (n>25) to develop an appropriate constitutive equation [147]. The mechanical properties of intraluminal thrombus have been less studied. The most extensive experimental study tested a number

of thrombus samples (n=14) uniaxially and determined that the deformation response of the material is nonlinear over large strains and can be described as quasi-isotropic, but highly non-homogeneous with stiffer material located in the luminal region of the thrombus than at its centre [148].

Initial numerical studies used a linearly elastic material model in conjunction with FEM and idealised geometries [149, 150]. Although linear elasticity is considered a crude approximation, these studies were able to establish a number of key factors in rupture risk such as wall thickness. One important development of this procedure was to include hyperleastic material models specific to aneurysmal tissue such as that discussed in Section 3.3. Additional developments include a two-layer model framework proposed by Holzapfel et al. [27] in which the constitutive relationship can be modified depending on the artery in question. These model developments have been incorporated into a number of more recent studies of aneurysmal wall mechanics [145, 151].

Patient-specific geometries have also been included within the analysis using CT scans [152, 2]. These models still include many assumptions such as a uniformly thin wall that will need to be excluded in future studies. However, a major finding in these studies was the correlation between a peak normal stress greater than 440kPa and the rupture potential, demonstrating the potential of the computational analysis in this application.

Given that reversed flow phenomena in the abdominal aorta is thought to be a major factor in the formation and growth of AAAs [153], there has been a push towards developing fluid-structure interaction models capable of simulating the complex conditions for this application. However, the focus here will remain primarily on the structural analysis models that are coupled to the fluid solvers. The majority of developed structural models incorporated into FSI methods are more simple than those used in standalone structural analysis of the aneurysm wall due to computational power restrictions and limitations. Generally, early models have represented the aneurysm wall as linearly elastic, homogeneous, isotropic and with properties that do not change with time [154, 155].

More recent FSI studies [156] have continued to employ similar material models as previous studies, representing the artery wall as a two-layer, isotropic and orthotropic material [27, 152]. The inclusion of patient-specific geometries from non-invasive imaging techniques such as computed tomography (CT) [156] scans and 3D ultrasound (3D US) [157] greatly increases the potential. Using CT scans in particular allows separation of the various components of the structure (artery wall, lumen, thrombus, areas of calcification) which can then be assigned appropriate mechanical properties individually which can then be analysed as a single component or as a system in both fluid-solid interaction and fluid-solid-growth methods. However, many limitations still exist, such as the assumption of uniform wall thickness of 2mm of the aneurysm while it has been found from experimental studies [158] that wall thickness can vary from 0.26mm in location of rupture to 4.26mm in areas of calcification.

Humphrey et al. [42, 137] identify that in order to correctly account for structural variations during aneurysm growth, it is necessary to develop a class of fluid-solid-growth models which are capable of accounting for disparate time-scale effects in a concurrent approach. Here, traditional FSI methods are incorporated within the FSG framework to predict the long term effects of disease based upon short-term predictions from a modelled cardiac cycle; i.e. the simulation becomes multi-scale. In this framework a mathematical model was developed by [44] based on a two-layered, cylindrical membrane using nonlinear elasticity and the constitutive model developed by Holzapfel et al. [27] to describe the stress-strain relationship. The approach was used to demonstrate formation of an aneurysm in an initially healty aorta via structural remodelling equations employing a prescribed degradation of elastic within the structure wall. While the model omitted a number of key features, such as the presence of ILT or calcification, and was limited to idealised geometries, it provided an important proof-of-concept. Fluid-solid-growth models are currently a topic of active development within a number of areas [6, 159, 160], having evolved somewhat further than the original method. To date they generally assume the artery wall to be a uniformly thin structure (membrane), limiting somewhat the scope of the model, although Grytsan et al. [46] have developed a more sophisticated method wherein a thick walled FE aneurysm model [161] is coupled to the FSG framework.

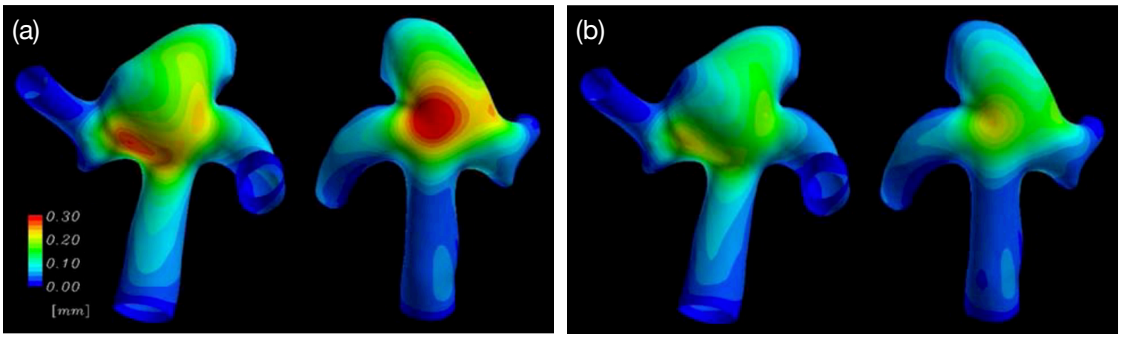

Figure 7: Comparison of (a) linear elastic and (b) nonlinear elastic constitutive relationships for the total deformation magnitude of a patient specific intracranial aneurysm. Profiles are qualitatively similar demonstrating the capability of linear elastic models given the easier implementation. However, the magnitude of maximum displacement of the nonlinear model was found to be 36% lower than the linear elastic model highlighting that for high-fidelity studies, nonlinear models should be used and the high significance of the constitutive model implemented [162].

4.3.2. Thoracic Aneurysms

While Thoracic aortic aneurysms (TAA) are relatively rare - with around 0.006% of a given population each year [163] - they can be catastrophic, with a 5 year survival rate less than 20% [164].

Statistical approaches were initially used when investigating the biomechanics of TAAs. Rizzo et al. [165] used clinical measurements to develop growth rate estimates using an approach known as instrumental variables estimations, an improvement upon conventional methods which were susceptible to a number of measurement errors. These methods have also been applied to other types of aneurysms [166] however, they cannot provide a patient-specific decision for surgical intervention and therefore numerical models have become increasingly popular.

Since TAAs are not as common as other types of aneurysm, they have not been as extensively researched. However, given that they occur in the aorta like AAAs, many of the same computational models can be adapted for TAA use.

Experimental studies on the mechanical properties of TAAs have compared aneurysmal and non-aneurysmal ascending aortic tissues, concluding that formation of the aneurysm is linked to the stiffening and weakening of the aortic wall [167]. Techniques have also been developed to produce patient-specific geometries from various imaging modalities [168]. Borghi et al. [169] proposed a new method of combining patient images obtained through MR with different levels of detail and resolutions in order to obtain good representations of all the important cardiovascular structures e.g. lumen, thrombus and wall. The geometries generated through this method were compared against those obtained from a single dataset with higher stresses found in coarser models. This method was used in further studies [20, 170] including a fluid-structure interaction, finite element study of three patient-specific geometries using a commercial solver, ADINA and a thrombus material model [148] . Results from these studies demonstrated that aneurysm shape and thrombus distribution have a significant effect on wall stress distribution and magnitude and that aneurysm diameter and maximum wall stress are not related.

An additional cardiovascular defect associated with TAAs is aortic dissection. This occurs when the haemodynamic loading on the aneurysmal wall is greater than the adhesive forces between the artery wall layers. Similarly to TAAs, aortic dissection is a relatively rare defect, however a strong link has been made between the congenital heart defect, bicuspid aortic valve (rather than tricuspid), and aortic dissection [171]. Numerical modelling of this defect has found that the difference in valve morphology and the elastic material properties leads to abnormal flow conditions and discontinuous high wall stress resulting in defects between arterial layers [172].

4.3.3. Intracranial Aneurysms

Intracranial aneurysms are commonly of the saccular type and therefore known as intracranial saccular aneurysms (ISAs). Mechanical risk factors are generally accepted as playing key roles in the pathogenesis of ISAs. Since arteries in this area do not have the external elastic lamina of larger arteries and they have less perivascular tissue supporting them, there is increased risk of local weakening of the artery wall under non-ideal haemodynamic conditions. This issue is exacerbated further by the irregularity of the bifurcation region. The rupture of an intracranial aneurysm can be simply summarised as the presence of mechanical stress greater than that of the strength of the vascular wall. In practice, evaluating the critical stress is not straight forward since the distribution and magnitude is affected by three key factors: geometry, material properties of tissue in the aneurysmal region and the applied loads.

ISA walls were initially modelled mathematically as well as their associated hemodynamics [173, 174], which were validated experimentally via glass tubes [175, 176]. These mathematical models included representation of the aneurysm wall via electrical circuits [173]. Results from these studies include the estimation of a critical atherosclerotic lesion diameter [174] and the identification of two geometric parameters relating to orifice size affecting rupture potential [177]. These mathematical models also identified daughter aneurysms as a significant rupture risk factor in intracranial aneurysms but had severe limitations including the inability to model material elasticity and restricted to idealised spherical geometries as a result of utilising the Law of Laplace [178, 177].

Early numerical approaches were also hindered by oversimplified assumptions such as linearly elastic behaviour of the artery walls. These assumptions were removed through the use of nonlinear FEM [179, 180] which implemented the constitutive relationship developed by Humphrey et al [181] that is generic to biomembranes. These studies used an idealised axisymmetric representation and like many methods where an idealised geometry is used, while they can provide validation and qualitative results in order to improve understanding of the problem, they cannot be used to model the most complex characterisations. However, these models did highlight the shortcomings of a critical lesion diameter, identifying the shape of the aneurysm rather than the size as a critical risk factor. In particular, they found that smaller lesions with a large neck to height ratio have much greater stresses than large lesions with a small neck to height ratio. [182, 183].

Two main material models are implemented, Fung-type strain energy density functions [184] developed for artery applications and Skalak-type strain energy functions [31] developed originally for red blood cell membranes. However, some studies also implemented the Mooney-Rivlin model [185]. Torii et al [162] compared the relative performance of linearly elastic and hyperelastic models in modelling artery and aneurysm walls as part of FSI methods as shown in Figure 4.3.1. It was found that the hyperelastic model produced structural deformations up to 36% smaller than linearly elastic models. However, the areas where maximum deformation occurred were consistent in each case suggesting that both types of wall models can be implemented.

In recent years, similar to modelling of AAAs, patient-specific geometries have been obtained through CT [186, 187] and MRI scans [188]. However, while these studies provide useful insight into the conditions experienced in an aneurysm, the computational and financial cost have significantly limited its use in clinical practice for monitoring aneurysm development through in silico methods. Research has also focused on the modelling of artificial devices placed within aneurysms such as stents and coils [189, 190]. Minimally invasive aneurysm repairs such as endovascular grafts (EVG) also known as stent-grafts have applications in AAAs and the thoracic aorta as well as in intercranial aneurysms [172, 191]. The stent can be either ballon expandable or self-expandable and is generally modelled as a linearly elastic material whereby the material properties such as Young's modulus, are measured experimentally [172]. For balloon expandable stents in particular, modelling the material as linearly elastic can be an oversimplification since they are often plastically deformed by the balloon once expanded.

The family of fluid-solid-growth models described in sections 3.3.1 and 4.3.1 have also been applied to cerebral aneurysms, under similar assumtions and hypotheses as for the AAA cases [192, 45]. Given the predictive potential of such approaches to quantify risk *prior* to aneurysm formation, this can be

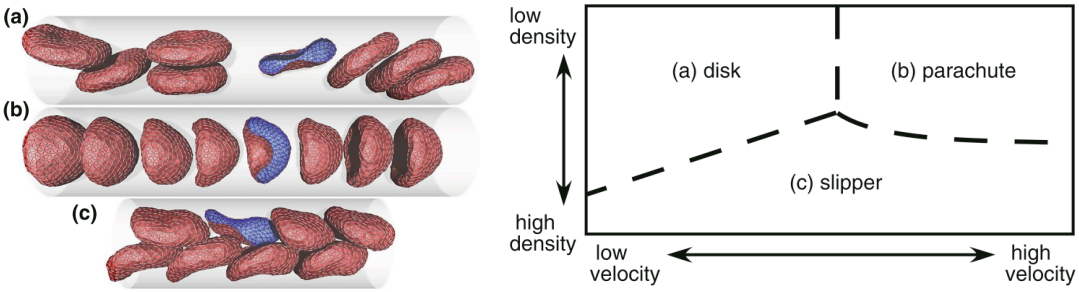

Figure 8: Coarse-grained worm-like chain model (discrete) representation of multiple RBCs subjected to various flow conditions. Method reproduced disk, parachute and slipper shapes observed experimentally (left) when flow velocity and fluid density was modified (right) [60].

considered to be an important area for ongoing study, and indeed a number of research groups currently work on refinement of FSG models for cerebral applications. It should however be understood that these approaches remain quite conceptual as their validation is particularly challenging given the long time-scales involved.

4.4. Red Blood Cells

The red blood cell is of particular interest for study for a number of reasons. Firstly, it has a relatively simple structure in comparison to other cells [193]; it is nucleus free, the cytosol contained within the membrane is of fixed volume and known viscosity [13]. This allows the mechanism of how the cell membrane converts mechanical forces to biological responses to be studied along with how structural, chemical and biological signals affect the response of the cell membrane. It also has a relatively simple shape and is axisymmetric when undeformed, allowing the development of computational models [194]. In terms of contribution to fluid characteristics, RBC are the most abundant constituent in plasma by volume and it is the deformation of the RBC that provides the shear-thinning of blood and it's non-Newtonian property [4].

An in depth review of the current state of the art for RBC modelling applications was published by Fedosov et al. [60], including the fluid solvers used in various numerical studies and the significance of findings from each. Here focus is maintained on the structural models. Red blood cells belong to a group of structures known as deformable particles. Deformable particles can be divided into three main groups: capsules, vesicles and red blood cells [195].

Capsules and vesicles are often modelled as a simple representation of the red blood cell. Comparison of results obtained using all three types of deformable particle allow improved evaluation of the importance of various cell material properties to flow characteristics. Initial attempts to model the deformation of a RBC were analytical using a capsule model [196] or axisymmetric shape [197]. These solutions could therefore only provide qualitative characteristics to problems, but since accurate RBC membrane rheology could be integrated, they can also be used to validate computational models [198].

According to Fedosov et al. [60], in order to realistically model the mechanics of a red blood cell, the membrane viscoelasticity (viscous contribution from lipid bilayer and elastic contribution from the spectrin network) and bending resistance must be accounted for along with the individual viscosities of the external (plasma) and internal (cytosol) viscosities. RBC structure has been modelled using both continuum and discrete methods. Continuum methods treat the lipid bilayer, cytoskeleton and cytosol as homogeneous materials using membrane and viscous stresses to determine RBC motion and deformation. In contrast, discrete based methods generally represent the cytoskeleton with a set of points that form a 2D or 3D triangular network. These points are related via various spring models to govern the deformation of the RBC.

4.4.1. Single Red Blood Cell

Evans et al. [199] proposed a 2D linear continuum model for the red blood cell membrane to study the deformation of an axisymmetric cell in response to flow. Using this model, the teardrop formation of an attached RBC was reproduced. An improved continuum model represented the RBC structure as a 2D shell (zero thickness) via finite elements [200]. Within this model, the constitutive relationship could be changed to suit the given application although neo-Hookean was used most commonly due to its simplicity [201].

Early discrete models focused on the structure of the cytoskeleton, modelling the surface of the cell using a triangular mesh with each vertex a six-fold junction [202, 203] connected via a Hookean or neo-Hookean springs. The triangular mesh assumption was based upon observations from a number of studies on the general structure of the cytoskeleton [37]. The topology of diseased or ageing cells is less consistent with four and five fold junctions present and therefore limited studies to healthy cells.

Improvements to the modelling of the mechanical characteristics of the cytoskeleton and in particular the behaviour of the spectrin network, involved the replacement of springs with a chain and bead network [203]. The chain and bead model prevented the cytoskeleton from extending unbounded as was possible with the linear spring models, through constraining the distance between beads. The model agreed qualitatively with experimental data for some shear modulus measurements. However, again the network was strictly six-fold and therefore was unable to provide results for diseased cells given the variation in topology of diseased cells.

The worm-like chain (WLC) model was an extension of the chain and bead model [204]. The WLC method had previously been used extensively in the study of DNA and other proteins since is its proposal by Marko & Siggia [205]. This approach includes the effect of a random spectrin network (not strictly six-fold) and the curvature of the lipid bilayer and gave close agreement with experimental data. Through coarse-graining this model, deformation of an entire 3D RBC cytoskeleton to be simulated with 100,000 spectrin in the network, consistent with microscopy observations [206] using a single desktop computer [14].

4.4.2. Multiple Red Blood Cells and Disease

Numerical study of RBCs tended to either model a single cell in high detail or multiple cells as highly simplified representations, often with little or no deformability [207]. However, coarse graining of high-fidelity models as well as an increase in obtainable computational power has resulted in rise in studies of multiple cells. This has enabled the effects of diseased cells to also be studied via numerical methods and the design and validation of microfluidic devices that can give further insight into various diseases [22]. One such example of coarse-graining existing models was developed by Pan et al. [208] based upon the original model of Fedosov et al. [13]. These methods have also been used to study RBC aggregation and the study the different deformation phases of multiple RBCs when subjected to various flow conditions as shown in Figure 8.

Many types of haematological disorders include the stiffening of RBC membrane. In order to accurately model the effect of diseased cells within a population of healthy RBCs, the multiphase nature of blood must be accounted for.

Sickle cell disease is a group of genetic disorders caused by sickle haemoglobin in the red blood cell [209]. The sickle haemoglobin causes the cell to deoxygenate, known as hypoxia, resulting in the change of shape associated with the disease. This shape change can damage the membrane of the cell, causing it to rupture. Multiple sickle shaped cells are unable to flow as readily as the healthy biconcave shape, leading to blockages in smaller vessels such as microcapillaries. These blockages can result in vasoocclusion and organ damage. Sickled RBCs have significantly larger shear moduli than healthy RBCs [210]. Lei et al. [211, 212] developed the first 3D multiscale model of sickled RBCs to capture heterogeneous nature of both realistic cell shapes and haemodynamics. The shape of the sickled RBC was developed using images taken using scanning electron microscopy. A surface tension was applied to the healthy RBC model, distorting the shape until it matched that obtained via imaging and a new equilibrium shape was defined for the model. Results of this study found that the cell morphology influences the shear viscosity with the granular shape increasing viscosity the most.

It has been shown that malaria infected RBCs have membranes that are stiffer than those of healthy RBCs. The invasion of the parasite plasomodium falciparum into RBCs occurs in the majority of malaria patients and causes the shear modulus to increase by an order of magnitude [213]. This limits their ability to deform in narrow capillaries, leading to reduced flow, clot formation and can cause complete blockages of the vessel lumen. The computational requirement of diseased RBC simulation is relatively high due to the low numbers of diseased RBCs within an RBC population. As a result, a large number of cells must be modelled in order to accurately represent the interaction between the majority of healthy RBCs and the minority of infected RBCs [214]. The effect of including the parasite structure within the RBC membrane has also been studied [215] and found that early ring stage malaria infected RBCs behaved similarly to healthy RBCs, flowing through vessels with diameter less than their own through deformation, while later stage infected RBCs could not, causing flow occlusion. However, the parasite structure was modelled as a rigid body and the author suggested a deformable representation of the parasite would improve the model. Some numerical studies of malaria infected RBCs have been motivated by the need to validate experimental devices that can be used to separate diseased cells from healthy ones [216, 22] based upon the changes in flow path with increased membrane rigidity.

5. Summary and Discussion

The purpose of this review is to provide an introduction to the field of cardiovascular structural modelling through an overview of the material models and discretisation methods implemented to numerically investigate various cardiovascular applications. A synopsis of the key modelling developments has been conducted, providing a basic understanding to each of these fields in order to improve reader access to specialised literature. A selection of the most important studies in each of the areas considered are summarised in Figure 9 as a timeline demonstrating the progression of cardiovascular structural modelling. The figure portrays an evolution in complexity of modelling of the cardiovascular system over the past 20 years and evidences an increasing trend towards FSI modelling.

The majority of studies employ continuum methods, particularly for larger length scales such as vessels and heart applications. For simulations of physical structures at larger scales, the efficiency of particle-based methods is generally much lower than continuum methods, due to the number of particles required to represent a given structure. There are a few exceptions to the rule such as venous valves [38] and atrial tissue [68] where simple discrete models have been implemented. In addition, coarse-graining of DEM models has allowed a larger number of structures to be represented in a single simulation. However, discrete methods require significant development from their current state in order to capture the properties of different layers and fibre orientations within the tissues.

In general, it appears that the majority of structural models incorporated into FSI methods are more simple than those used in standalone structural analysis of vascular structures due to computational power restrictions and limitations. However this trend is starting to shift, as partly evidenced by Figure 9; increasingly multiple material models and possibly also a combination of DEM and FEM will be needed to more efficiently and accurately model processes in the cardiovascular system.

In Section 3.3, the strain energy density functions of many commonly used material models are shown to be extensions of the incompressible neo-Hookean model. A comparison study has shown that in the case of aneurysm wall shear stress, changing the material model has minimal effect [162] as shown in Figure 5. This is perhaps due to the relatively low levels of deformation and therefore small differences caused by changing the material model. However, this may not be the case for all applications such as RBC deformation where larger deformations occur. The modeller therefore must make an assessment in order to find a suitable compromise between ease of implementation and the required level of detail for their specific application.

Another interesting development is the impact that emerging computer hardware such as GPUs is having on model development. Access to and use of GPUs has increased dramatically over the past decade, and discrete method algorithms are well suited to GPU acceleration since they contain a high number of simple calculations rather than the complex algorithm of continuum methods. The

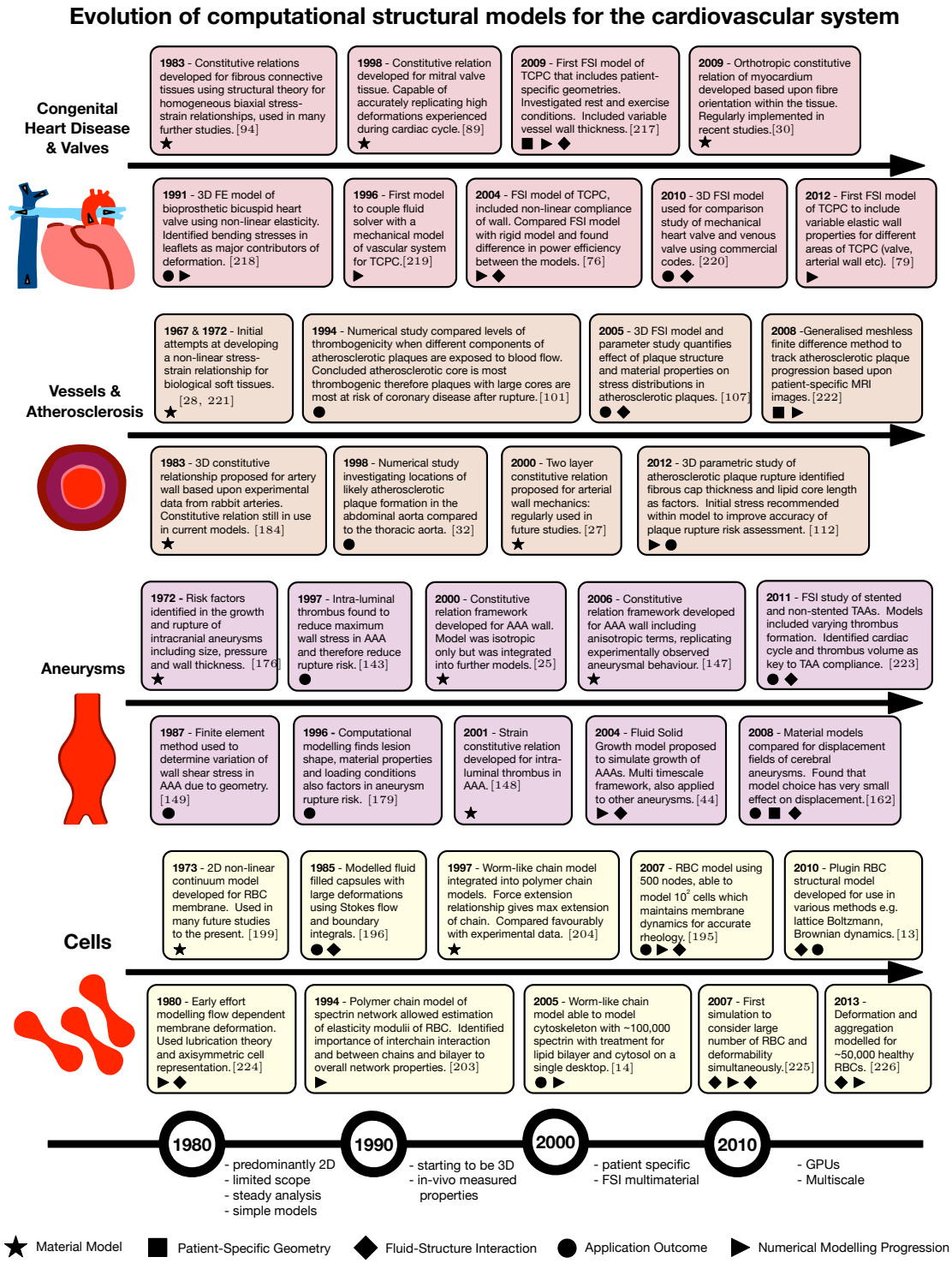

Figure 9: Timeline of a selected major studies published progressing the state of the art of cardiovascular structural modelling. Key features of each study are highlighted including the inclusion of patient-specific geometries and fluid-structure interaction methods.

prevalence of GPU and many-core compute looks likely to play an important role in extending the range of use of discrete methods [68].

Within this review, it has been demonstrated that numerical modelling has been able to improve our understanding of cardiovascular disease, both in terms of pathogenesis and treatment. By investigating the significant developments across a number applications, it has been shown that often the same modelling limitations have affected many applications. Therefore any advancement in the modelling of one application can be adapted to many others, or at least inspire future developments.

Recently the development of multi-scale models, such as the model for aneurysm growth [44], has been identified as critical to improving the understanding of cardiovascular structures and in particular disease progression. While multiscale methods are undoubtedly key, it would seem sensible here to reiterate the importance of developing models that can be included within clinical environments for patient diagnostics and assessment. These models will almost certainly have to be of lower fidelity in order to operate within the time constraints of practical modern medicine. Presently there are many examples of software developments for cardiovascular modelling intended to provide faster insight by trading accuracy with efficiency [227, 145]. In many cases even modest predictive insight may be considerably better than the standard practise.

Acknowledgements This research was supported by the Medical Research Council (MRC) through grant MR/P025463/1 and by the Economic and Social Research Council (ESRC) through grant ES/N01393X/1. BK is supported by a British Heart Foundation (BHF) Personal Chair..

Declaration of conflicting interests

The author(s) declared no potential conflicts of interest with respect to the research, authorship and/or publication of this article.

References

[1] Y. Sui, Y. T. Chew, P. Roy, Y. P. Cheng, H. T. Low, Dynamic motion of red blood cells in simple shear flow, Physics of Fluids 20 (11). doi:10.1063/1.3026569.

[2] M. L. Raghavan, B. Ma, R. E. Harbaugh, Quantified aneurysm shape and rupture risk, Journal of Neurosurgery 102 (2) (2005) 355–362. doi:10.3171/jns.2005.102.2.0355.

[3] J. Biasetti, T. C. Gasser, M. Auer, U. Hedin, F. Labruto, Hemodynamics of the normal aorta compared to fusiform and saccular abdominal aortic aneurysms with emphasis on a potential thrombus formation mechanism, Annals of Biomedical Engineering 38 (2) (2010) 380–390. doi:10.1007/s10439-009-9843-6.

[4] K. Boryczko, W. Dzwinel, D. A. Yuen, Dynamical clustering of red blood cells in capillary vessels, Journal of Molecular Modeling 9 (1) (2003) 16–33. doi:10.1007/s00894-002-0105-x.

[5] A. Hosoi, T. Washio, J. I. Okada, Y. Kadooka, K. Nakajima, T. Hisada, A multi-scale heart simulation on massively parallel computers, 2010 ACM/IEEE International Conference for High Performance Computing, Networking, Storage and Analysis, SC 2010 (November). doi:10.1109/SC.2010.5.

[6] C. Figueroa, S. Baek, C. A. Taylor, J. D. Humphrey, A computational framework for fluid-solid-growth modeling in cardiovascular simulations, Computer Methods in Applied Mechanics and Engineering 198 (45-46) (2009) 3583–3602. doi:10.1016/j.cma.2008.09.013.

[7] P. Di Achille, J. D. Humphrey, Toward large-scale computational fluid-solid-growth models of intracranial aneurysms., The Yale Journal of Biology and Medicine 85 (2) (2012) 217–28.

[8] A. Quarteroni, A. Veneziani, C. Vergara, Geometric multiscale modeling of the cardiovascular system , between theory and practice, Comput. Methods Appl. Mech. Engrg. 302 (2016) 193–252. doi:10.1016/j.cma.2016.01.007.

[9] Y. Zhang, H. Barocas, S. Berceli, C. Clancy, D. Eckmann, M. Garbey, G. Kassab, D. Lochner, A. McCulloch, R. Tran-Son-Tay, N. Trayanova, Multi-scale Modeling of the Cardiovascular System : Disease Development , Progression , and Clinical Intervention, Annals of Biomedical Engineering Engineering 44 (9) (2016) 2642–2660. doi:10.1007/s10439-016-1628-0.

[10] A. R. Zhao, M. L. Field, K. Digges, D. Richens, Blunt trauma and acute aortic syndrome: a three-layer finite-element model of the aortic wall, European Journal of Cardio-thoracic Surgery 34 (3) (2008) 623–629. doi:10.1016/j.ejcts.2008.02.032.

[11] C. A. Figueroa, I. E. Vignon-Clementel, K. E. Jansen, T. J. Hughes, C. A. Taylor, A coupled momentum method for modeling blood flow in three-dimensional deformable arteries, Computer Methods in Applied Mechanics and Engineering 195 (41-43) (2006) 5685–5706. doi:10.1016/j.cma.2005.11.011.

[12] P. Crosetto, P. Reymond, S. Deparis, D. Kontaxakis, N. Stergiopulos, A. Quarteroni, Fluidstructure interaction simulation of aortic blood flow, Computers & Fluids 43 (1) (2011) 46–57. doi:10.1016/j.compfluid.2010.11.032.

[13] D. A. Fedosov, B. Caswell, G. E. Karniadakis, A Multiscale Red Blood Cell Model with Accurate Mechanics, Rheology, and Dynamics, Biophysical Journal 98 (10) (2010) 2215–2225. doi:10.1016/j.bpj.2010.02.002.

[14] J. Li, M. Dao, C. T. Lim, S. Suresh, Spectrin-level modeling of the cytoskeleton and optical tweezers stretching of the erythrocyte., Biophysical Journal 88 (5) (2005) 3707–3719. doi:10.1529/biophysj.104.047332.

[15] M. Nakamura, S. Bessho, S. Wada, Spring-network-based model of a red blood cell for simulatiing mesoscopic blood flow, International Journal for Numerical Methods in Biomedical Engineering 29 (1) (2013) 114–128. doi:10.1002/cnm.2501.

[16] R. G. Dreslinski, M. Wieckowski, D. Blaauw, D. Sylvester, T. Mudge, Near-Threshold Computing: Reclaiming Moore's Law Through Energy Efficient Integrated Circuits, Proceedings of the IEEE 98 (2) (2010) 253–266. doi:10.1109/JPROC.2009.2034764.

[17] C. A. Mack, Fifty years of Moore's law, IEEE Transactions on Semiconductor Manufacturing 24 (2) (2011) 202–207. doi:10.1109/TSM.2010.2096437.

[18] S. W. Keckler, W. J. Dally, B. Khailany, M. Garland, D. Glasco, GPUs and the future of parallel computing, IEEE Micro 31 (5) (2011) 7–17. doi:10.1109/MM.2011.89.

[19] D. Matsunaga, Y. Imai, T. Yamaguchi, T. Ishikawa, Deformation of a spherical capsule under oscillating shear flow, Journal of Fluid Mechanics 762 (2014) 288–301. doi:10.1017/jfm.2014.649.

[20] A. Borghi, N. B. Wood, R. H. Mohiaddin, X. Y. Xu, Fluid-solid interaction simulation of flow and stress pattern in thoracoabdominal aneurysms: A patient-specific study, Journal of Fluids and Structures 24 (2) (2008) 270–280. doi:10.1016/j.jfluidstructs.2007.08.005.

[21] D. E. Discher, D. H. Boal, S. K. Boey, Simulations of the erythrocyte cytoskeleton at large deformation. II. Micropipette aspiration., Biophysical Journal 75 (3) (1998) 1584–1597. doi:10.1016/S0006-3495(98)74076-7.

[22] T. Krueger, D. Holmes, P. V. Coveney, Deformability-based red blood cell separation in deterministic lateral displacement devices-A simulation study, Biomicrofluidics 8 (5) (2014) 0–15. doi:10.1063/1.4897913.

[23] A. Munjiza, D. Owen, N. Bicanic, A combined finitediscrete element method in transient dynamics of fracturing solids, Engineering Computations 12 (2) (1995) 145–174. arXiv:A luxury brand management framework built from historical review and case study analysis, doi:10.1108/09574090910954864.

[24] A. N. Gent, Engineering with Rubber, Carl Hanser Verlag, 2012. doi:10.3139/9783446428713.

[25] M. L. Raghavan, D. A. Vorp, Toward a biomechanical tool to evaluate rupture potential of abdominal aortic aneurysm: Identification of a finite strain constitutive model and evaluation of its applicability, Journal of Biomechanics 33 (4) (2000) 475–482. doi:10.1016/S0021-9290(99)00201-8.

[26] G. A. Holzapfel, G. Sommer, C. T. Gasser, P. Regitnig, Determination of layer-specifc mechanical properties of human coronary arteries with nonatherosclerotic intimal thickening and related constitutive modeling, Heart and Circulatory Physiology (2005) 2048–2058doi:10.1152/ajpheart.00934.2004.

[27] G. A. Holzapfel, T. C. Gasser, R. W. Ogden, A new constitutive framework for arterial wall mechanics and a comparative study of material models, Journal of Elasticity 61 (1-3) (2000) 1–48. doi:10.1023/A:1010835316564.

[28] Y. C. Fung, Elasticity of soft tissues in simple elongation., The American Journal of Physiology 213 (6) (1967) 1532–1544. doi:10.1152/ajplegacy.1967.213.6.1532.

[29] F. B. C. Cansz, H. Dal, M. Kaliske, An orthotropic viscoelastic material model for passive myocardium: theory and algorithmic treatment, Computer Methods in Biomechanics and Biomedical Engineering 18 (11) (2015) 1160–1172. doi:10.1080/10255842.2014.881475.

[30] G. A. Holzapfel, R. W. Ogden, Constitutive modelling of passive myocardium: a structurally based framework for material characterization, Philosophical Transactions of the Royal Society A: Mathematical, Physical and Engineering Sciences 367 (1902) (2009) 3445–3475. doi:10.1098/rsta.2009.0091.

[31] R. Skalak, A. Tozeren, R. P. Zarda, S. Chien, Strain energy function of red blood cell membranes, Biophysical Journal 13 (3) (1973) 245–64. doi:10.1016/S0006-3495(73)85983-1.

[32] C. A. Taylor, T. J. Hughes, C. K. Zarins, Finite element modeling of three-dimensional pulsatile flow in the abdominal aorta: relevance to atherosclerosis, Annals of Biomedical Engineering 26 (6) (1998) 975–987. doi:10.1114/1.140.

[33] M. Oshima, R. Torii, T. Kobayashi, Finite element simulation of blood flow in the cerebral artery, Computer Methods in Applied Mechanics and Engineering 191 (2001) 661–671. doi:10.1016/S0045-7825(01)00307-3.

[34] H. J. Kim, K. E. Jansen, C. A. Taylor, Incorporating autoregulatory mechanisms of the cardiovascular system in three-dimensional finite element models of arterial blood flow, Annals of Biomedical Engineering 38 (7) (2010) 2314–2330. doi:10.1007/s10439-010-9992-7.

[35] Y. Abdelaziz, A. Hamouine, A survey of the extended finite element, Computers and Structures 86 (11-12) (2008) 1141–1151. doi:10.1016/j.compstruc.2007.11.001.

[36] W. K. Liu, Y. Liu, D. Farrell, L. Zhang, X. S. Wang, Y. Fukui, N. Patankar, Y. Zhang, C. Bajaj, J. Lee, J. Hong, X. Chen, H. Hsu, Immersed finite element method and its applications to biological systems, Computer Methods in Applied Mechanics and Engineering 195 (13-16) (2006) 1722–1749. doi:10.1016/j.cma.2005.05.049.

[37] F. F. Abraham, M. Goulian, Diffraction from polymerized membranes: Flat vs. Crumpled, Europhysics Letters 19 (4) (1992) 293–296. doi:10.1209/0295-5075/19/4/008.

[38] A. M. Nasar, Eulerian and Lagrangian Smoothed Particle Hydrodynamics as Models for the Interaction of Fluids and Flexible Structures in Biomedical Flows, Ph.D. thesis, University of Manchester (2016).

[39] D. A. Fedosov, B. Caswell, S. Suresh, G. E. Karniadakis, Quantifying the biophysical characteristics of Plasmodium-falciparum-parasitized red blood cells in microcirculation., Proceedings of the National Academy of Sciences of the United States of America 108 (1) (2011) 35–9. doi:10.1073/pnas.1009492108.

[40] S. Dokos, B. H. Smaill, A. A. Young, I. J. LeGrice, Shear properties of passive ventricular myocardium, American Journal of Physiology - Heart and Circulatory Physiology 283 (6) (2002) H2650–H2659. doi:10.1152/ajpheart.00111.2002.

[41] J. Bonet, R. D. Wood, Nonlinear Continuum Mechanics for Finite Element Analysis, Vol. 24, 2008. doi:10.1017/CBO9780511755446.

[42] J. Humphrey, C. Taylor, Intracranial and abdominal aortic aneurysms: similarities, differences, and need for a new class of computational models, Annual Review of Biomedical Engineering 10 (2008) 221–246. doi:10.1146/annurev.bioeng.10.061807.160439.

[43] C. Taylor, C. Figueroa, Patient-Specific Modeling of Cardiovascular Mechanics, Annual Review of Biomedical Engineering 11 (1) (2009) 109–134. doi:10.1146/annurev.bioeng.10.061807.160521.

[44] P. N. Watton, N. A. Hill, M. Heil, A mathematical model for the growth of the abdominal aortic aneurysm, Biomechanics and Modeling in Mechanobiology 3 (2) (2004) 98–113. doi:10.1007/s10237-004-0052-9.

[45] P. N. Watton, A. Selimovic, N. B. Raberger, P. Huang, G. A. Holzapfel, Y. Ventikos, Modelling evolution and the evolving mechanical environment of saccular cerebral aneurysms, Biomechanics and Modeling in Mechanobiology 10 (1) (2011) 109–132. doi:10.1007/s10237-010-0221-y.

[46] A. Grytsan, P. N. Watton, G. A. Holzapfel, A Thick-Walled FluidSolid-Growth Model of Abdominal Aortic Aneurysm Evolution: Application to a Patient-Specific Geometry, Journal of Biomechanical Engineering 137 (3) (2015) 031008. doi:10.1115/1.4029279.

[47] M. K. Rausch, N. Famaey, T. O. B. Shultz, W. Bothe, D. C. Miller, E. Kuhl, Mechanics of the mitral valve: A critical review, an in vivo parameter identification, and the effect of prestrain, Biomechanics and Modeling in Mechanobiology 12 (5) (2013) 1053–1071. doi:10.1007/s10237-012-0462-z.

[48] W. Sun, C. Martin, T. Pham, Computational Modeling of Cardiac Valve Function and Intervention, Annual Review of Biomedical Engineering 16 (1) (2014) 53–76. doi:10.1146/annurev-bioeng-071813-104517.

[49] A. L. Marsden, J. A. Feinstein, Computational modeling and engineering in pediatric and congenital heart disease, Current Opinion in Pediatrics 27 (5) (2015) 587–596. doi:10.1097/MOP.0000000000000269.

[50] A. Kheradvar, E. M. Groves, A. Falahatpisheh, M. K. Mofrad, S. Hamed Alavi, R. Tranquillo, L. P. Dasi, C. A. Simmons, K. Jane Grande-Allen, C. J. Goergen, F. Baaijens, S. H. Little, S. Canic, B. Griffith, Emerging Trends in Heart Valve Engineering: Part IV. Computational Modeling and Experimental Studies, Annals of Biomedical Engineering 43 (10) (2015) 2314–2333. arXiv:arXiv:1011.1669v3, doi:10.1007/s10439-015-1394-4.

[51] R. Chabiniok, V. Y. Wang, M. Hadjicharalambous, L. Asner, J. Lee, M. Sermesant, E. Kuhl, A. A. Young, P. Moireau, M. P. Nash, D. Chapelle, D. A. Nordsletten, Multiphysics and multiscale modelling, data-model fusion and integration of organ physiology in the clinic: ventricular cardiac mechanics., Interface Focus 6 (2) (2016) 20150083. doi:10.1098/rsfs.2015.0083.

[52] C. A. Taylor, Finite element modeling of blood flow: Relevance to atherosclerosis, Advances in Fluid Mechanics 23 (2000) 249–290.

[53] D. A. Steinman, D. A. Vorp, C. R. Ethier, Computational modeling of arterial biomechanics: insights into pathogenesis and treatment of vascular disease., Journal of Vascular Surgery 37 (5) (2003) 1118–28. doi:10.1067/mva.2003.122.

[54] P. Assemat, K. Hourigan, Evolution and rupture of vulnerable plaques: a review of mechanical effects, Chrono-Physiol. Ther 3 (2013) 23–40. doi:10.2147/CPT.S32050.

[55] M. T. Walsh, E. M. Cunnane, J. J. Mulvihill, A. C. Akyildiz, F. J. Gijsen, G. A. Holzapfel, Uniaxial tensile testing approaches for characterisation of atherosclerotic plaques, Journal of Biomechanics 47 (4) (2014) 793–804. doi:10.1016/j.jbiomech.2014.01.017.

[56] G. A. Holzapfel, J. J. Mulvihill, E. M. Cunnane, M. T. Walsh, Computational approaches for analyzing the mechanics of atherosclerotic plaques: A review, Journal of Biomechanics 47 (4) (2014) 859–869. doi:10.1016/j.jbiomech.2014.01.011.

[57] J. L. Brisman, J. K. Song, D. W. Newell, Cerebral aneurysms., The New England Journal of Medicine 355 (9) (2006) 928–39.

[58] J. Lee, N. P. Smith, Theoretical modeling in hemodynamics of microcirculation., Microcirculation (New York, N.Y. : 1994) 15 (8) (2008) 699–714. doi:10.1080/10739680802229589.

[59] T. Omori, T. Ishikawa, D. Barthès-Biesel, A.-V. Salsac, J. Walter, Y. Imai, T. Yamaguchi, Comparison between spring network models and continuum constitutive laws: Application to the large deformation of a capsule in shear flow, Physical Review E 83 (4) (2011) 041918.

[60] D. A. Fedosov, H. Noguchi, G. Gompper, Multiscale modeling of blood flow: From single cells to blood rheology, Biomechanics and Modeling in Mechanobiology 13 (2) (2014) 239–258. doi:10.1007/s10237-013-0497-9.

[61] B. Baillargeon, N. Rebelo, D. D. Fox, R. L. Taylor, E. Kuhl, The living heart project: A robust and integrative simulator for human heart function, European Journal of Mechanics, A/Solids 48 (1) (2014) 38–47. arXiv:NIHMS150003, doi:10.1016/j.euromechsol.2014.04.001.

[62] N. A. Trayanova, Whole-heart modeling : Applications to cardiac electrophysiology and electromechanics, Circulation Research 108 (1) (2011) 113–128. arXiv:NIHMS150003, doi:10.1161/CIRCRESAHA.110.223610.

[63] G. Sommer, A. J. Schriefl, M. Andrä, M. Sacherer, C. Viertler, H. Wolinski, G. A. Holzapfel, Biomechanical properties and microstructure of human ventricular myocardium, Acta Biomaterialia 24 (2015) 172–192. doi:10.1016/j.actbio.2015.06.031.

[64] C. Forsell, T. C. Gasser, Numerical simulation of the failure of ventricular tissue due to deep penetration: The impact of constitutive properties, Journal of Biomechanics 44 (1) (2011) 45–51. doi:10.1016/j.jbiomech.2010.08.022.

[65] T. C. Gasser, C. Forsell, The numerical implementation of invariant-based viscoelastic formulations at finite strains. An anisotropic model for the passive myocardium, Computer Methods in Applied Mechanics and Engineering 200 (49-52) (2011) 3637–3645. doi:10.1016/j.cma.2011.08.022.

[66] J. Aguado-Sierra, A. Krishnamurthy, C. Villongco, J. Chuang, E. Howard, M. J. Gonzales, J. Omens, D. E. Krummen, S. Narayan, R. C. Kerckhoffs, A. D. McCulloch, Patient-specific modeling of dyssynchronous heart failure: A case study, Progress in Biophysics and Molecular Biology 107 (1) (2011) 147–155. arXiv:PMC3190065, doi:10.1016/j.pbiomolbio.2011.06.014.

[67] A. Krishnamurthy, C. T. Villongco, J. Chuang, L. R. Frank, V. Nigam, E. Belezzuoli, P. Stark, D. E. Krummen, S. Narayan, J. H. Omens, A. D. McCulloch, R. C. Kerckhoffs, Patient-specific models of cardiac biomechanics, Journal of Computational Physics 244 (2013) 4–21. arXiv:PMC3667962, doi:10.1016/j.jcp.2012.09.015.

[68] P. Brocklehurst, I. Adeniran, D. Yang, Y. Sheng, H. Zhang, J. Ye, A 2D electromechanical model of human atrial tissue using the discrete element method, BioMed Research International 2015 (2015) 854953. doi:10.1155/2015/854953.

[69] J. S. Coogan, F. P. Chan, C. A. Taylor, J. A. Feinstein, Computational fluid dynamic simulations of aortic coarctation comparing the effects of surgical- and stent-based treatments on aortic compliance and ventricular workload, Catheterization and Cardiovascular Interventions 77 (5) (2011) 680–691. doi:10.1002/ccd.22878.

[70] M. J. Chern, M. T. Wu, H. L. Wang, Numerical investigation of regurgitation phenomena in pulmonary arteries of Tetralogy of Fallot patients after repair, Journal of Biomechanics 41 (14) (2008) 3002–3009. doi:10.1016/j.jbiomech.2008.07.017.

[71] A. L. Marsden, A. J. Bernstein, V. M. Reddy, S. C. Shadden, R. L. Spilker, F. P. Chan, C. A. Taylor, J. A. Feinstein, Evaluation of a novel Y-shaped extracardiac Fontan baffle using computational fluid dynamics, Journal of Thoracic and Cardiovascular Surgery 137 (2) (2009) 394–403.e2. doi:10.1016/j.jtcvs.2008.06.043.

[72] G. Biglino, C. Capelli, J. Bruse, G. M. Bosi, A. M. Taylor, S. Schievano, Computational modelling for congenital heart disease: how far are we from clinical translation?, Heart 103 (2017) 98–103. doi:10.1136/heartjnl-2016-310423.

[73] I. E. Vignon-Clementel, A. L. Marsden, J. A. Feinstein, A primer on computational simulation in congenital heart disease for the clinician, Progress in Pediatric Cardiology 30 (1-2) (2010) 3–13. doi:10.1016/j.ppedcard.2010.09.002.

[74] J. S. Tweddell, M. Nersesian, K. A. Mussatto, M. Nugent, P. Simpson, M. E. Mitchell, N. S. Ghanayem, A. N. Pelech, R. Marla, G. M. Hoffman, Fontan Palliation in the Modern Era: Factors Impacting Mortality and Morbidity, Annals of Thoracic Surgery 88 (4) (2009) 1291–1299. doi:10.1016/j.athoracsur.2009.05.076.

[75] R. Ogden, Large deformation isotropic elasticity: on the correlation of theory and experiment for compressible rubberlike solids, Proceedings of the Royal Society A 328 (1575) (1972) 567–583. doi:10.1098/rspa.1972.0096.

[76] J. C. Masters, M. Ketner, M. S. Bleiweis, M. Mill, A. P. Yoganathan, C. L. Lucas, The Effect of Incorporating Vessel Compliance in a Computational Model of Blood Flow in a Total Cavopulmonary Connection (TCPC) with Caval Centerline Offset, Journal of Biomechanical Engineering 126 (December 2004) (2004) 709–713. doi:10.1115/1.1824126.

[77] W. Orlando, R. Shandas, C. DeGroff, Efficiency differences in computational simulations of the total cavopulmonary circulation with and without compliant vessel walls, Computer Methods and Programs in Biomedicine 81 (3) (2006) 220–227. doi:10.1016/j.cmpb.2005.11.010.

[78] A. L. Marsden, I. E. Vignon-Clementel, F. P. Chan, J. a. Feinstein, C. a. Taylor, Effects of exercise and respiration on hemodynamic efficiency in CFD simulations of the total cavopulmonary connection, Annals of Biomedical Engineering 35 (2) (2007) 250–263. doi:10.1007/s10439-006-9224-3.

[79] C. C. Long, M.-C. Hsu, Y. Bazilevs, J. A. Feinstein, A. L. Marsden, Fluid-structure interaction simulations of the Fontan procedure using variable wall properties, International Journal for Numerical Methods in Biomedical Engineering 28 (1) (2012) 807–827. arXiv:NIHMS150003, doi:10.1002/cnm.

[80] J. F. LaDisa, C. A. Taylor, J. A. Feinstein, Aortic coarctation: Recent developments in experimental and computational methods to assess treatments for this simple condition, Progress in Pediatric Cardiology 30 (1-2) (2010) 45–49. doi:10.1016/j.ppedcard.2010.09.006.

[81] P. Segers, L. Taelman, J. Degroote, J. Bols, J. Vierendeels, The aortic reservoir-wave as a paradigm for arterial haemodynamics: insights from three-dimensional fluid-structure interaction simulations in a model of aortic coarctation., Journal of Hypertension 33 (3) (2015) 554–63; discussion 563. doi:10.1097/HJH.0000000000000449.

[82] R. van Loon, P. D. Anderson, F. N. van de Vosse, A fluid-structure interaction method with solid-rigid contact for heart valve dynamics, Journal of Computational Physics 217 (2) (2006) 806–823. doi:10.1016/j.jcp.2006.01.032.

[83] P. W. M. Fedak, M. P. L. De Sa, S. Verma, N. Nili, P. Kazemian, J. Butany, B. H. Strauss, R. D. Weisel, T. E. David, M. H. Yacoub, T. M. Sundt, F. W. Sellke, C. Pizarro, Vascular matrix remodeling in patients with bicuspid aortic valve malformations: Implications for aortic dilatation, Journal of Thoracic and Cardiovascular Surgery 126 (3) (2003) 797–806. doi:10.1016/S0022-5223(03)00398-2.

[84] J. M. T. Penrose, C. J. Staples, Implicit fluid-structure coupling for simulation of cardiovascular problems, International Journal for Numerical Methods in Fluids 40 (3-4) (2002) 467–478.

[85] K. Dumont, J. Vierendeels, R. Kaminsky, G. van Nooten, P. Verdonck, D. Bluestein, Comparison of the Hemodynamic and Thrombogenic Performance of Two Bileaflet Mechanical Heart Valves Using a CFD/FSI Model, Journal of Biomechanical Engineering 129 (4) (2007) 558–565. doi:10.1115/1.2746378.

[86] S. Krucinski, I. Vesely, M. A. Dokainish, G. Campbell, Numerical simulation of leaflet flexure in bioprosthetic valves mounted on rigid and expansile stents, Journal of Biomechanics 26 (8) (1993) 929–943. doi:10.1016/0021-9290(93)90055-J.

[87] G. Cacciola, G. W. M. Peters, P. J. G. Schreurs, A three-dimensional mechanical analysis of a stentless fibre-reinforced aortic valve prosthesis, Journal of Biomechanics 33 (5) (2000) 521–530. doi:10.1016/S0021-9290(99)00222-5.

[88] E. J. Weinberg, M. R. Kaazempur-Mofrad, On the constitutive models for heart valve leaflet mechanics, Cardiovascular Engineering 5 (1) (2005) 37–43. doi:10.1007/s10558-005-3072-x.

[89] K. May-Newman, F. C. P. Yin, A Constitutive Law for Mitral Valve Tissue, Journal of Biomechanical Engineering 120 (1) (1998) 38–47. doi:10.1115/1.2834305.

[90] K. L. Billiar, M. S. Sacks, Biaxial Mechanical Properties of the Native and Glutaraldehyde- Treated Aortic Valve Cusp : Part II A Structural Constitutive., Journal of Biomechanical Engineering 122 (4) (2000) 327–335. doi:10.1115/1.1287158.

[91] J. D. Humphrey, R. K. Strumpf, F. C. P. Yin, Determination of a constitutive relation for passive myocardium: I. A new functional form, Journal of Biomechanical Engineering 112 (3) (1990) 333–339. doi:10.1115/1.2891193.

[92] J. D. Humphrey, R. K. Strumpf, F. C. P. Yin, A Constitutive Theory for Biomembranes: Application to Epicardial Mechanics, Journal of Biomechanical Engineering 114 (4) (1992) 461–466. doi:10.1115/1.2894095.

[93] Y. Lanir, A structural theory for the homogeneous biaxial stress-strain relationships in flat collagenous tissues, Journal of Biomechanics 12 (6) (1979) 423–436. doi:10.1016/0021-9290(79)90027-7.

[94] Y. Lanir, Constitutive equations for fibrous connective tissues, Journal of Biomechanics 16 (1) (1983) 1–12. doi:10.1016/0021-9290(83)90041-6.

[95] A. J. Schriefl, H. Wolinski, P. Regitnig, S. D. Kohlwein, G. A. Holzapfel, An automated approach for three-dimensional quantification of fibrillar structures in optically cleared soft biological tissues., Journal of the Royal Society, Interface 10 (80) (2013) 20120760. doi:10.1098/rsif.2012.0760.

[96] V. Flamini, C. Kerskens, C. Simms, C. Lally, Fibre orientation of fresh and frozen porcine aorta determined non-invasively using diffusion tensor imaging, Medical Engineering and Physics 35 (6) (2013) 765–776. doi:10.1016/j.medengphy.2012.08.008.

[97] J. A. Niestrawska, C. Viertler, P. Regitnig, T. U. Cohnert, G. Sommer, G. A. Holzapfel, Microstructure and mechanics of healthy and aneurysmatic abdominal aortas: experimental analysis and modelling, Journal of The Royal Society Interface 13 (124) (2016) 20160620. doi:10.1098/rsif.2016.0620.

[98] G. A. Holzapfel, T. C. Gasser, M. Stadler, A structural model for the viscoelastic behavior of arterial walls : Continuum formulation and finite element analysis A structural model for the viscoelastic behavior of arterial walls : Continuum formulation and finite element analysis 21 (43) (2002) 441–463. doi:10.1016/S0997-7538(01)01206-2.

[99] M. A. Zulliger, N. Stergiopulos, Structural strain energy function applied to the ageing of the human aorta, Journal of Biomechanics 40 (14) (2007) 3061–3069. doi:10.1016/j.jbiomech.2007.03.011.

[100] A. Ivankovic, A. Karac, E. Dendrinos, K. Parker, Towards early diagnosis of atherosclerosis: the finite volume method for fluid-structure interaction., Biorheology 39 (3) (2002) 401–407.

[101] A. Fernandez-Ortiz, J. J. Badimon, E. Falk, V. Fuster, B. Meyer, A. Mailhac, Characterization of the Relative Thrombogenicity of Atherosclerotic Plaque Components : Implications for Consequences of Plaque Rupture, Journal of the American College of Cardiology 23 (7) (1994) 1–8. doi:10.1016/0735-1097(94)90657-2.

[102] H. Meng, V. M. Tutino, J. Xiang, a. Siddiqui, High WSS or Low WSS? Complex interactions of hemodynamics with intracranial aneurysm initiation, growth, and rupture: Toward a unifying hypothesis, American Journal of Neuroradiology 35 (7) (2014) 1254–1262. doi:10.3174/ajnr.A3558.

[103] D. Tang, C. Yang, S. Kobayashi, D. N. Ku, Effect of a lipid pool on stress/strain distributions in stenotic arteries: 3-D fluid-structure interactions (FSI) models., Journal of Biomechanical Engineering 126 (3) (2004) 363–370. doi:10.1115/1.1762898.

[104] H. M. Loree, R. D. Kamm, R. G. Stringfellow, R. T. Lee, Effects of fibrous cap thickness on peak circumferential stress in model atherosclerotic vessels, Circulation Research 71 (4) (1992) 850–858. doi:10.1161/01.RES.71.4.850.

[105] E. Maher, M. Early, A. Creane, C. Lally, D. J. Kelly, Site specific inelasticity of arterial tissue, Journal of Biomechanics 45 (8) (2012) 1393–1399.

[106] G. C. Cheng, H. M. Loree, R. D. Kamm, M. C. Fishbein, R. T. Lee, Distribution of circumferential stress in ruptured and stable atherosclerotic lesions. A structural analysis with histopathological correlation., Circulation 87 (4) (1993) 1179–1187. doi:10.1161/01.CIR.87.4.1179.

[107] D. Tang, C. Yang, J. Zheng, P. K. Woodard, J. E. Saffitz, G. a. Sicard, T. K. Pilgram, C. Yuan, Quantifying effects of plaque structure and material properties on stress distributions in human atherosclerotic plaques using 3D FSI models., Journal of Biomechanical Engineering 127 (7) (2005) 1185–94. doi:10.1115/1.2073668.

[108] J. Ohayon, G. Rioufol, O. Dubreuil, D. Lyon, A three-dimensional finite element analysis of stress distribution in a coronary atherosclerotic plaque:, Biomechanics Applied to Computer Assisted Surgery 661 (2) (2005) 225–41.

[109] F. Auricchio, M. Conti, M. De Beule, G. De Santis, B. Verhegghe, Carotid artery stenting simulation: From patient-specific images to finite element analysis, Medical Engineering and Physics 33 (3) (2011) 281–289. doi:10.1016/j.medengphy.2010.10.011.

[110] M. L. Raghavan, S. Trivedi, A. Nagaraj, D. D. McPherson, K. B. Chandran, Three-dimensional finite element analysis of residual stress in arteries, Annals of Biomedical Engineering 32 (2) (2004) 257–263. doi:10.1023/B:ABME.0000012745.05794.32.

[111] G. A. Holzapfel, G. Sommer, M. Auer, P. Regitnig, R. W. Ogden, Layer-specific 3D residual deformations of human aortas with non-atherosclerotic intimal thickening., Annals of Biomedical Engineering 35 (4) (2007) 530–45. doi:10.1007/s10439-006-9252-z.

[112] M. Cilla, E. Peña, M. A. Martínez, 3D computational parametric analysis of eccentric atheroma plaque: influence of axial and circumferential residual stresses., Biomechanics and Modeling in Mechanobiology 11 (7) (2012) 1001–13. doi:10.1007/s10237-011-0369-0.

[113] X. Huang, C. Yang, C. Yuan, F. Liu, G. Canton, J. Zheng, P. K. Woodard, G. A. Sicard, D. Tang, Patient-specific artery shrinkage and 3D zero-stress state in multi-component 3D FSI models for carotid atherosclerotic plaques based on in vivo MRI data., Molecular & Cellular Biomechanics 6 (2) (2009) 121–34.

[114] L. Speelman, A. C. Akyildiz, B. den Adel, J. J. Wentzel, A. F. W. van der Steen, R. Virmani, L. van der Weerd, J. W. Jukema, R. E. Poelmann, E. H. van Brummelen, F. J. H. Gijsen, Initial stress in biomechanical models of atherosclerotic plaques., Journal of Biomechanics 44 (13) (2011) 2376–82. doi:10.1016/j.jbiomech.2011.07.004.

[115] J. Ohayon, O. Dubreuil, P. Tracqui, S. Le Floc'h, G. Rioufol, L. Chalabreysse, F. Thivolet, R. I. Pettigrew, G. Finet, Influence of residual stress/strain on the biomechanical stability of vulnerable coronary plaques: potential impact for evaluating the risk of plaque rupture., American Journal of Physiology. Heart and Circulatory Physiology 293 (3) (2007) H1987–H1996. doi:10.1152/ajpheart.00018.2007.

[116] H. Huang, R. Virmani, H. Younis, a. P. Burke, R. D. Kamm, R. T. Lee, The impact of calcification on the biomechanical stability of atherosclerotic plaques., Circulation 103 (8) (2001) 1051–6. doi:10.1161/01.CIR.103.8.1051.

[117] A. H. Chau, R. C. Chan, M. Shishkov, B. MacNeill, N. Iftimia, G. J. Tearney, R. D. Kamm, B. E. Bouma, M. R. Kaazempur-Mofrad, Mechanical analysis of atherosclerotic plaques based on optical coherence tomography., Annals of Biomedical Engineering 32 (11) (2004) 1494–503. arXiv:17331558, doi:10.1114/B:ABME.0000049034.75368.4a.

[118] M. X. Li, J. J. Beech-Brandt, L. R. John, P. R. Hoskins, W. J. Easson, Numerical analysis of pulsatile blood flow and vessel wall mechanics in different degrees of stenoses., Journal of Biomechanics 40 (16) (2007) 3715–24. doi:10.1016/j.jbiomech.2007.06.023.

[119] G. A. Holzapfel, G. Sommer, P. Regitnig, Anisotropic mechanical properties of tissue components in human atherosclerotic plaques., Journal of Biomechanical Engineering 126 (5) (2004) 657–65. doi:10.1115/1.1800557.

[120] Z. Teng, G. Canton, C. Yuan, M. Ferguson, C. Yang, X. Huang, J. Zheng, P. K. Woodard, D. Tang, 3D critical plaque wall stress is a better predictor of carotid plaque rupture sites than flow shear stress: An in vivo MRI-based 3D FSI study., Journal of Biomechanical Engineering 132 (3) (2010) 031007. doi:10.1115/1.4001028.

[121] M. G. Lawlor, M. R. O'Donnell, B. M. O'Connell, M. T. Walsh, Experimental determination of circumferential properties of fresh carotid artery plaques., Journal of Biomechanics 44 (9) (2011) 1709–15. doi:10.1016/j.jbiomech.2011.03.033.

[122] X. Huang, Z. Teng, G. Canton, M. Ferguson, C. Yuan, D. Tang, Intraplaque hemorrhage is associated with higher structural stresses in human atherosclerotic plaques: an in vivo MRI-based 3D fluid-structure interaction study., Biomedical Engineering Online 9 (1) (2010) 86. doi:10.1186/1475-925X-9-86.

[123] D. Bluestein, Y. Alemu, I. Avrahami, M. Gharib, K. Dumont, J. J. Ricotta, S. Einav, Influence of microcalcifications on vulnerable plaque mechanics using FSI modeling., Journal of Biomechanics 41 (5) (2008) 1111–8. doi:10.1016/j.jbiomech.2007.11.029.

[124] D. Tang, Z. Teng, G. Canton, C. Yang, M. Ferguson, X. Huang, J. Zheng, P. K. Woodard, C. Yuan, Sites of rupture in human atherosclerotic carotid plaques are associated with high structural stresses: an in vivo MRI-based 3D fluid-structure interaction study., Stroke 40 (10) (2009) 3258–63. doi:10.1161/STROKEAHA.109.558676.

[125] M. Malve, A. Garcia, J. Ohayon, M. A. Martinez, Unsteady blood flow and mass transfer of a human left coronary artery bifurcation: FSI vs. CFD, International Communications in Heat and Mass Transfer 39 (6) (2012) 745–751. doi:10.1016/j.icheatmasstransfer.2012.04.009.

[126] D. Martin, F. J. Boyle, Computational structural modelling of coronary stent deployment: A review, Computer Methods in Biomechanics and Biomedical Engineering 14 (4) (2011) 331–348. doi:10.1080/10255841003766845.

[127] P. Zunino, C. D'Angelo, L. Petrini, C. Vergara, C. Capelli, F. Migliavacca, Numerical simulation of drug eluting coronary stents: Mechanics, fluid dynamics and drug release, Computer Methods in Applied Mechanics and Engineering 198 (45-46) (2009) 3633–3644. doi:10.1016/j.cma.2008.07.019.

[128] S. Morlacchi, Sequential Structural and Fluid Dynamic Numerical Simulations of a Stented Bifurcated Coronary Artery, Journal of Biomechanical Engineering 133 (12) (2011) 121010. doi:10.1115/1.4005476.

[129] W. Wu, M. Qi, X. P. Liu, D. Z. Yang, W. Q. Wang, Delivery and release of nitinol stent in carotid artery and their interactions: A finite element analysis, Journal of Biomechanics 40 (13) (2007) 3034–3040. doi:10.1016/j.jbiomech.2007.02.024.

[130] A. A. Veress, J. A. Weiss, G. T. Gullberg, D. G. Vince, R. D. Rabbitt, Strain Measurement in Coronary Arteries Using Intravascular Ultrasound and Deformable Images, Journal of Biomechanical Engineering 124 (6) (2002) 734. doi:10.1115/1.1519279.

[131] A. I. Veress, D. G. Vince, P. M. Anderson, J. F. Cornhill, E. E. Herderick, J. D. Klingensmith, B. D. Kuban, N. L. Greenberg, J. D. Thomas, Vascular mechanics of the coronary artery., Zeitschrift für Kardiologie 89 Suppl 2 (February) (2000) 92–100. doi:10.1007/s003920070106.

[132] F. Lurie, R. L. Kistner, B. Eklof, D. Kessler, Mechanism of venous valve closure and role of the valve in circulation: a new concept., Journal of Vascular Surgery 38 (5) (2003) 955–61. doi:10.1016/S0741.

[133] N. S. Wijeratne, K. A. Hoo, Numerical studies on the hemodynamics in the human vein and venous valve, in: American Control Conference, IEEE, 2008, pp. 147–152. doi:10.1109/ACC.2008.4586482.

[134] R. Chiao, L. Mo, A. Hall, S. Miller, B-mode blood flow (B-flow) imaging, in: Ultrasonics Symposium, 2000 IEEE, Vol. 2, IEEE, 2000, pp. 1469–1472 vol.2. doi:10.1109/ULTSYM.2000.921601.

[135] S. Shahriari, H. Maleki, I. Hassan, L. Kadem, Evaluation of shear stress accumulation on blood components in normal and dysfunctional bileaflet mechanical heart valves using smoothed particle hydrodynamics, Journal of Biomechanics 45 (15) (2012) 2637–2644. doi:10.1016/j.jbiomech.2012.08.009.

[136] Z. Xu, N. Chen, M. M. Kamocka, E. D. Rosen, M. Alber, Alber, Mark, A multiscale model of thrombus development., Journal of the Royal Society, Interface 5 (24) (2008) 705–22. doi:10.1098/rsif.2007.1202.

[137] J. D. Humphrey, G. A. Holzapfel, Mechanics , mechanobiology , and modeling of human abdominal aorta and aneurysms, Journal of Biomechanics 45 (5) (2012) 805–814. doi:10.1016/j.jbiomech.2011.11.021.

[138] J. F. Rodríguez, C. Ruiz, M. Doblaré, G. A. Holzapfel, Mechanical stresses in abdominal aortic aneurysms: influence of diameter, asymmetry, and material anisotropy., Journal of Biomechanical Engineering 130 (2) (2008) 021023. doi:10.1115/1.2898830.

[139] B. J. B. M. Wolters, M. C. M. Rutten, G. W. H. Schurink, U. Kose, J. de Hart, F. N. van de Vosse, A patient-specific computational model of fluid-structure interaction in abdominal aortic aneurysms., Medical Engineering & Physics 27 (10) (2005) 871–83. doi:10.1016/j.medengphy.2005.06.008.

[140] D. H. J. Wang, M. S. Makaroun, M. W. Webster, D. A. Vorp, Effect of intraluminal thrombus on wall stress in patient-specific models of abdominal aortic aneurysm, Journal of Vascular Surgery 36 (3) (2002) 598–604. doi:10.1067/mva.2002.126087.

[141] D. A. Vorp, P. C. Lee, D. H. Wang, M. S. Makaroun, E. M. Nemoto, S. Ogawa, M. W. Webster, Association of intraluminal thrombus in abdominal aortic aneurysm with local hypoxia and wall weakening., Journal of Vascular Surgery 34 (2) (2001) 291–9. doi:10.1067/mva.2001.114813.

[142] M. Kazi, J. Thyberg, P. Religa, J. Roy, P. Eriksson, U. Hedin, J. Swedenborg, Influence of intraluminal thrombus on structural and cellular composition of abdominal aortic aneurysm wall., Journal of Vascular Surgery 38 (6) (2003) 1283–92. doi:10.1016/S0741.

[143] W. R. Mower, W. J. Quinones, S. S. Gambhir, Effect of intraluminal thrombus on abdominal aortic aneurysm wall stress, Journal of Vascular Surgery 26 (4) (1997) 602–608. doi:10.1016/S0741-5214(97)70058-2.

[144] E. S. Di Martino, D. A. Vorp, Effect of variation in intraluminal thrombus constitutive properties on abdominal aortic aneurysm wall stress., Annals of Biomedical Engineering 31 (7) (2003) 804–9. doi:10.1114/1.1581880.

[145] M. Xenos, S. H. Rambhia, Y. Alemu, S. Einav, N. Labropoulos, A. Tassiopoulos, J. J. Ricotta, D. Bluestein, Patient-based abdominal aortic aneurysm rupture risk prediction with fluid structure interaction modeling., Annals of Biomedical Engineering 38 (11) (2010) 3323–37. doi:10.1007/s10439-010-0094-3.

[146] C. He, M. Roach, The composition and mechanical properties of abdominal aortic aneurysms., Journal of Vascular Surgery 20 (1) (1994) 6–13. doi:10.1016/0741-5214(94)90169-4.

[147] J. P. Vande Geest, M. S. Sacks, D. A. Vorp, The effects of aneurysm on the biaxial mechanical behavior of human abdominal aorta, Journal of Biomechanics 39 (7) (2006) 1324–1334. doi:10.1016/j.jbiomech.2005.03.003.

[148] D. H. Wang, M. Makaroun, M. W. Webster, D. A. Vorp, Mechanical properties and microstructure of intraluminal thrombus from abdominal aortic aneurysm., Journal of Biomechanical Engineering 123 (6) (2001) 536–9. doi:10.1115/1.1411971.

[149] M. M. Stringfellow, P. F. Lawrence, R. G. Stringfellow, The influence of aorta-aneurysm geometry upon stress in the aneurysm wall, Journal of Surgical Research 42 (4) (1987) 425–433. doi:10.1016/0022-4804(87)90178-8.

[150] F. Inzoli, F. Boschetti, M. Zappa, T. Longo, R. Fumero, Biomechanical factors in abdominal aortic aneurysm rupture., European Journal of Vascular Surgery 7 (6) (1993) 667–74. doi:10.1016/S0950-821X(05)80714-5.

[151] J. G. Isaksen, Y. Bazilevs, T. Kvamsdal, Y. Zhang, J. H. Kaspersen, K. Waterloo, B. Romner, T. Ingebrigtsen, Determination of wall tension in cerebral artery aneurysms by numerical simulation., Stroke 39 (12) (2008) 3172–8. doi:10.1161/STROKEAHA.107.503698.

[152] M. F. Fillinger, M. L. Raghavan, S. P. Marra, J. L. Cronenwett, F. E. Kennedy, In vivo analysis of mechanical wall stress and abdominal aortic aneurysm rupture risk, Journal of Vascular Surgery 36 (3) (2002) 589–597. doi:10.1067/mva.2002.125478.

[153] E. A. Finol, C. H. Amon, Blood flow in abdominal aortic aneurysms: pulsatile flow hemodynamics., Journal of Biomechanical Engineering 123 (October 2001) (2001) 474–484. doi:10.1115/1.1395573.

[154] E. Di Martino, G. Guadagni, A. Fumero, G. Ballerini, R. Spirito, P. Biglioli, A. Redaelli, Fluidstructure interaction within realistic three-dimensional models of the aneurysmatic aorta as a guidance to assess the risk of rupture of the aneurysm, Medical Engineering & Physics 23 (9) (2001) 647–655. doi:10.1016/S1350-4533(01)00093-5.

[155] C. M. Scotti, A. D. Shkolnik, S. C. Muluk, E. A. Finol, Fluid-structure interaction in abdominal aortic aneurysms: effects of asymmetry and wall thickness., Biomedical Engineering Online 4 (1) (2005) 64. doi:10.1186/1475-925X-4-64.

[156] M. Xenos, N. Labropoulos, S. Rambhia, Y. Alemu, S. Einav, A. Tassiopoulos, N. Sakalihasan, D. Bluestein, Progression of Abdominal Aortic Aneurysm Towards Rupture: Refining Clinical Risk Assessment Using a Fully Coupled Fluid-Structure Interaction Method, Annals of Biomedical Engineering 43 (1) (2014) 139–153. doi:10.1007/s10439-014-1224-0.

[157] B. Owen, C. Lowe, N. Ashton, P. Mandal, S. Rogers, W. Wein, C. Mccollum, A. Revell, Computational hemodynamics of abdominal aortic aneurysms : Three-dimensional ultrasound versus computed tomography, Journal of Engineering in Medicine 230 (3) (2016) 201–210. doi:10.1177/0954411915626742.

[158] M. L. Raghavan, J. Kratzberg, E. M. Castro de Tolosa, M. M. Hanaoka, P. Walker, E. S. da Silva, Regional distribution of wall thickness and failure properties of human abdominal aortic aneurysm., Journal of Biomechanics 39 (16) (2006) 3010–6. doi:10.1016/j.jbiomech.2005.10.021.

[159] A. Sheidaei, S. C. Hunley, S. Zeinali-Davarani, L. G. Raguin, S. Baek, Simulation of abdominal aortic aneurysm growth with updating hemodynamic loads using a realistic geometry, Medical Engineering and Physics 33 (1) (2011) 80–88. doi:10.1016/j.medengphy.2010.09.012.

[160] P. Aparicio, A. Mandaltsi, J. Boamah, H. Chen, A. Selimovic, J. Bratby, R. Uberoi, Y. Ventikos, P. N. Watton, Modelling the influence of endothelial heterogeneity on the progression of arterial disease: application to abdominal aortic aneurysm evolution, International Journal for Numerical Methods in Biomedical Engineering 30 (5) (2014) 563–586. doi:10.1002/cnm.2620.

[161] H. Schmid, A. Grytsan, E. Poshtan, P. N. Watton, M. Itsikov, Influence of differing material properties in media and adventitia on arterial adaptation – application to aneurysm formation and rupture, Computer Methods in Biomechanics and Biomedical Engineering 16 (1) (2013) 33–53. doi:10.1080/10255842.2011.603309.

[162] R. Torii, M. Oshima, T. Kobayashi, K. Takagi, T. E. Tezduyar, Fluid-structure interaction modeling of a patient-specific cerebral aneurysm: Influence of structural modeling, Computational Mechanics 43 (1) (2008) 151–159. doi:10.1007/s00466-008-0325-8.

[163] L. K. Bickerstaff, P. C. Pairolero, L. H. Hollier, L. J. Melton, H. J. Van Peenen, K. J. Cherry, J. W. Joyce, J. T. Lie, Thoracic aortic aneurysms: a population-based study., Surgery 92 (6) (1982) 1103–1108.

[164] M. P. Pitt, R. S. Bonser, The natural history of thoracic aortic aneurysm disease: an overview, Journal of Cardiac Surgery 12 (2 Suppl) (1997) 270–278. doi:10.1111/j.1540-8191.1997.tb00138.x.

[165] J. A. Rizzo, M. A. Coady, J. A. Elefteriades, Procedures for estimating growth rates in thoracic aortic aneurysms., Journal of Clinical Epidemiology 51 (9) (1998) 747–54. doi:10.1016/S0895-4356(98)00050-X.

[166] L.-D. Jou, M. E. Mawad, Growth rate and rupture rate of unruptured intracranial aneurysms: a population approach., Biomedical Engineering Online 8 (2009) 11. doi:10.1186/1475-925X-8-11.

[167] D. A. Vorp, B. J. Schiro, M. P. Ehrlich, T. S. Juvonen, M. A. Ergin, B. P. Griffith, Effect of aneurysm on the tensile strength and biomechanical behavior of the ascending thoracic aorta., The Annals of Thoracic Surgery 75 (4) (2003) 1210–4. doi:10.1016/S0003-4975(02)04711-2.

[168] Y. Kato, T. Matsumoto, K. Kumagai, H. Akimoto, K. Tabayashi, M. Sato, Development of a simple method to construct finite element models of aortas from MRI images and its application to thoracic aortic aneurysm, Annals of Biomedical Engineering 28 (SUPPL. 1) (2000) 1–6. doi:10.1299/jsmec.43.787.

[169] A. Borghi, N. B. Wood, R. H. Mohiaddin, X. Y. Xu, 3D geometric reconstruction of thoracic aortic aneurysms., Biomedical Engineering Online 5 (2006) 59. doi:10.1186/1475-925X-5-59.

[170] A. Borghi, N. B. Wood, R. H. Mohiaddin, X. Y. Xu, Patient-Specific Computational Modeling, in: Lecture Notes in Computational Vision and Biomechanics, Vol. 5, 2012, pp. 133–159.

[171] M. J. Davies, T. Treasure, P. D. Richardson, The pathogenesis of spontaneous arterial dissection., Heart 75 (5) (1996) 434–435. doi:10.1136/hrt.75.5.434.

[172] S. Pasta, J. S. Cho, O. Dur, K. Pekkan, D. A. Vorp, Computer modeling for the prediction of thoracic aortic stent graft collapse, Journal of Vascular Surgery 57 (5) (2013) 1353–1361. doi:10.1016/j.jvs.2012.09.063.

[173] G. Austin, Equation for model intracranial aneurysm with consideration of small dissipation term, Mathematical Biosciences 22 (C) (1974) 277–291. doi:10.1016/0025-5564(74)90095-9.

[174] P. B. Canham, G. G. Ferguson, A mathematical model for the mechanics of saccular aneurysms, Neurosurgery 17 (2) (1985) 291–295. doi:10.1227/00006123-198508000-00007.

[175] M. R. Roach, S. Scott, G. G. Ferguson, The hemodynamic importance of the geometry of bifurcations in the circle of Willis (glass model studies)., Stroke 3 (3) (1972) 255–267. doi:10.1161/01.STR.3.3.255.

[176] G. G. Ferguson, Physical factors in the initiation, growth, and rupture of human intracranial saccular aneurysms., Journal of Neurosurgery 37 (6) (1972) 666–677. doi:10.3171/jns.1972.37.6.0666.

[177] H. Meng, Y. Feng, S. H. Woodward, B. R. Bendok, R. a. Hanel, L. R. Guterman, L. N. Hopkins, Mathematical model of the rupture mechanism of intracranial saccular aneurysms through daughter aneurysm formation and growth., Neurological Research 27 (5) (2005) 459–65. doi:10.1179/016164105X25171.

[178] Y. Feng, H. Meng, A mathematical model on the rupture of intracranial aneurysms, in: Annual International Conference of the IEEE Engineering in Medicine and Biology - Proceedings, Vol. 2, IEEE, 2002, pp. 1335–1336. doi:10.1109/IEMBS.2002.1106415.

[179] S. K. Kyriacou, J. D. Humphrey, Influence of size, shape and properties on the mechanics of axisymmetric saccular aneurysms., Journal of Biomechanics 29 (8) (1996) 1015–22. doi:10.1016/0021-9290(96)00010-3.

[180] A. D. Shah, J. L. Harris, S. K. Kyriacou, J. D. Humphrey, Further Roles of Geometry and Properties in the Mechanics of Saccular Aneurysms, Computer Methods in Biomechanics and Biomedical Engineering 1 (2) (1998) 109–121. doi:10.1080/01495739708936698.

[181] J. D. Humphrey, R. K. Strumpf, F. C. P. Yin, A Constitutive Theory for Biomembranes: Application to Epicardial Mechanics, Journal of Biomechanical Engineering 114 (4) (1992) 461–466. doi:10.1115/1.2894095.

[182] P. Seshaiyer, J. D. Humphrey, On the potentially protective role of contact constraints on saccular aneurysms., Journal of Biomechanics 34 (5) (2001) 607–12. doi:10.1016/S0021-9290(01)00002-1.

[183] P. Seshaiyer, F. P. K. Hsu, A. D. Shah, S. K. Kyriacou, J. D. Humphrey, J. D. Humphrey, Multiaxial Mechanical Behavior of Human Saccular Aneurysms, Computer Methods in Biomechanics and Biomedical Engineering 4 (3) (2001) 281–289. doi:10.1080/10255840108908009.

[184] C. Chuong, Y. C. Fung, Three-Dimensional Stress Distribution in Arteries, Journal of Biomedical Engineering 105 (3) (1983) 268–274. doi:10.1115/1.3138417.

[185] A. A. Valencia, A. M. Guzmán, E. A. Finol, C. H. Amon, Blood flow dynamics in saccular aneurysm models of the basilar artery., Journal of Biomechanical Engineering 128 (4) (2006) 516–26. doi:10.1115/1.2205377.

[186] A. Valencia, D. Ledermann, R. Rivera, E. Bravo, M. Galvez, Blood flow dynamics and fluid-structure interaction in patient-specific bifurcating cerebral aneurysms, International Journal for Numerical Methods in Fluids 58 (10) (2008) 1081–1100. arXiv:fld.1, doi:10.1002/fld.1.

[187] R. Torii, M. Oshima, T. Kobayashi, K. Takagi, T. E. Tezduyar, Fluidstructure interaction modeling of blood flow and cerebral aneurysm: Significance of artery and aneurysm shapes, Computer Methods in Applied Mechanics and Engineering 198 (45-46) (2009) 3613–3621. doi:10.1016/j.cma.2008.08.020.

[188] X. Wang, X. Li, Biomechanical behaviour of cerebral aneurysm and its relation with the formation of intraluminal thrombus: a patient-specific modelling study, Computer Methods in Biomechanics and Biomedical Engineering 16 (11) (2012) 1–8. doi:10.1080/10255842.2011.652098.

[189] A. G. Radaelli, L. Augsburger, J. R. Cebral, M. Ohta, D. A. Rüfenacht, R. Balossino, G. Benndorf, D. R. Hose, A. Marzo, R. Metcalfe, P. Mortier, F. Mut, P. Reymond, L. Socci, B. Verhegghe, A. F. Frangi, Reproducibility of haemodynamical simulations in a subject-specific stented aneurysm model - A report on the Virtual Intracranial Stenting Challenge 2007, Journal of Biomechanics 41 (10) (2008) 2069–2081. doi:10.1016/j.jbiomech.2008.04.035.

[190] K. Takizawa, K. Schjodt, A. Puntel, N. Kostov, T. E. Tezduyar, Patient-specific computer modeling of blood flow in cerebral arteries with aneurysm and stent, Computational Mechanics 50 (6) (2012) 675–686. doi:10.1007/s00466-012-0760-4.

[191] D. S. Molony, A. Callanan, E. G. Kavanagh, M. T. Walsh, T. M. McGloughlin, Fluid-structure interaction of a patient-specific abdominal aortic aneurysm treated with an endovascular stent-graft., Biomedical Engineering Online 8 (24) (2009) 24. doi:10.1186/1475-925X-8-24.

[192] P. N. Watton, N. B. Raberger, G. A. Holzapfel, Y. Ventikos, Coupling the Hemodynamic Environment to the Evolution of Cerebral Aneurysms: Computational Framework and Numerical Examples, Journal of Biomedical Engineering 131 (10) (2009) 101003–101014. doi:10.1115/1.3192141.

[193] X. Li, P. Vlahovska, G. E. Karniadakis, Continuum and particle-based modeling of shapes and dynamics of red blood cells in health and disease, Soft Matter 9 (1) (2013) 28–37. arXiv:NIHMS150003, doi:10.1016/j.pestbp.2011.02.012.Investigations.

[194] G. Bao, S. Suresh, Cell and molecular mechanics of biological materials., Nature Materials 2 (11) (2003) 715–25. doi:10.1038/nmat1001.

[195] M. Dupin, I. Halliday, C. M. Care, L. Alboul, L. L. Munn, Modelling the flow of dense suspensions of deformable particles in three dimensions, Physical Review E - Statistical, Nonlinear, and Soft Matter Physics 75 (6 Pt 2) (2007) 066707. doi:10.1103/PhysRevE.75.066707.

[196] D. Barthes-Biesel, H. Sgaier, Role of membrane viscosity in the orientation and deformation of a spherical capsule suspended in shear flow, Journal of Fluid Mechanics 160 (1985) 119–135. doi:10.1017/S002211208500341X.

[197] T. W. Secomb, R. Skalak, N. Özkaya, J. F. Gross, Flow of axisymmetric red blood cells in narrow capillaries, Journal of Fluid Mechanics 163 (-1) (1986) 405. doi:10.1017/S0022112086002355.

[198] A. Leyrat-Maurin, D. Barthès-Biesel, Motion of a deformable capsule through a hyperbolic constriction, Journal of Fluid Mechanics 279 (1994) (1994) 135 – 163. doi:10.1017/S0022112094003848.

[199] E. Evans, New Membrane Concept Applied to the Analysis of Fluid Shear- and Micropipette-Deformed Red Blood Cells, Biophysical Journal 13 (9) (1973) 941–954. doi:10.1016/S0006-3495(73)86036-9.

[200] C. Pozrikidis, Effect of membrane bending stiffness on the deformation of capsules in simple shear flow, Journal of Fluid Mechanics 440 (2001) (2001) 269–291. doi:10.1017/S0022112001004657.

[201] M. Ju, S. Ye, B. Namgung, S. Cho, H. Low, H. Leo, S. Kim, A review of numerical methods for red blood cell flow simulation (2015). doi:10.1080/10255842.2013.783574.

[202] I. B. Petsche, G. S. Grest, Molecular dynamics simulations of the structure of closed tethered membranes, Journal de physique. I 3 (8) (1993) 1741–1755. doi:10.1051/jp1:1993213.

[203] D. H. Boal, Computer simulation of a model network for the erythrocyte cytoskeleton., Biophysical Journal 67 (2) (1994) 521–9. doi:10.1016/S0006-3495(94)80511-9.

[204] S. K. Boey, D. H. Boal, D. E. Discher, Simulations of the erythrocyte cytoskeleton at large deformation. Part 1: Microscopic models, Biophysical Journal 75 (3) (1997) 1573–1583. doi:10.1016/S0006-3495(98)74075-5.

[205] J. F. Marko, E. D. Siggia, Stretching DNA, Macromolecules 28 (26) (1995) 8759–8770. doi:10.1021/ma00130a008.

[206] M. Dao, C. Lim, S. Suresh, Mechanics of the human red blood cell deformed by optical tweezers, Journal of the Mechanics and Physics of Solids 51 (11-12) (2003) 2259–2280. doi:10.1016/j.jmps.2003.09.019.

[207] F. Janoschek, F. Toschi, J. Harting, Simplified particulate model for coarse-grained hemodynamics simulations., Physical Review. E, Statistical, Nonlinear, and Soft Matter Physics 82 (5 Pt 2) (2010) 056710. doi:10.1103/PhysRevE.82.056710.

[208] T. W. Pan, T. Wang, Dynamical simulation of red blood cell rheology in microvessels, International Journal of Numerical Analysis and Modeling 6 (3) (2009) 455–473. doi:10.1007/s11274-015-1903-5.

[209] M. Dupin, I. Halliday, C. Care, L. Munn, Lattice Boltzmann modelling of blood cell dynamics, International Journal of Computational Fluid Dynamics 22 (7) (2008) 481–492. doi:10.1080/10618560802238242.

[210] T. Itoh, S. Chien, S. Usami, Effects of hemoglobin concentration on deformability of individual sickle cells after deoxygenation., Blood 85 (8) (1995) 2245–53.

[211] H. Lei, G. E. Karniadakis, Quantifying the rheological and hemodynamic characteristics of sickle cell anemia, Biophysical Journal 102 (2) (2012) 185–194. doi:10.1016/j.bpj.2011.12.006.

[212] H. Lei, G. E. Karniadakis, Probing vasoocclusion phenomena in sickle cell anemia via mesoscopic simulations, Proceedings of the National Academy of Sciences 110 (28) (2013) 11326–11330. doi:10.1073/pnas.1221297110.

[213] D. A. Fedosov, M. Dao, G. E. Karniadakis, S. Suresh, Computational biorheology of human blood flow in health and disease, Annals of Biomedical Engineering 42 (2) (2014) 368–387. doi:10.1007/s10439-013-0922-3.

[214] H. Kondo, Y. Imai, T. Ishikawa, K. I. Tsubota, T. Yamaguchi, Hemodynamic analysis of microcirculation in malaria infection, Annals of Biomedical Engineering 37 (4) (2009) 702–709. doi:10.1007/s10439-009-9641-1.

[215] Y. Imai, H. Kondo, T. Ishikawa, C. Teck Lim, T. Yamaguchi, Modeling of hemodynamics arising from malaria infection, Journal of Biomechanics 43 (7) (2010) 1386–1393. doi:10.1016/j.jbiomech.2010.01.011.

[216] H. Bow, I. Pivkin, M. Diez-silva, S. J. Goldfless, M. Dao, J. C. Niles, S. Suresh, J. Han, A microfabricated deformability-based cytometer with application to malaria, Lab Chip 11 (6) (2011) 1065–1073. doi:10.1039/c0lc00472c.

[217] Y. Bazilevs, M. C. Hsu, D. J. Benson, S. Sankaran, A. L. Marsden, Computational fluid-structure interaction: Methods and application to a total cavopulmonary connection, Computational Mechanics 45 (1) (2009) 77–89. doi:10.1007/s00466-009-0419-y.

[218] M. M. Black, I. C. Howard, X. Huang, E. a. Patterson, A three-dimensional analysis of a bioprosthetic heart valve, Journal of Biomechanics 24 (9). doi:10.1016/0021-9290(91)90304-6.

[219] G. Dubini, M. R. de Leval, R. Pietrabissa, F. M. Montevecchi, R. Fumero, A Numerical Fluid Mechanical Study Of Repaired Congenital Heart Defects. Application To The Total Cavopulmonary Connection, Journal of Biomechanics 29 (1) (1996) 111 – 121. doi:10.1016/0021-9290(95)00021-6.

[220] A. J. Narracott, C. Zervides, V. Diaz, D. Rafiroiu, P. V. Lawford, D. R. Hose, Analysis of a mechanical heart valve prosthesis and a native venousvalve: Two distinct applications of FSI to biomedical applications, International Journal for Numerical Methods in Biomedical Engineering 26 (1) (2010) 421–434. arXiv:NIHMS150003, doi:10.1002/cnm.1323.

[221] E. Evans, Y. C. Fung, Improved measurements of the erythrocyte geometry, Microvascular Research 4 (4) (1972) 335–347.

[222] C. Yang, D. Tang, S. Atluri, Three-dimensional carotid plaque progression simulation using meshless generalized finite difference method based on multi-year MRI patient-tracking data, Computer Modeling in Engineering and Sciences 57 (1) (2010) 51–76. arXiv:NIHMS150003, doi:10.1016/j.drugalcdep.2008.02.002.A.

[223] X. Wang, X. Li, Fluid-structure interaction based study on the physiological factors affecting the behaviors of stented and non-stented thoracic aortic aneurysms, Journal of Biomechanics 44 (12) (2011) 2177–2184. doi:10.1016/j.jbiomech.2011.06.020.

[224] E. A. Evans, R. Skalak, Mechanics and Thermodynamics of Membranes, Journal of Biomechanical Engineering 102 (4) (1980) 345.

[225] P. Bagchi, Mesoscale Simulation of Blood Flow in Small Vessels, Biophysical Journal 92 (6) (2007) 1858–1877. doi:10.1529/biophysj.106.095042.

[226] D. Xu, E. Kaliviotis, A. Munjiza, E. Avital, C. Ji, J. Williams, Large scale simulation of red blood cell aggregation in shear flows, Journal of Biomechanics 46 (11) (2013) 1810–1817. doi:10.1016/j.jbiomech.2013.05.010.

[227] P. Rissland, Y. Alemu, S. Einav, J. Ricotta, D. Bluestein, Abdominal aortic aneurysm risk of rupture: patient-specific FSI simulations using anisotropic model., Journal of Biomechanical Engineering 131 (3) (2009) 031001. doi:10.1115/1.3005200.

Appendix C

Paper III - Vector-based discrete element method for solid elastic materials

The following journal paper has been submitted for review to *Computer Physics Communications*.

Vector-based discrete element method for solid elastic materials

Benjamin Owen*[a], Abouzied M.A. Nasar[a], Adrian R.G. Harwood[a], Sam Hewitt[a], Nicholas Bojdo[a], Bernard Keavney[b], Benedict D. Rogers[a], Alistair Revell[a]

[a] *School of Mechanical, Aerospace and Civil Engineering, University of Manchester, UK*
[b] *Division of Cardiovascular Sciences, University of Manchester, UK*

Abstract

This paper presents the vector-based discrete element method applied to elastic continua, including details of formulation, its implementation on graphics processing units (GPUs) for accelerating simulations and validation cases. Simulation of elastic continua has traditionally been realised through continuum-mechanics based methods such as finite elements while using discrete element methods have been restricted to small spatial and temporal scales due to the relatively high computational cost. The vector-based discrete element method, or V-model, overcomes the limitations of both traditional continuum-based mechanics and discrete element approaches to enable the possibility to model additional physics such as cracking, remodelling and rupture. However, for real applications, hardware acceleration of the simulations is required such as the successful execution of discrete methods on GPUs increases the feasibility of larger scale modelling. This paper presents the first implementation of the V-model on GPUs to model elastic continua. Implementations are developed and compared for both CPU and GPU with both static and dynamic validation studies to assess the performance of the method. Results demonstrate the ability of the method to model linear deformation within 1% of the analytical solution and provide qualitative representation of non-linear deformation. This highlights the need for future work to incorporate non-linear constitutive models to improve fidelity in these cases. The spatial rate of convergence with decreasing particle size is demonstrated to be approximately first order with a methodology to clarify selection of critical timesteps for a number of cases presented. The GPU implementation also demonstrates a 20x speed-up over the CPU implementation. The capabilities of the elastic V-model on a GPU is demonstrated by applying it to the stochastic modelling of material properties in a deforming beam.

Keywords: discrete element method, GPU acceleration, stochastic modelling

1. Introduction

Over the past 30 years, the use of numerical methods in the field of solid mechanics has vastly increased, modelling a range of applications including geological [1], energy generation [2], and biomedical [3]. Generally, these numerical methods belong to the continuum class whereby the solid is treated as a continuous mass rather than as a collection of discrete particles. The most common continuum-based method is the finite element method (FEM), utilised extensively in both academic and industrial applications, where the domain is discretised into a number of elements which have a specified number of nodes. The displacement of these nodes due to the effects of applied loads is dictated by an interpolation function known as a shape function. The combination of node and shape function specify the element type. The collection of nodal displacement thus gives the deformation of the discretised body. Several variants exist such as X-FEM which extends the governing differential equations to include discontinuous functions [4], allowing phenomena such as cracks and fractures to be more readily modelled without the need for remeshing of the domain as the feature develops.

Continuum methods are able to satisfy conservation laws and provide highly accurate results at large length scales for problems where material heterogeneity is well defined. However, at smaller scales,

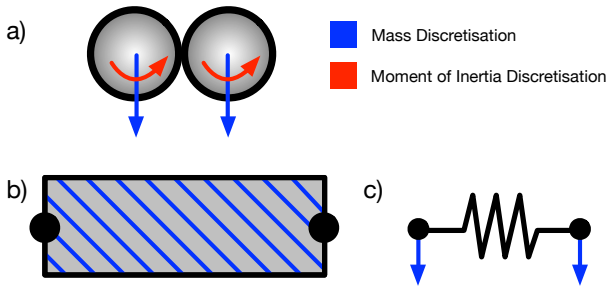

Figure 1: Mass and moment of inertia discretisation schematics of basic components of popular solid mechanics methods a) discrete element method (homogeneous, structured, connected at particle centre) b) finite element method (beam element), c) mass-spring model

the assumption of a continuous mass, neglecting the existence of space between particles within the solid, is questionable. Furthermore, when empty space or material heterogeneity is explicitly modelled with continuum-based methods dynamic contact variations and sliding introduce non-linearity to the governing equations thereby hindering convergence and stability [5].

At length scales for a given classification of material where its heterogeneity is important, the interface between volumes of material adjacent to voids or volumes of other materials must be clearly defined. A number of methods are inherently applicable to these problems such as molecular dynamics [6], lattice spring models [7] and discrete element methods [8]. These methods have traditionally been restricted to small length scales $O(10^{-3})$ due to the need for a large number of particles and hence a large computational cost. However, advances in computational architecture and the implementation of modelling techniques such as coarse graining [9], where the resolution of the model is reduced but the physics remain accurately represented, have resulted in the restrictions of spatial scales being relaxed. Furthermore, these methods are often based on local particle-particle relationships and explicit time integration procedures making them well-suited to parallelisation on both traditional architectures and more recent novel architectures such as Graphics Processing Units (GPUs).

A significant difference between various continuum and discrete approaches to modelling solid mechanics is the discretisation of the solid and the representation of mass, as shown in Figure 1. The simplest model, the mass-spring model, discretises the solid into a collection of point masses connected via springs. Usually only translational degrees of freedom are considered to reduce computational cost. Discrete element methods also discretise the solid into a collection of masses but additionally incorporate rotational degrees of freedom by modelling each mass as a particle of finite, non-zero size, to account for the moment of inertia. The commonly-implemented finite element method, on the other

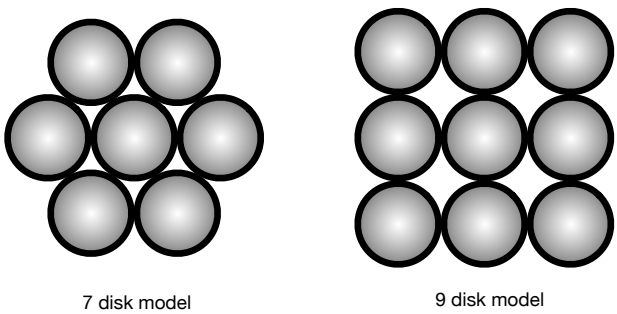

Figure 2: Structured discrete element arrangements commonly implemented for elastic continuous bodies. Left: 7-disk model. Right: 9-disk model. Constitutive models must be modified depending on implemented arrangement.

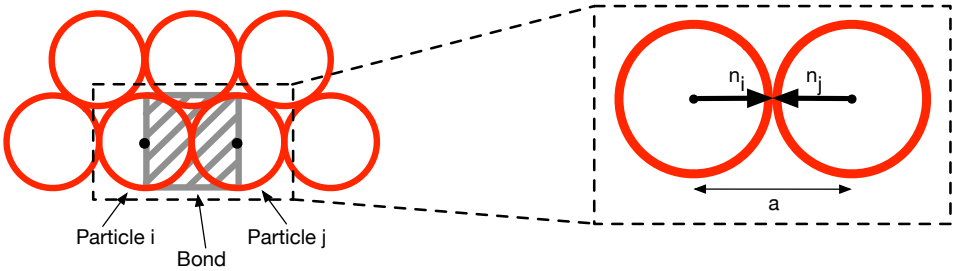

Figure 3: Bond connected to particle centres where bond length and particle diameter are equal.

hand, models the mass as a continuum and distributes it evenly across each element. Various element types exist that can model translational and rotational degrees of freedom as required, comparable to mass-spring models and discrete element methods.

The discrete element method (DEM), was originally proposed by Cundall in 1971 [10] for rock mechanics modelling and has since been utilised in a number of loose and bound granular material applications, to predict/simulate phenomena such as deformation [11], creep [12] and sintering [13]. More recently, a number of researchers have explored the possibility of using this method for elastic materials that have traditionally been modelled by continuum methods. The advantages include the ability to implement additional physics, such as fracture and aggregation, more readily within the model. This has made the technique attractive for complex multi-physics problems such as fluid-structure interaction [14] and electrically-induced structural deformation [8]. DEMs can represent elastic bodies by replacing contact forces between particles with bonds or connections that deform according to an elastic constitutive model.

However, developing constitutive models that are able to represent material properties that are mesh independent, such as Young's modulus and Poisson's ratio, is not trivial. Many constitutive models that have been developed are specific to a given particle arrangement such as the 7-disk and 9-disk arrangements shown in Figure 2, where the central element is connected to 6 and 8 surrounding elements respectively. The force and moments calculated between adjacent particles are generally split into normal and shear components and have been formulated for anisotropic [15] and non-linear [16] materials.

Here, a recent development of the discrete element method, known as the vector-based discrete element method (or V-model) is presented. Originally proposed by Kuzkin and Asonov [17], the method was further developed by Nasar et al. [14] for two dimensional representation of elastic solids. The V-model calculates forces and torques acting between bonded particles from a potential energy function, guaranteeing that the forces and torques are conservative and the bonds are perfectly elastic, while also being able to consider deformations due to longitudinal, shear, bending, and torsional loads. Furthermore, all displacements (translational and angular) are evaluated as total displacements in each degree of freedom using as single relationship. This ensures rotations are correctly evaluated for 3-D applications in comparison to DEMs where incremental updates are used.

In engineering applications, $O(10^8)$ DEM particles are generally required. This is infeasible with highly simplified codes that run on a single core and single thread since simulation results are required within a few days or less for many industrial applications. As a result, parallelisation of discrete element methods and in particular, implementation on GPU hardware due to the low cost in comparison to scientific computing grade CPU hardware, has become increasingly popular [18, 19]. In game physics, the key criterion is modelling in real-time, allowing some fidelity to be sacrificed in order to achieve this, while ensuring the deformation looks realistic to the user. Thanks to continuing performance improvements in computational hardware, the fidelity of models employed in games physics has greatly improved. As a result, DEM researchers have explored the possibility of using these models directly or exploiting the game physics optimisation procedures for their own discrete methods and applications

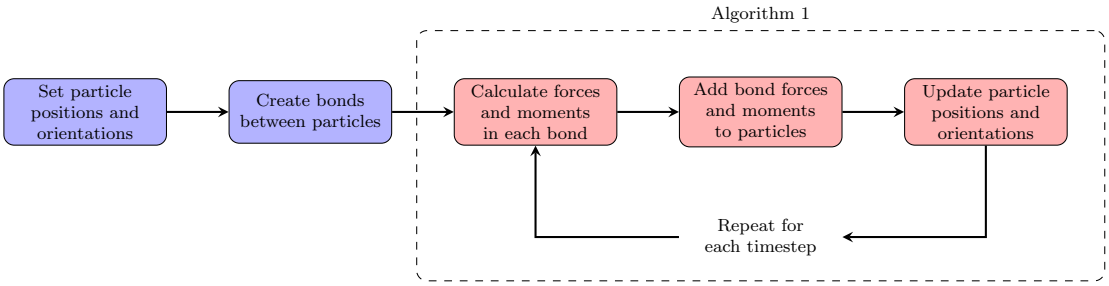

Figure 4: Flowchart of basic steps in V-model solver implemented on CPU architecture.

[20, 21]. Exploiting the computational acceleration of GPUs presents specific challenges including modification of solvers in order to leverage the massive throughput of data offered by GPUs. Herein, the V-model is implemented on a GPU for the first time.

This paper is structured as follows. First the methodology of the V-model is presented to enable the simulation of elastic continua. Then the numerical implementation of the two-dimensional model are explained in detail. Results are presented for static and dynamic validation cases to demonstrate the accuracy of the method and its suitability to model elastic continua. In particular, an investigation of the method's rate of convergence using standard procedures is the first of its kind for the V-model and allows comparison with traditional methods. This is followed by the implementation on GPU architecture and subsequent acceleration of computation. The GPU-accelerated elastic V-model is then applied to a deforming beam where stochastic variation of the material properties can be included. The paper finishes with conclusions and recommendations.

2. Methodology

2.1. Governing Equations

The discrete element method and its variants use Newton's second law to relate forces and moments within a system to particle positions and orientations as given in Eqns 1 and 2:

$$\boldsymbol{F}_i = m_i \boldsymbol{a}_i \tag{1}$$

$$\boldsymbol{M}_i = I_i \boldsymbol{\alpha}_i \tag{2}$$

where: $\boldsymbol{F}_i$ and $\boldsymbol{M}_i$ are the resultant force and moment on particle i; m_i and I_i are the mass and moment of inertia of particle i; and $\boldsymbol{a}_i$ and $\boldsymbol{\alpha}_i$ are the resulting translational and angular accelerations of particle i.

Discrete methods in macroscopic simulations consider forces and moments from a number of sources, both internal and external, including friction, contact forces between particles, body forces and attractive potentials. These are included in the governing equations:

$$\boldsymbol{F}_i = \boldsymbol{F}_i^{ext} + \sum \boldsymbol{F}_i^{int} \tag{3}$$

where $\boldsymbol{F}^{ext}$ and $\boldsymbol{F}^{int}$ are external and contact forces.

Discrete element methods at larger spatial scales ($x > 10^{-2}m$) have generally been applied to granular solids whereby the contact forces are modelled using collision models [22]. However, for elastic materials these contact forces can be modelled using constitutive relationships such as those provided by Griffiths and Mustoe for the 7 disk arrangement [23] and Liu and Liu for the 9 disk model [15]. For the work in this paper we use the method proposed by Griffiths and Mustoe.

The V-model, like many other DEM models, discretises the solid into a number of particles connected via bonds. While contact forces between particles not connected via a bond are not required for the tests in this paper, a number of contact models have been developed for cases where particle interactions between distinct bodies are under consideration [24].

In this method, bonds are modelled as if they were connected to particle centres, thus giving a bond length equal to the diameter of each particle as seen in Figure 3. V-model bond stiffness parameters, B_n, can be derived to represent the structural properties of a given material via its axial stiffness C_A, shear stiffness C_D and bending stiffness C_B. Kuzkin and Krivtsov [25] show that the relationship between the B_n parameters and the bond stiffnesses may be written as:

$$B_1 = C_A \tag{4}$$

$$B_2 = C_D L^2 \tag{5}$$

$$B_3 = C_B - \frac{B_2}{4} \tag{6}$$

Using the constitutive relationships derived by Griffiths and Mustoe for 2-D cases with plane stress, bond stiffnesses are defined as:

$$C_A = \frac{E}{\sqrt{3}(1-\nu)} \tag{7}$$

$$C_D = \frac{E(1-3\nu)}{\sqrt{3}(1-\nu^2)} \tag{8}$$

$$C_B = \frac{EI_b}{l} \tag{9}$$

where E is Young's modulus, ν is Poisson's ratio and I_b is the bond moment of inertia.

The forces and moments in the bonds are calculated in response to translational and rotational movement of particles i and j attached to each bond with respect to their initial configuration relative to each other. The governing equations are written as [17]:

$$\boldsymbol{F_{ij}} = B_1(r_{ij} - a)\boldsymbol{r_{ij}} + \frac{B_2}{2r_{ij}}(\boldsymbol{n_j} - \boldsymbol{n_i}) \cdot (\boldsymbol{I} - \boldsymbol{e_{ij}}\boldsymbol{e_{ij}}) \tag{10}$$

$$\boldsymbol{F_{ji}} = -\boldsymbol{F_{ij}} \tag{11}$$

$$\boldsymbol{M_{ij}} = -\frac{B_2}{2}\boldsymbol{e_{ij}} \times \boldsymbol{n_i} + B_3\boldsymbol{n_j} \times \boldsymbol{n_i} \tag{12}$$

$$\boldsymbol{M_{ji}} = \frac{B_2}{2}\boldsymbol{e_{ij}} \times \boldsymbol{n_j} - B_3\boldsymbol{n_j} \times \boldsymbol{n_i} \tag{13}$$

Vectors $\boldsymbol{n}$ are used to evaluate the relative orientation of bonded particles at each instance of time. These vectors are rigidly attached to the particles at the point where the bond and particle are connected as shown in Figure 3 and follow the angular and translational displacement of the particle. $\boldsymbol{r_{ij}}$ is the position vector between particles i and j, $\boldsymbol{r_{ij}} = \boldsymbol{r_j} - \boldsymbol{r_i}$, $r_{ij} = |\boldsymbol{r_{ij}}|$, $\boldsymbol{e_{ij}} = \frac{\boldsymbol{r_{ij}}}{r_{ij}}$ and I is the identity matrix. From Eqns. 10-13 it is clear that the forces and moments are a function not only of the relative orientation of bonded particles but also the relative orientation of the particles with respect to the bond connecting them. Detailed derivations of Eqns. 10-13 can be found in [17]. Once the forces and moments in each bond have been calculated and applied to particles i and j, the resultant forces and moments on each particle are calculated using:

$$\boldsymbol{F_i} = \sum_{k=1}^{b} \boldsymbol{F_{ij}} - \sum_{k=1}^{c} \boldsymbol{F_{ji}} \tag{14}$$

$$\boldsymbol{M_i} = \sum_{k=1}^{b} \boldsymbol{M_{ij}} - \sum_{k=1}^{c} \boldsymbol{M_{ji}} \tag{15}$$

where limits b and c are the number of bonds where the particle under consideration is assigned as particle i and particle j respectively. Note that the sum of b and c is equal to the total number of bonds connected to the particle under consideration, which in this implementation is 6 except for particles located at the boundary of the geometry where fewer bonds are formed.

Our applications of the V-model consist primarily of fluid-structure interaction problems and hence our solver is being designed to integrate with the LUMA flow solver [26] where damping due to fluid viscosity will dominate. As a result, damping within the structure is not implemented within the model for the dynamic validation cases. However, in order to obtain quasi-static results in our isolated validation case, a simple viscous damping model proportional to the relative velocity of the V-model particles and a mesh dependent damping coefficient, η, is used as an artificial damping source defined as:

$$\eta = 2\sqrt{m_i C_A} \tag{16}$$

where the V-model differs from traditional DEMs is that forces and moments within the bond are calculated not only as a function of the particles connected together, but also with respect to the orientation of the bond itself. This distinction is important for some cases. Consider a case where two connected particles are rotated equally in the same direction without any translational displacement. Using traditional DEM, calculating forces and moments as a function of orientation with respect to the connected particles only, results in no forces and moments since there has been no displacement relative to the other particle where as the V-model calculates the force and moment with respect to the bond and therefore provides a force within the system.

3. Numerical implementation

In order to carry out a simulation, Eqns. 10-13 need to be calculated at discrete points in time given a set of initial conditions for the particles and bonds. Computed forces and moments are then integrated over the time step to allow updating of the positions and orientations of bonds. Figure 4 illustrates the simulation steps with **Algorithm 1** providing a description of the steps involved in performing the updates. Algorithm 1 may be adapted during implementation to allow optimisation for a given architecture as discussed in Section 6.

The basic premise of the algorithm is to set up vectors containing particle positions and orientations in a decomposed 2-D Cartesian coordinate system, one vector per axis is created to store particle positions in each Cartesian coordinate and a vector is created to represent orientation, whereby the indices of the vectors correspond to particle identification (ID) numbers. A matrix of dimension [2 $\times$ number of bonds] stores pairs of IDs for particle i and particle j attached to each end of a bond. The algorithm loops over this bond matrix, calculating the forces and moment in each bond via Eqns 10-13 and applying them to particles i and j via Eqns 14 and 15. Once the total forces and moments acting on each particle have been calculated, Eqns 1 and 2 are used to evaluate the translational, $\boldsymbol{a}$ and angular, $\boldsymbol{\alpha}$ accelerations. An explicit numerical time integration scheme is then used to update the position $\boldsymbol{x}$ and orientation $\boldsymbol{\theta}$ of each particle via their linear $\boldsymbol{u}$ and angular $\boldsymbol{\omega}$ velocities. The numerical time integration scheme implemented in this article is commonly known as Beeman's method [27, 28] and is defined in Eqns 17-20:

$$\boldsymbol{u}_i^{t+\Delta t} = \boldsymbol{u}_i^t + \frac{1}{6}(2\boldsymbol{a}_i^{t+\Delta t} + 5\boldsymbol{a}_i^t + \boldsymbol{a}_i^{t-\Delta t})\Delta t \tag{17}$$

$$\boldsymbol{x}_i^{t+\Delta t} = \boldsymbol{x}_i^t + \boldsymbol{u}_i^{t+\Delta t}\Delta t + \frac{1}{6}(4\boldsymbol{a}_i^t - \boldsymbol{a}_i^{t-\Delta t})\Delta t^2 \tag{18}$$

$$\boldsymbol{\omega}_i^{t+\Delta t} = \boldsymbol{\omega}_i^t + \frac{1}{6}(2\boldsymbol{\alpha}_i^{t+\Delta t} + 5\boldsymbol{\alpha}_i^t + \boldsymbol{\alpha}_i^{t-\Delta t})\Delta t \tag{19}$$

$$\boldsymbol{\theta}_i^{t+\Delta t} = \boldsymbol{\theta}_i^t + \boldsymbol{\omega}_i^{t+\Delta t}\Delta t + \frac{1}{6}(4\boldsymbol{\alpha}_i^t - \boldsymbol{\alpha}_i^{t-\Delta t})\Delta t^2 \tag{20}$$

where t is the current time and Δt is the size of the time step. Once the orientations of the particles have been updated, vector $\boldsymbol{n}$ can be updated for each bond the particle is connected to using its initial value, $\boldsymbol{n}^0$, and the updated particle orientation via a rotation matrix:

$$\begin{bmatrix} \boldsymbol{n}_{i,x}^{t+\Delta t} \\ \boldsymbol{n}_{i,y}^{t+\Delta t} \end{bmatrix} = \begin{bmatrix} cos\theta_i^{t+\Delta t} & -sin\theta_i^{t+\Delta t} \\ sin\theta_i^{t+\Delta t} & cos\theta_i^{t+\Delta t} \end{bmatrix} \begin{bmatrix} \boldsymbol{n}_{i,x}^0 \\ \boldsymbol{n}_{i,y}^0 \end{bmatrix} \tag{21}$$

A key modification in this algorithm from traditional discrete element implementations is that the creation of bonds only occurs once, during the initialisation stage of the model rather than once per timestep. Given that in an elastic body, particles are robustly connected (assuming that they remain elastic hence avoiding modelling fracture, cracking or aggregation) one can assume that these connections are independent of time and therefore a nearest neighbour search to find each connection is unnecessary, improving the computational efficiency of the method.

Algorithm 1 V-model Solver - psuedocode syntax. Algorithm includes time dependent solver components only as indicated by the dashed box in Figure 4

```
for No. of Timesteps do
    for No. of Bonds do
        Calculate F_ij and M_ij using Eqn 10 & 12 and add to F_i and M_i
        Calculate F_ji and M_ji using Eqn 11 & 13 and add to F_j and M_j
    end for
    for No. of Particles do
        Apply external loads to each particle
    end for
    for No. of Particles do
        Calculate linear and angular accelerations of each particle using Newton's 2nd law using Eqn 1 & 2
        Update linear and angular velocities of particles via time integration scheme using Eqn 17 & 19
        Update position and orientation of particles via time integration scheme using Eqn 18 & 20
    end for
    for No. of Particles do
        Apply boundary conditions
    end for
    for No. of Bonds do
        Update particle vectors n_i, n_j using initial particle vectors and updated orientations using Eqn. 21
    end for
    for No. of Particles do
        Update values stored for particle properties at t − Δt and t using the values currently stored for t and t + Δt respectively
    end for
end for
```

3.1. Critical timestep

Using the explicit time stepping scheme presented in Section 3, if the timestep size is too large, the simulation will be numerically unstable causing significant errors to occur. The value between a stable and unstable timestep size is known as the critical time step. Critical time steps are much smaller for DEMs, which rely on explicit time integration schemes, than for traditional continuum methods such as FEM where implicit schemes are more common.

A number of previous works have proposed various criteria for defining a critical timestep based upon empirical data and Gerschgorin's theorem [29, 30]. Many of these criteria relate the critical timestep size to the smallest period of oscillation resulting from the highest natural frequency [31] and are functions of minimum particle mass, particle connection stiffness coefficients and the number of connections per particle, known as coordination number. However, these criteria include a *safety factor* less than 1 in order to ensure stability of the simulation and are recommended as estimates rather than definitive criteria. The critical timestep Δt_{crit} used for the work in this article is given as:

$$\Delta t_{crit} = \beta \sqrt{\frac{m_i}{k}} \tag{22}$$

where m_i is the mass of a particle i and k is equal to the largest material stiffness coefficient, C_A. For the purposes of this work a conservative factor, $\beta = 0.05$ has been used to ensure stability of the method and robustness of validation results. Values of β lower than 0.05 can be implemented but will produce the same results and require greater computational resource.

4. Validation Cases

4.1. Quasi-static cantilever beam

To demonstrate the ability of the V-model to represent macroscopic problems, the well-studied tip-loaded cantilever beam test is chosen as a validation case and the results predicted by the V-model solver are compared against the analytical solution proposed by Wang et al. [32]. The cantilever beam studied has a length of 1m and width of 0.0683 m as shown in Figure 5. The dimensions of the beam were chosen so that the aspect ratio of the discretised beam remains constant when discretised into a structured triangular arrangement (7-disk) and the resolution is increased by a factor of two. In addition, the aspect ratio of the beam is chosen to be large enough to provide the opportunity to test the solver for linear and non-linear deformation. With the structural analysis restricted to two-dimensions, the beam has unit depth perpendicular to the 2-D plane. The material properties of the beam are given in Table 1, and loads between 100 and 500N were applied in 100N increments.

To find the static equilibrium position of the beam for a given load, viscous damping was applied to the V-model particles using Eqn 16. Tip deflection time histories for the under-damped, critically damped and over-damped cases shown in Figure 6. In each case, the beam tip settles to the same equilibrium position as shown in Figure 7. For the quasi-static validation presented, the beam is critically

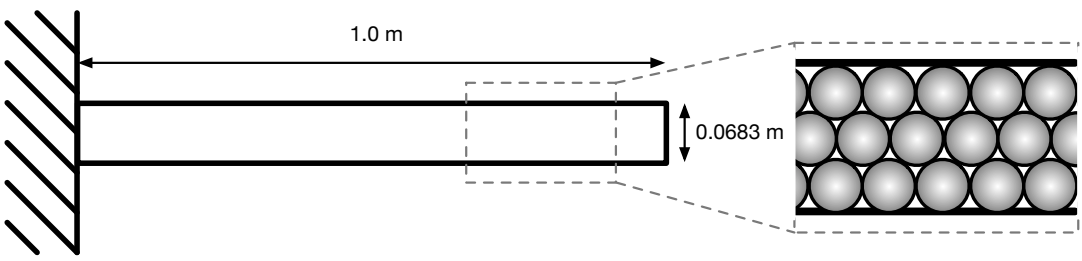

Figure 5: Schematic of validation case (left) with V-model particle discretisation (right). Beam dimensions chosen to ensure that as resolution is doubled, aspect ratio of the beam remains constant.

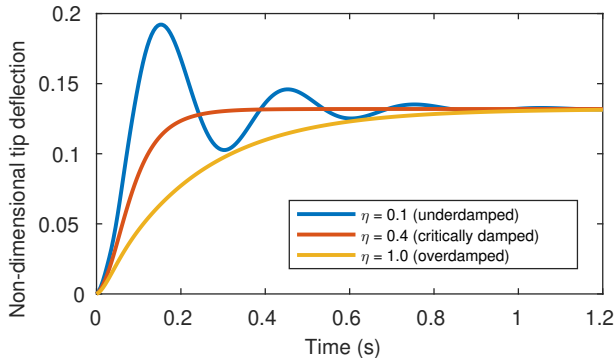

Figure 6: Cantilever beam test - tip deflection time history for 3 cases using different values for η.

damped for each load and resolution case and results are presented in terms of non-dimensionalised (ND) loads and tip deflections.

Results shown in Figure 8 for the error are in good agreement with the analytical solution, especially at lower deflections (<20% of beam length) where at the highest resolution an error of $< 1\%$ is observed. At higher deflections, the V-model does not perform as well. However, this is to be expected since the governing equations do not account for geometric non-linearity in bond deformation; the derivations of Kuzkin and Asonov [17] and Griffiths and Mustoe [23] both assume bonds undergo small deflections since the cross-sections of the bonds are not updated while undergoing deformation. Still, resolution refinement improves the results since the deflection experienced by each bond becomes smaller with refinement. The development and implementation of constitutive relationships capable of capturing this geometric non-linearity is currently ongoing.

When the condition of constant aspect ratio is not imposed to the discretisation of the beam, as resolution increases fluctuations in the tip deflection error occur despite a general trend of reducing error as shown in Figure 9. Here, the resolution has been increased by adding an extra particle across the beam width, effectively adding a row of particles each increment, without the requirement of aspect ratio remaining exact. The error for each resolution is defined as:

$$error = \frac{x_{max}^{V-model} - x_{max}^{analytical}}{x_{max}^{analytical}} \tag{23}$$

Reduction in error is larger in the low deformation case since this is in the linear geometric region

Property	Value
Beam Dimensions	
Length (m)	1
Width (m)	0.0683
Depth (m)	1
Material Properties	
Density (kgm^{-3})	100
Young's modulus (Pa)	10^7
Poisson's ratio	0.33

Table 1: Dimensions and material properties of the beam under investigation in the quasi-static tip loaded cantilever beam case.

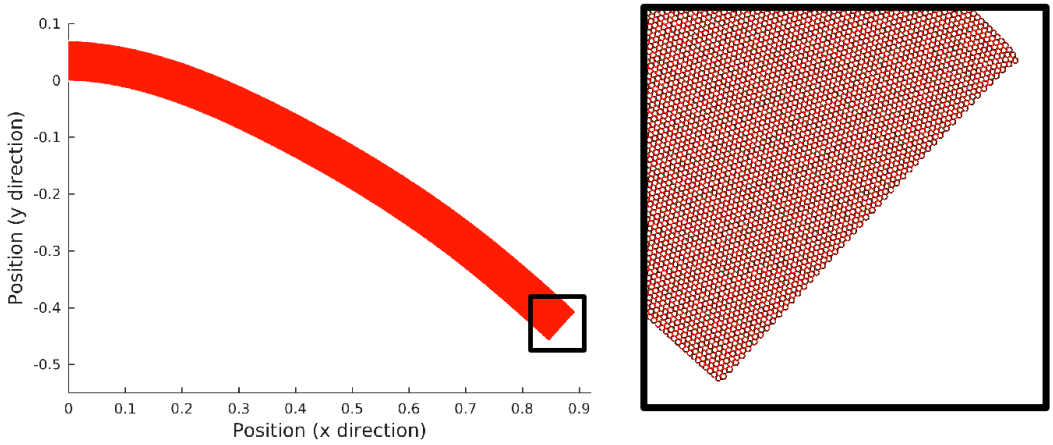

Figure 7: Particle positions at static equilibrium using highest resolution model: 117024 particles (96 particles across beam width).

in which the constitutive model is valid where as in the high deformation case it is highly non-linear. These fluctuations are caused due to inconsistencies discretising geometries using structured particle arrangements; it may not be possible to discretise the geometry exactly although in the validation cases presented here, the geometric dimensions of the beam have been chosen to allow exact discretisation.

4.2. Dynamic cantilever beam

The ability of the model to predict transient behaviour with high fidelity, is critical in applications such as fluid-structure interaction. In order to assess the capabilities of the method, a cantilever beam with the same properties as the quasi-static case, is subjected to a constant tip load of 100N. The

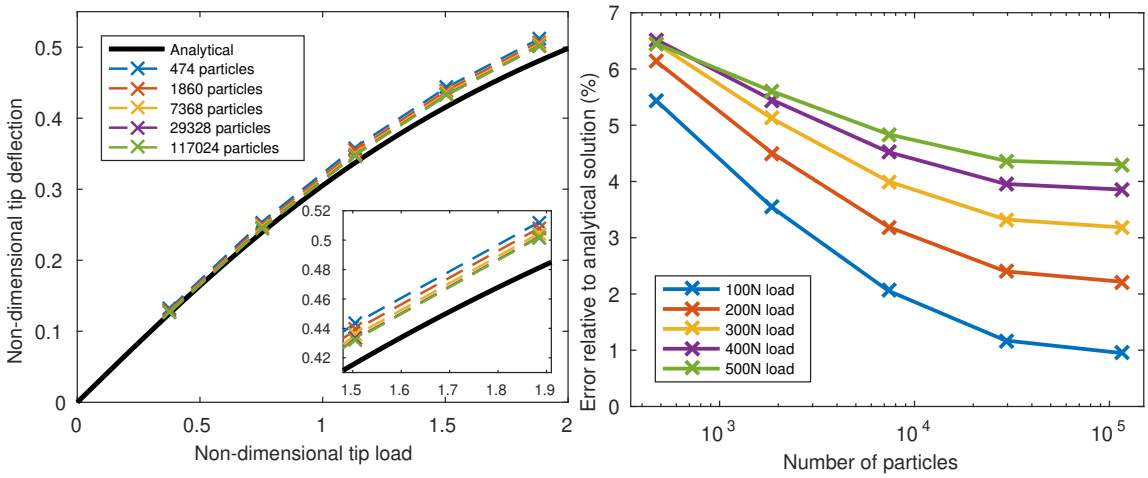

Figure 8: Quasi-static tip loaded cantilever beam. Left: Comparison of analytical solution and V-model results for tip deflection with increasing non-dimensionalised load. Right: Tip deflection error at static equilibrium for V-model resolutions relative to analytical solution with increasing spatial resolution for different non-dimensionalised loads.

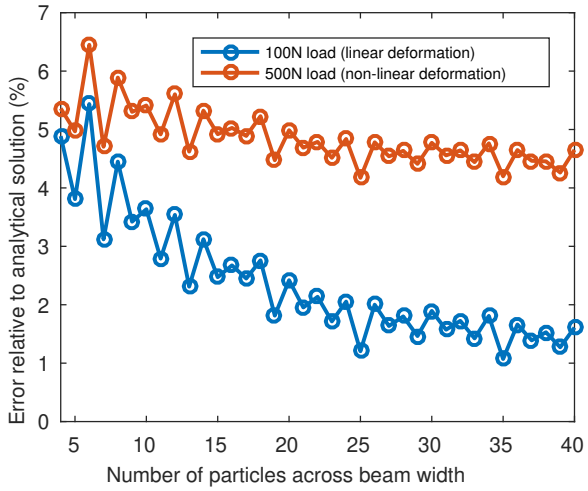

Figure 9: Quasi-static tip loaded cantilever beam test. Errors relative to analytical solution for low and high deformations corresponding to the lowest and highest loads shown in Figure 8.

tip deflection profile time history is recorded with no viscous damping within the system. Again, the resolution of the V-model was increased and the results compared with a grid independent solution obtained through a commercial non-linear FEM solver (ABAQUS 17).

From tip deflection time histories shown in Figure 10, it can be seen that the V-model provides excellent agreement in terms of amplitude and phase with the non-linear FEM solution, even where the level of deformation is non-linear. Furthermore, the V-model is able to capture higher-order modes of vibration. These modes of vibration are evident even when the resolution of the V-model is very low, demonstrating the robustness of the method.

The final case replaces the constant load with a time dependent load ($\boldsymbol{F}_{ext} = 100\cos(40t)$), rep-

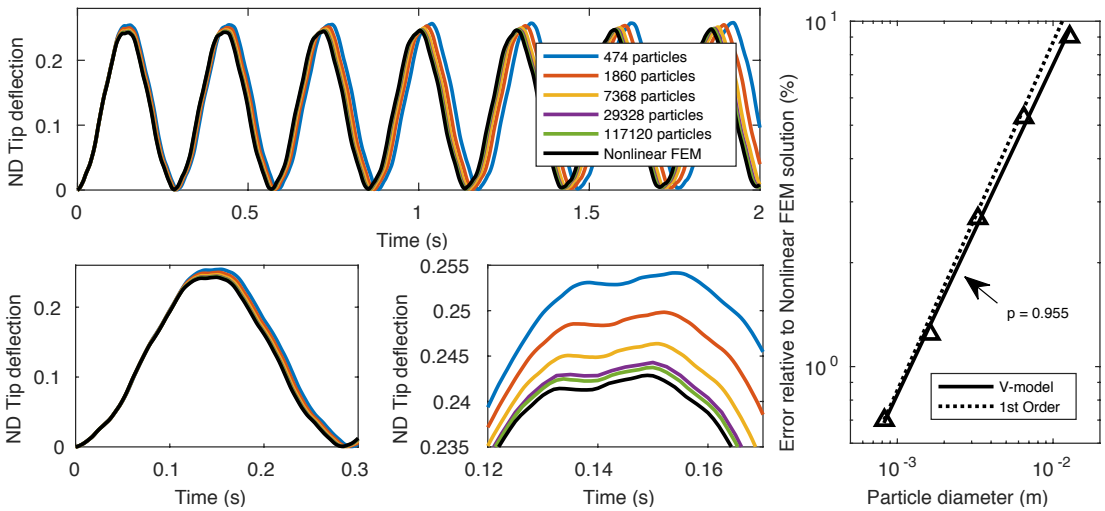

Figure 10: Left: Comparison of non-linear FEM solution (ABAQUS 17) and increasing V-model resolution results for tip deflection of constant tip loaded cantilever beam with. Right: Convergence rate with increasing spatial resolution (number of particle across beam width) for the dynamic tip-loaded cantilever beam case.

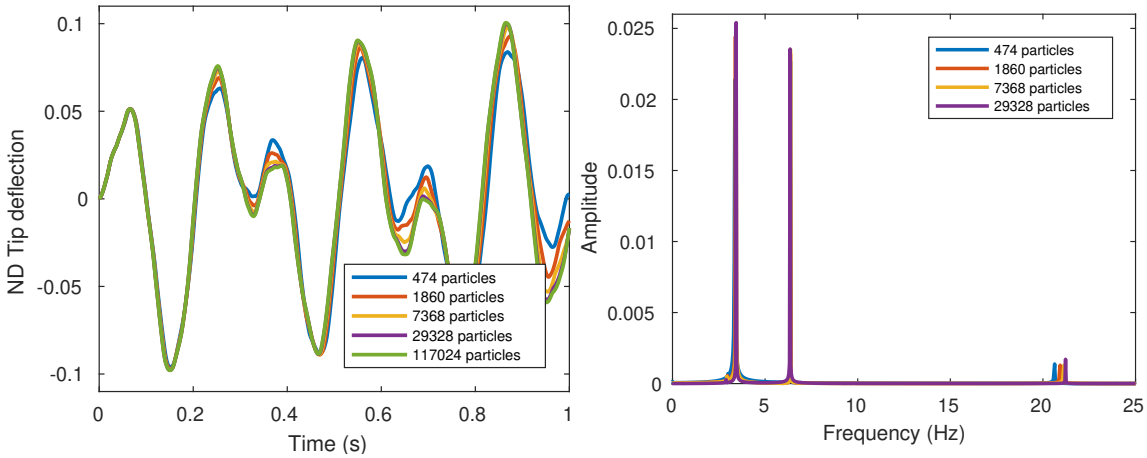

Figure 11: Left: Forced vibration case: Tip deflection for beam with increasing V-model resolution. Right: Power spectrum for forced vibration case with increasing V-model resolution.

resenting a forcing frequency. Tip deflection time histories shown in Figure 11 demonstrate good convergence despite the complex nature of the case. A power spectrum of the tip deflection time history shows the first harmonic is modelled well even at low resolutions, meaning that any differences in the tip deflection are a result of the differences in the second natural frequency which exhibits greater dependence on resolution. Also worth noting is that the desired forcing frequency is accurately modelled despite being applied to a single particle at the tip whose properties, including position, mass and moment of inertia, are dependent on resolution.

Although these cases demonstrate that the V-model is capable of achieving a high degree of accuracy, it is worth noting that for high resolutions the computational time required by the V-model is not insignificant with the highest resolution V-model case using GPU architecture requiring an order of magnitude higher computational time than that for the non-linear FEM solver.

4.3. Rate of Convergence

There have been few studies of convergence properties in discrete element methods due to the difficulty in identifying a factor to base the rate of convergence on. Tavarez & Plesha [33] reported the first convergence rates for DEMs in elastic bodies. However, it was stated that the validity was restricted to relatively high resolutions i.e. low resolutions would not provide a constant rate of convergence. This phenomenon was independently observed by the authors, also observed in 9. The fluctuation in relative accuracy decreases with increasing resolution defined by the number of particles across the beam in the y direction. Interestingly, it can be seen that resolutions with an odd number of particles across the beam are consistently more accurate than those that are even with similar resolution.

A convergence study was performed by comparing the maximum tip deflection predicted by the V-model for the dynamic tip loaded cantilever to that predicted by the non-linear FEM solver. The error was evaluated for 5 resolutions using Eqn 24:

$$error = \frac{x_{max}^{V-model} - x_{max}^{FEM}}{x_{max}^{FEM}} \tag{24}$$

In order to avoid the fluctuations in error seen in Figure 9 the resolution is doubled across the width of the beam, ensuring the aspect ratio of the beam remains constant. An order of convergence of ≈ 0.95 can be observed in Figure 10 which is in approximate agreement with the first-order convergence of [33].

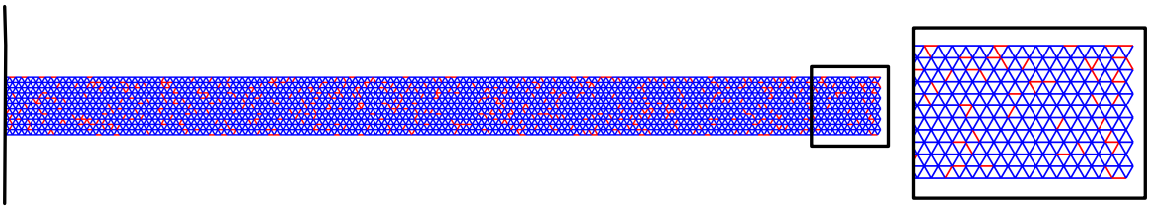

Figure 12: Example Young's Modulus distribution in a beam where 90% of the bonds are E_1 (blue) and 10% are E_2 (red).

5. Stochastic Modelling of Material Properties

A significant advantage of the V-model is its ability to include variation in material properties with no additional mathematical treatment required within the solver or increase in computational load. The possibility to integrate stochastic material properties is thus straightforward. Within this section, the constant load validation case presented in Section 4.2 is used to investigate two stochastic material property cases.

The first, with applications in additive manufacturing, consists of a beam made up of two different materials (represented by different Young's modulus values) randomly dispersed within the structure. The distribution of the two materials is random. This case is representative of 3-D printing composites where the structure of the composite is not uniform, for example, in 3-D printed graphene where graphene flakes are dispersed within a polymer [34]. Homogeneous beams with Young's Modulus values of $E_1 = 10$ MPa and $E_2 = 50$ MPa are used as validated reference results, acting as likely bounds to stochastic results. One hundred random distributions of bond stiffnesses within this range are used to generate test cases. An example distribution is shown in Figure 12.

Instantaneous tip deflection for each test beam (distribution of the combinations) is presented in Figure 13 along with the mean deflection for a set of test beams. A linear trend towards the homogeneous E_2 beam can be seen for the mean deflection as the component of E_2 is increased, as is expected. However, this case highlights the requirement to test multiple distributions given the

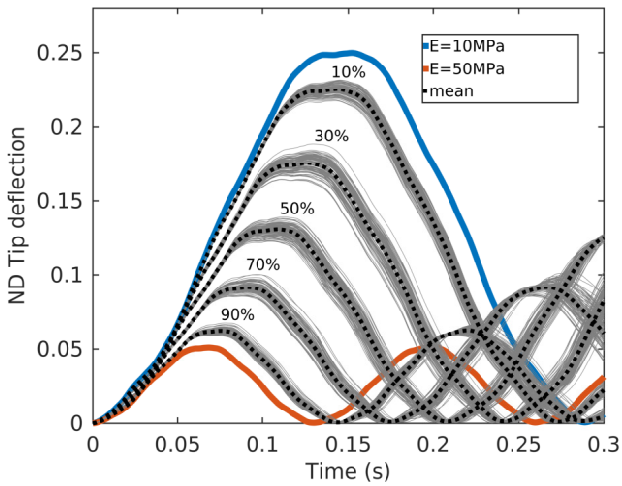

Figure 13: Non-dimensional tip deflection for sets of beam containing bonds of two different Young's moduli. 100 distributions are modelled for each configuration (grey) where the labelled percentage refers to the proportion of the E_2 material. Mean tip deflection time histories (black dashed) for each set are presented.

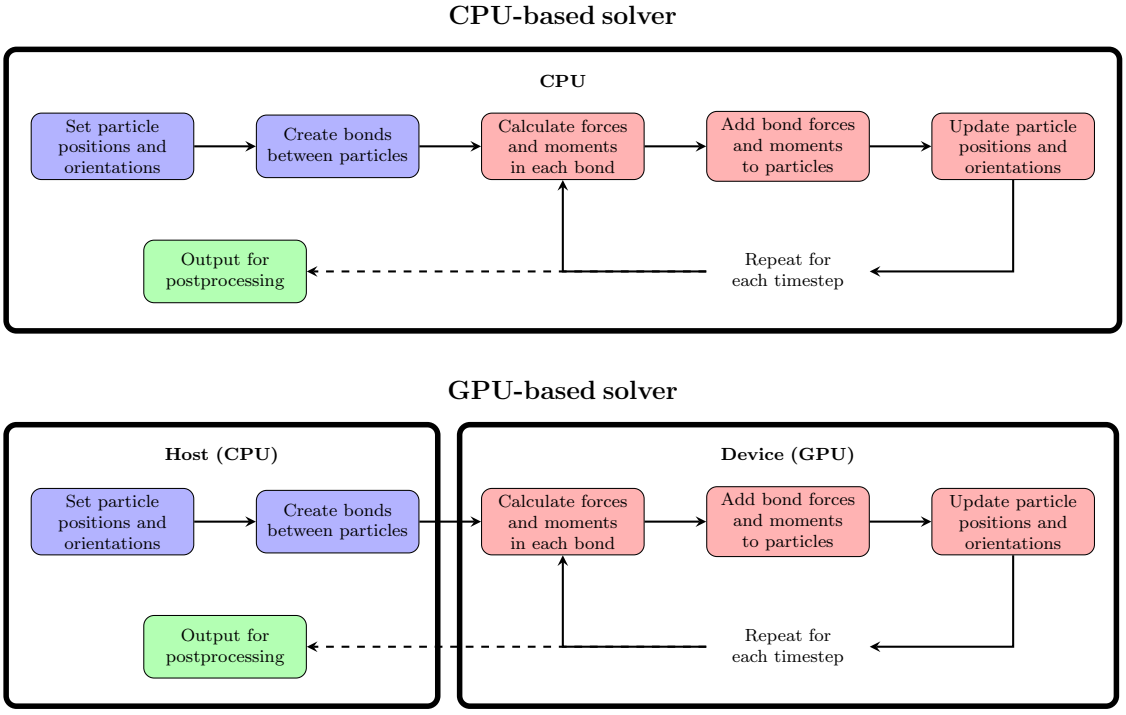

Figure 14: Overview of code architecture for CPU (top) and GPU (bottom) implementation. All code is executed on the CPU in the CPU-based solver whereas in the GPU-based solver, set-up and initialisation of the method remains on CPU, while Algorithm 1 (Figure 4) is passed to device memory and is executed by the GPU. Output for post-processing occurs at specified time intervals.

large variation in the tip deflection for the same quantity of each component material, illustrating the sensitivity to material and therefore stiffness distribution.

6. GPU implementation

Implementation of numerical analysis on GPU architecture can lead to significant reductions in computational times in comparison to CPU architecture and has been applied to fluid mechanics [35] as well as discrete element methods [18]. Given the spatially local and explicit nature of the V-model, it is well suited to implementation on GPU architecture where the relatively simple instructions can be parallelised across a greater number of GPU threads compared to parallelised CPU architecture. Here the GPU solver is implemented using the NVIDIA CUDA API [36] and tests are run on a GTX1060 GPU with 6GB of RAM while the serial CPU solver was run on an Intel Core i7-7700HQ 2.8GHz/3.80 GHz with 16GB of RAM. Figure 15 shows the execution time per timestep and relative speed-up between CPU and GPU implementations.

Data layout has a critical role to play in the performance of GPU applications given the relatively high cost for compute threads to access data stored in global memory (DRAM). Our solver arranges data in 1-D arrays where each position in the array corresponds to bonds or particles depending on the variable and its usage pattern in the related kernel.

The GPU implementation is developed by modifying **Algorithm 1** such that outer loops may be removed and replaced with many-thread parallelisation. Furthermore, the layout of data in the GPU memory is designed to keep costly memory transactions to a minimum. Data is initialised first using the CPU-based (host) application thread and stored in system memory (host memory) before being copied to GPU memory (device memory). The process is depicted in Figure 14. Time stepping is

Kernel ID	Thread Count	Lines
1	Bonds	3,4
2	Particles	7
3	Particles	10-12
4	Particles	15
5	Bonds	18
6	Particles	21

Table 2: Thread count parameter and corresponding lines of pseudo-code in Algorithm 1 for each kernel launched by GPU solver.

then carried out by the GPU on the device through launching a number of kernels each time step with details of each provided in Table 2.

Given the data organisation, the GPU spawns parallel computing threads such that one thread is capable of calculating the forces and moments in a single bond. In order to output data for post-processing, time dependent particle properties must be copied back to host memory. This process can be costly in terms of computational time and therefore takes place at specified intervals only.

The GPU implementation of the V-model can be summarised as follows:

1. Create vectors of size equal to the total numbers of particles/bonds for each particle/bond property in host memory
2. Create space on GPU in global memory for each of vector using cudaMalloc()
3. Pass contents of each vector to GPU global memory using cudaMemcpy(cudaMemcpyHostToDevice)
4. Calculate number of blocks required for each kernel launch based on thread counts in Table 2.
5. Launch kernels 1-6 sequentially, repeating the desired number of timesteps
6. Pass required particle/bond properties back to host global memory at specified intervals for output using cudaMemcpy(cudaMemcpyDeviceToHost)

Figure 15 (left) shows the computational time required for a single timestep at different resolutions using the V-model solver implemented on each architecture type. At low resolutions, the CPU solver performance is greater than that of the GPU solver due to the associated overheads of data copying and thread creation when using GPUs. In addition, at these low resolutions, there are fewer particles and bonds than can be parallelised by the GPU simultaneously and therefore the GPU is not fully utilised. This is highlighted by the small increase in computational time per timestep when using GPU hardware up to particle resolutions of $O(10^3)$ where the GPU is reaches the point of full parallelisation. A second order increase in computational time per timestep for the serial CPU solver can be seen, as expected, while the GPU solver also exhibits this behaviour beyond the point of full parallelisation. However, as the resolution is increased, GPU solution time is shown to drop to approximately 1/20 of the time required by the CPU solver for the test with resolution of $> 100,000$ particles. This is due to the significant reduction in computational time required to complete 1 time step per particle using the GPU while it remains relatively constant using the CPU as shown in Figure 15 (middle). Further reduction should be possible through the use of the GPUs specifically designed for scientific computing rather than graphics rendering such as the NVIDIA Tesla series. The reason for this is that owing to the small particle rotations, the V-model is currently reliant on double precision calculations. Consumer-grade GPU processors are designed and optimised for single precision calculations, leading to sub-optimal performance in this application.

In the current implementation of the V-model solver, particle and bond properties are stored in individual vectors whereby the index of the vector corresponds to the particle or bond ID. Alternative

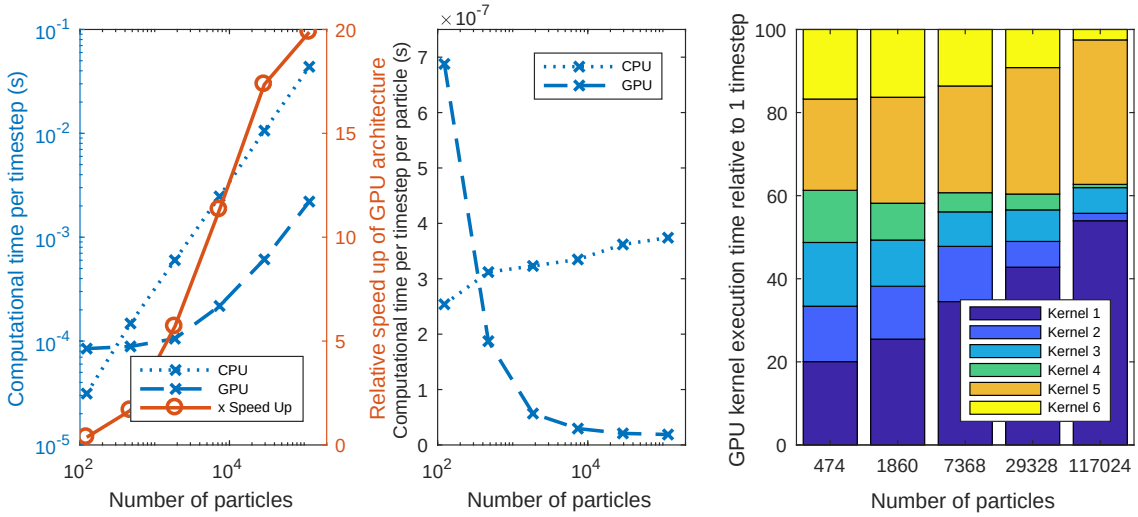

Figure 15: Left: Comparison of computational time between serial CPU V-model and GPU V-model solvers. Right: Contribution of each kernel launch within the GPU algorithm to the total time per timestep. Details of each kernel are provided in Table 2.

data arrangements are possible with the potential for both positive and negative effects on computational performance. A comparison of possible implementations will be explored in a future article with the aim of reducing the number of kernels launched per timestep and in particular reducing the computational cost of kernels 1 and 5 (calculating forces and moments in the bonds, and updating bond orientations). Both kernels have thread counts governed by the number of bonds in the model and their computational cost significantly increases when the resolution increases as shown in Figure 15.

It is also worth noting that, while the V-model solver is currently restricted to 2-D problems, future work will focus on extending the solver to three dimensions in which the computational load will be far greater and therefore significantly increase the necessity of using GPUs for execution.

7. Conclusions

A detailed description of the governing equations and numerical implementation of the modified vector-based discrete element method, known as the V-model, for elastic body applications has been presented. The method has been validated for static and dynamic cases with excellent quantitative agreement in linear geometrical deformation regions and qualitative agreement in non-linear deformation regions. A numerical convergence study has shown that the method is approximately first-order accurate. However it has been demonstrated that care must be taken when discretising the geometry at low resolution given the structured arrangement of the particles and the variation in discretised geometry this can cause. To the best of the authors' knowledge, this is one of the first reported rates of convergence for a discrete element method representation of an elastic body.

The method has been implemented on GPU architecture. Comparison with a serial CPU implementation has shown significant reductions in computational time, approximately 20x. This is due to the explicit and local nature of the method. Future work will focus on investigation of different implementations of the method for GPU architecture which may lead to higher speed-ups, implementation of non-linear constitutive relationships between connected particles and the development of unstructured particle arrangements for complex geometries. With these developments implemented, the V-model has the potential to directly model additional physics such as cracking, rupture, aggregation, growth

and remodelling in elastic materials which have traditionally been modelled using FEM while also modelling heterogeneous materials such as biological tissue without the need for representative macroscale material models.

Acknowledgements This research was supported by the Medical Research Council (MRC) through Grant MR/P025463/1 and by the Economic and Social Research Council (ESRC) through Grant ES/N01393X/1. BO is supported by an EPSRC Doctoral Prize Fellowship (EPSRC Grant EP/N509565/1). BK is supported by a British Heart Foundation (BHF) Personal Chair.

Declaration of conflicting interests
The author(s) declared no potential conflicts of interest with respect to the research, authorship and/or publication of this article.

References

[1] P. Cleary, Large scale industrial DEM modelling, Engineering Computations 21 (2/3/4) (2004) 169–204.

[2] S. Hewitt, L. Margetts, A. Revell, Building a Digital Wind Farm, Archives of Computational Methods in Engineering 0 (0) (2017) 1–21. doi:10.1007/s11831-017-9222-7.

[3] B. Owen, N. Bojdo, A. Jivkov, B. Keavney, A. Revell, Structural modelling of the cardiovascular system, Biomechanics and Modeling in Mechanobiology 17 (5) (2018) 1–26. doi:10.1007/s10237-018-1024-9.

[4] T. Crump, G. Ferté, A. Jivkov, P. Mummery, V. X. Tran, Dynamic fracture analysis by explicit solid dynamics and implicit crack propagation, International Journal of Solids and Structures 110-111 (2017) 113–126. doi:10.1016/j.ijsolstr.2017.01.035.

[5] H. Kim, M. P. Wagoner, W. G. Buttlar, Simulation of Fracture Behavior in Asphalt Concrete Using a Heterogeneous Cohesive Zone Discrete Element Model, Journal of Materials in Civil Engineering 20 (8) (2008) 552–563. doi:10.1061/(ASCE)0899-1561(2008)20:8(552).

[6] I. B. Petsche, G. S. Grest, Molecular dynamics simulations of the structure of closed tethered membranes, Journal de physique. I 3 (8) (1993) 1741–1755. doi:10.1051/jp1:1993213.

[7] D. A. Fedosov, B. Caswell, G. E. Karniadakis, A Multiscale Red Blood Cell Model with Accurate Mechanics, Rheology, and Dynamics, Biophysical Journal 98 (10) (2010) 2215–2225. doi:10.1016/j.bpj.2010.02.002.

[8] P. Brocklehurst, I. Adeniran, D. Yang, Y. Sheng, H. Zhang, J. Ye, A 2D electromechanical model of human atrial tissue using the discrete element method, BioMed Research International 2015 (2015) 854953. doi:10.1155/2015/854953.

[9] D. A. Fedosov, B. Caswell, G. E. Karniadakis, Systematic coarse-graining of spectrin-level red blood cell models, Computer Methods in Applied Mechanics and Engineering 199 (29-32) (2010) 1937–1948. arXiv:NIHMS150003, doi:10.1016/j.cma.2010.02.001.

[10] P. Cundall, A Computer Model for Simulating Progressive, Large-scale Movement in Blocky Rock System, in: Proceedings of the International Symposium on Rock Mechanics, Nancy, 1971, pp. 129–136.

[11] T. M. Evans, J. D. Frost, Multiscale investigation of shear bands in sand: Physical and numerical experiments, International Journal for Numerical and Analytical Methods in Geomechanics 34 (2010) 1634–1650. arXiv:nag.2347, doi:10.1002/nag.

[12] Y. Wang, D. Xu, K. Tsui, Discrete element modeling of contact creep and aging in sand, Journal of Geotechnical and Geoenvironmental Engineering 134 (September) (2008) 1407–1411. doi:10.1061/(ASCE)1090-0241(2008)134:9(1407).

[13] C. L. Martin, H. Camacho-Montes, L. Olmos, D. Bouvard, R. K. Bordia, Evolution of defects during sintering: Discrete element simulations, Journal of the American Ceramic Society 92 (7) (2009) 1435–1441. doi:10.1111/j.1551-2916.2009.03014.x.

[14] A. M. Nasar, Eulerian and Lagrangian Smoothed Particle Hydrodynamics as Models for the Interaction of Fluids and Flexible Structures in Biomedical Flows, Ph.D. thesis, University of Manchester (2016).

[15] K. Liu, W. Liu, Application of discrete element method for continuum dynamic problems, Archive of Applied Mechanics 76 (3-4) (2006) 229–243. doi:10.1007/s00419-006-0018-8.

[16] M. Holeček, F. Moravec, Hyperelastic model of a material which microstructure is formed by balls and springs, International Journal of Solids and Structures 43 (24) (2006) 7393–7406. doi:10.1016/j.ijsolstr.2006.06.031.

[17] V. A. Kuzkin, I. E. Asonov, Vector-based model of elastic bonds for simulation of granular solids, Physical Review E - Statistical, Nonlinear, and Soft Matter Physics 86 (5) (2012) 1–10.

[18] N. Govender, D. N. Wilke, S. Kok, Blaze-DEMGPU: Modular high performance DEM framework for the GPU architecture, SoftwareX 5 (2015) 62–66. doi:10.1016/j.softx.2016.04.004.

[19] L. Zhang, S. F. Quigley, A. H. Chan, A fast scalable implementation of the two-dimensional triangular Discrete Element Method on a GPU platform, Advances in Engineering Software 60-61 (2013) 70–80. doi:10.1016/j.advengsoft.2012.10.006.

[20] S. M. Longshaw, M. J. Turner, E. Finch, R. Gawthorpe, P. Engine, Physics engine based parallelised discrete element model, International Conference on Particle-Based Methods (December 2014) (2009) 1–4.

[21] E. Izadi, A. Bezuijen, Simulating direct shear tests with the Bullet physics library: A validation study, PLoS ONE 13 (4) (2018) 1–28. doi:10.1371/journal.pone.0195073.

[22] A. Di Renzo, F. P. Di Maio, Comparison of contact-force models for the simulation of collisions in DEM-based granular flow codes, Chemical Engineering Science 59 (3) (2004) 525–541. doi:10.1016/j.ces.2003.09.037.

[23] D. V. Griffiths, G. G. W. Mustoe, Modelling of elastic continua using a grillage of structuralelements based on discete element concepts, International Journal for Numerical Methods in Engineering 50 (7) (2001) 1759–1775.

[24] A. Nasar, B. Rogers, A. Revell, P. Stansby, Flexible Slender Body Fluid Interaction: Vector-based Discrete Element Method with Eulerian Smoothed Particle Hydrodynamics, Computers & Fluids 179 (2018) 563–578. doi:10.1016/J.COMPFLUID.2018.11.024.

[25] V. A. Kuzkin, A. M. Krivtsov, Enhanced vector-based model for elastic bonds in solids, arXiv preprint-arXiv:1506.00427, doi:10.1089/ees.2013.0366.

[26] A. R. Harwood, J. O'Connor, J. Sanchez Muñoz, M. Camps Santasmasas, A. J. Revell, LUMA: A many-core, FluidStructure Interaction solver based on the Lattice-Boltzmann Method, SoftwareX 7 (2018) 88–94. doi:10.1016/j.softx.2018.02.004.

[27] P. Schofield, Computer simulation studies of the liquid state, Computer Physics Communications 5 (1) (1973) 17–23. doi:10.1016/0010-4655(73)90004-0.

[28] D. Beeman, Some multistep methods for use in molecular dynamics calculations, Journal of Computational Physics 20 (2) (1976) 130–139. doi:10.1016/0021-9991(76)90059-0.

[29] M. Otsubo, C. O'Sullivan, T. Shire, Empirical assessment of the critical time increment in explicit particulate discrete element method simulations, Computers and Geotechnics 86 (2017) 67–79. doi:10.1016/j.compgeo.2016.12.022.

[30] J.A. Fleischmann, Micromechanics-Based Continuum Constitutive Modeling of Isotropic Non-Cohesive Particulate Materials, Informed and Validated by the Discrete Element Method, Ph.D. thesis, Univeristy of Wisconsin-Madison (2013).

Appendix D

Paper IV - A novel, discrete fluid-structure interaction method: the lattice Boltzmann method, vector-based discrete element method and immersed boundary method.

The following journal paper requires some revision and the addition of an application test case before submission to a journal. The *Journal of Fluids and Structures* has been targeted.

A discrete fluid-structure interaction approach for highly deformable elastic bodies

Benjamin Owen*[a], Joseph O'Connor[a], Adrian R.G. Harwood[a], Nicholas Bojdo[a], Bernard Keavney[b], Alistair Revell[a]

[a]*School of Mechanical, Aerospace and Civil Engineering, University of Manchester, UK*
[b]*Division of Cardiovascular Sciences, University of Manchester, UK*

Abstract

A novel fluid-structure interaction (FSI) method is presented based on discrete numerical methods, where the lattice Boltzmann method models the fluid, the vector-based discrete element method (V-model) represents the structure and the immersed boundary method provides a strong coupling via a block Gauss-Seidel scheme. Each solver is first validated in isolation before the full approach is validated against the well known numerical benchmarking case proposed by Turek and Hron. for the first time the material properties of the structure in this case are modelled directly using a constitutive model in the V-model. The lattice Boltzmann fluid solver is shown to be second order accurate in isolation, while the V-model compares well (<2%) with numerical benchmark data. This represents the first time the V-model has been validated with elastic bodies with large Poisson's ratio ($> 1/3$). Validation of the full approach demonstrates good agreement with the numerical benchmark data with approximately 5% error for the tip deflection Strouhal number. The use of discrete methods allows complex phenomena such as fracture and aggregation to be more readily incorporated in future developments of the presented FSI method.

Keywords: lattice Boltzmann, V-model, FSI, immersed boundary

1. Introduction

The interaction between fluids and structures plays a key role in the dynamics of many complex engineering applications including biomedical flows [1], wind-energy harvesting [2] and aerodynamic flow control [3]. Traditionally, modelling this interaction has required large computational resources for realistic geometries, and has therefore been restricted to simplified representations of problems. However, with the ever increasing power and availability of computational resources, in conjunction with advancements in numerical methods, the complexity of problems modelled by so-called fluid-structure interaction (FSI) methods is increasing rapidly.

The FSI method presented here has been developed for cardiovascular applications. These applications are notoriously difficult to model since they incorporate high levels of deformation and a large added-mass effect due to the similarity of the fluid and structure densities. Despite this, a number of studies have effectively modelled applications across a range of length and time scales, from the flow characteristics of red blood cells through capillaries [4] to the haemodynamics through abdominal aortic aneurysms [5]. In the smaller scale applications, discrete and continuum numerical methods have been used to model cardiovascular structures. However, at larger scales such as aneurysms, continuum methods have generally been used due to the prohibitive computational cost of discrete methods at such scales. However, discrete methods are able to model complex phenomena such as fracture and agglomeration more readily than continuum methods. These complex phenomena often occur in cardiovascular diseases in the form of growth and rupture of atherosclerotic plaques and aneurysms and as a result, developing the ability to efficiently represent these via discrete methods has the potential to significantly improve our understanding of such diseases. However, before representation of such

complex phenomena is possible, careful assessment of the discrete methods should be made to ensure comparative fidelity with currently implemented continuum-based methods.

There are two main approaches to developing FSI methods; known as monolithic and partitioned respectively. The monolithic approach solves the governing equations of the fluid and structure simultaneously, and in general produces highly accurate results since it naturally satisfies the kinematic and dynamic interface conditions between the fluid and structure [6]. In contrast, the partitioned approach solves the governing equations of the fluid and structure sequentially. This can lead to a lag between the fluid and structure dynamics [7]. For problems with a high density ratio between the fluid and structure, this may not pose a large issue. However, for fluid and structure densities within the same order of magnitude, the lag can result in significant energy generation at the boundary which can not only reduce accuracy of the method, but also reduce the stability of the simulation to the point of failure [8]. This type of coupling can be referred to as weak coupling. The issues associated with the lag in partitioned approaches can be overcome using an iterative technique to directly ensure the interface conditions are satisfied before moving onto the next timestep [9]. When the interface conditions are directly satisfied the method can be classified as strongly coupled. Given the motivation behind the development of the FSI solver presented here is cardiovascular applications where density ratios are much less than 10, a strongly coupled approach has been implemented as will be discussed.

For large temporal and spatial scales, the finite volume (FVM) or finite element (FEM) method has generally been employed to model fluids and structures due to their accuracy and computational efficiency at such scales. The use of discrete methods such as the discrete element method (DEM) at such scales has often required prohibitive computational expense. However, the rapid advancement of Graphics Processing Units (GPUs) to which explicit, discrete methods are well suited, has relaxed the limitation of scale somewhat. The lattice Boltzmann method (LBM), which is incorporated here as the fluid solver, uses a structured, uniform grid where operations are local which allows for excellent parallelisation performance [10], particularly on GPUs [11], while the vector-based discrete element method (V-model) has also demonstrated good scalability on GPU architecture [12].

While the computational performance of these methods may not exceed those of traditional methods, their ability to more readily include complex phenomena such as fracture and aggregation, makes them attractive modelling techniques. These phenomena occur in many cardiovascular diseases such as atherosclerotic plaques and aneurysms. However, the ability of the FSI method presented here to accurately model the dynamic interaction between the fluid and structure must be demonstrated before extending the method to included additional physical effects in future work.

In this article, a novel FSI method is presented consisting of an LBM fluid solver, V-model structural solver, coupled using the immersed boundary method in an iterative block Gauss-Seidel scheme. In Section 2 details of these methods are included alongside discussion of the coupling algorithm. Section 3 presents validation cases for the fluid and structure solver in isolation, before validation of the fully-coupled FSI solver before discussion of future work and conclusions including extending the model into three dimensions.

2. Methodology

2.1. Lattice Boltzmann method

The lattice Boltzmann method (LBM) is a mesoscale method capable of modelling fluid flow via the Boltzmann transport equation, as opposed to the traditional Navier-Stokes equations. In recent years, there has been a increasing trend towards the use of the LBM in part due to its superior parallelisation performance to Navier-Stokes solvers such as the Finite Element and Finite Volume methods. As part of the FSI method developed within this work, the ease of coupling with the immersed boundary method (IBM), which a significant number of studies have also utilised [13, 14], as well as its parallelisation performance, in particular in conjunction with GPUs [15], makes it an ideal choice. Here a brief overview of the method implemented within this work is provided, however the interested reader is directed to [16] for more in-depth details of the method as well as discussion of its programming implementation.

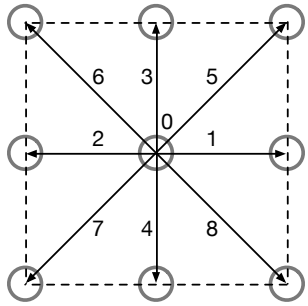

Figure 1: Discrete velocity set for LBM implemented in this work. Numbering corresponds to columns in Eqn 6.

In order to allow for efficient computational calculation, the Boltzmann transport equation is discretised in velocity space via Hermite series expansion [17] and a reduced set of velocities i, is enforced, ensuring that the distribution function components are located at a lattice point on the uniform grid at the end of each timestep. This results in the discrete lattice Boltzmann equation (LBE) which governs the evolution of the flow:

$$f_i(\mathbf{x} + \mathbf{c}_i \Delta t, t + \Delta t) - f_i(\mathbf{x}, t) = \Omega_i \tag{1}$$

where $\mathbf{c}_i$ is the discrete lattice velocity, Δt is the timestep size, Ω_i is the collision operator and $f_i(\mathbf{x}, t)$ is a probability distribution function representing the proportion of particles at lattice site $\mathbf{x}$ and time t with velocity i. It is this use of the probability distribution function as a representation of a number of fluid particles that classifies the LBM as a mesoscale method, somewhere between particle or continuum methods.

The collision operator, difficult to solve in its original double integral form, is simplified via the BGK approximation [18]; the most commonly implemented approximation:

$$\Omega_i = \frac{1}{\tau}(f_i^{eq} - f_i) \tag{2}$$

where τ is the relaxation time and f_i^{eq} is the local equilibrium distribution function, which is dependent on the local macroscopic flow properties only and is defined as:

$$f^{eq}(\boldsymbol{x}, t) = w_i \rho (1 + \frac{\boldsymbol{c}_i \cdot \boldsymbol{u}}{c_s^2} + \frac{(\boldsymbol{c}_i \cdot \boldsymbol{u})^2}{2c_s^4} - \frac{\boldsymbol{u} \cdot \boldsymbol{u}}{2c_s^2}) \tag{3}$$

where w_i are the weights associated with the lattice model which is discussed later in this section. The BGK approximation reduces the complexity of the collision operator by assuming a single relaxation time and is valid for any fluid since Eqn. 2 will relax towards local equilibrium, while f^{eq} contains the non-linearity required to recover macroscopic quantities of the fluid. The relaxation time is calculated with respect to the fluid viscosity ν via:

$$\tau = \frac{\nu}{c_s^2} + \frac{\Delta t}{2} \tag{4}$$

The use of the BGK approximation leads to what is commonly referred to as the lattice BGK (LBGK) model:

$$f_i(\boldsymbol{x} + \boldsymbol{c}_i \Delta t, t + \Delta t) - f_i(\boldsymbol{x}, t) = \frac{\Delta t}{\tau}[f_i^{eq}(\boldsymbol{x}, t) - f_i(\boldsymbol{x}, t)] \tag{5}$$

Within this LBM implementation, the D2Q9 lattice model was adopted defining values for the discretised lattice velocities $\mathbf{c}_i$ (Figure 1), lattice speed of sound c_s and weights w_i as:

$$\boldsymbol{c} = \begin{bmatrix} 0 & 1 & -1 & 0 & 0 & 1 & -1 & 1 & -1 \\ 0 & 0 & 0 & 1 & -1 & 1 & -1 & -1 & 1 \end{bmatrix} \frac{\Delta x}{\Delta t} \tag{6}$$

$$w_i = \begin{cases} 4/9 & i = 0 \\ 1/9 & i = 1, 2, 3, 4 \\ 1/36 & i = 5, 6, 7, 8 \end{cases}$$

$$c_s = \frac{\Delta x}{\Delta t} \frac{1}{\sqrt{3}} \tag{7}$$

where Δt and Δx are the timestep size and lattice spacing in lattice units, therefore $\Delta t = \Delta x = 1$.

The macroscopic density and velocity are evaluated at each lattice point through the sum of moments of each component of the probability distribution function:

$$\rho(\boldsymbol{x}, t) = \sum_{i=0}^{8} f_i(\boldsymbol{x}, t) \tag{8}$$

$$\rho \boldsymbol{u}(\boldsymbol{x}, t) = \sum_{i=0}^{8} \boldsymbol{c}_i f_i(\boldsymbol{x}, t) \tag{9}$$

An additional force is applied to the flow through the immersed boundary coupling, in the form of body force, $\boldsymbol{F}$. A discretised force F_i is calculated using the method proposed by Guo et al. [19]:

$$F_i = w_i (1 - \frac{1}{2\tau})(\frac{\boldsymbol{c}_i - \boldsymbol{u}}{c_s^2} + \frac{\boldsymbol{c}_i \cdot \boldsymbol{u}}{c_s^4} \boldsymbol{c}_i) \cdot \boldsymbol{F} \tag{10}$$

This term is added to Eqn 5 to give:

$$f_i(\boldsymbol{x} + \boldsymbol{c}_i \Delta t, t + \Delta t) - f_i(\boldsymbol{x}, t) = \frac{\Delta t}{\tau} [f_i^{eq}(\boldsymbol{x}, t) - f_i(\boldsymbol{x}, t)] + F_i \tag{11}$$

and also results in modified macroscopic quantity relationships:

$$\rho(\boldsymbol{x}, t) = \sum_{i=0}^{8} f_i(\boldsymbol{x}, t) \tag{12}$$

$$\rho \boldsymbol{u}(\boldsymbol{x}, t) = \sum_{i=0}^{8} \boldsymbol{c}_i f_i(\boldsymbol{x}, t) + \frac{\Delta t}{2} \boldsymbol{F} \tag{13}$$

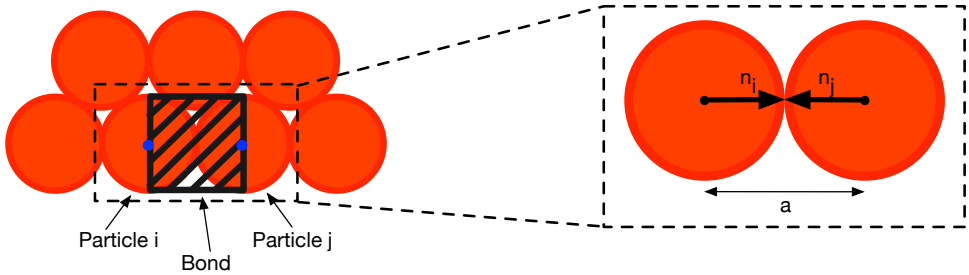

Figure 2: Bond connected to particle centres where bond length and particle diameter are equal.

2.2. Vector-based discrete element method

The vector-based discrete element model, or V-model, is a variant of the Discrete Element Method (DEM) originally proposed by Kuzkin and Asanov [20]. The method was further developed by Nasar et al. for elastic bodies [21]. The basic premise of the V-model, like any DEM applied to elastic bodies, is to discretise a geometry into a collection of particles connected via rigidly attached flexible bonds. Where the V-model differs from conventional DEMs is that displacements are evaluated as total displacements as opposed to an incremental approach. This is significant since the approximation that the sum of incremental displacements is equal to the total displacement of a particle is only appropriate in 2D for small deflections. As a result, on extension of DEMs into 3D, errors can occur in the evaluation of the rotational displacements due to their reliance on the order in which the displacements are evaluated [22]. In contrast the V-model evaluates all displacements, including both translational and angular, as total displacements using one relationship based on the potential energy of the bond which leads to a single total displacement in each degree of freedom. An additional advantage of this approach is the V- model does not suffer from the additional time step limitations required for conventional DEMs.

Once a body has been discretised into a collection of bonded V-model particles, a number of vectors, denoted by $\boldsymbol{n}$, are rigidly attached to each particle that indicate the orientation of the particle in global space and co-rotate with the particle. The number of vectors that exist is governed by the number of particles connected to the particle under consideration. For each connection, one particle is denoted particle i with an orientation vector $\boldsymbol{n}_i$ while the other is particle j with an orientation vector $\boldsymbol{n}_j$ and when the body is in an equilibrium state, are opposite vectors.

The forces and moments within each bond due to the displacement and/or rotation of its connecting particle resulting from an external load are calculated using Eqns. 14-16. Derivation of the governing equations through potential energy of the bond can be found in [20]. Here, the bonds are assumed to connect at the centre of each particle as shown in Figure 2:

$$\boldsymbol{F}_{ij} = B_1(r_{ij} - a) + \frac{B_2}{2r_{ij}}(\boldsymbol{n}_j^1 - \boldsymbol{n}_i^1) \cdot (\boldsymbol{E} - \boldsymbol{e}_{ij}\boldsymbol{e}_{ij}) \tag{14}$$

$$\boldsymbol{M}_{ij} = \frac{B_2}{2}\boldsymbol{e}_{ij} \times \boldsymbol{n}_i^1 + B_3\boldsymbol{n}_j^1 \times \boldsymbol{n}_i^1 \tag{15}$$

$$\boldsymbol{M}_{ji} = \frac{B_2}{2}\boldsymbol{e}_{ij} \times \boldsymbol{n}_j^1 - B_3\boldsymbol{n}_j^1 \times \boldsymbol{n}_i^1 \tag{16}$$

where $\boldsymbol{F}_{ij}$ is the force exerted on particle i by particle j and the opposing force exerted on particle j by particle i, $\boldsymbol{F}_{ji} = -\boldsymbol{F}_{ij}$. Model stiffness coefficients B_{1-3} are related to the macroscopic material stiffness coefficients through analysis of Eqns 14-16 under pure axial, shear and bending deformations as follows:

$$B_1 = C_A \tag{17}$$

$$B_2 = C_D a^2 \tag{18}$$

$$B_3 = C_B - \frac{B_2}{4} \tag{19}$$

where C_A, C_D and C_B are the axial, shear and bending material stiffness coefficients. A number of constitutive relationships can be used to calculate the material stiffness coefficients in relation to the material properties of the body such as Young's Modulus E and Poisson's Ratio ν. Kuzkin and Asonov proposed the use of Euler-Bernoulli and Timoschenko beam theory for granular materials while the relationship developed by Griffiths and Mustoe for 2D implementations of DEMs [23] has been utilised for V-model applications with excellent agreement with analytical results for static and dynamic validation cases and shown first order convergence [24, 12]. However, this model is limited to Poisson ratio's of less than 1/3, else a negative shear coefficient will occur. In the validation cases presented here for the FSI method, the flexible flag has a Poisson's ratio of 0.4 and therefore an alternative constitutive relationship with no Poisson ratio limitation, proposed by Gaeini et al [25], is utilised. This model relates the material stiffness coefficients to the material properties via:

$$C_A = \frac{E}{\sqrt{3}(1-\nu)} \tag{20}$$

$$C_D = \frac{E}{4(1+\nu)} \tag{21}$$

This model was derived for a discrete element method that does not directly consider bending unlike the V-model and therefore an addition relationship is utilised to relate the bending coefficient to the material properties as proposed by Nasar [24]:

$$C_B = \frac{EI_b}{a} \tag{22}$$

where I_b is the moment of inertia of the bond which has a rectangular cross section and a is the equilibrium length of the bond.

Once the forces and moments have been calculated in each of the bonds, the resultant forces $\boldsymbol{F}_i$ and moments $\boldsymbol{M}_i$ can be evaluated on each particle:

$$\boldsymbol{F}_i = \sum_{N_i} \boldsymbol{F}_{ij} + \sum_{N_j} \boldsymbol{F}_{ji} \tag{23}$$

$$\boldsymbol{M}_i = \sum_{N_i} \boldsymbol{M}_{ij} + \sum_{N_j} \boldsymbol{M}_{ji} \tag{24}$$

where N_i and N_j refers to the number of bonds connected to the particle which considers that particle to be particle i or particle j. The translational $\boldsymbol{a}_i$ and angular $\boldsymbol{\alpha}_i$ acceleration of each particle are calculated using Newton's 2nd Law:

$$\boldsymbol{a}_i = \frac{\boldsymbol{F}_i}{m_i} \tag{25}$$

$$\boldsymbol{\alpha}_i = \frac{\boldsymbol{M_i}}{I_i} \tag{26}$$

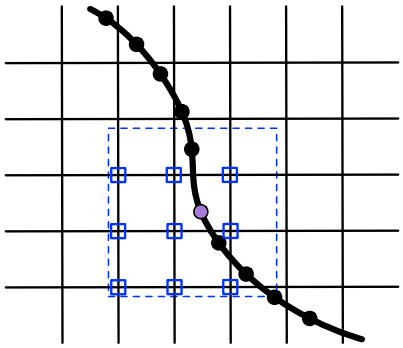

Figure 3: Independent Eulerian (fluid) and Lagrangian (structure) grids, coupled via immersed boundary markers (purple) with associated stencil (blue) spreading required force for no slip condition at the boundary, onto the fluid.

where m_i and I_i are the mass and moment of inertia of particle i. The positions and orientations of each particle are updated at the end of each timestep using Beeman's explicit time integration scheme [26]. Before the algorithm moves on to the next timestep, the vectors $\boldsymbol{n}_{i,j}$ on each particle are updated using a 2D rotation matrix with respect to the new orientation of the particle calculated from the time integration scheme.

2.3. Immersed boundary method

The immersed boundary method (IBM), originally proposed by Peskin [27], interpolates forces between fluid (Eulerian) and structure (Lagrangian) grids that remain independent of each other. This dispenses the need for remeshing due to the deformation of the structure as is required by other coupling methods such as the arbitrary Lagrangian-Eulerian (ALE), which reduces the computational resource requirements of the method.

The IBM implemented here uses Lagrangian markers located along the fluid-structure boundary to interpolate and spread forces between the Eulerian (lower-case notation) and Lagrangian grids (upper-case notation) using the procedure proposed by [28]. The LBM-IBM coupling employs a three point stencil as shown in Figure 3 which will be discussed later in this section. The predicted Eulerian velocity field $\boldsymbol{u}^p$ (where the flow is calculated without consideration of the structure) is interpolated from the Eulerian lattice sites $\boldsymbol{x}$ within the stencil onto the Lagrangian marker position $\boldsymbol{X}$ to predict the velocity at the boundary in Lagrange space using the interpolation function:

$$\Phi(\boldsymbol{X}) = \sum_{\Omega} \phi(\boldsymbol{x})\tilde{\delta}(\boldsymbol{x} - \boldsymbol{X})\Delta x \Delta y \Delta z \tag{27}$$

where ϕ and Φ are the same quantity in the Eulerian and Lagrangian frames, $\boldsymbol{x} = (x, y, z)$, Ω is the computational domain on the Eulerian grid and $\tilde{\delta}$ is the discrete Dirac delta function which will be discussed later in the section. The shorthand notation $I[\phi(\boldsymbol{x})]$ will be used for the interpolation function. Once the LBM step has been completed without consideration of the structure, the macroscopic fluid velocity is defined using Eqn 13 as:

$$\rho \boldsymbol{u}(\boldsymbol{x}, t) = \rho \boldsymbol{u}^p(\boldsymbol{x}, t) + \frac{\Delta t}{2} \boldsymbol{f}_{ib}(\boldsymbol{x}, t) \tag{28}$$

where the corrective force $\boldsymbol{f}_{ib}$, is the force required to impose a no-slip velocity $\boldsymbol{u}$ at the boundary. As a result of the no-slip condition, the fluid velocity at the boundary must be equal to that of the boundary $\boldsymbol{U}^b$, converting Eqn. 28 into the Lagrangian frame yields:

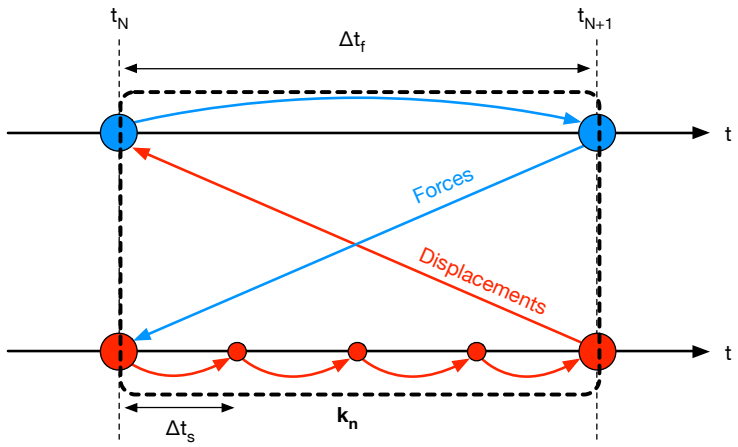

Figure 4: Schematic of the strongly coupled block Gauss-Siedel Scheme. Iterative procedure is indicated through the black dashed box.

$$I[\rho(\boldsymbol{x},t)]\boldsymbol{U}^b(\boldsymbol{X},t) = I[\rho\boldsymbol{u}^p(\boldsymbol{x},t)] + \frac{\Delta t}{2}\boldsymbol{F}_{ib}(\boldsymbol{X},t) \tag{29}$$

The velocity of the boundary is known therefore the above can be rearranged and solved for the corrective force in the Lagrangian frame, which is then spread back to the lattice sites within the stencil using the spreading function:

$$\phi(\boldsymbol{x}) = \sum_{\Gamma} \Phi(\boldsymbol{X})\tilde{\delta}(\boldsymbol{x}-\boldsymbol{X})\epsilon\Delta q\Delta r\Delta s \tag{30}$$

where $\boldsymbol{x} = (x, y, z)$, Γ is the length along the boundary over which the marker acts and ϵ is a scaling factor that ensures reciprocity between the interpolation and spreading functions. The velocity field of the fluid in the vicinity of the boundary can then updated using the corrective force.

The discrete Dirac Delta function $\tilde{\delta}$ is a weighting function used to define the support stencil and the contributions of a quantity at a given location within the stencil. The version of $\tilde{\delta}$ used within this implementation of the immersed boundary method is the three-point version proposed by Roma et al. [29]:

$$\hat{\delta}(r) = \begin{cases} \frac{1}{3}(1+\sqrt{-3r^2+1} & |r| \leq 0.5 \\ \frac{1}{6}(5-3|r|-\sqrt{-3(1-|r|)^2+1} & 0.5 \geq |r| \leq 1.5 \\ 0 & \text{otherwise} \end{cases} \tag{31}$$

2.4. Coupling scheme

The FSI method proposed here is known as a partitioned approach, since the governing equations of the fluid and structure are solver sequentially. While partitioned approaches have a number of advantages over monolithic approaches (where the governing equations are solved simultaneously) such as the ability to use different numerical methods for the fluid and structure, partitioned approaches must explicitly satisfy the kinematic and dynamic conditions at the boundary or else suffer from a reduction in accuracy due to the generation of the energy at the boundary [6].

For a problem under investigation has a large difference in density ratios between the fluid and structure, the issue of energy generation at the boundary is not significant and a weakly coupled scheme, whereby the kinematic and dynamic conditions are not explicitly satisfied, is often sufficient to gain reasonable accuracy. However, for problems where the densities are within an order of magnitude, such as blood and cardiovascular structures, a strongly coupled scheme is essential to ensure both accuracy and stability. The strongly coupled scheme employed here is known as the block Gauss-Seidel scheme and is an iterative approach as shown in Figure 4, which ensures that the velocity of the fluid at the location of the immersed boundary markers, and the velocity of the immersed boundary markers themselves, are equal to within a user-specified tolerance before moving on the next timestep. The full algorithm for a the FSI coupling scheme can summarised as follows:

1. Execute the LBM solver to obtain predicted fluid velocity field
2. Interpolate forces from the fluid to the boundary
3. Calculate correction force required for no slip condition
4. Spread force back to fluid and correct predicted velocity field
5. Execute the V-model solver, updating particle positions based on IBM force
6. Calculate the interface velocity residual
7. if converged, advance to Step 9
8. else relax the boundary displacement and return to Step 2
9. Advance to the next timestep

3. Validation

3.1. Lattice Boltzmann method

The LBM is validated for a simple Poiseuille flow as an intermediary step towards the fully coupled FSI validation. The purpose of the validation is to ensure the LBM solver is able to model the correct velocity profile across the channel, in comparison to the analytical solution, and exhibits the second-order convergence in line with LBM theory when using appropriate boundary conditions.

The case presented here considers a pressure-driven flow between two parallel plates represented using the second-order accurate regularised technique to enforce the no-slip boundary condition [30]. The plates can be consider infinitely long using periodic boundary conditions at the left and right boundaries. The flow, initially at rest, is subject to a pressure gradient in the form of a body force using the method proposed by Guo et al. [19]. The analytical solution to this problem provides a parabolic velocity profile defined by:

$$u_x(y) = -\frac{dp}{dx}\frac{1}{2\rho\nu}y(H-y) \tag{32}$$

where x and y are the streamwise and transverse coordinates respectively, u_x is the streamwise velocity, $\frac{dp}{dx}$ is the pressure gradient, ρ is the fluid density, ν is the kinematic viscosity, and H is the channel height. The analytical and computed velocity profiles are compared in Figure 5, showing excellent agreement.

In order to test the order of convergence of the LBM solver, the error relative to the analytical solution at the centreline ($y = H/2$) is evaluated for a range of grid resolutions. To assess the order of convergence correctly, the compressible error term $O(Ma^2 \propto \Delta t^2/\Delta x^2)$ must scale with resolution, known as diffusive scaling. As a result, as the grid resolution increases, the timestep size scales according to $\Delta t \propto \Delta x^2$. The relative error at the centreline of the channel is compared in Figure 5 and demonstrates second-order rate of convergence.

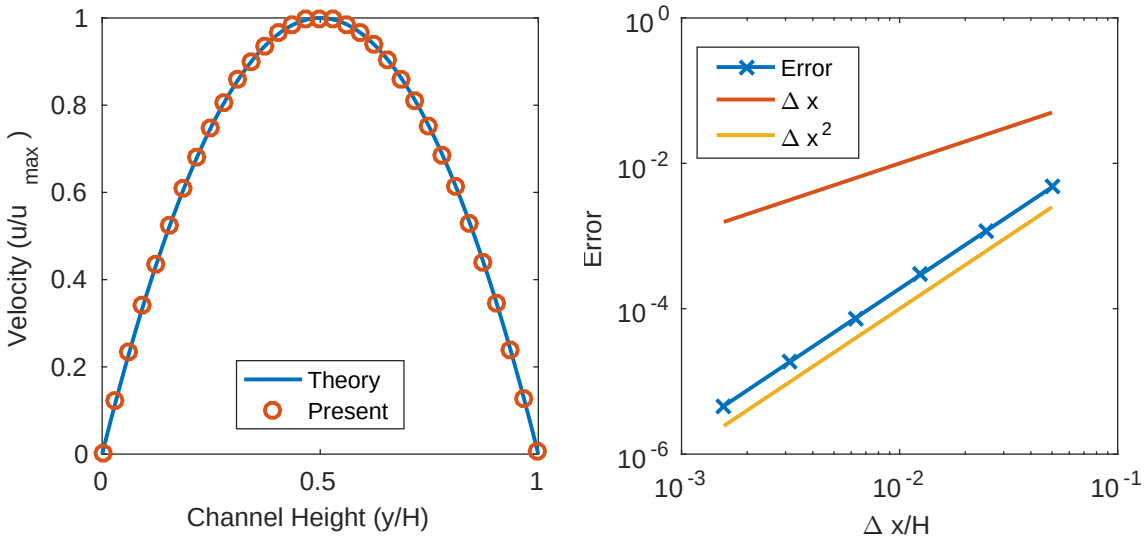

Figure 5: Comparison of the simulated normalised velocity profile of the flow in a channel with the analytical solution (left). Relative error of the simulated centreline velocity in comparison to the analytical solution with increasing grid resolution (right).

3.2. Vector-based discrete element

As part of the numerical benchmarking case used for FSI validation, a preceding case was proposed to validate the structure solver in isolation for the flexible flag included in the FSI case discussed in Section 3.3. The flexible flag, of same dimensions but with density an order of magnitude smaller than the FSI case, is subjected to a reduced gravitational load of 2 m/s^2 while being clamped at one end, analogous to a cantilever beam. The material properties of the flag are provided in Table 1.

Table 1: Material properties of flexible flag in structure validation case.

Material Property	Value (Units)
Young's Modulus	1.4 (MPa)
Poisson's Ratio	0.4
Density	10^3 (kg/m^3)

The maximum and minimum tip deflections for increasing spatial resolutions of the V-model are compared against the benchmark validation data and the results of other studies [8] validated using this case in Table 2. As the resolution of the V-model is increased, the agreement with the benchmark results also improves with the amplitude and frequency of oscillation in close agreement. However, a small difference exists between the equilibrium position of the oscillation. This could indicate that some of the higher order modes of oscillation are not captured by the V-model since the tip deflection does not move beyond the initial position, as is the case with the benchmark and previous study results.

Table 2: Tip deflection results in the y-direction

Solver (Resolution)	Equilibrium Position	Amplitude	Frequency
Turek & Hron [31]	0.0636	0.0652	1.100
O'Connor [8]	0.0642	0.0643	1.099
V-model (144 particles)	0.0698	0.0697	1.053
V-model (1870 particles)	0.0665	0.0665	1.087
V-model (5529 particles)	0.0650	0.0649	1.094

Figure 6 shows tip deflection time history of the V-model at each resolution compared against the non-linear FEM solver implemented in [8]. Here, it is clear that while the highest resolution of V-model provides accurate tip deflections, when the V-model is under-resolved the amplitude of oscillation is over-predicted and the frequency under-predicted. These results are in keeping with previous studies of the V-model [12].

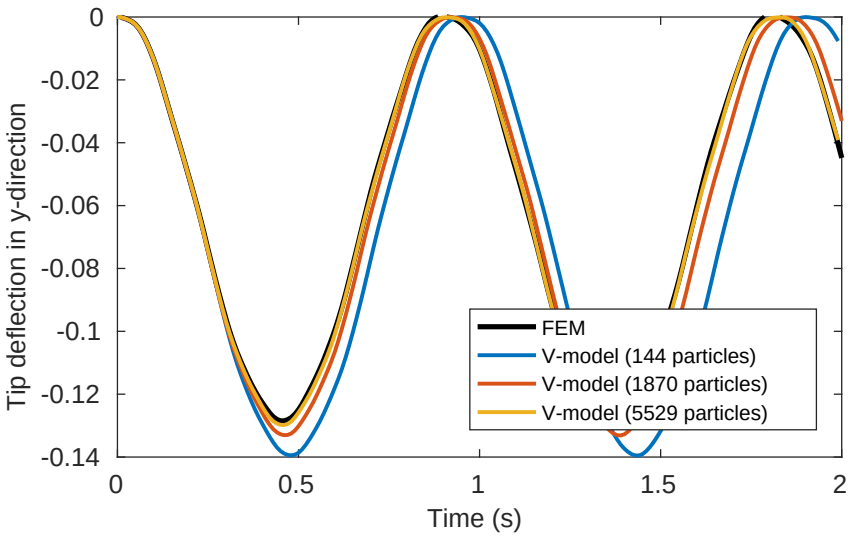

Figure 6: Tip deflection time history of the V-model solver at increasing resolution in comparison to a non-linear FEM solver.

3.3. Fluid-structure interaction

The numerical benchmarking case proposed by Turek and Hron [31] is used to assess the performance of the discrete FSI model presented in this work. The case consists of a rigid cylinder with a flexible flag attached aft of the cylinder, placed in a laminar channel flow as shown in Figure 7. The flexible flag oscillates due to the vortex shedding induced by the flow around the rigid cylinder, eventually reaching a self-sustaining flapping motion.

A parabolic velocity profile is set at the inlet which is ramped over the first two seconds of the simulation according to Eqn 33, while zero-velocity initial conditions are set throughout the domain.

$$u_x(t) = \begin{cases} u_x^{in}(t)\frac{1-cos(\pi t/2}{2} & t \leq 2 \\ u_x^{in}(t) & t > 2 \end{cases} \tag{33}$$

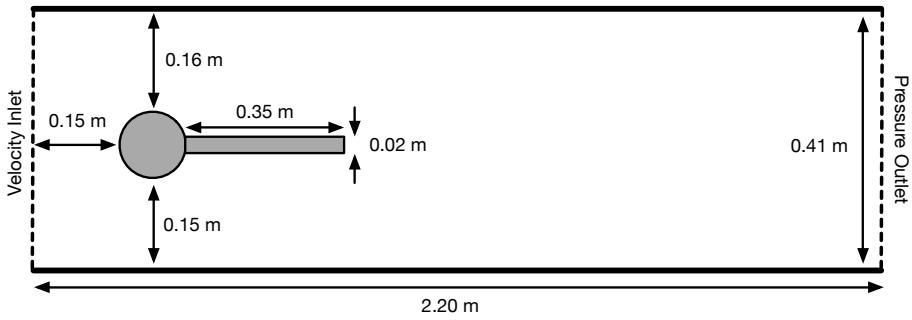

Figure 7: Schematic of the laminar flow around a rigid cylinder with flexible flag in a channel case. Solid lines indicate no-slip boundary conditions.

No-slip conditions are imposed on the walls of the channel using the regularised technique also used in the validation of the LBM solver in isolation presented in Section 3.1. A fixed pressure/density is set at the outlet, where the value is equal to the initial conditions. The material properties of the fluid and structure are included in Table 3.

The rigid cylinder and flexible flag are both discretised into V-model particles. The flexible flag is discretised in the same way as the highest resolution configuration in the V-model only validation case with 5529 particles. Clamped V-model particles are used for the cylinder bringing the total particles to 6543. An example discretisation of the geometry is shown in Figure 8 with reduced resolution of approximately 2000 particles for visualisation purpose.

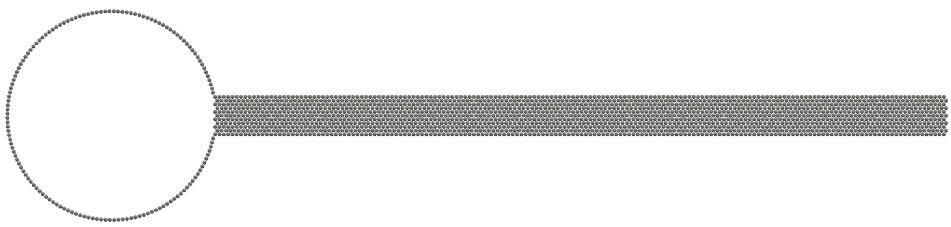

Figure 8: Discretisation of the rigid cylinder and flexible flag into approximately 2000 V-model particles.

Table 3: Laminar flow around a rigid cylinder with flexible flag in a channel case properties.

Fluid Property	Value (Units)	Structure Property	Value (Units)
Density	10^3 (kg/m^3)	Density	10^4 (kg/m^3)
Viscosity	10^{-3} (Pa.s)	Poison's Ratio	0.4
Mean Inlet Velocity	1 (m/s)	Young's Modulus	1.4 (MPa)

The velocity field around the oscillating flag is shown in Figure 9 when the tip is at maximum deflection. The time history of the flexible flag tip deflection is compared to that of the benchmark results of the original study in Figure 10 showing reasonable agreement. The amplitude is over-predicted and the frequency under-predicted, demonstrating similar characteristics to the under-resolved V-model in the

structure only validation case. These characteristics have also been seen in validation cases for the V-model presented in prior studies [21, 12].

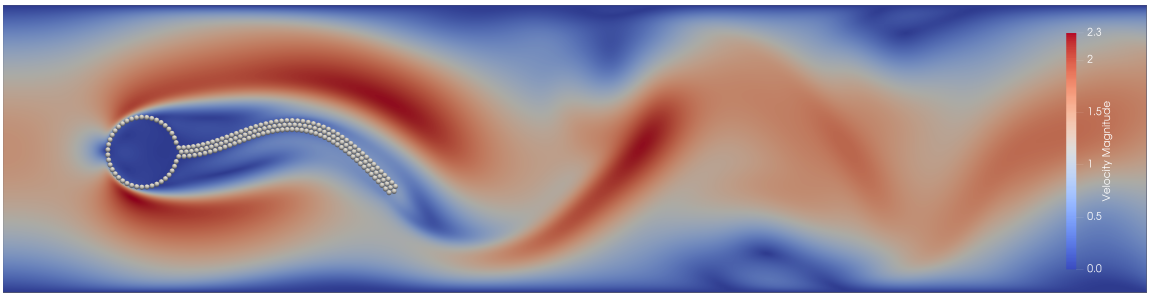

Figure 9: Velocity field around the rigid cylinder and flexible flag when the tip deflection of the flag is at its maximum. V-model resolution of 183 particle shown for visualisation purposes.

Comparison of the Strouhal numbers in Table 4 shows good agreement with the benchmark data as well as results from prior studies using immersed boundary coupling [32, 8]. It is worth noting that in each of these studies used for comparison here, a non-linear finite element solver has been utilised to represent the structure. Since the deflection of the flexible flag is within the geometrically non-linear region ($\Delta x > 20\%$), it is to expected that a non-linear finite element solver performs well. The V-model does not account for the non-linearity directly, since the cross-section of the bonds are not strain dependent and instead relies on increased resolution to capture the correct response. Despite this, the V-model integrated in to the FSI method developed here, performs remarkably well.

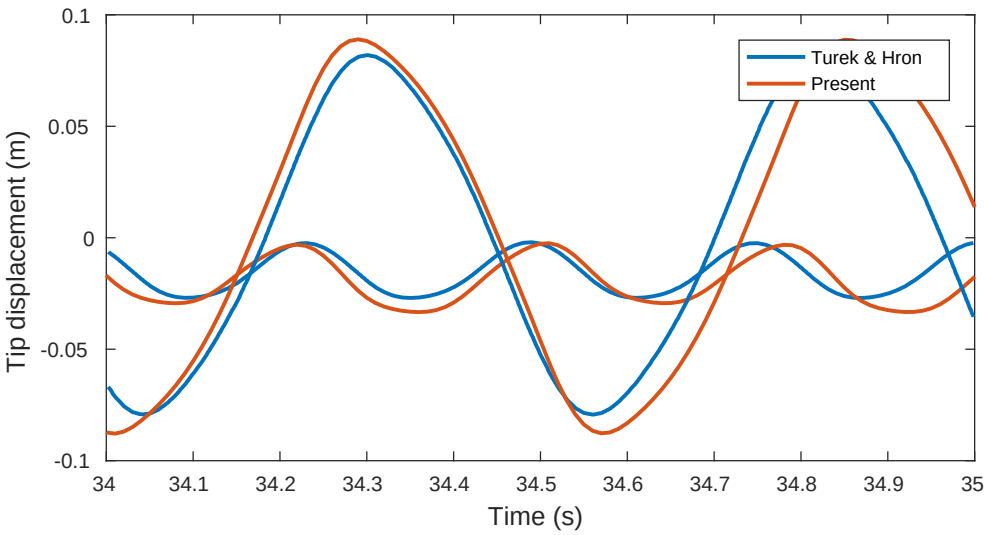

Figure 10: Transverse and axial tip deflection time histories of the V-model in comparison to benchmark data from Turek and Hron [31]

4. Conclusions

A novel fluid-structure interaction method has been developed consisting of discrete numerical methods, namely the lattice Boltzmann method as the fluid solver, the vector-based discrete element method

Table 4: Strouhal numbers of tip deflection in comparison with benchmark data from Turek and Hron [31].

Method (Units)	St (axial)	St (transverse)
Turek and Hron [31]	0.384	0.192
Bhardwaj and Mittal [32]	0.380	0.190
O'Connor [8]	0.370	0.185
Present	0.364	0.182

as the structural solver, strongly coupled using the immersed boundary method using a iterative block Gauss-Siedel scheme. The fluid and structure solver have demonstrated excellent agreement with validation data in isolation, while good agreement has been found with the classic numerical benchmarking case proposed by Turek and Hron [31] for large deformation of a flexible flag induced by laminar flow around a rigid cylinder. The discrete methods employed, and the vector-based discrete element method in particular, present the possibility for the FSI method to include complex phenomena such as fracture and aggregation in future development of the method. Furthermore, each of the numerical methods incorporated into the FSI method, is well suited to implementation on GPU architecture, having been implemented in isolation on such hardware previously [11, 12]. Implementation of the FSI method presented here on GPU architecture presents the next stage in development of this work.

Declaration of conflicting interests

The author(s) declared no potential conflicts of interest with respect to the research, authorship and/or publication of this article.

References

[1] P. Crosetto, P. Reymond, S. Deparis, D. Kontaxakis, N. Stergiopulos, A. Quarteroni, Fluid-structure interaction simulation of aortic blood flow, Computers & Fluids 43 (1) (2011) 46–57. doi:10.1016/j.compfluid.2010.11.032.

[2] S. Hewitt, L. Margetts, A. Revell, Building a Digital Wind Farm, Archives of Computational Methods in Engineering 0 (0) (2017) 1–21. doi:10.1007/s11831-017-9222-7.

[3] J. O'Connor, A. Revell, Dynamic interactions of multiple wall-mounted flexible flaps, Journal of Fluid Mechanics In Press.

[4] T. Krüger, M. Gross, D. Raabe, F. Varnik, Crossover from tumbling to tank-treading-like motion in dense simulated suspensions of red blood cells, Soft Matter 9 (37) (2013) 9008–9015. arXiv:arXiv:1307.0695v2, doi:10.1039/c3sm51645h.

[5] M. Xenos, N. Labropoulos, S. Rambhia, Y. Alemu, S. Einav, A. Tassiopoulos, N. Sakalihasan, D. Bluestein, Progression of Abdominal Aortic Aneurysm Towards Rupture: Refining Clinical Risk Assessment Using a Fully Coupled Fluid-Structure Interaction Method, Annals of Biomedical Engineering 43 (1) (2014) 139–153. doi:10.1007/s10439-014-1224-0.

[6] M. Heil, A. L. Hazel, J. Boyle, Solvers for large-displacement fluid-structure interaction problems: Segregated versus monolithic approaches, Computational Mechanics 43 (1) (2008) 91–101. doi:10.1007/s00466-008-0270-6.

[7] C. Farhat, M. Lesoinne, P. LeTallec, Load and motion transfer algorithms for fluid/structure interaction problems with non-matching discrete interfaces: Momentum and energy conservation, optimal discretization and application to aeroelasticity, Computer Methods in Applied Mechanics and Engineering 157 (1-2) (1998) 95–114. doi:10.1016/S0045-7825(97)00216-8.

[8] J. O'Connor, Fluid-structure interactions of wall-mounted flexible slender structures, Ph.D. thesis, University of Manchester (2018).

[9] S. Desparis, M. A. Fernandez, L. Formaggia, Acceleration of a fixed point algorithm for fluid-structure interaction using transpiration conditions, ESAIM: Mathematical Modelling and Numerical Analysis 37 (2003) 601–616. arXiv:0608007.

[10] A. R. G. Harwood, J. O'Connor, J. Sanchez Muñoz, M. Camps Santasmasas, A. J. Revell, LUMA: A many-core, FluidStructure Interaction solver based on the Lattice-Boltzmann Method, SoftwareX 7 (2018) 88–94. doi:10.1016/j.softx.2018.02.004.

[11] A. R. G. Harwood, A. J. Revell, Interactive flow simulation using Tegra-powered mobile devices, Advances in Engineering Software 115 (August 2017) (2018) 363–373. doi:10.1016/j.advengsoft.2017.10.005.

[12] B. Owen, A. Nasar, A. Harwood, S. Hewitt, N. Bojdo, B. Keavney, B. Rogers, A. Revell, Vector-based discrete element method for solid elastic materials, Under Review.

[13] C. K. Aidun, J. R. Clausen, Lattice-Boltzmann Method for Complex Flows, Annual Review of Fluid Mechanics 42 (1) (2009) 439–472. doi:10.1146/annurev-fluid-121108-145519.

[14] T. Krüger, F. Varnik, D. Raabe, Efficient and accurate simulations of deformable particles immersed in a fluid using a combined immersed boundary lattice Boltzmann finite element method, Computers and Mathematics with Applications 61 (12) (2011) 3485–3505. doi:10.1016/j.camwa.2010.03.057.

[15] M. J. Mawson, A. J. Revell, Memory transfer optimization for a lattice Boltzmann solver on Kepler architecture nVidia GPUs, Computer Physics Communications 185 (10) (2014) 2566–2574. doi:10.1016/j.cpc.2014.06.003.

[16] T. Krüger, H. Kusumaatmaja, A. Kuzmin, O. Shardt, G. Silva, E. M. Viggen, The Lattice Boltzmann Method: Principles and Practice, Springer Nature, 2017.

[17] X. Shan, X. He, Discretization of the velocity space in the solution of the boltzmann equation, Physical Review Letters 80 (1) (1998) 65–68. doi:10.1103/PhysRevLett.80.65.

[18] P. Bhathagar, E. Gross, M. Krook, A model for collision processes in gases, Physical Review 94 (3) (1954) 515–525. doi:10.1103/PhysRev.94.511.

[19] Z. Guo, C. Zheng, B. Shi, Discrete lattice effects on the forcing term in the lattice Boltzmann method, Physical Review E - Statistical Physics, Plasmas, Fluids, and Related Interdisciplinary Topics 65 (4) (2002) 6. doi:10.1103/PhysRevE.65.046308.

[20] V. A. Kuzkin, I. E. Asonov, Vector-based model of elastic bonds for DEM simulation of solids, Mechanical Engineering 86 (5) (2012) 1–10.

[21] A. M. A. Nasar, B. D. Rogers, A. Revell, P. K. Stansby, Flexible slender body fluid interaction: Vector-based discrete element method with Eulerian smoothed particle hydrodynamics, Computers and Fluids 179 (2019) 563–578. doi:10.1016/j.compfluid.2018.11.024.

[22] Y. Wang, A new algorithm to model the dynamics of 3-D bonded rigid bodies with rotations, Acta Geotechnica 4 (2) (2009) 117–127. doi:10.1007/s11440-008-0072-1.

[23] D. V. Griffiths, G. G. W. Mustoe, Modelling of elastic continua using a grillage of structural elements based on discete element concepts, International Journal for Numerical Methods in Engineering 50 (7) (2001) 1759–1775.

[24] A. M. A. Nasar, Eulerian and Lagrangian Smoothed Particle Hydrodynamics as Models for the Interaction of Fluids and Flexible Structures in Biomedical Flows, Ph.D. thesis, University of Manchester (2016).

[25] M. Gaeini, S. Mihradi, H. Homma, Discrete Element Model for Continuum Dynamic Problems, Journal of Solid Mechanics and Materials Engineering 2 (12) (2008) 1478–1486. doi:10.1299/jmmp.2.1478.

[26] D. Beeman, Some multistep methods for use in molecular dynamics calculations, Journal of Computational Physics 20 (2) (1976) 130–139. doi:10.1016/0021-9991(76)90059-0.

[27] C. S. Peskin, Flow patterns around heart valves: A numerical method, Journal of Computational Physics 10 (2) (1972) 252–271.

[28] Z. Li, J. Favier, A non-staggered coupling of finite element and lattice Boltzmann methods via an immersed boundary scheme for fluid-structure interaction, Computers and Fluids 143 (2017) 90–102. doi:10.1016/j.compfluid.2016.11.008.

[29] A. M. Roma, C. S. Peskin, M. J. Berger, An Adaptive Version of the Immersed Boundary Method, Journal of Computational Physics 153 (2) (1999) 509–534. doi:10.1006/jcph.1999.6293.

[30] J. Latt, B. Chopard, O. Malaspinas, M. Deville, A. Michler, Straight velocity boundaries in the lattice Boltzmann method, Physical Review E - Statistical, Nonlinear, and Soft Matter Physics 77 (5) (2008) 1–16. doi:10.1103/PhysRevE.77.056703.

[31] S. Turek, J. Hron, Proposal for Numerical Benchmarking of Fluid-Structure Interaction between an Elastic Object and Laminar Incompressible Flow, Fluid-Structure Interaction (2007) 371–385doi:10.1007/3-540-34596-5-15.

[32] R. Bhardwaj, R. Mittal, Benchmarking a Coupled Immersed-Boundary-Finite-Element Solver for Large-Scale Flow-Induced Deformation, AIAA Journal 50 (7) (2012) 1638–1642. doi:10.2514/1.j051621.